



MONASH University

**The Synthesis of Nanomaterials via Polymerisation-Induced Self-
Assembly and their Biological Interactions**

Song Yang Khor

Bachelor of Pharmaceutical Science (Honours)

A thesis submitted for the degree of Doctor of Philosophy at

Monash University in Feb 2019

Drug Delivery, Disposition and Dynamics

Monash Institute of Pharmaceutical Sciences

Copyright notice

© Song Yang Khor (2019).

I certify that I have made all reasonable efforts to secure copyright permissions for third-party content included in this thesis and have not knowingly added copyright content to my work without the owner's permission.

Table of Contents

Abstract.....	7
Declaration.....	9
Publications during enrolment	10
Thesis including published works declaration.....	11
Acknowledgements.....	14
Abbreviations.....	16
CHAPTER 1: General Introduction	19
1.1 The current state of polymeric nanoparticles for human health.....	20
1.2 Polymeric nanoparticles for nanomedicine.....	23
1.3 A brief overview of RAFT polymerisation.....	27
1.4 The RAFT polymerisation mechanism.....	28
1.5 Polymerisation-Induced Self-Assembly: Nanoparticles with bespoke size and morphology	36
1.6 Biomedical applications of PISA.....	51
1.7 Emerging challenges of nanomedicine	55
1.8 Bio-nano interactions of polymeric nanoparticles	58
1.9 Aims.....	70
1.10 References	72
CHAPTER 2: Elucidating the Influences of Size, Surface Chemistry, and Dynamic Flow on Cellular Association of Nanoparticles Made by Polymerization-Induced Self-Assembly....	102
Supporting information.....	116
CHAPTER 3: Nanoparticle Size and Surface Chemistry Dictates the Abundance of Linear Fibrinogen Proteins in the Protein Corona When Exposed to Human Plasma.....	132
3.1 Introduction.....	133
3.2 Materials and methods	135
3.2.1 Materials	135
3.2.2 Dyanmic light scattering and zeta potential.....	136

3.2.3	Collection and processing of human plasma	136
3.2.4	Protein corona formation and isolation.....	137
3.2.5	In-gel proteolytic digestion, plasma control sample preparation, LC-MS/MS analysis and label-free quantification....	137
3.2.6	Method of protein hit filtering and significance	138
3.3	Results and discussion	138
3.3.1	Synthesis of PISA Nanoparticles with Various Surface Chemistries and Sizes 139	
3.3.2	Summary of the human protein coronae	140
3.3.3	Serotransferrin and immunoglobulin proteins are highly enriched in the protein corona	149
3.3.4	Nanoparticle surface chemistry and size dictate fibrinogen association	152
3.4	Conclusion	153
3.5	References.....	155

CHAPTER 4: Nanoparticle Size and Surface Chemistry Influences Phagocytic Cell

	Association in Whole Human Blood	161
4.1	Introduction.....	162
4.2	Experimental Section	165
4.2.1	Nanoparticle Synthesis.....	165
4.2.1.1	Materials	165
4.2.1.2	Synthesis of Cy5-labelled nanoparticles.....	167
4.2.2	Measurement of nanoparticle fluorescence intensity.....	167
4.2.3	Blood acquisition	168
4.2.4	High-Throughput Screening (HTS) Assay for Particle Association with WBC Populations	168
4.2.5	HTS Assay for Association with Peripheral Blood Mononuclear Cells.....	169
4.2.6	Statistical Analyses	171
4.2.7	Multiple Linear Regression Analyses.....	171

4.3	Results.....	171
4.3.1	Nanoparticle Synthesis and Characterization	171
4.3.2	Quantification of nanoparticle fluorescence intensity via Cy5 MESF beads ...	173
4.3.3	Analysis of nanoparticle-WBC association data.....	175
4.3.4	TA Surface Chemistry Enhances Association with Phagocytic WBC Population	176
4.3.5	Phagocytic and Nonphagocytic Cell Association Increases as Nanoparticle Size Increases.....	177
4.3.6	Blood proteins affect immune cell association with COOH- and PEG-terminated Nanoparticles	184
4.3.7	Phagocytic Association with Nanoparticles is Strongly Predicted by Nanoparticle Size and Surface Chemistry	186
4.4	Conclusoin	191
4.5	References.....	192
CHAPTER 5: Polymerization-Induced Self-Assembly: The Effect of End Group and Initiator Concentration on Morphology of Nanoparticles Prepared via RAFT Aqueous Emulsion Polymerization.....		
	Supporting information.....	206
CHAPTER 6: Conclusion.....		
6.1	Conclusion.....	225
Appendix		
Controlling Nanomaterial Size and Shape for Biomedical Applications via Polymerization-Induced Self-Assembly		
		228
Thiol-Reactive Star Polymers Display Enhanced Association with Distinct Human Blood Components.....		
		250

Abstract

Advancing the use of polymeric nanoparticles for human health has the potential to improve clinical applications such as drug delivery, diagnostic imaging, and immunotherapy. A key advantage in the clinical use of polymeric nanoparticles lies in the configurability of their physicochemical properties, which imparts a high degree of adaptability to navigate various biological environments. However, there is a scarcity of polymeric nanoparticle systems wherein the main physicochemical properties (size, shape, and surface chemistry) may be systematically tuned in a facile and reproducible manner. Consequently, there is key knowledge gap in the biological interactions of such nanoparticle systems with human cells. This thesis details the development of a polymeric nanoparticle platform that enables the synthesis of a library of nanoparticles with tuneable size, shape, and surface chemistry, and investigates how such material properties influence biological interactions. Ultimately, the development of an advanced nanoparticle platform and the characterisation of their biological interactions has the potential to guide the rational design of novel nanoparticles for clinical use.

Chapter 1 provides an overview of the current landscape of polymeric nanoparticles for clinical applications. Then, the synthesis of functional nanoparticles via polymerisation-induced self-assembly (PISA) and their potential clinical applications is discussed. Lastly, the biological interactions that nanoparticles undergo after administration is detailed.

In Chapter 2, the facile synthesis of a library of polystyrene nanoparticles with various sizes and surface chemistries via a one-pot PISA methodology is reported. This library of fluorescent nanoparticles was subjected to a cellular association assay under dynamic flow conditions and static conditions. Interestingly, the results showed that increasing the size of carboxylic acid-functionalised nanoparticles led to higher cellular association under static conditions but lower cellular association under flow conditions. Conversely, increasing the size of tertiary amine-decorated nanoparticles resulted in high cellular association under both static and flow conditions.

In Chapter 3, a quantitative and qualitative analysis of the protein corona of the aforementioned library of polystyrene nanoparticles was carried out. When incubated in human plasma for 16 h, the nanoparticles possessed substantially similar compositions of proteins regardless of size and surface chemistry. Also, the protein coronas of all nanoparticles were found to be enriched in transferrin and immunoglobulin proteins. Finally, tertiary amine-terminated nanoparticles displayed a size-dependent association with linear fibrinogen proteins and an inverse size-dependent association with the alpha-2-macroglobulin protein.

In Chapter 4, the library of nanoparticles disclosed in Chapter 2 was subjected to a whole human blood assay. The nanoparticles were incubated in fresh whole human blood and their association with immune cells characterised on a flow cytometer. The results in Chapter 4 showed that i) surface chemistry significantly influences association with monocytes and neutrophils, ii) larger nanoparticles are more avidly associated with immune cells compared to smaller nanoparticles, iii) the absence of plasma proteins increases peripheral blood mononuclear cell association with carboxylic acid- and poly(ethylene glycol)-terminated nanoparticles, and iv) size is a statistically more significant predictor of immune cell association than surface chemistry.

In Chapter 5, the formation of nanoparticles with spherical, vesicular, and worm-like morphologies via PISA under reversible addition-chain transfer (RAFT) aqueous emulsion polymerisation conditions is reported. The formation of the vesicle morphology was triggered upon increasing the RAFT end-group hydrophobicity or manipulating the radical initiator concentration. Furthermore, decreasing the molecular weight of the polystyrene domain led to the formation of worms. Importantly, this work demonstrated that RAFT end-group hydrophobicity and radical initiator concentration are new parameters which can be exploited to gain access to spherical, worm-like, and vesicular nanoparticle morphologies.

Declaration

This thesis contains no material which has been accepted for the award of any other degree or diploma at any university or equivalent institution and that, to the best of my knowledge and belief, this thesis contains no material previously published or written by another person, except where due reference is made in the text of the thesis.

Signature:

Print Name:

Date:

Publications during enrolment

Khor SY, Quinn JF, Whittaker MR, Truong NP, Davis TP. Controlling Nanomaterial Size and Shape for Biomedical Applications via Polymerization-Induced Self-Assembly. *Macromolecular rapid communications*. **2019** Jan;40(2):1800438.

Khor SY, Vu MN, Pilkington EH, Johnston AP, Whittaker MR, Quinn JF, Truong NP, Davis TP. Elucidating the Influences of Size, Surface Chemistry, and Dynamic Flow on Cellular Association of Nanoparticles Made by Polymerization-Induced Self-Assembly. *Small*. **2018** Aug;14(34):1801702.

Khor SY, Truong NP, Quinn JF, Whittaker MR, Davis TP. Polymerization-induced self-assembly: The effect of end group and initiator concentration on morphology of nanoparticles prepared via RAFT aqueous emulsion polymerization. *ACS Macro Letters*. **2017** Aug 31;6(9):1013-9.

Glass JJ, Li Y, De Rose R, Johnston AP, Czuba EI, **Khor SY**, Quinn JF, Whittaker MR, Davis TP, Kent SJ. Thiol-Reactive Star Polymers display enhanced association with distinct human blood components. *ACS applied materials & interfaces*. **2017** Apr 3;9(14):12182-94.

Khor SY, Hu J, McLeod VM, Quinn JF, Porter CJ, Whittaker MR, Kaminskas LM, Davis TP. The pharmacokinetics and biodistribution of a 64 kDa PolyPEG star polymer after subcutaneous and pulmonary administration to rats. *Journal of pharmaceutical sciences*. **2016** Jan 1;105(1):293-300.

Khor SY, Hu J, McLeod VM, Quinn JF, Williamson M, Porter CJ, Whittaker MR, Kaminskas LM, Davis TP. Molecular weight (hydrodynamic volume) dictates the systemic pharmacokinetics and tumour disposition of PolyPEG star polymers. *Nanomedicine: Nanotechnology, Biology and Medicine*. **2015** Nov 1;11(8):2099-108.

Thesis including published works declaration

I hereby declare that this thesis contains no material which has been accepted for the award of any other degree or diploma at any university or equivalent institution and that, to the best of my knowledge and belief, this thesis contains no material previously published or written by another person, except where due reference is made in the text of the thesis.

This thesis includes 2 original papers published in peer reviewed journals and no submitted publications. The core theme of the thesis is the synthesis of polymeric nanoparticles and their biological interactions with human cells. The ideas, development and writing up of all the papers in the thesis were the principal responsibility of myself, the student, working within the Drug Delivery, Disposition and Dynamics, Monash Institute of Pharmaceutical Sciences under the supervision of Prof. Thomas Davis, Prof. Stephen Kent, Dr Michael Whittaker, and Dr John Quinn.

The inclusion of co-authors reflects the fact that the work came from active collaboration between researchers and acknowledges input into team-based research.

In the case of Chapters 2 and 5, my contribution to the work involved the following:

Thesis Chapter	Publication Title	Status	Nature and % of student contribution	Co-author name(s) Nature and % of Co-author's contribution	Co-author(s), Monash student Y/N*
2	Elucidating the Influences of Size, Surface Chemistry, and Dynamic Flow on Cellular Association of Nanoparticles Made by Polymerization-Induced Self Assembly	Published	50% Developed synthesis protocol for the production of a library of fluorescent nanoparticles, analysed biological data with MNV, prepared manuscript	MNV, EHP, APRJ, MRW, JFQ, NPT, TPD developed and carried out the biological testing, provided supervision, and edited and provided input into manuscript preparation (50%)	MNV is a Monash student

5	Polymerization-Induced Self-Assembly: The Effect of End Group and Initiator Concentration on Morphology of Nanoparticles Prepared via RAFT Aqueous Emulsion Polymerization	Published	70% Experimental design, data collection, analysis, manuscript preparation	1) NPT provided expertise and supervision on experimental design, data collection, analysis, and manuscript preparation (20%) 2) JFQ, MRW, TPD provided supervision and provided input into manuscript preparation (10%)	None
---	--	-----------	---	---	------

I have renumbered sections of submitted or published papers in order to generate a consistent presentation within the thesis.

Student signature:

Date:

The undersigned hereby certify that the above declaration correctly reflects the nature and extent of the student's and co-authors' contributions to this work. In instances where I am not the responsible

author I have consulted with the responsible author to agree on the respective contributions of the authors.

Main Supervisor signature:

Date:

Acknowledgements

I sincerely express my gratitude to Professor Thomas Davis, Dr Michael Whittaker, Dr John Quinn, for their tireless supervision since the start of my PhD at Monash University in 2015. Tom's leadership and expertise in the field of nanomedicine resulted PhD projects that were both timely and of keen interest to the scientific community. Mikey and John have provided me with excellent supervision and inspiration throughout my Honours and PhD years. Without them, this thesis would not have been possible.

I would also like to sincerely thank Professor Stephen Kent and members of the Kent lab (Hannah Kelly, Adam Wheatley, Joshua Glass, Vinca Alcantara, Thaksila Amarasena). Stephen has always provided critical insight and timely feedback throughout my work, for which I am very grateful.

To all members of the CBNS lab at MIPS past and present, including Nghia, Pu-Chun, Kristian, Ximo, Fran, Adrian, Lars, Qiuming, Yuhuan, Ruirui, Emily, Ayaat, Joanne, James, Carlos, Paulina, Jeffri, May, Marvin, Mai, Alex M., Alex K., Stefan, Aadarash, and Ibrahim, I am very grateful for many years of support, friendship, and joy. In particular, I would like to extend my gratitude to Nghia, who has provided me with invaluable advice on my research direction and also mentorship in the laboratory. Everyone in the CBNS lab at MIPS have made the lab an awesome place to work and I hope that we can stay in touch for many years.

The research carried out at the CBNS lab at MIPS would not have been possible without the incredible support provided by Natalie, Anne, Charlotte, and, of course, Katrina.

I also extend my gratitude to all members of the technical staff at MIPS for their technical expertise and care. In addition, I am grateful for the critical advice provided by PhD panel members Dr Angus Johnston, Professor Colin Pouton, and Associate Professor Erica Sloan.

This research was supported by an Australian Government Research Training Program (RTP) Scholarship.

To Ma, Pa, and Jing, I love you all very much and I am very grateful to all the endless love and support you have provided.

Finally, to my lovely wife, my best friend, and my soul mate, Elly Yu. This thesis marks the culmination of your years of love and unconditional support for me. I am infinitely blessed that I met you during our PhD and we could spend every day in the lab together. I look forward to having you by my side as we journey through life together.

Song Yang Khor

Abbreviations

A2M	Alpha 2 macroglobulin
ACPA	4,4' Azobis(4-cyanopentanoic acid)
CDCl ₃	Deuterated chloroform
CTA	Chain transfer agent
D ₂ O	Deuterium oxide
DCC	Dicyclohexylcarbodiimide
DLS	Dynamic light scattering
DMAC	N,N-Dimethylacetamide
DMAP	4-dimethylaminopyridine
DMF	Dimethylformamide
DMSO	Dimethyl sulfoxide
ECT	4-Cyano-4-(ethylthiocarbonothioylthio) pentanoic acid
FGA	Fibrinogen alpha chain
FGB	Fibrinogen beta chain
FGG	Fibrinogen gamma chain
HEAA	N-hydroxyethyl acrylamide
HEPES	4-(2-hydroxyethyl)-1-piperazineethanesulfonic acid

HUVEC	Human umbilical vein cells
HTS	High-throughput system
IGHG1	Immunoglobulin heavy constant gamma 1
IGHG2	Immunoglobulin heavy constant gamma 2
LC-MS/MS	Liquid chromatography-tandem mass spectrometry
LFQ	Label-free quantification
Macro-CTA	Macromolecular chain transfer agent
MESF	Molecules of equivalent soluble fluorochrome
MFI	Median fluorescence intensity
MLR	Multiple linear regression
MRI	Magnetic resonance imaging
NMR	Nuclear magnetic resonance
PBMC	Peripheral blood mononuclear cell
PBS	Phosphate Buffered Saline
PDI	Polydispersity index
PEG	Poly(ethylene glycol) methyl ether
PEGA	Poly(ethylene glycol) methyl ether acrylate
PISA	Polymerisation-induced self-assembly
PSD	Particle size distribution

RAFT	Reversible addition-fragmentation chain transfer
RBC	Red blood cell
RPA	Relative protein abundance
RT	Room temperature
SEC	Size exclusion chromatography
SEM	Standard error of the mean
SMN	Synthetic microvascular network
Sty	Styrene
TEM	Transmission electron microscopy
TF	Transferrin
THF	Tetrahydrofuran
WBC	White blood cell

Chapter 1: General Introduction

1.1 The current state of polymeric nanoparticles for human health

Over the past few decades, the application of polymeric nanoparticles towards the diagnosis and treatment of human diseases (commonly referred to as nanomedicine) has emerged as an important development in modern medicine (1-4). This trend is largely attributed to the unique physicochemical properties of polymeric nanoparticles, which has enabled them to be applied towards applications in drug delivery, imaging, diagnosis, vaccines, and medical devices (Figure 1). Importantly, polymeric nanoparticles may be modified via various chemical conjugation and loading techniques to carry drugs and imaging agents (5-7) (Figure 1) that enable both the diagnosis and treatment of diseases. Therefore, it is no surprise that a great amount of promise has been associated with the application of polymeric nanoparticles towards diseases such as cancer (1, 8), infectious and immune diseases (9, 10), neurodegenerative diseases (11, 12), diabetes (13), and orthopaedic problems (14). Yet, many in the field believe that there is a long road ahead before nanomedicines can fulfil their potential (15, 16). To advance the field towards clinical applications of polymeric nanoparticles, this thesis investigates the novel synthesis of a polymeric nanoparticle platform with several tuneable physicochemical properties and establishes structure-property relationships with respect to human cell interactions.

In recent years, there is a need to increase the tunability of the physicochemical properties of polymeric nanoparticles based on the desired medical application in light of growing evidence in the literature that the physicochemical properties of polymeric nanoparticles dictate their biological interactions and biological fate (17, 18). For instance, polymeric nanoparticles with a higher-order morphology (such as worm-like nanoparticles) have displayed a more persistent circulation time than spherical nanoparticles in biological systems (19). In another example, the hydrodynamic diameter of core crosslinked star polymers has

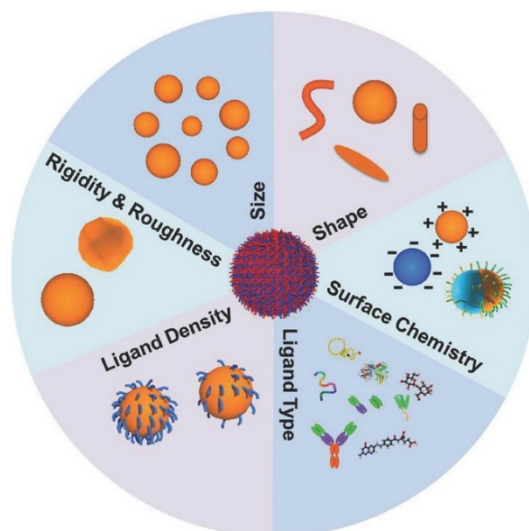


Figure 1. Several of the tunable physicochemical properties of nanoparticles. Adapted from Dai *et al.* (20) with permission from Wiley.

been shown to significantly influence their pharmacokinetics and biodistribution *in vivo* (21). The increased interest in the systematic modification of nanoparticle physicochemical properties has consequently spurred the development of new synthesis technologies that enable facile control over multiple nanoparticle physicochemical properties. Recently, the development of an alternative self-assembly strategy, termed polymerisation-induced self-assembly (PISA) has shown great potential for the facile synthesis of nanoparticles with several tuneable physicochemical properties (22, 23). For example, for some PISA conditions, a myriad of nanoparticle morphologies including worm-like, vesicle, lamella, etc. with controllable particle sizes and surface chemistries have been achieved (24, 25). Furthermore, the significant advantage of PISA formulations is that they are conducted at relatively high solids content (25 -50% wt) (26, 27); an attractive proposition for industrial-scale manufacturing. In practice, PISA may be conducted with any type of living polymerisation technique (28-30). Yet, most PISA syntheses in the literature are conducted under reversible addition-fragmentation chain transfer (RAFT) polymerisation conditions (31-35). RAFT

polymerisation enables the PISA technique to be conducted with a diverse range of monomers and solvents (aqueous and non-aqueous). While PISA syntheses conducted via RAFT polymerisation has made significant progress, further advancements in the technology will better equip scientists for the rational design of nanoparticles for human health.

Forthcoming developments in the use of polymeric nanoparticles such as PISA nanoparticles for human health must be informed by a better understanding of their interactions with biological systems. Specifically, due to the versatility of their physicochemical characteristics, it is imperative to investigate the biological impact of their various physicochemical characteristics (Figure 2). However, much of the current knowledge of bio-nano interactions based on a nanoparticle's physicochemical characteristics is derived from studies in cell lines and rodent models. Consequently, there is a gap in our understanding of how nanomedicines interact with primary human systems. In particular, there is a dearth of

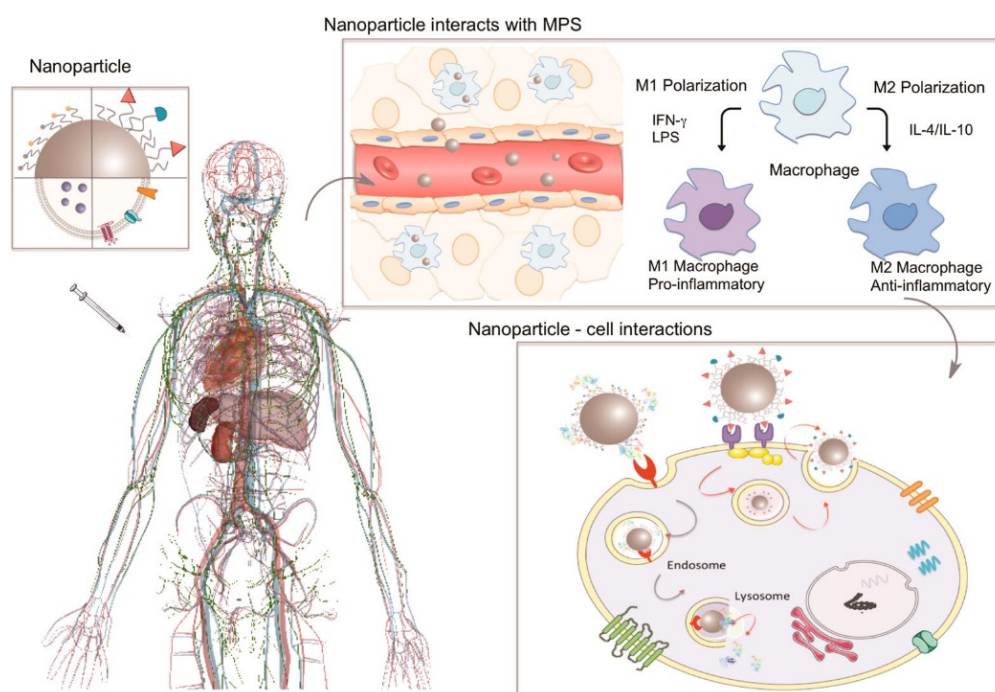


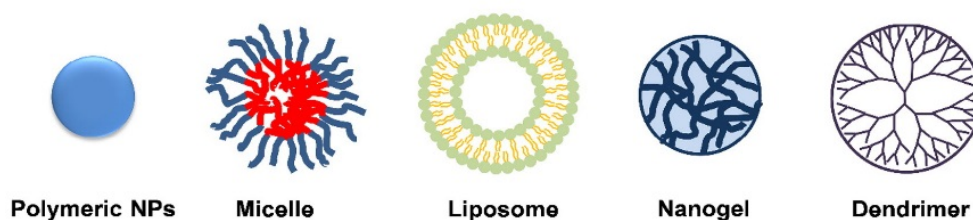
Figure 2. Various biological barriers and interactions post-administration of nanoparticles. Adapted from Polo *et al.* (36) with permission from the American Chemical Society.

knowledge on how nanomedicines interact with human blood components; which represents a nanoparticle’s first biological point of contact during intravenous administration (37). This thesis characterises the biological interactions of PISA nanoparticles that have well-characterised physicochemical properties by subjecting them to primary human samples of whole blood or plasma. It is expected that the data generated from these studies will aid the rational design of nanoparticles and help bridge the gap between basic research and clinical translation.

1.2 Polymeric nanoparticles for nanomedicine

Nanoparticles applied in nanomedicine applications are commonly constructed from “soft” materials such as polymer and lipid, and “hard” materials such as silica and gold (Figure 3). Such nanoparticles can be designed to carry chemotherapeutic drugs, imaging contrast agents, nucleic acids, and proteins for various biomedical applications (38). In this context, polymeric nanoparticles have particularly received the most interest because of the flexibility they offer in tuning their chemical

(a) Organic nanomaterials



(b) Inorganic NPs

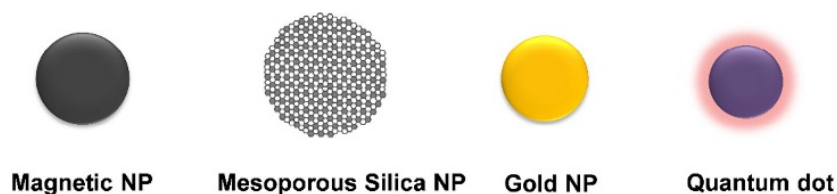


Figure 3. Common types of (a) organic and (b) inorganic materials and structures for nanoparticles used in nanomedicine. Adapted from Jia *et al.* (39) with permission from Elsevier.

composition, molecular weight, biodegradability, biocompatibility, size, morphology, and surface chemistry (40, 41). The incorporation of functionalities through judicious selection of monomers can control the responsiveness of the resultant polymer in biological environments (pH, oxidative stress, enzymatic, etc.) or when an external stimuli such as temperature, IR or UV irradiation, magnetic fields, etc. is applied. While intravenous administration is a common route of administration for polymeric nanoparticles, less invasive administration techniques such as oral, subdermal, transdermal, and mucosal delivery has been shown to be suitable for use with polymeric nanoparticles. Ultimately, polymeric nanoparticles can be designed for a wider scope of biomedical applications than other types of nanoparticle materials due to the flexibility in which their architecture, composition, and physical and chemical properties can be tuned.

1.2.1 Examples of polymeric nanoparticle systems

The polymeric nanoparticles systems discussed hereunder are some of the most common examples cited in the literature. In particular, simple linear polymer chains (polymer-drug conjugates) and spherical polymeric systems (micelles and dendrimers) are highly represented in nanomedicine literature.

Polymer-drug conjugates

In 1974, Ringsdorf and colleagues proposed the concept of “polymeric prodrug” (42). In Ringsdorf’s seminal work, three components were incorporated into the biocompatible polymeric backbone; (i) a targeting agent that can recognise a specific physiological target, (ii) a bioactive molecule that can influence pharmacodynamics, and (iii) a hydrophilic segment to improve solubility of the system in an aqueous environment. This idea provided the theoretical platform for modern polymer-drug conjugates that are currently in clinical trials (43). Such polymer-drug conjugates can be constructed from natural and synthetic polymers having

different functional groups and compositions, which can spontaneously self-assemble to form polymeric micelle nanoparticles.

Examples of natural polymers include polysaccharides (e.g., dextran, hyaluronic acid, heparin and chitosan). These polymers typically display desirable properties for biomedical applications such as low toxicity, non-immunogenicity, biodegradability, and good biocompatibility (44). For example, dextran derivatives have been used to conjugate several chemotherapeutic drugs such as doxorubicin (DOX), camptothecin (CPT), mitomycin C, and methotrexate (45-48). Furthermore, dextran-DOX and dextran-CPT polymer-drug conjugates have undergone clinical testing (49, 50). Another natural polymer, hyaluronic acid, is a linear anionic polysaccharide that is a main component in the extracellular matrix and plays a vital role in proliferation, differentiation, migration, and cellular growth (51, 52). An increase in hyaluronic acid content is considered a reliable disease progression index for some types of malignant tumours (e.g., bladder cancer) (44). Furthermore, hyaluronic acid is often used for drug delivery in the absence of additional ligands due to its strong affinity with the receptor for hyaluronate-mediated motility (RHAMM), which is overexpressed in many malignant cells (53, 54). Anti-tumour drugs such as DOX, CPT, paclitaxel, and curcumin have been easily conjugated to the hyaluronate backbone due to the abundance of hydroxyl and carboxylic groups (55).

Synthetic polymers such as poly(ethylene glycol) (PEG), poly(*L*-glutamic acid) (PGA), *N*-(2-hydroxypropyl) methacrylamide (HPMA), poly(amino acid), and their copolymers have been used to synthesise polymeric prodrugs. PEG is a commonly used hydrophilic synthetic polymer for biomedical applications. The favourable use of PEG is largely attributed to its approval by the FDA as an excipient for many pharmaceutical formulations due to its low toxicity and negligible immunogenicity. Nevertheless, with regard to the immunogenicity of PEG, this topic has proven divisive in the literature with several studies suggesting that PEG is indeed

immunogenic (56, 57). Conversely, other studies suggest that the instant studies are flawed (58). Nonetheless, the use of PEG in polymeric systems remains prevalent as discussed herein. In 1983, Duncan and colleagues first reported the use of HPMA copolymers to enhance polymer uptake by the liver in rats (59). Since then, HPMA copolymers have been polymerised with functional monomers that allow conjugation of different chemotherapeutic drugs. An example of a HPMA polymeric prodrug is the HPMA copolymer-DOX conjugate PK1, which entered clinical trial testing in 1994 (60). Polymeric micelles

The advent of polymeric micelles may be traced back to the early 1990s when Katoaka and colleagues first developed block copolymer micelles conjugated with DOX (61). Since then, polymeric micelles are commonly used to encapsulate anti-cancer drugs for preclinical and clinical studies because of their high loading capacity, enhanced circulation times, biodegradability, and the enhanced permeation and retention (EPR) effect (62). The corona of the micelle is formed from hydrophilic polymers that enhance the solubility of the micelle and shields the micelle from mononuclear phagocytic system (MPS) recognition while the core is formed from hydrophobic polymers that protect the anti-cancer agent cargo. Since most anti-cancer drugs are hydrophobic, they are usually encapsulated in polymeric micelles via hydrophobic interactions. Anti-cancer drugs may also be encapsulated via other methods including π - π interactions, hydrogen bonding, and electrostatic interactions (63, 64).

The formation of polymeric micelles occurs through the self-assembly of amphiphilic block copolymers. Specifically, when the concentration of amphiphilic block copolymers reaches their critical micelle concentration (CMC), micelle formation is entropically favoured to minimise energetically unfavourable hydrophobic water interactions (62). Since the CMC of polymeric micelles (approximately 10^{-7} M) is significantly lower than the CMC of surfactants (approximately 10^{-4} M), polymeric micelles are more stable than surfactant-based

micelles (62). Another key advantage of polymeric micelles over conventional surfactant-based micelles is that polymeric micelles may be core-crosslinked to stabilise the micellar structure and modulate drug release (65). Advantageously, this stability can be tuned to create responsive amphiphilic block copolymer micelles that release their cargo under specific conditions. For example, the tumour microenvironment is known to have a lower pH than healthy tissue (approximately pH 5.0 to 6.0 versus pH 7.4) (66). As a result, pH-responsive polymeric micelles have been developed with polybase (e.g. poly(L-histidine)) and titrable moieties (e.g. ethylazepene and methacrylic acid). Further examples of pH-responsive polymeric micelles have been reviewed extensively in the literature (67, 68).

Dendrimers

Dendrimers are a unique class of nanoparticles, which consists of well-defined supramolecular architectures consisting of hyper-branched units (69, 70). However, dendrimers require intricate stepwise synthesis techniques to achieve their well-defined macromolecular properties, thereby reducing their commercial viability. Nonetheless, dendrimers have been investigated for several biomedical applications ranging from sensing to drug delivery due to their small and monodispersed size (< 20 nm in diameter) (71). For drug delivery applications, drugs are encapsulated into the dendrimer core branch points with the drug content controlled via the generation number. Drugs may also be attached to a branch through a biodegradable chemical linker for controlled release of the drug. Additionally, the corona of the dendrimer may be functionalised with various chemical groups such as PEG. For example, PEGylated polylysine dendrimers have been conjugated with drugs such as doxorubicin and methotrexate and administered to rats to investigate drug release profile and anti-cancer activity of the drug cargo (72-74).

1.3 A brief overview of RAFT polymerisation

The ability to rationally design polymeric nanoparticles with desired chemical and physical properties is enhanced by advances in polymer synthetic techniques. In particular, living radical polymerisation (LRP) techniques are among the most robust and readily applicable polymer synthetic technique. Compared to conventional radical polymerisation, LRP techniques such as Nitroxide Mediated Polymerisation (NMP) (75), Atom Transfer Reduction Polymerisation (ATRP) (76, 77), and Reversible Addition Fragmentation chain Transfer (RAFT) polymerisation (78, 79) afford greater control over the final molecular mass of the polymer along with a narrower polydispersity. Among these LRP techniques, RAFT is one of the most versatile because it can be conducted under a wide range of reaction conditions and functionalities, thereby enabling control over a larger variety of monomers among other LRP techniques. First reported in 1998 by the CSIRO group (78), RAFT polymerisations proceed via a degenerative transfer process that is mediated by a chain transfer agent; commonly termed RAFT agents. RAFT agents are organic compounds that possess a thiocarbonylthio moiety (Figure 4; in red). The R group (Figure 4; in green) is responsible for initiating the growth of polymeric chains, and the Z group (Figure 4; in blue) is involved in activating the thiocarbonyl bond towards radical addition and subsequently stabilises the resultant adduct radical. To this end, the addition of RAFT agents to existing polymerisation conditions has yielded complex polymeric structures such as block copolymers, bottle brush polymers, hyper branched polymers, star polymers, among others, all with well-defined properties (79).

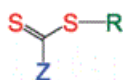
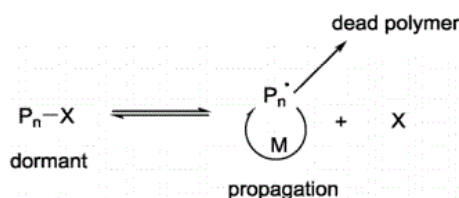


Figure 4. A typical RAFT agent structure with thiocarbonylthio moiety (in red), R group (in green), and Z group (in blue).

1.4 The RAFT polymerisation mechanism

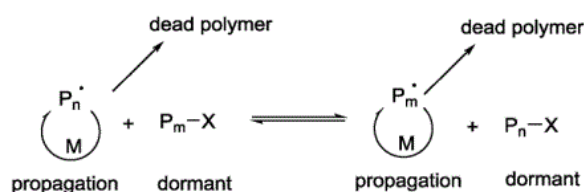
The principle of LRP techniques such as RAFT lies within the shuttling of propagating polymer radicals between active and dormant states through a reversible/activation/deactivation equilibrium. In the case of NMP and ATRP, this equilibrium is established via a mechanism of reversible termination of a propagating chain (Scheme 1). This action is facilitated by nitroxide capping (as in the case of NMP) or a redox process with a metal halide salt (ATRP), such that the equilibrium is biased towards the dormant species. Since radicals are formed from activation of the dormant species, the concentration of propagating radicals remains low. By doing so, the formation of undesired dead polymer by irreversible termination is significantly reduced. Furthermore, by dictating the rate of polymerisation via the position of the activation/deactivation equilibrium, the molecular weight and dispersity is well-controlled via statistical probability of chain activation.



Scheme 1: Reversible-deactivation radical polymerisation by reversible termination. Adapted from Keddie DJ *et al.* (80) with permission from the Royal Society of Chemistry.

Unlike NMP and ATRP, RAFT provides a fundamentally different method of control over this activation/deactivation equilibrium. Specifically, RAFT is carried out via a degenerative chain transfer process in which the propagating species equilibrate with the dormant species (Scheme 2). Since, the degenerative chain transfer process does not produce radicals, the radical required to maintain a constant rate of polymerisation is derived from an

external source. For RAFT polymerisations, this is commonly found in the form of a thermal initiator such as 2,2'-azobisisobutyronitrile (AIBN).



Scheme 2: Reversible-deactivation radical polymerisation via degenerative chain transfer.

Adapted from Keddie DJ (80) with permission from the Royal Society of Chemistry.

The degenerative chain transfer events in RAFT polymerisation is facilitated by an organic compound that possess a thiocarbonylthio moiety (i.e. a RAFT agent). Essentially, the addition of a RAFT agent is the only modification to the conventional radical polymerisation protocol (80). This simple modification means that RAFT polymerisation formulations do not require extensive process development. RAFT techniques have therefore been widely adopted by basic and industry researchers (81, 82). During the initial stages of RAFT polymerisation, the initiator derived radical propagates with the monomer to produce a polymeric radical. The addition of the propagating polymeric radical to the RAFT agent is followed by fragmentation of the intermediate radical, which results in a polymeric RAFT agent (also known as a macromolecular-RAFT agent) and a radical. This radical reacts with a monomer to create an active propagating radical. The equilibrium between the active propagating radicals and the non-active macro-RAFT equates to equal statistical probability for all chains to grow and leads to polymers with low polydispersity and pre-determined molecular weight.

1.4.1 RAFT polymers in nanomedicine

Due to the versatility of the RAFT polymerisation technique, it is possible to design synthetic polymers with tuneable chemistry and architecture. As a result, researchers are able to customise the critical features of RAFT polymers (size, surface chemistry, shape, etc.) according to their intended application in the body. Several key examples of RAFT polymers classed according to their functional properties are described below.

RAFT polymer-drug conjugates

Over the past decade or so, research has been focused on improving the utility of drugs by overcoming common limitations such as suboptimal absorption, stability during circulation, biodistribution, and elimination. In this regard, a commonly employed tactic is the attachment of PEG (also known as PEGylation) to a therapeutic agent and thus, generating a polymer-drug conjugate (83-85). Furthermore, promising alternatives to PEG such as zwitterionic polymers and poly(glycerol)s are being investigated (86).

To produce RAFT polymer-drug conjugates, RAFT agents have been functionalised via their R and Z groups (79). Although either substituent may be functionalised, most RAFT agents are modified via their R group because of the lower stability of the thiocarbonylthio group that is adjacent to the Z group of a RAFT polymer (87). Typically, RAFT agents are used to synthesise homopolymers or copolymers with a reactive moiety for subsequent conjugation to small molecule therapeutic agents or peptides. For example, Davis and colleagues synthesised an amine-functional RAFT polymer through the polymerisation of poly(*N*-(2-hydroxypropyl) methacrylamide) (PHPMA) in the presence of a thiazolidine-2-thione RAFT agent (88). Lysozyme, a model protein, was conjugated to PHPMA via an amide bond by incubating both substituents together. In this example, amine represented an excellent choice of functional group because of its ubiquity in proteins. Other amine-reactive chemical

handles often included on RAFT agents include pentafluorophenyl esters and succinimidyl esters. Similarly, thiol-reactive RAFT agents have also been utilised for drug conjugation. In an example, Tao *et al.* synthesised a bis-trithiocarbonate RAFT agent that possessed a pendant pyridyldisulfide group in the middle (89). This RAFT agent was polymerised with HPMA and the centrally located pyridyldisulfide group was exploited to conjugate with the cysteine thiol groups found on bovine serum albumin (BSA). The central position of BSA is essentially designed to shield it from proteolytic cleavage.

Aside from linear RAFT polymers, more advanced architectures such as block copolymers offer increased functionality. For example, Duvall *et al.* produced a diblock copolymer that contains a proapoptotic peptide (90). To achieve this diblock copolymer, a RAFT agent with a pyridyl disulphide group was selected for attachment to the terminal cysteine on the proapoptotic peptide. Next, the initial block consisted of PHPMA for aqueous solubility and the second block consisted similar units of propylacrylic acid (PAA) and dimethylaminoethyl methacrylate (DMAEMA), and butyl methacrylate (BMA). This diblock copolymer demonstrated membrane-disruptive properties at pH = 5.8 (compared to its inert state at pH = 7.0), thus facilitating endosomal escape and intracellular delivery of the proapoptotic agent.

Stimuli-responsive polymeric systems

Another layer of functionality that may be imparted to RAFT polymers is the ability to respond to external stimuli. Specifically, the release of therapeutic cargo as a result of the change in physical properties of a polymer to external cue/s. For example, thermal-responsive polymers such as poly(NIPAM) exhibit hydrophobic properties at temperatures above its lower critical solution temperature (LCST) of 32 °C but become hydrophilic at lower temperatures. Summerlin and colleagues demonstrated this effect through the synthesis of azido-terminal

copolymers of NIPAM and dimethylacrylamide (DMA) in the presence of an azide functionalised trithiocarbonate RAFT agent (91). This copolymer was then conjugated to alkyne-functional propargyl folate using a copper-catalysed azide-alkyne cycloaddition reaction. Then, the hydrophobic polymer aggregates were imbibed with dipyridamole (a model hydrophobic drug), and drug release was observed at temperatures below the LCST. In another example, Pan and coworkers attached a RAFT agent to silica nanoparticles before grafting DMAEMA polymers onto the surface (92). Next, the tertiary amine groups were quaternised with 1,3 propanesulfone to obtain a random copolymer with both zwitterionic and cationic monomers. Finally, a fluorescent dye (Rhodamine B) was grafted onto the polymer surface of the silica nanoparticles and shown to be released at 37 °C after the surface polymers swelled and ejected their payload.

Redox responsive RAFT polymers are also of significant interest to the scientific community. For example, selenide-containing copolymer nanoparticles were loaded with doxorubicin and shown to release their payload upon exposure to 0.1 wt% H₂O₂ (93). Significantly, this copolymer may be complexed with platinum cation (Pt²⁺) for the formation of redox-sensitive micelles that were loaded with doxorubicin. Following exposure to GSH or dithiothreitol (DTT), the micelles disassembled due to the competitive coordination of Pt²⁺ with either GSH or DTT, releasing the doxorubicin payload.

Star polymers

Star polymers are a type of branched polymeric architecture that comprises linear polymer “arms” that radiate from a “core” branching point. These polymers are classified according to the molecular composition of the arms, sequence distribution of the arms, and the chemical properties of the core. Among the various RAFT polymers, star polymers represent

one of the simplest linear polymer structures and are favoured by polymer chemists that seek nanoparticles that are spatially well defined (i.e., core-shell-end group structure).

Over the preceding years, intensive research efforts into star polymer synthesis via RAFT polymerisation has led to the development of facile access to star polymers with predetermined molecular weights and narrow size distributions. There are two key approaches to the synthesis of star polymers: core-first and arm-first. Each technique possesses their own set of advantages and drawbacks which the user must take into account in planning the target application of the star polymer. The core-first approach typically involves a prepared multifunctional initiator (i.e. the core) for linear polymers (i.e. the arms) to grow out from. In order to produce well-defined star polymers (i.e. similar arm numbers and arm length), the initiating sites on the core should ideally have similar reactivity and near-complete initiation efficiency. Contrary to the core-first approach, the arm-first approach is performed by cross-linking linear polymers via a coupling reaction in a convergent manner; forming the arm-core structure. An advantage of this approach is that linear arm polymers can be pre-synthesised and characterised before star polymer formation. However, star polymers derived from the arm-first approach have broader arm number distributions in comparison with those obtained via the core-first approach or grafting-onto approach.

Star polymers have been investigated for their potential utility in various wide-ranging nanomedicine applications through the functionalisation of star polymer arms and/or cores. Firstly, star polymers have shown promise for controlled and sustained drug release via the loading of star polymer cores with chemotherapeutics such as, but not limited to, doxorubicin, paclitaxel, and progesterone (94). In 2012, Liu *et al.* synthesised core-crosslinked star polymers that consisted of poly(oligo(ethylene glycol)) methyl ether acrylate (POEGA) arms and benzaldehyde groups in the core (95). The aldehyde groups in the star polymer core was

exploited to conjugate doxorubicin and was shown to be released in the acidic endosomal environment of cancer cells. POEGA star polymers were also synthesised via a similar approach and administered intravenously into rats bearing MDA-MB-231 human breast cancer tumour xenografts (21). It was observed that the plasma circulation time and tumour accumulation correlated with the molecular weight of the star polymers. Aside from chemotherapeutic drugs, star polymers have also been loaded with small-interfering RNA (siRNA) for the treatment of orthotopic pancreatic tumours (96, 97). In addition, star polymers have also been loaded with contrast agents for magnetic resonance imaging (MRI) and positron emission tomography (PET) applications (98-100). Esser *et al.* demonstrated that it was possible to simultaneously label core-crosslinked azide-functionalised star polymers with a radioisotope (radioiodine) and a magnetic resonance imaging (MRI) contrast agent (gadoteric acid), and overcome inherent drawbacks of individual imaging modalities and access the best of two different imaging techniques (101). In fact, the nanoparticles outperformed commercially available Magnevist in terms of longitudinal relaxivity. Further uses of star polymers in nanomedicine have been reviewed extensively in the literature (94, 102).

Drug-loaded self-assembled structures

RAFT polymerisation has also been used to generate self-assembled diblock copolymers loaded with therapeutic agents. Amphiphilic block copolymers may self-assemble to form micelles, which can be loaded with hydrophobic therapeutic agents for drug delivery. This approach protects the therapeutic cargo from degradation and also shields healthy cells from the toxic side-effects of some types of drugs such as cytotoxic drugs (e.g. doxorubicin). However, the successful execution of this concept is reliant on the stability of the self-assembled structure in a biological environment. To mitigate premature dissociation, a common approach is to cross-link the micelle structure. For example, Dhara and colleagues

polymerised 2-(methacryloyloxy)ethyl 5-(1,2-dithiolan-2-yl)pentanoate (LAHEMA) in the presence of a PEGylated macro-RAFT agent under RAFT conditions to obtain an amphiphilic diblock copolymer that self-assembled to form micelles (103). Such micelle structures were then conveniently cross-linked in the presence of 10 μ M L-glutathione (GSH), which led to ring opening of the 1,2-dithiolane moiety on the LAHEMA units based on thiol-disulfide exchanges. This reaction yielded dihydrolipoyl groups which subsequently led to exchange reactions with other 1,2-dithiolane rings in the poly(LAHEMA) block resulting in the formation of linear disulphide bonds. Notably, upon extensive dilution to a point below their critical micellar concentration, the amphiphilic diblock copolymer micelles proved their stability by retaining their micellar size and distribution as assessed by DLS and TEM. Similarly, block glycopolymers possessing galactose, dopamine, and cholic acid pendants were synthesised via RAFT polymerisation and self-assembled into micelles in water (104). The dopamine pendants in the hydrophobic core were then cross-linked via oxidative cross-linking in a weakly basic solution (pH = 8.5); with the cross-linking confirmed via UV-vis spectroscopy.

1.5 Polymerisation-Induced Self-Assembly: Nanoparticles with bespoke size and morphology

The self-assembly behaviour of amphiphilic block copolymers has been comprehensively studied since the early 1960s (105-107) following the development of living anionic polymerisation techniques (108); leading to well-defined block copolymers. Typically, amphiphilic block copolymer self-assembly is realised in a two-step process: i) dissolution of copolymer chains in a suitable solvent, and ii) the decrease of solvency of one of the blocks to promote micro-phase separation. As an example, Eisenberg and colleagues synthesised poly(4-vinylpyridine)-polystyrene (P4VP-PS) diblock copolymers, dissolved them in *N,N*-

dimethylformamide (DMF) and progressively added either water or methanol (both are non-solvents for PS) to obtain spherical micelles (109). Next, they demonstrated that high-order morphologies such as rods and vesicles were obtainable by varying the degrees of polymerisation (DPs) of poly(acrylic acid)-PS (PAA-PS) diblock copolymers (110, 111). Since the development of LRP techniques, diblock copolymers with even more complex morphologies have been possible (112). However, a major drawback of the aforementioned approaches is that the final diblock copolymer concentrations are too low (<1.0% w/w) (113) for industrial scale-up, thus precluding many potential commercial applications.

Recently, polymerisation-induced self-assembly (PISA) has emerged as a promising alternative route to amphiphilic block copolymers with higher-order morphologies. Essentially, PISA allows the process of block copolymer synthesis and self-assembly to be combined into a single step. PISA proceeds via the chain-extension of a soluble homo- or copolymer with a monomer such that the growing block eventually becomes insoluble in the continuous phase, which then triggers *in situ* self-assembly to form diblock copolymer nanoparticles. Through the variation of DPs of the blocks in the block copolymer, many different higher order morphologies could be obtained (e.g., worms, rods, vesicles). Perhaps most importantly, PISA formulations are routinely conducted at relatively higher solids content (up to 50% w/w); making them favourable for industrial scale-up for commercial applications (26, 27, 114).

In 2002, Ferguson and colleagues reported the first literature example of PISA. Firstly, acrylic acid (AA) was polymerised to form a hydrophilic macromolecular chain transfer agent (macro-CTA) (115). After that, RAFT aqueous emulsion polymerisation of butyl acrylate (BA) was carried out in the presence of the PAA macro-CTA to form a poly(AA)-poly(BA) (PAA-PBA) diblock copolymer. Once the PBA block became sufficiently hydrophobic, the PAA-PBA chains self-assembled into RAFT-containing seed particles and the emulsion

polymerisation continued. As demonstrated by this example, PISA does not require the preformation of seed particles via the solvent exchange method (addition of water to acetone) and thereby overcomes a longstanding challenge for large-scale manufacturing. Interestingly, this approach was not termed PISA at the time. Instead, it was Hashimoto and colleagues who coined the term PISA later on in 2006 (116). At that time, PISA still had not attracted broad interest across the polymer chemistry community because of initial limitations in controlling particle size and morphology. However, as advancements in size and morphology control are made, PISA has become a synthetic technique of significant interest to not only polymer chemists but also to the nanomedicine community.

Following the advancements in size and morphology control, PISA has been keenly explored for a plurality of applications including catalysis, coatings, Pickering emulsifiers, lubricants (27, 117-122). However, it is arguably their use in nanomedicine that is the most exciting. Both size and morphology have been demonstrated to be crucial factors in influencing the biological properties of nanoparticles (17, 18, 123). For example, a recent study by Kaga *et al.* demonstrated the effect of size and morphology on the biodistribution of PISA nanoparticles *in vivo* (124). Lately, PISA has been utilised to make so-called nanoworms, a subclass of polymeric nanoparticles with high surface area and aspect ratio (125). So far, these nanoworms have attracted substantial interest in applications such as drug delivery, tissue engineering, and immunology (19, 126, 127). Other than nanoworms, amphiphilic block copolymer vesicles or polymersomes have also been explored for nanomedicine (128-130).

To gain access to nanoparticles with bespoke sizes and morphologies for desired applications in the field of nanomedicine, there has been an increase in research efforts focused on advancing the PISA technique. While PISA is capable of producing other morphologies such as crew-cut micelles, lamella, oligolamellar vesicles, jellyfish-like structures, and

yolk/shell particles (24, 25), PISA nanoparticles with spherical, worm-like, and vesicle structures are of particular interest in the realm of biomedical applications. Hence, this section will cover the latest developments and current challenges of PISA nanoparticles with spherical, worm-like, and vesicle structures and the control of their respective sizes, and their use in nanomedicine.

1.5.1 PISA via RAFT-mediated polymerisation

Though PISA syntheses have been conducted with various LRP techniques (29, 131-133), the literature is replete with examples of PISA syntheses employed in RAFT polymerisation conditions (23, 31, 34, 35, 134, 135). As discussed above, RAFT enables PISA syntheses to be conducted with a diversity of monomers in an equally diverse range of solvents (113, 136-138). Under RAFT polymerisation conditions, PISA proceeds via either RAFT dispersion or RAFT emulsion polymerisation. In RAFT dispersion polymerisation conditions, the second monomer is soluble in the continuous phase and the resultant block polymer is insoluble in the continuous phase (for example benzyl methacrylate and poly(benzyl methacrylate) in ethanol). Whereas under RAFT emulsion polymerisation conditions, either the monomer or the resultant polymer is insoluble in the continuous phase (for example styrene and polystyrene in water). Typically, a macro-CTA is chain extended with a second monomer and the growing amphiphilic block copolymer chains self-assemble to form spherical micelles (Figure 5). Under certain conditions, increasing the DP of the second block results in subsequent transformation of spherical micelles, to worms, and finally to vesicles (130). The facile access to all three morphologies within a single amphiphilic block copolymer composition is an important advance of PISA over traditional self-assembly techniques. Yet, while many RAFT dispersion polymerisation formulations enable access to all three main

morphologies, this morphological transition has only been observed for a small subset of RAFT *emulsion* polymerisation formulations (22).

In fact, many RAFT emulsion polymerisation formulations solely result in kinetically-trapped spheres even when targeting higher core DP diblock copolymer compositions (139-141). The lack of worm-like and vesicle morphologies for RAFT emulsion polymerisation limits the overall applicability of PISA. Thus, there is an urgent need to advance our understanding of the factors that lead to morphological evolution in RAFT emulsion polymerisation. The following sections will describe the current progress in understanding the experimental conditions that dictate the size and morphology of PISA nanoparticles.

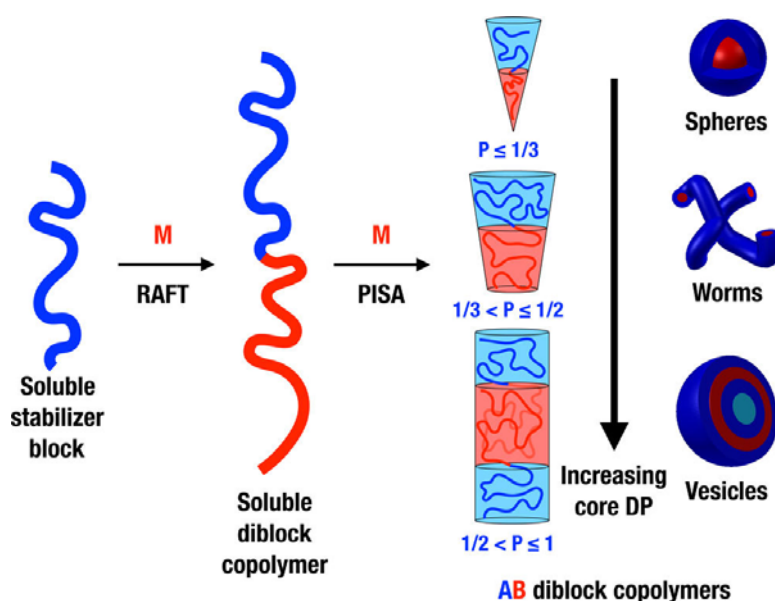


Figure 5. A schematic representation of the synthesis of diblock copolymer nanoparticles via PISA; P represents the packing parameter value of the diblock copolymer. Reproduced with permission (22). Copyright 2016, American Chemical Society.

1.5.2 Size control of PISA formulations

While spherical nanoparticles could be produced via PISA formulations, it was not until 2010 where the Armes group demonstrated control over the diameter of such nanoparticles

(138). In this study, a series of RAFT aqueous dispersion polymerisations of HPMA mediated by a poly(glycerol methacrylate) (PGMA) macro-CTA was conducted. The systematic variation of the core PHPMA DP from 30 to 300 correlated with the increase in mean micelle diameter from 26 to 105 nm. A similar observation was made when Fielding *et al.* carried out RAFT dispersion polymerisation of benzyl methacrylate (BnMA) in the presence of a poly(lauryl methacrylate) (PLMA) macro-CTA in *n*-heptane (142). While relatively longer PLMA macro-CTAs could not form higher order morphologies, increasing the core PBnMA DP from 100 to 900 consequently led to an increase in the diameter of spherical micelles from 41 to 139 nm.

The effect of increasing the diameter of spherical micelles via the monotonic increase in core DP also extends to RAFT emulsion polymerisation formulations. For instance, Truong *et al.* reported the use of a novel macro-CTA consisting of *N*-hydroxyethyl acrylamide (HEAA) and PEGA units in the RAFT aqueous emulsion polymerisation of styrene (141). Through the judicious selection of macro-CTA composition and polymerisation conditions, highly-defined diblock copolymers with low polydispersity ($PDI < 1.20$) and well-defined spherical nanoparticles were obtained. Specifically, it was found that the macro-CTA with PHEAA₂₁-PEGA₂₁ was the best stabiliser for RAFT emulsion polymerisation in styrene. Using this PHEAA₂₁-PEGA₂₁ macro-CTA, a series of polystyrene diblock copolymers were synthesised with increasing ratio of styrene:macro-CTA. The authors witnessed a correlation between particle diameter and molecular weight, causing a range of particles with diameters ranging from 124 to 183 nm with corresponding molecular weights of 2.9×10^5 to 1.2×10^6 g mol⁻¹. These works and others since then establish that spherical micelles with well-controlled diameters could be obtained via adjusting core DP.

Aside from tuning the size of spherical micelles, the diameter and length of worms may also be altered by adjusting certain experimental factors. As an example, Zhang and colleagues employed a poly(*N,N'*-dimethylamino)ethyl methacrylate) (PDMAEMA) macro-CTA to mediate the RAFT dispersion polymerisation of styrene in methanol and found that the PDMAEMA macro-CTA DP had a profound effect on the size of the resultant worm-like nanoparticles (143). There were two key observations made in this study. Firstly, the authors observed that the diameters (or the width) of the worm-like nanoparticles increased when the DP of the PDMAEMA macro-CTA was increased (Figure 6). Secondly, the overall length of the worm-like nanoparticles appeared to decrease as the PDMAEMA macro-CTA DP increased. A separate study by Pei *et al.* discovered that altering the solids content of the poly(oligo(ethyleneglycol)methacrylate)-poly(3-phenylpropyl methacrylate) (POEGMA-PPMA) diblock copolymer consequently changed the cross-sectional diameter of the resultant worm-like nanoparticles (144). For example, a mixture of spherical micelles and short worms was obtained when the polymerisation was conducted at 10 wt%. Whereas the 20 wt% formulation yielded longer worms and the 40 wt% formulation produced a pure worm phase with even longer worm-like nanoparticles. Altogether, these studies show the possibility of controlling both the length and diameter of worm-like nanoparticles via the macro-CTA DP and solids content.

The diameter of vesicles may also be controlled via PISA. This effect has mainly been achieved via two methodologies: i) using a binary mixture of relatively long and short poly(methacrylic acid) macro-CTAs (145), and more recently ii) the topological engineering of the core block of the amphiphilic block copolymer (146). In the latter methodology, RAFT dispersion polymerisation of BnMA and stearyl methacrylate (SMA) was carried out. The feed ratio of BnMA/SMA was varied and resulted in vesicles with diameters ranging from 200 to 1500 nm. Other novel morphologies such as large compound micelles and large compound

vesicles were also obtained by varying the DP of BnMA/SMA. To investigate this phenomenon, the authors carried out molecular simulations. The outcome of these simulations suggested that the topological composition of the core-forming block could change the packing parameter; which is thought to dictate the final nanoparticle morphology. To demonstrate the utility of topological engineering of the core-forming block, the authors carried out RAFT dispersion polymerisation of BnMA and 2-(perfluorooctyl)ethyl methacrylate. This polymerisation was also successful in generating vesicles that had controllable diameters, thus confirming that topological engineering could be considered as an experimental factor for controlling the size of vesicles.

So far, the control of nanoparticle size is shown to be dictated by not only core polymer DP, but also extended to macro-CTA DP, binary mixture of macro-CTAs, and topological engineering of the core polymer. What is also clear that while the aforementioned experimental factors were readily applied to RAFT dispersion polymerisations, further work needs to be carried out to find out if such experimental factors could also be applied to RAFT emulsion polymerisations. Chapter 5 of this thesis discloses the discovery of two new experimental factors that influence the final morphology of nanoparticles synthesised via RAFT aqueous emulsion polymerisation.

1.5.3 Morphology control of PISA formulations

Prior to 2009, PISA formulations were limited to the production of spherical micelles. This occurred because the spherical micelles synthesised were kinetically trapped as a result of the solvophobic block being below its T_g and therefore precluding morphological evolution. In the spirit of promoting morphological transition to higher order morphologies, Pan and coworkers hypothesised that the compatibility of the core-forming block with the continuous phase could be improved by significantly increasing the core monomer feed ratio (147).

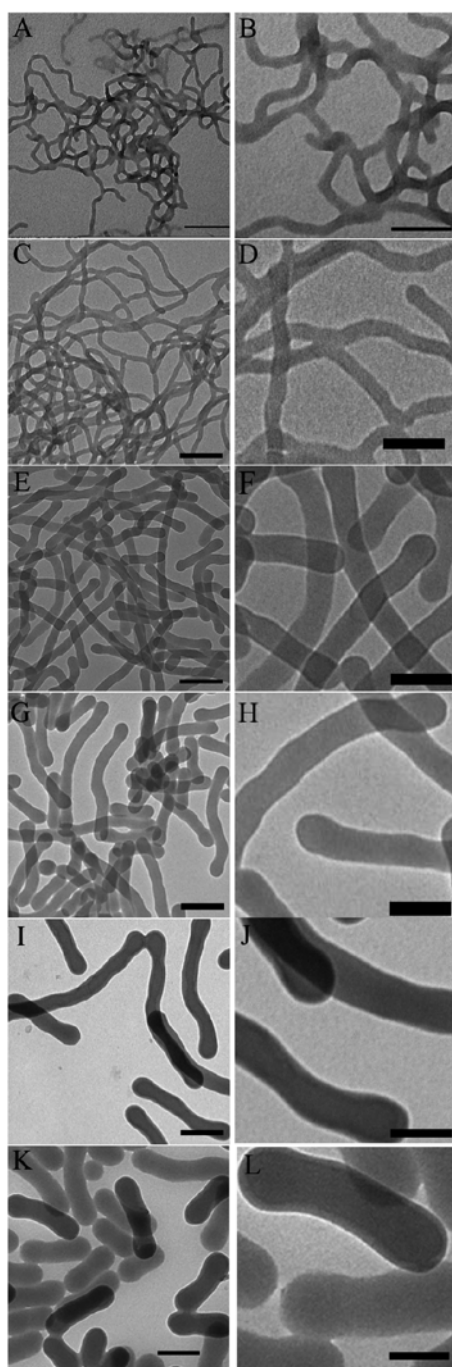


Figure 6. TEM images of the PDMAEMA-PSt block copolymers with different PDMAEMA DP; (A) & (B) PDMAEMA DP = 22, (C) & (D) PDMAEMA DP = 36, PDMAEMA DP; (E) & (F) PDMAEMA DP = 60, PDMAEMA DP; (G) & (H) PDMAEMA DP = 98, PDMAEMA DP; (I) & (J) PDMAEMA DP = 113, PDMAEMA DP; (K) & (L) PDMAEMA DP = 247
Reproduced with permission (143). Copyright 2014, The Royal Society of Chemistry.

Hence, a series of RAFT dispersion polymerisation of styrene in methanol using a trithiocarbonate-terminated poly(4-vinylpyridine) macro-CTA was carried out. After two hours of polymerisation, the presence of spherical nanoparticles was observed under transmission electron microscope (TEM). At 24 hours, higher-order morphologies such as lamellae, doughnuts, and vesicles were observed. In fact, by systematically varying the core DP, relatively pure morphologies could be obtained. This seminal work by Pan and coworkers represented the first study to demonstrate that the core polymer DP has a relationship with the final nanoparticle morphology, thereby differentiating PISA from conventional self-assembly where the copolymer solubility was mainly exploited to obtain different nanoparticle morphologies (135, 148). Since then, more experimental factors have been discovered to promote morphological transitions in PISA formulations to obtain the desired nanoparticle morphology (22). Compared with size control, the experimental factors that dictate the final copolymer morphology in PISA formulations are far more numerous. Furthermore, the experimental factors that promote morphological transition are sometimes not shared across RAFT dispersion and RAFT emulsion polymerisations. For that reason, this section will be segmented into RAFT dispersion polymerisation and RAFT emulsion polymerisation

RAFT dispersion polymerisation

In a follow-up study, Pan and colleagues explored the effect of the solids content of the reaction by conducting a series of RAFT dispersion polymerisations of styrene in methanol using a poly(ethylene oxide) (PEO) macro-CTA (149, 150). The authors observed that spherical micelles were formed first, which then transitioned to other non-spherical morphologies as the polymerisation continued. In total, the determining factors of the final nanoparticle morphology were the concentration of styrene in methanol and the DP of

polystyrene block. As a result, spherical micelles, nanowires, and vesicles can be synthesised from changing the styrene feed ratio and concentration of styrene.

In 2012, the Armes group showed that block copolymer concentration and the DP of the macro-CTA were also factors that could affect the morphology of PISA nanoparticles (150, 151). To reproducibly obtain pure phases of the desired morphology, the authors executed a series of RAFT aqueous dispersion polymerisation of 2-hydroxy-propyl methacrylate (HPMA) using poly(glycerol methacrylate) (PGMA) macro-CTA and input the results into a phase diagram (Figure 7). Based on the phase diagrams, the authors reported several interesting findings. Firstly, when the PGMA macro-CTA with the lowest DP was used (DP = 47), there was no dependence on morphology based on concentration. For instance, increasing the block copolymer concentration of the reaction from 10 to 25 w/w% did not result in any morphological change. Nonetheless, when the DP of the core PHPMA block was increased, spherical micelles, worms-like micelles, and vesicles could be obtained. When the PGMA macro-CTA with a DP of 78 was used, the morphology of the resultant nanoparticles was highly dependent on the total solids content of the reaction (Figure 7). Then, for the PGMA with a DP of 112, the phase diagram is mostly occupied by the spherical micelle phase. To explain this phenomenon, the authors hypothesise that the longest PGMA macro-CTA resulted in block copolymer chains that were significantly less mobile and thus precluded the *in situ* morphological evolution from spherical micelles to higher order morphologies. The authors supported this hypothesis by adding ethanol to a RAFT aqueous dispersion polymerisation of HPMA with the longest PGMA macro-CTA in order to increase the mobility of the block copolymer chains. As a result, worms and vesicles were observed. This study provided important insight into the importance of well-populated phase diagrams for the reproducible synthesis of nanoparticles with desired morphologies.

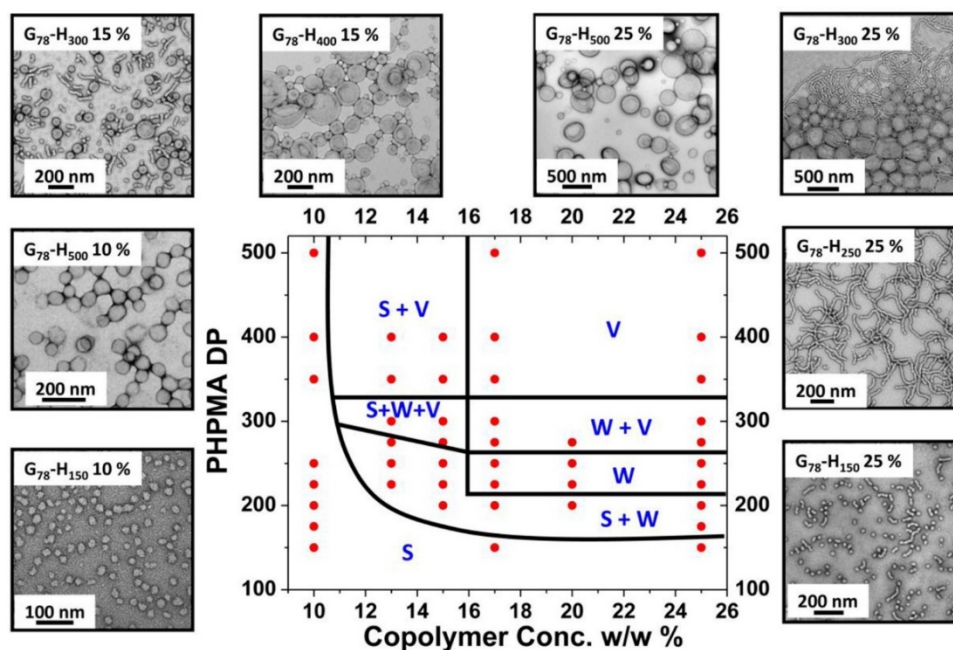


Figure 7. TEM images and the corresponding phase diagram for a series of RAFT aqueous dispersion polymerizations of HPMA in the presence of a P(GMA)₇₈ macro-CTA. Reproduced with permission (151). Copyright 2012, American Chemical Society.

In a recent study, Wang *et al.* investigated the effect of polymer architecture on the final morphology of diblock copolymers that were synthesised via PISA (152). Mono- and bifunctionalised poly(ethylene glycol) PEG-based macro-CTA were employed for the RAFT aqueous dispersion polymerisation of diacetone acrylamide (DAAM) to synthesise both linear PEG-PDAAM and star-shaped PEG-(DAAM)₂ nanoparticles. This study showed that when compared to the linear PEG-PDAAM, the star architecture of the PEG-(PDAAM)₂ was more efficient at promoting morphological transitions from spherical micelles to vesicles (no worm phase was observed). These findings suggest that the star architecture increased the packing parameter and was able to promote morphological evolutions during PISA conducted at high solids content.

Another interesting facet of morphology control is the use of diblock copolymers that display thermoresponsive properties (113, 153). After conducting RAFT alcoholic dispersion polymerisation of BnMA with a PLMA macro-CTA in *n*-dodecane, Armes and colleagues were able to prepare spherical micelles, worm-like micelles, and vesicles by plotting a phase diagram with PLMA DP versus PBnMA DP. Interestingly, the authors noticed that the worm-like micelle nanoparticles formed a free-standing gel at room temperature. This observation was attributed to the multiple worm-worm contacts. Upon heating the gel above 50 °C, degelation of the worm phase occurred and spherical micelles were obtained. Furthermore, this thermally-induced morphological transition was irreversible at a dilute concentration (10% w/w) but reversible at a more concentrated dispersion (20% w/w). In a similar investigation, PEG₁₁₃-PHPMA gels (at 10% w/w solids content) were heated above its critical gelation temperature (i.e., 40 °C) and a worm-to-vesicle transition occurred (also accompanied by degelation) (153). After cooling the PEG₁₁₃-PHPMA vesicles at 2 °C overnight, the vesicles transformed back to spherical micelles. Furthermore, this morphological transition proved reversible as small vesicles were produced after warming the gel to 50 °C.

In addition to the thermoresponsive properties of the PGMA-PHPMA diblock copolymer, Lovett *et al.* also explored the pH-responsive properties of this unique polymer (154, 155). To do so, the solution pH was increased from 3.5 to 6.0 to induce ionisation of terminal carboxylic acid groups on the PGMA stabiliser block polymer and increase the hydrophilicity of the overall block copolymer. This action caused a vesicle to spherical micelle transition for PHPMA₁₇₅ and a vesicle to worm-like micelle transition for PHPMA₂₀₀. No morphological transformation occurred when the PHPMA block DP was at 225 or 250. During the testing of thermoresponsive behaviour, only the PHPMA₁₇₅ vesicle were observed to have any morphological change, with the PHPMA₁₇₅ vesicles forming worms after cooling to 5 °C. Whereas subjecting the PGMA-PHPMA vesicles to both temperature and pH switch caused a

vesicle-to-sphere transition. In summary, the stimulus-triggered morphological transition behaviour of the PGMA-PHPMA block copolymer nanoparticles depends on the block DP of the PHPMA block and the ionisable groups in the chain terminus.

RAFT emulsion polymerisation

The first report of non-spherical PISA particles prepared via RAFT emulsion polymerisation was in 2010 by Boisse *et al.* (156). For this work, nanofiber particles were synthesised by using surfactant-free RAFT aqueous emulsion polymerisation of styrene in the presence of a poly(acrylic acid)-poly(ethylene glycol) methyl ether acrylate (PEGA) macro-CTA. When homopolymer macro-CTAs consisting of either PAA or PEGA were used, only spherical-micelles were obtained. After the use of the copolymer PAA-PEGA, worm-like micelles and vesicles could be produced. It was also discovered that pH and salt concentration of the polymerisation heavily affected the final block copolymer morphology. Increasing the degree of ionisation of the AA units (through increasing the solution pH) caused a morphological transition from mostly vesicles/fibers to mostly spheres. These morphological transitions were attributed to electrostatic repulsion between the stabiliser chains at lower pH, thus inhibiting the reorganisation of spherical micelles to form nanofiber structures.

To explore other experimental factors that impact on final copolymer morphology, Charleux and colleagues studied the effect of styrene/macro-CTA ratio, macro-CTA composition, and polymerisation conditions (157). By carrying out a series of RAFT aqueous emulsion polymerisations of styrene with a PMAA-PEOMA macro-CTA, the authors found that decreasing the [macro-CTA] while keeping other factors constant resulted in a final block copolymer transition from spherical micelles, to fibers, and finally to vesicles. However, compared with the spherical and vesicular morphology, the worm phase only existed in a narrow range of polystyrene chain lengths. Similarly, when the authors targeted high styrene

feed ratios while keeping other experimental factors constant, the same morphological evolution of spherical-micelles, to fibers, and finally vesicles was observed. Also, the worm phase only existed for a narrow window of polystyrene chain lengths. These experiments ultimately demonstrate that the final block copolymer morphology is dependent on the length of the hydrophobic polystyrene block relative to the overall length of the block copolymer. In total, these observations are comparable to those commonly made for RAFT dispersion polymerisations in that spherical micelles are formed from shorter hydrophobic blocks and morphologically evolve as the hydrophobic block lengthens. The authors' reasoned that at an intermediate monomer conversion, the nascent core is swelled with unreacted monomer which enables chain mobility and thus promotes chain reorganisation. At near-complete consumption of the monomer, the nanoparticles are kinetically frozen (i.e., the morphology persists after post-polymerisation dilution or pH change).

In the follow-up study, the chain length of the PEO monomers and the reaction pH were demonstrated to be vital parameters that dictated the final block copolymer morphology (158). At pH 3.5, the RAFT aqueous emulsion polymerisation of styrene only formed spherical-micelles. This result was linked to the poor separation between the hydrophilic and hydrophobic segments of the block copolymer because the macro-CTA ($pK_a = 5.8$) was in a low-ionisation state. Subsequently, the reaction pH was increased to 5.0 to increase the ionisation state of the MAA units in the macro-CTA (approximately 20-24% ionisation). Under this condition, an increase in the molecular weight of the polystyrene block resulted in the formation of spherical micelles, then worms, and finally vesicles. The stability of the macro-CTA chain was further increased by increase of the reaction pH to 7.0 (which theoretically corresponds to 62% ionisation). Of this reaction condition, only spherical micelles were observed. Clearly, the more stabilised macromolecular chains were not able to undergo the reorganisation process necessary for higher order morphologies. Finally, the authors altered

the molar mass of both the PMAA-PEOMA macro-CTA and the polystyrene block in the same reaction. It was found when the ratio of PMAA-PEOMA molar mass to polystyrene molar mass was between 70/30 and 80/20, the formation of worms was favoured. In total, these results show that for ionisable macro-CTAs, careful control of polymerisation pH was required in order to access multiple morphologies.

In 2017, an intriguing study found that the insertion of a short PEGA block into a poly(*N*-acryloylmorpholine) (PNAM) macro-CTA chain was able to promote a sphere to vesicle morphological transition (159). The authors synthesised four hydrophilic macro-CTAs with PEGA units at the beginning, statistically, or at the end of the PNAM polymer chain; PNAM, P(NAM-PEGA)-PNAM, PNAM-PEGA, and PNAM-P(NAM-PEGA). Then, RAFT aqueous emulsion polymerisation of styrene was conducted with these four hydrophilic macro-CTAs. As expected according to previous studies, the use of a pure PNAM macro-CTA for the emulsion polymerisation of styrene resulted only in spherical micelles. Conversely, the use of PNAM-P(NAM-PEGA) macro-CTA resulted in purely vesicles rather than spherical micelles. Furthermore, this morphology persisted regardless of the molecular weight of the polystyrene block. To investigate if either the presence of PEGA units or the specific location of the PEGA units that inspired this morphological change, the PNAM-PEGA macro-CTA was used for the emulsion polymerisation of styrene. Interestingly, only spherical micelles were obtained, which confirms that the specific location of the PEGA unit was responsible for the morphology transition. The use of P(NAM-PEGA)-PNAM macro-CTA resulted in a mixture of small spherical micelles and vesicles. In total, the results of this study demonstrated for the first time that the presence of hydrophilic side chains in the macro-CTA could be used to control block copolymer morphology for RAFT emulsion polymerisation systems.

1.6 Biomedical applications of PISA

1.6.1 Drug delivery

With the advantage of manufacturing concentrated solutions of nanoparticles, PISA has addressed a longstanding challenge in the scaling-up of nanoparticle systems that are intended for commercial applications (160). Therefore, PISA is of significant interest for application as a reproducible and scalable method for the facile production of nanoparticles for drug delivery. Another advantage is that RAFT emulsion polymerisation is environmentally friendly and already widely used in industry (24, 161). PISA is also a convenient synthetic route towards nanoparticles with different shapes and controlled sizes as noted above.

An early example of the use of PISA nanoparticles for drug delivery was synthesised by Karagoz *et al.* where vinyl benzaldehyde (VBA) units were copolymerised with styrene under RAFT dispersion polymerisation conditions with a POEGMA macro-CTA (162). After the polymerisation, the aldehyde functional groups in the polystyrene core were conjugated with doxorubicin via pH-labile bonds. By modulating the molar mass of the core polystyrene-VBA block, a family of doxorubicin-loaded polymeric nanoparticles with spherical, worm-like, rod-like, and vesicular morphologies were obtained. Next, the effect of nanoparticle shape on both the cellular uptake in MCF-7 breast cancer cells and the IC_{50} of doxorubicin was studied. After 1 h of treatment of the MCF-7 breast cancer cells with the doxorubicin loaded nanoparticles, differences in the rate of nanoparticle cell uptake was observed. Specifically, the worm-like micelles displayed the highest MCF-7 cell uptake and the spherical micelles showed the lowest MCF-7 cell uptake (Figure 8). After 24 h, increased cellular uptake was observed for rod-like micelles and worm-like micelles. This observation was attributed to the high aspect ratio of the worm- and rod-like morphologies, leading to increased surface contact with cell membranes and promoting higher cell uptake. The IC_{50} values for worm- and rod-like micelles

were seven times lower than that for spherical micelles, which was most likely due to the increased cell uptake. This study indicated that nanoparticles with higher aspect ratio morphologies (such as rod-like or worm-like) could be employed as a strategy for increasing the cytotoxic activity of doxorubicin loaded nanoparticles.

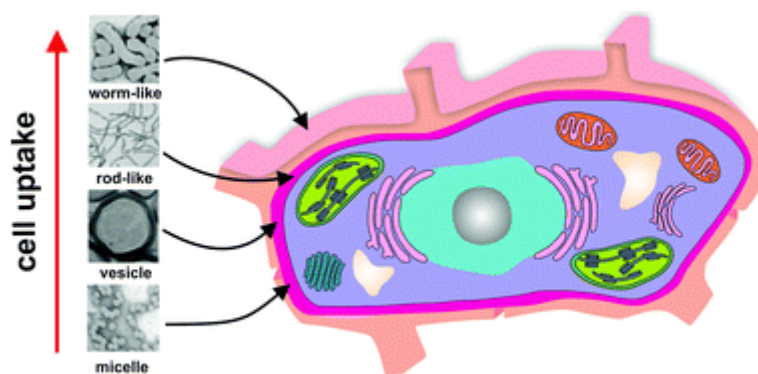


Figure 8. The morphology of POEGMA-P(St-VBA) block copolymer dictates cellular uptake by MCF-7 breast cancer cells. Adapted with permission from Karagoz *et al.* (162) with permission from the Royal Society of Chemistry.

To examine the cellular uptake of nanoparticles with different morphologies in greater detail, Hinde *et al.* used the same POEGMA-P(St-VBA) block copolymer nanoparticles with spherical, worm-like, and rod-like morphologies and observed their cellular behaviour in the MCF-7 cell line with pair correlation microscopy (163). By using a pair correlation microscopy fluorescence imaging technique, the investigators were able to track the mobility of administered nanoparticles across the extracellular space, the cytoplasm, and the nucleus. After administration to MCF-7 cell, a similar observation was made in that worm-like and rod-like nanoparticles were found in the nucleus at significantly higher levels whereas the spherical micellar nanoparticles were detected at far lower levels. The investigators hypothesised that the nuclear envelope acted as a barrier against the spherical nanoparticles but not the worm-like and rod-like nanoparticles. Therefore, nanoparticles with worm- and rod-like

morphologies could deliver more doxorubicin and account for their higher toxicity. Furthermore, through pair correlation microscopy, the authors observed that the higher aspect ratio nanoparticles gained nucleus entry through passive diffusion. Secondly, the passive diffusion occurred in a bidirectional manner, resulting in a plateau of rod and worm accumulation even after extended incubation times. Thirdly, the authors wanted to improve nuclear accumulation of PISA nanoparticles by tagging a nuclear localisation signal (NLS) protein. Covalent attachment of the NLS protein resulted in enhanced accumulation of worm-like nanoparticles but not the spherical nanoparticles. The authors concluded that the physical barrier function of the nuclear envelope clearly superseded the biochemical selection conferred by the NLS protein.

1.6.2 Imaging contrast agent delivery

PISA has also been employed for the delivery of inorganic contrast agents for magnetic resonance imaging (MRI) applications. Recently, the *in situ* preparation of PISA nanoparticles functionalised with iron oxide nanoparticles was demonstrated (164). To obtain such particles, RAFT alcoholic dispersion polymerisations of styrene were carried out with a POEGMA-PMAA diblock copolymer. The polystyrene DP of the triblock copolymers were tuned to obtain spherical micelles, rod-like micelles, and vesicles. The presence of MAA units provides carboxylic acid groups that could be used to complex a mixture of ferrous and ferric ions ($\text{Fe}^{2+}/\text{Fe}^{3+}$) and form iron oxide nanoparticles. This iron oxide-complexing protocol did not affect the final morphology of the triblock copolymer/iron oxide nanoparticle hybrids. Since superparamagnetic iron oxide nanoparticles have been used as negative MRI contrast agents, the nanoparticle hybrids were tested using a high field MRI scanner. These tests showed that the spherical micelle morphology had a transverse relaxivity that was several times higher than those for commercially available contrast agents such as Feridex. Furthermore, the rod-like

micelles and vesicles displayed lower measured relaxivity. The authors attributed the difference in relaxivity between morphologies to the distribution of the iron oxide nanoparticles within the polymer structure. For micelles, the iron oxide nanoparticles are more compacted which then results in the enhancement of their relaxivity.

For the delivery of positive contrast agents for MRI, Esser *et al.* synthesised gadolinium-loaded nanoparticles with the PISA technique (130). A novel macro-CTA of poly(glycidyl methacrylate)-POEGMA (PGlyMA-POEGMA) was synthesised for the RAFT alcoholic dispersion polymerisation of styrene. The core polystyrene DP of the PGlyMA-POEGMA-PS triblock copolymer was adjusted to obtain a range of sizes and shapes (spherical micelles, filament-like micelles, and vesicles). A pre-synthesised cyclic gadolinium chelate was conjugated to PGlyMA-POEGMA-PS spherical micelles, filament-like micelles, and vesicles via primary amines and their application as positive contrast MRI agents was tested. Of the various morphologies, the filament morphology was the most promising candidate due to its combination of good gadolinium-labelling efficiency with high T_1 relaxivity. The vesicular nanoparticles also had a comparable relaxivity but lower gadolinium loading efficiency. In light of other results showing longer blood circulation times for polymeric nanoparticles with a filament-like morphology, such nanoparticles could have potential applications in magnetic resonance angiography and cancer diagnostics/theranostics (19).

1.7 Emerging challenges of nanomedicine

Historically, nanoparticles were developed to encapsulate small therapeutic agents that are poorly soluble, display less than desirable pharmacokinetic profile, and high off-target toxicity (165). In the 1960s, liposomes were developed based on the structure of a phospholipid bilayer and capable of solubilising both hydrophilic and lipophilic molecules (166). In 1980, it was demonstrated that pH-sensitive liposomes that could preferentially disassemble in acidic

microenvironments and release their drug cargo (167). In 1987, the concept of PEGylation was introduced, whereby PEG chains were conjugated to the liposome surface to inhibit opsonisation, therefore increasing blood circulation times and enhancing tumour accumulation (168). Then, in 1995, the US Food and Drug Administration (FDA) approved the use of Doxil, a PEGylated liposomal formulation of doxorubicin for the treatment of HIV-related Kaposi's sarcoma, metastatic ovarian cancer, and metastatic breast cancer (169). A major advantage of using Doxil is in the improvement of doxorubicin safety profile when managing solid tumours in patients. Specifically, the formulation of doxorubicin into liposome limits doxorubicin exposure to cardiac tissue and consequently reduces cardiotoxicity (170). It has also been reported that the clinical therapeutic efficacy of Doxil was superior in HIV-related Kaposi's sarcoma and metastatic ovarian cancer when compared to conventional therapies and was equivalent in metastatic breast cancer and multiple myeloma (170, 171). Although the use of Doxil has shown better safety and increased clinical therapeutic efficacy in patients, adverse effects from the use of Doxil have been reported. For example, skin toxicity in the form of hand-foot syndrome or Palmar Plantar erythrodysesthesia have been reported following Doxil administration in patients (172, 173). The administration of liposomal drugs such as Doxil can be recognised by the immune system as foreign, leading to adverse immune phenomenon such as complement activation-related pseudoallergy – a type of acute hypersensitivity reaction (174). These side effects were not observed with free doxorubicin, and thus emphasised the complexity and variety of biological systems.

Following the initial approval of Doxil, other liposomal formulations also gained regulatory approval for the treatment of various types of medical conditions. For example, DaunoXome (liposomal daunorubicin) is approved for AIDS-associated Kaposi's sarcoma, Marqibo (liposomal vincristine) is approved for acute lymphoblastic leukemia, Myocet (non-PEGylated liposomal doxorubicin) is approved in Europe and Canada for metastatic breast

cancers, and Onivyde MM-398 (liposomal irinotecan) is approved for pancreatic ductal adenocarcinoma (175-178). Aside from liposomal nanomedicines, other nanoformulations have also gained regulatory approval. For example, Abraxane (albumin-bound paclitaxel) is indicated for metastatic breast cancer, Feraheme (superparamagnetic iron oxide nanoparticles) is used to treat iron deficiency in anemic patients, and Genexol-PM (polymeric micelle formulation of paclitaxel) is approved in South Korea for metastatic breast cancer (14). From a commercial perspective, Abraxane is one of the most successful nanomedicines on the market with an estimated annual revenue at \$967 million (in comparison, Doxil has an estimated annual revenue of \$181 million) (179). The Abraxane formulation mitigates the toxicities associated with the emulsifier Cremophor EL in Taxol, the commercial paclitaxel formulation. The result is a paclitaxel formulation that can be used at high doses and administered more quickly, thus enabling a higher volume of distribution and higher intratumoral concentration when compared to Taxol (180).

Many nanomedicines rely on the appropriate accumulation of drug at specific site/s in the body. Arguably, cancer represents the best example of a disease where the adequate delivery of highly potent, albeit toxic, chemotherapeutic drugs at the desired site in the body can mean the difference between efficacy and severe morbidity (181, 182). While liposomal encapsulation of chemotherapeutic agents has been generally shown to improve pharmacokinetics and biodistribution, there has not been an appreciable benefit to overall patient survival when compared to the use of the chemotherapeutic drug alone (183). For example, although Doxil displays enhanced tolerability and tumour drug delivery, clinical trials have not demonstrated clear evidence of superior efficacy over conventional formulations of doxorubicin (183). Non-liposomal nanomedicine formulations have also failed to demonstrate a clear clinical advantage over their free drug formulations. For example, whilst an every-3-week dosing schedule of Abraxane is superior to paclitaxel with regards to response rate and

time to progression for breast cancer patients, the once-a-week dosing schedule did not exhibit similar behaviour in progression rate and overall patient survival and even showed increased toxicity (184). More recently, Farokhzad and colleagues pointed out that polymeric nanoparticles (BIND-014, CRLX101 and NK105) were also underperforming in clinical trials (1). Intriguingly, several prominent groups in the field have opined that the translation of nanomedicines from laboratory bench to bedside relative to the immense research effort expanded by academics appears to be exceedingly low (185-188). Clearly, despite the exciting concept of how nanoparticles can be used in the body, the disappointing clinical results underpin the need to rethink existing development strategies.

The prevailing belief in the nanomedicine community is that nanoparticles preferentially accumulate in solid tumours because nanoparticles extravasate from tumour blood vessels into the tumour microenvironment through gaps between adjacent endothelial cells (189). This phenomenon is a key principle of the enhanced permeability and retention (EPR) effect (190-193) and forms the foundation of nanoparticle delivery to solid tumours. While healthy vessels are systematically lined by an endothelial cell monolayer that only allows passage of small molecules (water, salts, oxygen, glucose etc.), tumour blood vessels possess irregular size and shape, forming interendothelial cell gaps across the vessel walls (194). These gaps are measured at between 100 nm and 500 nm in diameter, depending on the tumour type and stage as derived from mouse models (195). Aside from the leaky tumour vasculature, the solid tumour accumulation of nanoparticles is enhanced by impaired lymphatic drainage system and upregulation of permeability mediators (196). In a clinical setting, the EPR effect can be further amplified by increasing systolic blood pressure via nitric oxide-releasing agents such as topical nitroglycerin or angiotension II infusion (197). Yet, in light of the recent clinical shortcomings of nanoparticle delivery systems, it is plausible that this interpretation of the EPR effect could be too simplistic and that over-reliance on the EPR effect could preclude the

successful clinical translation of advanced nanoparticle systems (1, 198). Further evidence that the EPR-centric approach is flawed is presented in a recent meta-analysis of the nanoparticle drug delivery literature from the past decade showing that only 0.7% (median) of administered nanoparticles in mouse models are delivered to solid tumours (199). It should be noted that this meta-analysis appears to under represent those nanomedicines that display significantly higher accumulation than 0.7%. Nonetheless, in this hotly debated work (200-202), Wilhelm *et al.* suggests that the low delivery efficiency is a key challenge with successful clinical translation of nanoparticles for oncological applications since the nanoparticles do not accumulate at high enough concentration in tumours to produce a desired outcome. This low delivery efficiency of nanoparticles also adversely affects the application of nanoparticles towards other biomedical applications such as imaging and diagnostics.

1.8 Bio-Nano Interactions of Polymeric Nanoparticles

In light of compelling evidence that the current nanomedicine development approach requires substantial improvements, researchers in the field have recently turned their attention to the nanoparticle-biological (nano-bio) interactions that occur after nanoparticle administration. Nano-bio interactions dictate the cellular and physiological fate of the administered nanoparticles based on their physicochemical properties (e.g., size, surface chemistry, and shape). However, there remains an incomplete understanding of how the physicochemical properties of nanoparticles dictate their biological behaviour. Since many nanoparticles will be intravenously administered, blood and endothelial cells are the first organs that nanoparticles commonly encounter (37). Yet, the knowledge of nano-bio interactions has been derived mostly from immortalised cell lines and rodent models. There is only a limited understanding of how nanoparticles interact with human cells and components

(203-209). This represents a key knowledge gap in the rational design of polymeric nanoparticles for medicine.

The future development of polymeric nanoparticles for medicine will benefit from a better understanding of the interactions between polymeric nanoparticles and human cells such as endothelial cells, blood-bound proteins and immune cells. This thesis adds to this growing body of knowledge by characterising nano-bio interactions with human blood components (endothelial cells, proteins, immune cells) according to the size and surface chemistry of PISA nanoparticles. Chapters 2, 3, and 4 investigate the biological interactions of a library of nanoparticles with a range of sizes and surface chemistries with human endothelial cells, proteins, and immune cells respectively. The results from the aforementioned thesis chapters are expected to be used for the rational design of polymeric nanoparticle for human use.

1.8.1 Bio-Nano interactions with endothelial cells

Recently, nanoparticles for the treatment of cardiovascular diseases (CVDs) has attracted major interest. In particular, nanoparticle targeting of atherosclerotic plaque is a promising strategy to combat atherosclerosis; the chronic inflammatory disease of the vascular wall and a major contributor of ischemic heart disease (17, 210). Endothelial cell targeting by nanoparticles is based on specific vascular wall endothelial cell receptors associated with both acute and chronic inflammations. So far, endothelial cell receptors such as intracellular adhesion molecule 1 (ICAM-1), vascular cell adhesion molecule 1 (VCAM-1), and selectins have been identified as major components in the pathology of atherosclerosis and therefore present as local targeting epitopes (211). To ensure efficient targeting of such receptors, the impact of nanoparticle physicochemical properties on their association with endothelial cells have been investigated.

Effect of nanoparticle size on endothelial cell interactions

So far, nanoparticles with a spherical morphology have been commonly studied for targeting CVDs because they are easier to produce and modify. The size, in terms of spherical diameter is relatively more straightforward to quantify compared to other non-spherical morphologies. For instance, carboxylated polystyrene nanoparticles with a spherical diameter of 500 nm to 5 μm were functionalised with various antibodies (human ICAM-1 antibody, human VCAM-1 antibody, sialyl Lewis^A) which targeted molecules that were over-expressed on the inflamed vascular wall (212). The authors found that the efficiency of particle binding in a disturbed reconstituted blood flow model increased according to nanoparticle spherical diameter. The carboxylated polystyrene particles in the nanometre size range showed minimal adhesion to the endothelium, which was attributed to their entrapment among red blood cells midstream of the blood flow. The authors also found that the 2 μm spherical polystyrene particles displayed 2.5-3.5 times greater adhesion to the aortic wall in *in vivo* models when compared to 500 nm spherical particles. This observation agrees with results obtained in Namdee *et al* wherein the authors demonstrated that the adhesion of dual-functional (E-selectin and VCAM-1) 2 μm polystyrene particles to the inflamed aorta was at least 4.0 times greater than that of their 500 nm counterparts (211).

Effect of nanoparticle shape on endothelial cell interactions

In light of advanced synthesis techniques (such as PISA) that enable facile access to non-spherical nanoparticles and the accompanying biological studies that show that nanoparticle shape has a profound impact on biological interactions, the effects of nanoparticle shape on endothelial cell interactions have been investigated. Thompson *et al.* characterised nanoparticle shape parameters into volume, axis length, and aspect ratio for polystyrene spherical and rod-like particles, and tested their adhesion to an inflamed endothelial wall (213).

Under high shear rates, the rod-like particles displayed significantly higher association compared with spherical particles of an equal volume; leading the authors to opine that aspect ratio of the particles rather than shape determined particle adhesion efficiency. More recently, Wen *et al.* showed that rod-like particles functionalised with binding peptides and contrast agents could activate platelets/thrombus in mouse carotid artery more readily compared to spherical particles (214).

Effect of nanoparticle surface chemistry on endothelial cell interactions

So far, evidence in the literature suggest that nanoparticle interaction with endothelial cells is influenced by surface chemistry. For instance, when injected into a developing zebrafish, circulating quantum dots associated with endothelial cells over a time period of 20 hours (215). Overall, amino-functionalised quantum dots associated with human umbilical vein endothelial cells (HUVECs) more than carboxy-functionalised quantum dots. The authors highlighted that the endothelial membrane possesses a negative electrostatic charge which potentially promoted a stronger interaction with amino quantum dots. Another study by Bartczak *et al.* also demonstrated that surface chemistry influences endothelial cell interactions (216). Bartczak *et al.* functionalised nanoparticles with a ‘mutant’ and ‘inhibitor’ type of the KATWLPRR peptide; a peptide previously shown to bind to receptors on the endothelial plasma membrane but endocytose via different pathways with both pathways capable of promoting the down-regulation of angiogenic genes (217). Interestingly, both types of ‘mutant’ and ‘inhibitor’ type nanoparticles were uptaken by endothelial cells in greater numbers than just the PEGylated particles. Both nanoparticles also appear to have distinct exocytosis profiles, thereby suggesting that some of the ‘mutant’ particles were re-uptaken by cells after 4 h while for a period of 6 h the ‘inhibitor’ nanoparticles were progressively exocytosed.

1.8.2 Bio-Nano interactions with proteins

Human blood plasma contains a complex milieu of biomolecules including proteins, nucleic acids, metabolites, etc. Of these biomolecules in the bloodstream, it is well-established that nanoparticles are rapidly coated with proteins resulting in the formation of a protein corona (218). The formation of this nanoparticle-protein complex is driven by a number of forces including van der Waals interactions, electrostatic interactions, hydrogen bonding, hydrophobic interactions, and π - π stacking interactions (219). Over a period of exposure to proteins, the 'Vroman effect' states that proteins with high abundance but low affinity will be dynamically displaced by proteins with low abundance but high affinity (220, 221). These proteins form a soft and hard portion of the protein corona, respectively. The formation of both soft and hard protein corona is dynamic and are highly dependent on a nanoparticle's physicochemical properties (222).

Effect of nanoparticle physical properties on protein corona formation

Proteins adopt various configurations based on the curvature of a surface, resulting in different protein binding affinities (223). Therefore, it is no surprise that the literature has shown that protein binding constant is related to nanoparticle size. For instance, both the groups of Yin and Lundqvist have shown that the size of gold and polystyrene nanoparticle is directly correlated with the binding constant of human serum albumin (HSA), gamma-globulin proteins, and transferrin (224, 225). A study has suggested that smaller gold nanoparticles are adept at reducing the adsorption of plasma protein (226). Clearly, there is a relationship between the size of a nanoparticle and the quantity of proteins formed on its surface. Aside from the quantity of proteins, the density of the protein corona has been investigated. Piella *et al.* incubated citrate-stabilised gold nanoparticles with sizes ranging from 3.5 to 150 nm in whole plasma and found that protein corona density was also directly correlated with nanoparticle size (i.e.

smaller nanoparticles had less dense protein coronas) (227). Another study demonstrated the time to reach maximum protein adsorption was also dependent on nanoparticle size by showing that the adsorption of lysozyme on 100 nm nanodiamonds reach peak adsorption at 10-15 min and the 5 nm nanodiamonds took 30-40 min under the same conditions (228).

In vitro studies such as the aforementioned are important in developing a fundamental understanding of such bio-nano interactions. However, clinically-relevant data can only be obtained through *in vivo* studies. Through the limited number of *in vivo* studies on protein corona formation that has been conducted to date, the trends observed from the *in vitro* data is generally agreeable. In 2018, Garcia-Alvarez *et al.* showed that *in vivo* protein corona formation on gold nanostars (40 and 70 nm) also correlated with size (i.e. more proteins and more protein types formed on the 70 nm nanostars compared to the 40 nm nanostars) (229).

Effect of nanoparticle surface chemistry on protein corona formation

The surface chemistry of a nanoparticle may be tuned to modify its charge, hydrophobicity/hydrophilicity, binding affinity, etc. Critically, surface modification of a nanoparticle is another factor influencing the formation and evolution of protein corona on NP. For example, the use of PEG for covalent attachment to nanoparticles is a common strategy to increase nanoparticle biocompatibility due to the reduction of protein adsorption on nanoparticle surfaces (230-232). It should be noted that even with extensive PEGylation, it is still not possible to eliminate the formation of a protein corona (233, 234). With the reduction of protein adsorption, opsonisation by reticuloendothelial system (RES) cells are consequently reduced and blood circulation times improved (235). For example, Benetti and coworkers have shown that 60 nm PEGylated gold nanoparticles had significantly lower protein adsorption compared to 60 nm citrate-functionalised gold nanoparticles (236). Curiously the same study showed that there were no differences for 10 and 200 nm sized nanoparticles when comparing

PEGylated gold nanoparticles and citrate-functionalised nanoparticles. Therefore, both size and surface chemistry have to be considered concurrently when studying the protein corona. Ligand modification has also been demonstrated to induce different effects on protein corona formation. For example, Xiao *et al.* has demonstrated that nanoparticles that were functionalised with the larger molecular weight transferrin (Tf) had a stronger association of plasma proteins compared to nanoparticles functionalised with smaller molecular weight peptides (226). In a follow up study, the authors used polystyrene nanoparticles with three types of Tf-targeting ligands of various sizes and conformation (237). The use of different Tf-targeting ligands resulted in significant differences in association with clusterin, apolipoprotein A-I, and fibrinogen chain. Moreover, varying the grafting density of glycopolymer chains on a nanoparticle's surface also affects the composition of protein corona (238). By analysing complement activation C3a and SC5b-9, Yu *et al.* observed that a higher surface grafting density was correlated with two pro-complement proteins, factors B and C3 on the nanoparticle surface.

1.8.3 Bio-Nano Interactions with Immune Cells

Similar to proteins, the physicochemical properties of nanoparticles also determine their interactions with immune cell in biological fluids (e.g. blood plasma and alveolar fluid). This structure-activity relationship is explored below:

Effect of nanoparticle surface chemistry on immune cell association

Cell-specific targeting by nanoparticles reduces the undesired effects of off-target association and improves patient outcomes. A widely used example is the use of folate to improve the affinity of nanoparticles towards cancer cells (239). For example, folic acid-functionalised gold nanoparticles displayed selectivity of folate linker conjugates towards cells with high folate expression (e.g. HeLa cells) (240). In 2012, Hrkach and colleagues synthesised

a polymeric nanoparticle that contained docetaxel (241). This nanoparticle was comprised of a poly(D,L-lactide) core that contained the docetaxel, and a PEG outer shell. Furthermore, the PEG shell was surface-decorated with a targeting ligand, S,S-2-(3-(5-amino-1-carboxypentyl)-ureido)-pentanedioic acid (ACUPA), which has a strong affinity for prostate specific membrane antigen (PSMA). Initial *in vitro* tests using a PSMA prostate cancer cell line (LNCaP) demonstrated that the nanoparticles with ACUPA enhanced overall cytotoxicity. The intravenous administration of this nanoparticle in a range of hosts (primates, mice, and rats) showed enhanced circulation of docetaxel, resulting in a plasma concentration of docetaxel that was 100 times higher than free docetaxel at 24 h post-administration.

Nanoparticles with surface charge may be introduced to affect cellular uptake and immune response (242). So far, literature evidence has established that non-phagocytic cell lines, such as HeLa human cervical epithelial cells (243), show a preference for the accumulation of cationic nanoparticles. Whereas phagocytic cell association with surface charged nanoparticles is less resolved. For instance, anionic polystyrene nanoparticles have shown preferential uptake by immortalised monocytes, cultured human macrophages, and murine liver cells (244). Yet, other studies report that primary mouse alveolar macrophages (245) and human U-937 monocytes (246) are more strongly associated with cationic nanoparticles. Another study showed the use of 120 nm liposomes with a range of surface charges showed no charge preference when incubated with mouse macrophages (247). Notably, instead of HeLa cells or immortalised monocytes and the like, Glass *et al.* used fresh human blood to investigate the association of 5 nm hyper-branched polymers (HBPs) with six white blood cell populations (248). The study revealed that although most cell types were associated with cationic HBPs at 4 °C (i.e. in the near-absence of biological activity), at 37 °C similar/greater phagocytic cell association with anionic HBPs compared to cationic HBPs was observed with neutral HBPs displaying stealth-like properties.

Various chemical functional groups commonly found engineering onto nanoparticles change their nano-bio interactions. To characterise this effect, Bai *et al.* synthesised a library of gold nanoparticles with different sizes and functional groups, and measured the HeLa cell uptake efficiency of these nanoparticles (249). The authors varied the number of hydroxyl and methyl side groups in the polymer chain, as well as the length of the side groups. HeLa cell uptake efficiency was measured via flow cytometry. The results showed that an increase in the length of hydroxyl side chains, the number of hydroxyl groups in each side chain, or the total number of methyl groups was accompanied by an increase in HeLa cell uptake. Other functional groups such as pyridyl disulfides have been attached to nanoparticle surfaces for increased affinity with bloodstream components such as peptides, and thiol-reactive molecules (250, 251). In fact, a multitude of cells including cancer cells display a high concentration of thiol groups on their membrane. Many studies have shown that the presence of such thiol-groups on drug-delivery nanoparticles increase their delivery efficiency to specific cells.

Effect of nanoparticle size on immune cell association

With respect to their size, nanoparticles are internalised by antigen-presenting cells (APCs) via different pathways, including both pinocytosis and phagocytosis (252, 253). Furthermore, macrophages may take several routes to uptake even the same type of nanoparticle (254). A few studies have reported that smaller nanoparticles (20-200 nm) stimulate stronger immune responses than their larger counterparts (255, 256). For example, the Plebanski group showed that 40-50nm polystyrene nanoparticles could induce potent CD4 + and CD8 + T-cell responses at a higher efficiency compared to larger polystyrene nanoparticles (>500 nm). Whereas, the larger nanoparticles were more active in eliciting interferon (IFN)- γ and antibody responses. Other studies have observed that smaller (<100 nm) nanoparticles rapidly locate to the draining lymph nodes after intradermal injection and efficiently target native lymph node dendritic cells,

B-cells, and macrophages (256). In general, the manipulation of nanoparticle size has been used to maximise antigen delivery to dendritic cells. For example, small (<100 nm) nanoparticles are more readily uptaken by dendritic cells whereas larger (1000 nm) particles were preferentially internalised by macrophages (253). Also, it has been reported that a nanoparticle size of ~50 nm is optimal for uptake by dendritic cells (257-259).

Nanoparticle size has also been observed to be a deciding factor in the immunostimulatory profiles of vaccine formulations. For example, Rettig *et al.* showed that smaller nanoparticles (~220 nm) promoted stronger IFN- α responses and larger nanoparticles (~1200 nm) induced tumour necrosis factor (TNF)- α (260). The authors hypothesise that the type of cells determined the internalisation of these nanoparticles; plasmacytoid dendritic cells consumed smaller nanoparticles while macrophages prefer larger nanoparticles. Nanoparticle size was also proposed as an important factor in the type of immunity induced. For example, 40 nm nanoparticles promoted Th1 and CD8 + T-cell reactions, while larger 100 nm nanoparticles induced Th2 responses (255).

Effect of multiple nanoparticle physicochemical properties on immune cell interactions

To date, our group has investigated several aspects of nanoparticle interactions with immune cells in whole human blood. Aside from the impact of the surface charge of HBPs on immune cell association (248), our group has also observed enhanced association of thiol-reactive star polymers with primary human cells such as monocytes, granulocytes, and dendritic cells in comparison with control star polymers in whole human blood (261). Platelet association increased with the use of thiol-reactive star polymers compared with control star polymers, but were found to be inactive for the duration examined. The evaluation of charged HBPs association with immune cells in a clinically-relevant model will richly enable future translation of HBPs to the clinic. To evaluate immune cell nanoparticle targeting in primary

human cells rather than monocultured cell line models, Kent and colleagues produced caveolin-1 nanoparticles and functionalised them with monoclonal antibodies. CD4⁺ T cell and CD20⁺ B cell targeting by the caveolin-1 nanoparticles in fresh human blood was carried out via flow cytometry (262). The results showed that antibody-functionalised significantly enhanced nanoparticle binding to targeted immune cells in whole human blood. Ultimately, immune cell-targeted caveolin-1 nanoparticles is shown to be an efficient system for the development of advanced immunotherapeutics.

To further enhance our understanding of nanoparticle interactions with immune cells, there is a gap in knowledge on the systematic study of the biological interactions of a matrix of nanoparticles that possesses controllable size and surface chemistry in whole human blood. This simultaneous variation of physicochemical properties would reflect the high degree of physicochemical flexibility afforded by polymeric nanoparticles. That is, the physicochemical properties of polymeric nanoparticles may be tuned in a facile and flexible manner. To that end, in Chapter 4, a matrix of nanoparticles with varying size and varying surface chemistry was produced and their association with white blood cells in whole human blood was investigated.

1.9 Aims

The overall objective of this thesis is to develop a nanoparticle platform based on PISA that could be used to access nanoparticles with multiple tuneable physicochemical properties (namely size, surface chemistry, and shape). For the rationale design of nanoparticles for biomedical applications, the biological interactions of these unique nanoparticles within several clinically relevant environments were characterised. The aims for each chapter are outlined hereunder:

1. In Chapter 2, a library of nanoparticles with tuneable size and surface chemistry was synthesised via PISA. The impact of nanoparticle size and surface chemistry on association with human umbilical vein endothelial cells (HUVECs) was tested under both static and dynamic flow conditions.
2. In Chapter 3, a library of nanoparticles with tuneable size and surface chemistry was incubated with human plasma and their protein coronas were characterised via mass spectrometry. Specifically, the proteins in the protein coronas were quantified to investigate the impact of nanoparticle size and surface chemistry on protein corona composition.
3. In Chapter 4, a library of nanoparticles with tuneable size and surface chemistry was incubated with fresh and whole human blood. The nanoparticle association with white blood cell populations was characterised through flow cytometric techniques.
4. In Chapter 5, the morphology of nanoparticles synthesised via RAFT aqueous emulsion polymerisation was demonstrably controlled via the end group and initiator concentration. The formation of spherical, worm-like, and vesicular nanoparticles was made possible by manipulating the end group and initiator concentration. The results in Chapter 5 demonstrated

two new experimental parameters that could be exploited to access multiple nanoparticle morphologies.

1.10 References

1. Shi J, Kantoff PW, Wooster R, Farokhzad OC. Cancer nanomedicine: progress, challenges and opportunities. *Nat Rev Cancer*. 2017;17(1):20-37.
2. Swartz MA, Hirose S, Hubbell JA. Engineering approaches to immunotherapy. *Sci Transl Med*. 2012;4(148):148rv9.
3. Riehemann K, Schneider SW, Luger TA, Godin B, Ferrari M, Fuchs H. Nanomedicine—challenge and perspectives. *Angewandte Chemie International Edition*. 2009;48(5):872-97.
4. Sahoo SK, Misra R, Parveen S. Nanoparticles: a boon to drug delivery, therapeutics, diagnostics and imaging. *Nanomedicine in Cancer: Pan Stanford*; 2017. p. 73-124.
5. Srinivasarao M, Galliford CV, Low PS. Principles in the design of ligand-targeted cancer therapeutics and imaging agents. *Nature reviews Drug discovery*. 2015;14(3):203.
6. Blanco E, Shen H, Ferrari M. Principles of nanoparticle design for overcoming biological barriers to drug delivery. *Nature biotechnology*. 2015;33(9):941.
7. Ling D, Lee N, Hyeon T. Chemical synthesis and assembly of uniformly sized iron oxide nanoparticles for medical applications. *Accounts of chemical research*. 2015;48(5):1276-85.
8. Adisheshaiah PP, Crist RM, Hook SS, McNeil SE. Nanomedicine strategies to overcome the pathophysiological barriers of pancreatic cancer. *Nat Rev Clin Oncol*. 2016;13(12):750-65.
9. Gause KT, Wheatley AK, Cui J, Yan Y, Kent SJ, Caruso F. Immunological Principles Guiding the Rational Design of Particles for Vaccine Delivery. *ACS Nano*. 2017;11(1):54-68.
10. Irvine DJ, Hanson MC, Rakhra K, Tokatlian T. Synthetic Nanoparticles for Vaccines and Immunotherapy. *Chem Rev*. 2015;115(19):11109-46.

11. Saraiva C, Praca C, Ferreira R, Santos T, Ferreira L, Bernardino L. Nanoparticle-mediated brain drug delivery: Overcoming blood-brain barrier to treat neurodegenerative diseases. *J Control Release*. 2016;235:34-47.
12. Vio V, Marchant MJ, Araya E, Kogan MJ. Metal Nanoparticles for the Treatment and Diagnosis of Neurodegenerative Brain Diseases. *Curr Pharm Des*. 2017;23(13):1916-26.
13. Veisheh O, Tang BC, Whitehead KA, Anderson DG, Langer R. Managing diabetes with nanomedicine: challenges and opportunities. *Nat Rev Drug Discov*. 2015;14(1):45-57.
14. Petros RA, DeSimone JM. Strategies in the design of nanoparticles for therapeutic applications. *Nat Rev Drug Discov*. 2010;9(8):615-27.
15. Wilhelm S, Tavares AJ, Dai Q, Ohta S, Audet J, Dvorak HF, et al. Analysis of nanoparticle delivery to tumours. *Nature reviews materials*. 2016;1(5):16014.
16. Anchordoquy TJ, Barenholz Y, Boraschi D, Chorny M, Decuzzi P, Dobrovolskaia MA, et al. Mechanisms and Barriers in Cancer Nanomedicine: Addressing Challenges, Looking for Solutions. *ACS Nano*. 2017;11(1):12-8.
17. Ta HT, Truong NP, Whittaker AK, Davis TP, Peter K. The effects of particle size, shape, density and flow characteristics on particle margination to vascular walls in cardiovascular diseases. *Expert opinion on drug delivery*. 2018;15(1):33-45.
18. Truong NP, Whittaker MR, Mak CW, Davis TP. The importance of nanoparticle shape in cancer drug delivery. *Expert opinion on drug delivery*. 2015;12(1):129-42.
19. Geng Y, Dalhaimer P, Cai S, Tsai R, Tewari M, Minko T, et al. Shape effects of filaments versus spherical particles in flow and drug delivery. *Nature nanotechnology*. 2007;2(4):249.
20. Dai Q, Bertleff - Zieschang N, Braunger JA, Björnholm M, Cortez - Jugo C, Caruso F. Particle targeting in complex biological media. *Advanced healthcare materials*. 2018;7(1):1700575.

21. Khor SY, Hu J, McLeod VM, Quinn JF, Williamson M, Porter CJ, et al. Molecular weight (hydrodynamic volume) dictates the systemic pharmacokinetics and tumour disposition of PolyPEG star polymers. *Nanomedicine: Nanotechnology, Biology and Medicine*. 2015;11(8):2099-108.
22. Canning SL, Smith GN, Armes SP. A critical appraisal of RAFT-mediated polymerization-induced self-assembly. *Macromolecules*. 2016;49(6):1985-2001.
23. Derry MJ, Fielding LA, Armes SP. Polymerization-induced self-assembly of block copolymer nanoparticles via RAFT non-aqueous dispersion polymerization. *Progress in Polymer Science*. 2016;52:1-18.
24. Velasquez E, Rieger J, Stoffelbach F, D'Agosto F, Lansalot M, Dufils P-E, et al. Surfactant-free poly (vinylidene chloride) latexes via one-pot RAFT-mediated aqueous polymerization. *Polymer*. 2016;106:275-84.
25. Huang CQ, Wang Y, Hong CY, Pan CY. Spiropyran - Based Polymeric Vesicles: Preparation and Photochromic Properties. *Macromolecular rapid communications*. 2011;32(15):1174-9.
26. Semsarilar M, Jones ER, Blanazs A, Armes SP. Efficient Synthesis of Sterically - Stabilized Nano - Objects via RAFT Dispersion Polymerization of Benzyl Methacrylate in Alcoholic Media. *Advanced Materials*. 2012;24(25):3378-82.
27. Derry MJ, Fielding LA, Armes SP. Industrially-relevant polymerization-induced self-assembly formulations in non-polar solvents: RAFT dispersion polymerization of benzyl methacrylate. *Polymer Chemistry*. 2015;6(16):3054-62.
28. Delaittre G, Nicolas J, Lefay C, Save M, Charleux B. Surfactant-free synthesis of amphiphilic diblock copolymer nanoparticles via nitroxide-mediated emulsion polymerization. *Chem Commun (Camb)*. 2005(5):614-6.

29. Brusseau Sgn, D'Agosto F, Magnet S, Couvreur L, Chamignon C, Charleux B. Nitroxide-Mediated copolymerization of methacrylic acid and sodium 4-styrenesulfonate in water solution and one-pot synthesis of amphiphilic block copolymer nanoparticles. *Macromolecules*. 2011;44(14):5590-8.
30. Kim KH, Kim J, Jo WH. Preparation of hydrogel nanoparticles by atom transfer radical polymerization of N-isopropylacrylamide in aqueous media using PEG macro-initiator. *Polymer*. 2005;46(9):2836-40.
31. Rieger J. Guidelines for the synthesis of block copolymer particles of various morphologies by RAFT dispersion polymerization. *Macromolecular rapid communications*. 2015;36(16):1458-71.
32. Sun J-T, Hong C-Y, Pan C-Y. Formation of the block copolymer aggregates via polymerization-induced self-assembly and reorganization. *Soft Matter*. 2012;8(30):7753-67.
33. Chong Y, Le TP, Moad G, Rizzardo E, Thang SH. A more versatile route to block copolymers and other polymers of complex architecture by living radical polymerization: the RAFT process. *Macromolecules*. 1999;32(6):2071-4.
34. Hill MR, Carmean RN, Sumerlin BS. Expanding the scope of RAFT polymerization: recent advances and new horizons. *Macromolecules*. 2015;48(16):5459-69.
35. Sun J-T, Hong C-Y, Pan C-Y. Recent advances in RAFT dispersion polymerization for preparation of block copolymer aggregates. *Polymer Chemistry*. 2013;4(4):873-81.
36. Polo E, Collado M, Pelaz B, del Pino P. Advances toward more efficient targeted delivery of nanoparticles in vivo: understanding interactions between nanoparticles and cells. *ACS nano*. 2017;11(3):2397-402.
37. Cheng CJ, Tietjen GT, Saucier-Sawyer JK, Saltzman WM. A holistic approach to targeting disease with polymeric nanoparticles. *Nature reviews Drug discovery*. 2015;14(4):239.

38. Tang Z, He C, Tian H, Ding J, Hsiao BS, Chu B, et al. Polymeric nanostructured materials for biomedical applications. *Progress in Polymer Science*. 2016;60:86-128.
39. Jia F, Liu X, Li L, Mallapragada S, Narasimhan B, Wang Q. Multifunctional nanoparticles for targeted delivery of immune activating and cancer therapeutic agents. *Journal of Controlled Release*. 2013;172(3):1020-34.
40. Leo E, Scatturin A, Vighi E, Dalpiaz A. Polymeric nanoparticles as drug controlled release systems: A new formulation strategy for drugs with small or large molecular weight. *Journal of Nanoscience and Nanotechnology*. 2006;6(9-10):3070-9.
41. Uhrich KE, Cannizzaro SM, Langer RS, Shakesheff KM. Polymeric systems for controlled drug release. *Chemical Reviews*. 1999;99(11):3181-98.
42. Ringsdorf H. Structure and Properties of Pharmacologically Active Polymers. *Journal of Polymer Science Part C-Polymer Symposium*. 1975(51):135-53.
43. Larson N, Ghandehari H. Polymeric Conjugates for Drug Delivery. *Chemistry of Materials*. 2012;24(5):840-53.
44. Goodarzi N, Varshochian R, Kamalinia G, Atyabi F, Dinarvand R. A review of polysaccharide cytotoxic drug conjugates for cancer therapy. *Carbohydrate Polymers*. 2013;92(2):1280-93.
45. Okuno S, Harada M, Yano T, Yano S, Kiuchi S, Tsuda N, et al. Complete regression of xenografted human carcinomas by camptothecin analogue-carboxymethyl dextran conjugate (T-0128). *Cancer Research*. 2000;60(11):2988-95.
46. Sugahara S, Kajiki M, Kuriyama H, Kobayashi TR. Complete regression of xenografted human carcinomas by a paclitaxel-carboxymethyl dextran conjugate (AZ10992). *Journal of Controlled Release*. 2007;117(1):40-50.
47. Ueda Y, Munechika K, Kikukawa A, Kanoh Y, Yamanouchi K, Yokoyama K. Comparison of Efficacy, Toxicity and Pharmacokinetics of Free Adriamycin and Adriamycin

- Linked to Oxidized Dextran in Rats. *Chemical & Pharmaceutical Bulletin*. 1989;37(6):1639-41.
48. Shih LB, Goldenberg DM, Xuan H, Lu H, Sharkey RM, Hall TC. Anthracycline Immunoconjugates Prepared by a Site-Specific Linkage Via an Amino-Dextran Intermediate Carrier. *Cancer Research*. 1991;51(16):4192-8.
49. Danhauser-Riedl S, Hausmann E, Schick H-D, Bender R, Dietzfelbinger H, Rastetter J, et al. Phase I clinical and pharmacokinetic trial of dextran conjugated doxorubicin (AD-70, DOX-OXD). *Investigational new drugs*. 1993;11(2-3):187-95.
50. Kumazawa E, Ochi Y. DE - 310, a novel macromolecular carrier system for the camptothecin analog DX - 8951f: Potent antitumor activities in various murine tumor models. *Cancer science*. 2004;95(2):168-75.
51. Liu ZH, Wang YT, Zhang N. Micelle-like nanoassemblies based on polymer-drug conjugates as an emerging platform for drug delivery. *Expert Opinion on Drug Delivery*. 2012;9(7):805-22.
52. Oh EJ, Park K, Kim KS, Kim J, Yang JA, Kong JH, et al. Target specific and long-acting delivery of protein, peptide, and nucleotide therapeutics using hyaluronic acid derivatives. *Journal of Controlled Release*. 2010;141(1):2-12.
53. Lee H, Lee K, Park TG. Hyaluronic acid-paclitaxel conjugate micelles: synthesis, characterization, and antitumor activity. *Bioconjug Chem*. 2008;19(6):1319-25.
54. Yang B, Zhang L, Turley EA. Identification of two hyaluronan-binding domains in the hyaluronan receptor RHAMM. *J Biol Chem*. 1993;268(12):8617-23.
55. Goodarzi N, Varshochian R, Kamalinia G, Atyabi F, Dinarvand R. A review of polysaccharide cytotoxic drug conjugates for cancer therapy. *Carbohydr Polym*. 2013;92(2):1280-93.

56. Garay RP, El-Gewely R, Armstrong JK, Garratty G, Richette P. Antibodies against polyethylene glycol in healthy subjects and in patients treated with PEG-conjugated agents. Taylor & Francis; 2012.
57. Webster R, Elliott V, Park BK, Walker D, Hankin M, Taupin P. PEG and PEG conjugates toxicity: towards an understanding of the toxicity of PEG and its relevance to PEGylated biologicals. PEGylated protein drugs: Basic science and clinical applications: Springer; 2009. p. 127-46.
58. Schellekens H, Hennink WE, Brinks V. The immunogenicity of polyethylene glycol: facts and fiction. *Pharmaceutical research*. 2013;30(7):1729-34.
59. Duncan R, Kopecek J, Rejmanova P, Lloyd JB. Targeting of N-(2-hydroxypropyl)methacrylamide copolymers to liver by incorporation of galactose residues. *Biochim Biophys Acta*. 1983;755(3):518-21.
60. Vasey PA, Kaye SB, Morrison R, Twelves C, Wilson P, Duncan R, et al. Phase I clinical and pharmacokinetic study of PK1 [N-(2-hydroxypropyl)methacrylamide copolymer doxorubicin]: first member of a new class of chemotherapeutic agents-drug-polymer conjugates. Cancer Research Campaign Phase I/II Committee. *Clin Cancer Res*. 1999;5(1):83-94.
61. Yokoyama M, Kwon GS, Okano T, Sakurai Y, Seto T, Kataoka K. Preparation of micelle-forming polymer-drug conjugates. *Bioconjugate chemistry*. 1992;3(4):295-301.
62. Kedar U, Phutane P, Shidhaye S, Kadam V. Advances in polymeric micelles for drug delivery and tumor targeting. *Nanomedicine: Nanotechnology, Biology and Medicine*. 2010;6(6):714-29.
63. Yang C, Attia ABE, Tan JP, Ke X, Gao S, Hedrick JL, et al. The role of non-covalent interactions in anticancer drug loading and kinetic stability of polymeric micelles. *Biomaterials*. 2012;33(10):2971-9.

64. Kim B-S, Park SW, Hammond PT. Hydrogen-bonding layer-by-layer-assembled biodegradable polymeric micelles as drug delivery vehicles from surfaces. *ACS nano*. 2008;2(2):386-92.
65. Rösler A, Vandermeulen GW, Klok H-A. Advanced drug delivery devices via self-assembly of amphiphilic block copolymers. *Advanced drug delivery reviews*. 2012;64:270-9.
66. Van Sluis R, Bhujwalla ZM, Raghunand N, Ballesteros P, Alvarez J, Cerdán S, et al. In vivo imaging of extracellular pH using ¹H MRSI. *Magnetic Resonance in Medicine: An Official Journal of the International Society for Magnetic Resonance in Medicine*. 1999;41(4):743-50.
67. Gao GH, Li Y, Lee DS. Environmental pH-sensitive polymeric micelles for cancer diagnosis and targeted therapy. *Journal of controlled release*. 2013;169(3):180-4.
68. Torchilin VP. Multifunctional, stimuli-sensitive nanoparticulate systems for drug delivery. *Nature reviews Drug discovery*. 2014;13(11):813.
69. Kesharwani P, Jain K, Jain NK. Dendrimer as nanocarrier for drug delivery. *Progress in Polymer Science*. 2014;39(2):268-307.
70. Kannan R, Nance E, Kannan S, Tomalia DA. Emerging concepts in dendrimer - based nanomedicine: from design principles to clinical applications. *Journal of internal medicine*. 2014;276(6):579-617.
71. Kesharwani P, Iyer AK. Recent advances in dendrimer-based nanovectors for tumor-targeted drug and gene delivery. *Drug discovery today*. 2015;20(5):536-47.
72. Leong NJ, Mehta D, McLeod VM, Kelly BD, Pathak R, Owen DJ, et al. Doxorubicin conjugation and drug linker chemistry alter the intravenous and pulmonary pharmacokinetics of a PEGylated Generation 4 polylysine dendrimer in rats. *Journal of pharmaceutical sciences*. 2018.

73. Ryan GM, McLeod VM, Mehta D, Kelly BD, Stanislawski PC, Owen DJ, et al. Lymphatic transport and lymph node targeting of methotrexate-conjugated PEGylated dendrimers are enhanced by reducing the length of the drug linker or masking interactions with the injection site. *Nanomedicine: Nanotechnology, Biology and Medicine*. 2017;13(8):2485-94.
74. Mehta D, Leong N, McLeod VM, Kelly BD, Pathak R, Owen DJ, et al. Reducing Dendrimer Generation and PEG Chain Length Increases Drug Release and Promotes Anticancer Activity of PEGylated Polylysine Dendrimers Conjugated with Doxorubicin via a Cathepsin-Cleavable Peptide Linker. *Molecular pharmaceutics*. 2018.
75. Moad G, Rizzardo E, Thang SH. Toward living radical polymerization. *Acc Chem Res*. 2008;41(9):1133-42.
76. Wang J-S, Matyjaszewski K. Controlled/" living" radical polymerization. Atom transfer radical polymerization in the presence of transition-metal complexes. *Journal of the American Chemical Society*. 1995;117(20):5614-5.
77. Kato M, Kamigaito M, Sawamoto M, Higashimura T. Polymerization of methyl methacrylate with the carbon tetrachloride/dichlorotris-(triphenylphosphine) ruthenium (II)/methylaluminum bis (2, 6-di-tert-butylphenoxide) initiating system: possibility of living radical polymerization. *Macromolecules*. 1995;28(5):1721-3.
78. Chiefari J, Chong Y, Ercole F, Krstina J, Jeffery J, Le TP, et al. Living free-radical polymerization by reversible addition– fragmentation chain transfer: the RAFT process. *Macromolecules*. 1998;31(16):5559-62.
79. Moad G, Rizzardo E, Thang SH. Living radical polymerization by the RAFT process– a third update. *Australian Journal of Chemistry*. 2012;65(8):985-1076.

80. Keddie DJ. A guide to the synthesis of block copolymers using reversible-addition fragmentation chain transfer (RAFT) polymerization. *Chemical Society Reviews*. 2014;43(2):496-505.
81. Destarac M. Industrial development of reversible-deactivation radical polymerization: is the induction period over? *Polymer Chemistry*. 2018;9(40):4947-67.
82. Perrier Sb. 50th Anniversary Perspective: RAFT Polymerization A User Guide. *Macromolecules*. 2017;50(19):7433-47.
83. Kolate A, Baradia D, Patil S, Vhora I, Kore G, Misra A. PEG—a versatile conjugating ligand for drugs and drug delivery systems. *Journal of controlled release*. 2014;192:67-81.
84. Knop K, Hoogenboom R, Fischer D, Schubert US. Poly (ethylene glycol) in drug delivery: pros and cons as well as potential alternatives. *Angewandte chemie international edition*. 2010;49(36):6288-308.
85. Pfister D, Morbidelli M. Process for protein PEGylation. *Journal of Controlled Release*. 2014;180:134-49.
86. Lowe S, O'Brien-Simpson NM, Connal LA. Antibiofouling polymer interfaces: poly (ethylene glycol) and other promising candidates. *Polymer Chemistry*. 2015;6(2):198-212.
87. Fairbanks BD, Gunatillake PA, Meagher L. Biomedical applications of polymers derived by reversible addition–fragmentation chain-transfer (RAFT). *Advanced drug delivery reviews*. 2015;91:141-52.
88. Tao L, Liu J, Xu J, Davis TP. Synthesis and bioactivity of poly (HPMA)–lysozyme conjugates: the use of novel thiazolidine-2-thione coupling chemistry. *Organic & biomolecular chemistry*. 2009;7(17):3481-5.
89. Tao L, Liu J, Davis TP. Branched Polymer– Protein Conjugates Made From Mid-Chain-Functional P (HPMA). *Biomacromolecules*. 2009;10(10):2847-51.

90. Duvall CL, Convertine AJ, Benoit DS, Hoffman AS, Stayton PS. Intracellular delivery of a proapoptotic peptide via conjugation to a RAFT synthesized endosomolytic polymer. *Molecular pharmaceutics*. 2010;7(2):468-76.
91. De P, Gondi SR, Sumerlin BS. Folate-conjugated thermoresponsive block copolymers: highly efficient conjugation and solution self-assembly. *Biomacromolecules*. 2008;9(3):1064-70.
92. Sun JT, Yu ZQ, Hong CY, Pan CY. Biocompatible Zwitterionic Sulfobetaine Copolymer - Coated Mesoporous Silica Nanoparticles for Temperature - Responsive Drug Release. *Macromolecular rapid communications*. 2012;33(9):811-8.
93. Ma N, Li Y, Ren H, Xu H, Li Z, Zhang X. Selenium-containing block copolymers and their oxidation-responsive aggregates. *Polymer Chemistry*. 2010;1(10):1609-14.
94. Ren JM, McKenzie TG, Fu Q, Wong EH, Xu J, An Z, et al. Star polymers. *Chemical reviews*. 2016;116(12):6743-836.
95. Liu J, Duong H, Whittaker MR, Davis TP, Boyer C. Synthesis of functional core, star polymers via RAFT polymerization for drug delivery applications. *Macromolecular rapid communications*. 2012;33(9):760-6.
96. Boyer C, Teo J, Phillips P, Erlich RB, Sagnella S, Sharbeen G, et al. Effective delivery of siRNA into cancer cells and tumors using well-defined biodegradable cationic star polymers. *Molecular pharmaceutics*. 2013;10(6):2435-44.
97. Teo J, McCarroll JA, Boyer C, Youkhana J, Sagnella SM, Duong HT, et al. A rationally optimized nanoparticle system for the delivery of RNA interference therapeutics into pancreatic tumors in vivo. *Biomacromolecules*. 2016;17(7):2337-51.
98. Cha RT, Li JJ, Liu Y, Zhang YF, Xie Q, Zhang MM. Fe₃O₄ nanoparticles modified by CD-containing star polymer for MRI and drug delivery. *Colloids and Surfaces B-Biointerfaces*. 2017;158:213-21.

99. Esser L, Lengkeek NA, Moffat BA, Vu MN, Greguric I, Quinn JF, et al. A tunable one-pot three-component synthesis of an I-125 and Gd-labelled star polymer nanoparticle for hybrid imaging with MRI and nuclear medicine. *Polymer Chemistry*. 2018;9(25):3528-35.
100. Huang ZJ, Chen YC, Liu DJ, Lu C, Shen ZW, Zhong SP, et al. Gadolinium-conjugated star-block copolymer polylysine-modified polyethylenimine as highperformance T-1 MR imaging blood pool contrast agents. *Rsc Advances*. 2018;8(9):5005-12.
101. Esser L, Lengkeek N, Moffat BA, Vu M, Greguric I, Quinn JF, et al. A Tunable One-Pot Three-Component Synthesis of an 125I and Gd-Labelled Star Polymer Nanoparticle for Hybrid Imaging with MRI and Nuclear Medicine. *Polymer Chemistry*. 2018.
102. Georgiou TK. Star polymers for gene delivery. *Polymer International*. 2014;63(7):1130-3.
103. Maiti C, Parida S, Kayal S, Maiti S, Mandal M, Dhara D. Redox-Responsive Core-Cross-Linked Block Copolymer Micelles for Overcoming Multidrug Resistance in Cancer Cells. *ACS applied materials & interfaces*. 2018;10(6):5318-30.
104. Ma Z, Zhu X. Core Cross-linked Micelles Made of Glycopolymers Bearing Dopamine and Cholic Acid Pendants. *Molecular pharmaceutics*. 2018;15(6):2348-54.
105. Climie I, White E. The aggregation of random and block copolymers containing acrylonitrile in mixed solvents. *Journal of Polymer Science*. 1960;47(149):149-56.
106. Newman S. Note on colloidal dispersions from block copolymers. *Journal of Applied Polymer Science*. 1962;6(21):S15-S6.
107. Krause S. Dilute solution properties of a styrene—methyl methacrylate block copolymer. *The Journal of Physical Chemistry*. 1964;68(7):1948-55.
108. SZWARC M. 'Living' polymers. *Nature*. 1956;178(4543):1168.
109. Gao Z, Varshney SK, Wong S, Eisenberg A. Block copolymer" crew-cut" micelles in water. *Macromolecules*. 1994;27(26):7923-7.

110. Zhang L, Eisenberg A. Multiple morphologies of "crew-cut" aggregates of polystyrene-*b*-poly (acrylic acid) block copolymers. *Science*. 1995;268(5218):1728-31.
111. Zhang L, Eisenberg A. Multiple morphologies and characteristics of "crew-cut" micelle-like aggregates of polystyrene-*b*-poly (acrylic acid) diblock copolymers in aqueous solutions. *Journal of the American Chemical Society*. 1996;118(13):3168-81.
112. Christian DA, Tian A, Ellenbroek WG, Levental I, Rajagopal K, Janmey PA, et al. Spotted vesicles, striped micelles and Janus assemblies induced by ligand binding. *Nature materials*. 2009;8(10):843.
113. Fielding LA, Lane JA, Derry MJ, Mykhaylyk OO, Armes SP. Thermo-responsive diblock copolymer worm gels in non-polar solvents. *Journal of the American Chemical Society*. 2014;136(15):5790-8.
114. Jones ER, Semsarilar M, Blanazs A, Armes SP. Efficient synthesis of amine-functional diblock copolymer nanoparticles via RAFT dispersion polymerization of benzyl methacrylate in alcoholic media. *Macromolecules*. 2012;45(12):5091-8.
115. Ferguson CJ, Hughes RJ, Pham BT, Hawke BS, Gilbert RG, Serelis AK, et al. Effective *ab initio* emulsion polymerization under RAFT control. *Macromolecules*. 2002;35(25):9243-5.
116. Tanaka H, Yamauchi K, Hasegawa H, Miyamoto N, Koizumi S, Hashimoto T. In situ and real-time small-angle neutron scattering studies of living anionic polymerization process and polymerization-induced self-assembly of block copolymers. *Physica B: Condensed Matter*. 2006;385:742-4.
117. Cardozo AF, Julcour C, Barthe L, Blanco J-F, Chen S, Gayet F, et al. Aqueous phase homogeneous catalysis using core-shell nanoreactors: Application to rhodium-catalyzed hydroformylation of 1-octene. *Journal of Catalysis*. 2015;324:1-8.

118. Nguyen D, Zondanos HS, Farrugia JM, Serelis AK, Such CH, Hawckett BS. Pigment encapsulation by emulsion polymerization using macro-RAFT copolymers. *Langmuir*. 2008;24(5):2140-50.
119. Thompson KL, Mable CJ, Lane JA, Derry MJ, Fielding LA, Armes SP. Preparation of Pickering double emulsions using block copolymer worms. *Langmuir*. 2015;31(14):4137-44.
120. Karagoz B, Boyer C, Davis TP. Simultaneous Polymerization - Induced Self - Assembly (PISA) and Guest Molecule Encapsulation. *Macromolecular rapid communications*. 2014;35(4):417-21.
121. Zhang Q, Wang C, Fu M, Wang J, Zhu S. Pickering high internal phase emulsions stabilized by worm-like polymeric nanoaggregates. *Polymer Chemistry*. 2017;8(36):5474-80.
122. Engström J, Hatton FL, Wågberg L, D'Agosto F, Lansalot M, Malmström E, et al. Soft and rigid core latex nanoparticles prepared by RAFT-mediated surfactant-free emulsion polymerization for cellulose modification—a comparative study. *Polymer Chemistry*. 2017;8(6):1061-73.
123. Albigès R, Klein P, Roi S, Stoffelbach F, Creton C, Bouteiller L, et al. Water-based acrylic coatings reinforced by PISA-derived fibers. *Polymer Chemistry*. 2017;8(34):4992-5.
124. Kaga S, Truong NP, Esser L, Senyschyn D, Sanyal A, Sanyal R, et al. Influence of Size and Shape on the Biodistribution of Nanoparticles Prepared by Polymerization-Induced Self-Assembly. *Biomacromolecules*. 2017;18(12):3963-70.
125. Truong NP, Quinn JF, Whittaker MR, Davis TP. Polymeric filomicelles and nanoworms: two decades of synthesis and application. *Polymer Chemistry*. 2016;7(26):4295-312.
126. Mandal S, Eksteen-Akeroyd ZH, Jacobs MJ, Hammink R, Koepf M, Lambeck AJ, et al. Therapeutic nanoworms: towards novel synthetic dendritic cells for immunotherapy. *Chemical Science*. 2013;4(11):4168-74.

127. Canton I, Warren NJ, Chahal A, Amps K, Wood A, Weightman R, et al. Mucin-Inspired Thermoresponsive synthetic hydrogels induce stasis in human pluripotent stem cells and human embryos. *ACS central science*. 2016;2(2):65-74.
128. Blackman LD, Varlas S, Arno MC, Houston ZH, Fletcher NL, Thurecht KJ, et al. Confinement of Therapeutic Enzymes in Selectively Permeable Polymer Vesicles by Polymerization-Induced Self-Assembly (PISA) Reduces Antibody Binding and Proteolytic Susceptibility. *ACS Central Science*. 2018.
129. Blackman LD, Varlas S, Arno MC, Fayter A, Gibson MI, O'Reilly RK. Permeable protein-loaded polymersome cascade nanoreactors by polymerization-induced self-assembly. *ACS macro letters*. 2017;6(11):1263-7.
130. Esser L, Truong NP, Karagoz B, Moffat BA, Boyer C, Quinn JF, et al. Gadolinium-functionalized nanoparticles for application as magnetic resonance imaging contrast agents via polymerization-induced self-assembly. *Polymer Chemistry*. 2016;7(47):7325-37.
131. Groison E, Brusseau Sgn, D'Agosto F, Magnet Sp, Inoubli R, Couvreur L, et al. Well-defined amphiphilic block copolymer nanoobjects via nitroxide-mediated emulsion polymerization. *ACS Macro Letters*. 2011;1(1):47-51.
132. Sugihara S, Sugihara K, Armes SP, Ahmad H, Lewis AL. Synthesis of biomimetic poly (2-(methacryloyloxy) ethyl phosphorylcholine) nanolatexes via atom transfer radical dispersion polymerization in alcohol/water mixtures. *Macromolecules*. 2010;43(15):6321-9.
133. Sugihara S, Armes SP, Lewis AL. One - Pot Synthesis of Biomimetic Shell Cross - Linked Micelles and Nanocages by ATRP in Alcohol/Water Mixtures. *Angewandte Chemie International Edition*. 2010;49(20):3500-3.
134. Charleux B, Delaittre G, Rieger J, D'Agosto F. Polymerization-induced self-assembly: from soluble macromolecules to block copolymer nano-objects in one step. *Macromolecules*. 2012;45(17):6753-65.

135. Khor SY, Quinn JF, Whittaker MR, Truong NP, Davis TP. Controlling Nanomaterial Size and Shape for Biomedical Applications via Polymerization - Induced Self - Assembly. *Macromolecular rapid communications*. 2018;1800438.
136. Warren NJ, Armes SP. Polymerization-induced self-assembly of block copolymer nano-objects via RAFT aqueous dispersion polymerization. *Journal of the American Chemical Society*. 2014;136(29):10174-85.
137. Zhang Q, Zhu S. Ionic liquids: versatile media for preparation of vesicles from polymerization-induced self-assembly. *ACS Macro Letters*. 2015;4(7):755-8.
138. Li Y, Armes SP. RAFT synthesis of sterically stabilized methacrylic nanolatexes and vesicles by aqueous dispersion polymerization. *Angewandte Chemie International Edition*. 2010;49(24):4042-6.
139. Cunningham VJ, Alswieleh AM, Thompson KL, Williams M, Leggett GJ, Armes SP, et al. Poly (glycerol monomethacrylate)–poly (benzyl methacrylate) diblock copolymer nanoparticles via RAFT emulsion polymerization: Synthesis, characterization, and interfacial activity. *Macromolecules*. 2014;47(16):5613-23.
140. Rieger J, Zhang W, Stoffelbach Fo, Charleux B. Surfactant-free RAFT emulsion polymerization using poly (N, N-dimethylacrylamide) trithiocarbonate macromolecular chain transfer agents. *Macromolecules*. 2010;43(15):6302-10.
141. Truong NP, Dussert MV, Whittaker MR, Quinn JF, Davis TP. Rapid synthesis of ultrahigh molecular weight and low polydispersity polystyrene diblock copolymers by RAFT-mediated emulsion polymerization. *Polymer Chemistry*. 2015;6(20):3865-74.
142. Fielding LA, Derry MJ, Ladmiral V, Rosselgong J, Rodrigues AM, Ratcliffe LP, et al. RAFT dispersion polymerization in non-polar solvents: facile production of block copolymer spheres, worms and vesicles in n-alkanes. *Chemical Science*. 2013;4(5):2081-7.

143. Zhang W-J, Hong C-Y, Pan C-Y. Fabrication and characterization of silica nanotubes with controlled dimensions. *Journal of Materials Chemistry A*. 2014;2(21):7819-28.
144. Pei Y, Jarrett K, Garces LG, Saunders M, Croue J-P, Roth PJ, et al. Synthesis and characterisation of non-ionic AB-diblock nanoparticles prepared by RAFT dispersion polymerization with polymerization-induced self-assembly. *RSC Advances*. 2016;6(33):28130-9.
145. Gonzato C, Semsarilar M, Jones ER, Li F, Krooshof GJ, Wyman P, et al. Rational synthesis of low-polydispersity block copolymer vesicles in concentrated solution via polymerization-induced self-assembly. *Journal of the American Chemical Society*. 2014;136(31):11100-6.
146. Huo M, Xu Z, Zeng M, Chen P, Liu L, Yan L-T, et al. Controlling vesicular size via topological engineering of amphiphilic polymer in polymerization-induced self-assembly. *Macromolecules*. 2017;50(24):9750-9.
147. Wan W-M, Hong C-Y, Pan C-Y. One-pot synthesis of nanomaterials via RAFT polymerization induced self-assembly and morphology transition. *Chemical Communications*. 2009(39):5883-5.
148. Truong NP, Quinn JF, Dussert MV, Sousa NB, Whittaker MR, Davis TP. Reproducible access to tunable morphologies via the self-assembly of an amphiphilic diblock copolymer in water. *ACS Macro Letters*. 2015;4(4):381-6.
149. Huang C-Q, Pan C-Y. Direct preparation of vesicles from one-pot RAFT dispersion polymerization. *Polymer*. 2010;51(22):5115-21.
150. Doncom KE, Warren NJ, Armes SP. Polysulfobetaine-based diblock copolymer nano-objects via polymerization-induced self-assembly. *Polymer Chemistry*. 2015;6(41):7264-73.

151. Blanazs A, Ryan A, Armes S. Predictive phase diagrams for RAFT aqueous dispersion polymerization: effect of block copolymer composition, molecular weight, and copolymer concentration. *Macromolecules*. 2012;45(12):5099-107.
152. Zhang WJ, Hong CY, Pan CY. Polymerization - Induced Self - Assembly of Functionalized Block Copolymer Nanoparticles and Their Application in Drug Delivery. *Macromolecular rapid communications*. 2018:1800279.
153. Warren NJ, Mykhaylyk OO, Mahmood D, Ryan AJ, Armes SP. RAFT aqueous dispersion polymerization yields poly (ethylene glycol)-based diblock copolymer nano-objects with predictable single phase morphologies. *Journal of the American Chemical Society*. 2014;136(3):1023-33.
154. Lovett JR, Warren NJ, Armes SP, Smallridge MJ, Cracknell RB. Order–order morphological transitions for dual stimulus responsive diblock copolymer vesicles. *Macromolecules*. 2016;49(3):1016-25.
155. Lovett JR, Warren NJ, Ratcliffe LP, Kocik MK, Armes SP. pH - Responsive Non - Ionic Diblock Copolymers: Ionization of Carboxylic Acid End - Groups Induces an Order–Order Morphological Transition. *Angewandte Chemie International Edition*. 2015;54(4):1279-83.
156. Boissé S, Rieger J, Belal K, Di-Cicco A, Beaunier P, Li M-H, et al. Amphiphilic block copolymer nano-fibers via RAFT-mediated polymerization in aqueous dispersed system. *Chemical communications*. 2010;46(11):1950-2.
157. Zhang X, Boissé S, Zhang W, Beaunier P, D’Agosto F, Rieger J, et al. Well-defined amphiphilic block copolymers and nano-objects formed in situ via RAFT-mediated aqueous emulsion polymerization. *Macromolecules*. 2011;44(11):4149-58.
158. Zhang W, D’Agosto F, Boyron O, Rieger J, Charleux B. Toward a better understanding of the parameters that lead to the formation of nonspherical polystyrene

- particles via RAFT-mediated one-pot aqueous emulsion polymerization. *Macromolecules*. 2012;45(10):4075-84.
159. Lesage de la Haye J, Zhang X, Chaduc I, Brunel F, Lansalot M, D'Agosto F. The Effect of Hydrophile Topology in RAFT - Mediated Polymerization - Induced Self - Assembly. *Angewandte Chemie International Edition*. 2016;55(11):3739-43.
160. Devadasu VR, Bhardwaj V, Kumar MR. Can controversial nanotechnology promise drug delivery? *Chemical reviews*. 2012;113(3):1686-735.
161. Chaduc I, Reynaud E, Dumas L, Albertin L, D'Agosto F, Lansalot M. From well-defined poly (N-acryloylmorpholine)-stabilized nanospheres to uniform mannuronan-and guluronan-decorated nanoparticles by RAFT polymerization-induced self-assembly. *Polymer*. 2016;106:218-28.
162. Karagoz B, Esser L, Duong HT, Basuki JS, Boyer C, Davis TP. Polymerization-Induced Self-Assembly (PISA)–control over the morphology of nanoparticles for drug delivery applications. *Polymer Chemistry*. 2014;5(2):350-5.
163. Hinde E, Thammasiraphop K, Duong HT, Yeow J, Karagoz B, Boyer C, et al. Pair correlation microscopy reveals the role of nanoparticle shape in intracellular transport and site of drug release. *Nature nanotechnology*. 2017;12(1):81.
164. Karagoz B, Yeow J, Esser L, Prakash SM, Kuchel RP, Davis TP, et al. An efficient and highly versatile synthetic route to prepare iron oxide nanoparticles/nanocomposites with tunable morphologies. *Langmuir*. 2014;30(34):10493-502.
165. Blanco E, Hsiao A, Mann AP, Landry MG, Meric-Bernstam F, Ferrari M. Nanomedicine in cancer therapy: innovative trends and prospects. *Cancer Sci*. 2011;102(7):1247-52.
166. Bangham AD, Standish MM, Watkins JC. Diffusion of univalent ions across the lamellae of swollen phospholipids. *J Mol Biol*. 1965;13(1):238-52.

167. Yatvin MB, Kreutz W, Horwitz BA, Shinitzky M. pH-sensitive liposomes: possible clinical implications. *Science*. 1980;210(4475):1253-5.
168. Allen TM, Chonn A. Large unilamellar liposomes with low uptake into the reticuloendothelial system. *FEBS Lett*. 1987;223(1):42-6.
169. Jain RK, Stylianopoulos T. Delivering nanomedicine to solid tumors. *Nat Rev Clin Oncol*. 2010;7(11):653-64.
170. Gordon AN, Fleagle JT, Guthrie D, Parkin DE, Gore ME, Lacave AJ. Recurrent epithelial ovarian carcinoma: a randomized phase III study of pegylated liposomal doxorubicin versus topotecan. *J Clin Oncol*. 2001;19(14):3312-22.
171. Nichols JW, Bae YH. EPR: Evidence and fallacy. *J Control Release*. 2014;190:451-64.
172. Soloman R, Gabizon AA. Clinical pharmacology of liposomal anthracyclines: focus on pegylated liposomal Doxorubicin. *Clin Lymphoma Myeloma*. 2008;8(1):21-32.
173. Gabizon A, Catane R, Uziely B, Kaufman B, Safra T, Cohen R, et al. Prolonged circulation time and enhanced accumulation in malignant exudates of doxorubicin encapsulated in polyethylene-glycol coated liposomes. *Cancer Res*. 1994;54(4):987-92.
174. Szebeni J, Muggia F, Gabizon A, Barenholz Y. Activation of complement by therapeutic liposomes and other lipid excipient-based therapeutic products: prediction and prevention. *Adv Drug Deliv Rev*. 2011;63(12):1020-30.
175. Anselmo AC, Mitragotri S. Nanoparticles in the clinic. *Bioeng Transl Med*. 2016;1(1):10-29.
176. Pillai G, Ceballos-Coronel ML. Science and technology of the emerging nanomedicines in cancer therapy: A primer for physicians and pharmacists. *SAGE Open Med*. 2013;1:2050312113513759.

177. Etheridge ML, Campbell SA, Erdman AG, Haynes CL, Wolf SM, McCullough J. The big picture on nanomedicine: the state of investigational and approved nanomedicine products. *Nanomedicine*. 2013;9(1):1-14.
178. Hafner A, Lovric J, Lakos GP, Pepic I. Nanotherapeutics in the EU: an overview on current state and future directions. *Int J Nanomedicine*. 2014;9:1005-23.
179. Ragelle H, Danhier F, Preat V, Langer R, Anderson DG. Nanoparticle-based drug delivery systems: a commercial and regulatory outlook as the field matures. *Expert Opin Drug Deliv*. 2017;14(7):851-64.
180. Desai N. Challenges in development of nanoparticle-based therapeutics. *AAPS J*. 2012;14(2):282-95.
181. Peer D, Karp JM, Hong S, Farokhzad OC, Margalit R, Langer R. Nanocarriers as an emerging platform for cancer therapy. *Nat Nanotechnol*. 2007;2(12):751-60.
182. Chen G, Roy I, Yang C, Prasad PN. Nanochemistry and Nanomedicine for Nanoparticle-based Diagnostics and Therapy. *Chem Rev*. 2016;116(5):2826-85.
183. Petersen GH, Alzghari SK, Chee W, Sankari SS, La-Beck NM. Meta-analysis of clinical and preclinical studies comparing the anticancer efficacy of liposomal versus conventional non-liposomal doxorubicin. *J Control Release*. 2016;232:255-64.
184. Rugo HS, Barry WT, Moreno-Aspitia A, Lyss AP, Cirrincione C, Leung E, et al. Randomized Phase III Trial of Paclitaxel Once Per Week Compared With Nanoparticle Albumin-Bound Nab-Paclitaxel Once Per Week or Ixabepilone With Bevacizumab As First-Line Chemotherapy for Locally Recurrent or Metastatic Breast Cancer: CALGB 40502/NCCTG N063H (Alliance). *J Clin Oncol*. 2015;33(21):2361-9.
185. Sainz V, Conriot J, Matos AI, Peres C, Zupancic E, Moura L, et al. Regulatory aspects on nanomedicines. *Biochemical and Biophysical Research Communications*. 2015;468(3):504-10.

186. Tinkle S, McNeil SE, Muhlebach S, Bawa R, Borchard G, Barenholz Y, et al. Nanomedicines: addressing the scientific and regulatory gap. *Annals Reports*. 2014;1313:35-56.
187. Weissig V, Pettinger TK, Murdock N. Nanopharmaceuticals (part I): products on the market. *International Journal of Nanomedicine*. 2014;9:4357-73.
188. Ragelle H, Danhier F, Preat V, Langer R, Anderson DG. Nanoparticle-based drug delivery systems: a commercial and regulatory outlook as the field matures. *Expert Opinion on Drug Delivery*. 2017;14(7):851-64.
189. Nel AE, Madler L, Velegol D, Xia T, Hoek EMV, Somasundaran P, et al. Understanding biophysicochemical interactions at the nano-bio interface. *Nature Materials*. 2009;8(7):543-57.
190. Matsumura Y, Maeda H. A new concept for macromolecular therapeutics in cancer chemotherapy: mechanism of tumoritropic accumulation of proteins and the antitumor agent smancs. *Cancer Res*. 1986;46(12 Pt 1):6387-92.
191. Gerlowski LE, Jain RK. Microvascular permeability of normal and neoplastic tissues. *Microvasc Res*. 1986;31(3):288-305.
192. Bertrand N, Wu J, Xu X, Kamaly N, Farokhzad OC. Cancer nanotechnology: the impact of passive and active targeting in the era of modern cancer biology. *Adv Drug Deliv Rev*. 2014;66:2-25.
193. Maeda H. Toward a full understanding of the EPR effect in primary and metastatic tumors as well as issues related to its heterogeneity. *Adv Drug Deliv Rev*. 2015;91:3-6.
194. Dvorak HF. Tumors: Wounds That Do Not Heal-Redux. *Cancer Immunology Research*. 2015;3(1):1-11.
195. Hobbs SK, Monsky WL, Yuan F, Roberts WG, Griffith L, Torchilin VP, et al. Regulation of transport pathways in tumor vessels: Role of tumor type and

microenvironment. *Proceedings of the National Academy of Sciences of the United States of America*. 1998;95(8):4607-12.

196. Maeda H, Wu J, Sawa T, Matsumura Y, Hori K. Tumor vascular permeability and the EPR effect in macromolecular therapeutics: a review. *Journal of Controlled Release*. 2000;65(1-2):271-84.

197. Fang J, Nakamura H, Maeda H. The EPR effect: Unique features of tumor blood vessels for drug delivery, factors involved, and limitations and augmentation of the effect. *Advanced Drug Delivery Reviews*. 2011;63(3):136-51.

198. Chauhan VP, Jain RK. Strategies for advancing cancer nanomedicine. *Nature Materials*. 2013;12(11):958-62.

199. Wilhelm S, Tavares AJ, Dai Q, Ohta S, Audet J, Dvorak HF, et al. Analysis of nanoparticle delivery to tumours. *Nature Reviews Materials*. 2016;1(5).

200. Torrice M. Does Nanomedicine Have a Delivery Problem? *Acs Central Science*. 2016;2(7):434-7.

201. McNeil SE. Evaluation of nanomedicines: stick to the basics. *Nature Reviews Materials*. 2016;1(10).

202. Wilhelm S, Tavares AJ, Chan WCW. Reply to "Evaluation of nanomedicines: stick to the basics". *Nature Reviews Materials*. 2016;1(10).

203. Cui JW, De Rose R, Alt K, Alcantara S, Paterson BM, Liang K, et al. Engineering Poly(ethylene glycol) Particles for Improved Biodistribution. *Acs Nano*. 2015;9(2):1571-80.

204. De Rose R, Zelikin AN, Johnston APR, Sexton A, Chong SF, Cortez C, et al. Binding, Internalization, and Antigen Presentation of Vaccine-Loaded Nanoengineered Capsules in Blood. *Advanced Materials*. 2008;20(24):4698-+.

205. Baumann D, Hofmann D, Nullmeier S, Panther P, Dietze C, Musyanovych A, et al. Complex encounters: nanoparticles in whole blood and their uptake into different types of white blood cells. *Nanomedicine*. 2013;8(5):699-713.
206. Inturi S, Wang GK, Chen FF, Banda NK, Holers VM, Wu LP, et al. Modulatory Role of Surface Coating of Superparamagnetic Iron Oxide Nanoworms in Complement Opsonization and Leukocyte Uptake. *Acs Nano*. 2015;9(11):10758-68.
207. Glass JJ, Chen LY, Alcantara S, Crampin EJ, Thurecht KJ, De Rose R, et al. Charge Has a Marked Influence on Hyperbranched Polymer Nanoparticle Association in Whole Human Blood. *Acs Macro Letters*. 2017;6(6):586-92.
208. Glass JJ, Li Y, De Rose R, Johnston APR, Czuba EI, Khor SY, et al. Thiol-Reactive Star Polymers Display Enhanced Association with Distinct Human Blood Components. *Acs Applied Materials & Interfaces*. 2017;9(14):12182-94.
209. Glass JJ, Yuen D, Rae J, Johnston APR, Parton RG, Kent SJ, et al. Human immune cell targeting of protein nanoparticles - caveospheres. *Nanoscale*. 2016;8(15):8255-65.
210. Hansson GK, Robertson A-KL, Söderberg-Nauclér C. Inflammation and atherosclerosis. *Annu Rev Pathol Mech Dis*. 2006;1:297-329.
211. Namdee K, Thompson AJ, Golinski A, Mocherla S, Bouis D, Eniola-Adefeso O. In vivo evaluation of vascular-targeted spheroidal microparticles for imaging and drug delivery application in atherosclerosis. *Atherosclerosis*. 2014;237(1):279-86.
212. Charoenphol P, Mocherla S, Bouis D, Namdee K, Pinsky DJ, Eniola-Adefeso O. Targeting therapeutics to the vascular wall in atherosclerosis—carrier size matters. *Atherosclerosis*. 2011;217(2):364-70.
213. Thompson AJ, Mastria EM, Eniola-Adefeso O. The margination propensity of ellipsoidal micro/nanoparticles to the endothelium in human blood flow. *Biomaterials*. 2013;34(23):5863-71.

214. Wen AM, Wang Y, Jiang K, Hsu GC, Gao H, Lee KL, et al. Shaping bio-inspired nanotechnologies to target thrombosis for dual optical-magnetic resonance imaging. *Journal of Materials Chemistry B*. 2015;3(29):6037-45.
215. Jiang X-Y, Sarsons CD, Gomez-Garcia MJ, Cramb DT, Rinker KD, Childs SJ. Quantum dot interactions and flow effects in angiogenic zebrafish (*Danio rerio*) vessels and human endothelial cells. *Nanomedicine: Nanotechnology, Biology and Medicine*. 2017;13(3):999-1010.
216. Bartczak D, Nitti S, Millar TM, Kanaras AG. Exocytosis of peptide functionalized gold nanoparticles in endothelial cells. *Nanoscale*. 2012;4(15):4470-2.
217. Bartczak D, Sanchez - Elsner T, Louafi F, Millar TM, Kanaras AG. Receptor - Mediated Interactions between Colloidal Gold Nanoparticles and Human Umbilical Vein Endothelial Cells. *Small*. 2011;7(3):388-94.
218. Tenzer S, Docter D, Kuharev J, Musyanovych A, Fetz V, Hecht R, et al. Rapid formation of plasma protein corona critically affects nanoparticle pathophysiology. *Nature nanotechnology*. 2013;8(10):772.
219. Yang ST, Liu Y, Wang YW, Cao A. Biosafety and bioapplication of nanomaterials by designing protein - nanoparticle interactions. *Small*. 2013;9(9 - 10):1635-53.
220. Dell'Orco D, Lundqvist M, Oslakovic C, Cedervall T, Linse S. Modeling the time evolution of the nanoparticle-protein corona in a body fluid. *PloS one*. 2010;5(6):e10949.
221. Vroman L, Adams A, Fischer G, Munoz P. Interaction of high molecular weight kininogen, factor XII, and fibrinogen in plasma at interfaces. *Blood*. 1980;55(1):156-9.
222. Charbgo F, Nejabat M, Abnous K, Soltani F, Taghdisi SM, Alibolandi M, et al. Gold nanoparticle should understand protein corona for being a clinical nanomaterial. *Journal of controlled release*. 2018.

223. Hill HD, Millstone JE, Banholzer MJ, Mirkin CA. The role radius of curvature plays in thiolated oligonucleotide loading on gold nanoparticles. *ACS nano*. 2009;3(2):418-24.
224. Yin M-M, Dong P, Chen W-Q, Xu S-P, Yang L-Y, Jiang F-L, et al. Thermodynamics and mechanisms of the interactions between ultrasmall fluorescent gold nanoclusters and human serum albumin, γ -globulins, and transferrin: a spectroscopic approach. *Langmuir*. 2017;33(21):5108-16.
225. Lundqvist M, Stigler J, Elia G, Lynch I, Cedervall T, Dawson KA. Nanoparticle size and surface properties determine the protein corona with possible implications for biological impacts. *Proceedings of the National Academy of Sciences*. 2008.
226. Xiao W, Xiong J, Zhang S, Xiong Y, Zhang H, Gao H. Influence of ligands property and particle size of gold nanoparticles on the protein adsorption and corresponding targeting ability. *International journal of pharmaceutics*. 2018;538(1-2):105-11.
227. Piella J, Bastús NG, Puentes V. Size-dependent protein–nanoparticle interactions in citrate-stabilized gold nanoparticles: the emergence of the protein corona. *Bioconjugate chemistry*. 2016;28(1):88-97.
228. Perevedentseva E, Cai P-J, Chiu Y-C, Cheng C-L. Characterizing protein activities on the lysozyme and nanodiamond complex prepared for bio applications. *Langmuir*. 2010;27(3):1085-91.
229. García-Álvarez R, Hadjidemetriou M, Sánchez-Iglesias A, Liz-Marzán LM, Kostarelos K. In vivo formation of protein corona on gold nanoparticles. The effect of their size and shape. *Nanoscale*. 2018;10(3):1256-64.
230. Natte K, Friedrich JF, Wohlrab S, Lutzki J, von Klitzing R, Österle W, et al. Impact of polymer shell on the formation and time evolution of nanoparticle–protein corona. *Colloids and Surfaces B: Biointerfaces*. 2013;104:213-20.

231. Sacchetti C, Motamedchaboki K, Magrini A, Palmieri G, Mattei M, Bernardini S, et al. Surface polyethylene glycol conformation influences the protein corona of polyethylene glycol-modified single-walled carbon nanotubes: potential implications on biological performance. *ACS nano*. 2013;7(3):1974-89.
232. Murthy AK, Stover RJ, Borwankar AU, Nie GD, Gourisankar S, Truskett TM, et al. Equilibrium gold nanoclusters quenched with biodegradable polymers. *ACS Nano*. 2012;7(1):239-51.
233. Monopoli MP, Åberg C, Salvati A, Dawson KA. Biomolecular coronas provide the biological identity of nanosized materials. *Nature nanotechnology*. 2012;7(12):779.
234. Pozzi D, Colapicchioni V, Caracciolo G, Piovesana S, Capriotti AL, Palchetti S, et al. Effect of polyethyleneglycol (PEG) chain length on the bio–nano-interactions between PEGylated lipid nanoparticles and biological fluids: from nanostructure to uptake in cancer cells. *Nanoscale*. 2014;6(5):2782-92.
235. Docter D, Strieth S, Westmeier D, Hayden O, Gao M, Knauer SK, et al. No king without a crown–impact of the nanomaterial-protein corona on nanobiomedicine. *Nanomedicine*. 2015;10(3):503-19.
236. Benetti F, Fedel M, Minati L, Speranza G, Migliaresi C. Gold nanoparticles: role of size and surface chemistry on blood protein adsorption. *Journal of nanoparticle research*. 2013;15(6):1694.
237. Zhang H, Wu T, Yu W, Ruan S, He Q, Gao H. Ligand Size and Conformation Affect the Behavior of Nanoparticles Coated with in Vitro and in Vivo Protein Corona. *ACS applied materials & interfaces*. 2018;10(10):9094-103.
238. Yu K, Lai BF, Foley JH, Krisinger MJ, Conway EM, Kizhakkedathu JN. Modulation of complement activation and amplification on nanoparticle surfaces by glycopolymer conformation and chemistry. *ACS nano*. 2014;8(8):7687-703.

239. Xia W, Low PS. Folate-targeted therapies for cancer. *Journal of medicinal chemistry*. 2010;53(19):6811-24.
240. Garcia-Bennett A, Nees M, Fadeel B. In search of the Holy Grail: folate-targeted nanoparticles for cancer therapy. *Biochemical pharmacology*. 2011;81(8):976-84.
241. Hrkach J, Von Hoff D, Ali MM, Andrianova E, Auer J, Campbell T, et al. Preclinical development and clinical translation of a PSMA-targeted docetaxel nanoparticle with a differentiated pharmacological profile. *Science translational medicine*. 2012;4(128):128ra39-ra39.
242. Fröhlich E. The role of surface charge in cellular uptake and cytotoxicity of medical nanoparticles. *International journal of nanomedicine*. 2012;7:5577.
243. Villanueva A, Cañete M, Roca AG, Calero M, Veintemillas-Verdaguer S, Serna CJ, et al. The influence of surface functionalization on the enhanced internalization of magnetic nanoparticles in cancer cells. *Nanotechnology*. 2009;20(11):115103.
244. Lunov O, Syrovets T, Loos C, Beil J, Delacher M, Tron K, et al. Differential uptake of functionalized polystyrene nanoparticles by human macrophages and a monocytic cell line. *ACS nano*. 2011;5(3):1657-69.
245. Makino K, Yamamoto N, Higuchi K, Harada N, Ohshima H, Terada H. Phagocytic uptake of polystyrene microspheres by alveolar macrophages: effects of the size and surface properties of the microspheres. *Colloids and Surfaces B: Biointerfaces*. 2003;27(1):33-9.
246. Roser M, Fischer D, Kissel T. Surface-modified biodegradable albumin nano- and microspheres. II: effect of surface charges on in vitro phagocytosis and biodistribution in rats. *European Journal of Pharmaceutics and Biopharmaceutics*. 1998;46(3):255-63.
247. Miller CR, Bondurant B, McLean SD, McGovern KA, O'Brien DF. Liposome– cell interactions in vitro: effect of liposome surface charge on the binding and endocytosis of conventional and sterically stabilized liposomes. *Biochemistry*. 1998;37(37):12875-83.

248. Glass JJ, Chen L, Alcantara S, Crampin EJ, Thurecht KJ, De Rose R, et al. Charge Has a Marked Influence on Hyperbranched Polymer Nanoparticle Association in Whole Human Blood. *ACS Macro Letters*. 2017;6(6):586-92.
249. Bai Y, Xing H, Wu P, Feng X, Hwang K, Lee JM, et al. Chemical control over cellular uptake of organic nanoparticles by fine tuning surface functional groups. *ACS nano*. 2015;9(10):10227-36.
250. Van Der Vlies AJ, O'Neil CP, Hasegawa U, Hammond N, Hubbell JA. Synthesis of pyridyl disulfide-functionalized nanoparticles for conjugating thiol-containing small molecules, peptides, and proteins. *Bioconjugate chemistry*. 2010;21(4):653-62.
251. Vázquez-Dorbatt V, Tolstyka ZP, Chang C-W, Maynard HD. Synthesis of a pyridyl disulfide end-functionalized glycopolymer for conjugation to biomolecules and patterning on gold surfaces. *Biomacromolecules*. 2009;10(8):2207-12.
252. O'Hagan DT, MacKichan ML, Singh M. Recent developments in adjuvants for vaccines against infectious diseases. *Biomolecular engineering*. 2001;18(3):69-85.
253. Fifis T, Gamvrellis A, Crimeen-Irwin B, Pietersz GA, Li J, Mottram PL, et al. Size-dependent immunogenicity: therapeutic and protective properties of nano-vaccines against tumors. *The Journal of Immunology*. 2004;173(5):3148-54.
254. França A, Aggarwal P, Barsov EV, Kozlov SV, Dobrovolskaia MA, González-Fernández Á. Macrophage scavenger receptor A mediates the uptake of gold colloids by macrophages in vitro. *Nanomedicine*. 2011;6(7):1175-88.
255. Mottram PL, Leong D, Crimeen-Irwin B, Gloster S, Xiang SD, Meanger J, et al. Type 1 and 2 immunity following vaccination is influenced by nanoparticle size: formulation of a model vaccine for respiratory syncytial virus. *Molecular pharmaceutics*. 2007;4(1):73-84.

256. Manolova V, Flace A, Bauer M, Schwarz K, Saudan P, Bachmann MF. Nanoparticles target distinct dendritic cell populations according to their size. *European journal of immunology*. 2008;38(5):1404-13.
257. Wang J, Fu L, Gu F, Ma Y. Notch1 is involved in migration and invasion of human breast cancer cells. *Oncology reports*. 2011;26(5):1295-303.
258. Nakai T, Kanamori T, Sando S, Aoyama Y. Remarkably size-regulated cell invasion by artificial viruses. Saccharide-dependent self-aggregation of glycoviruses and its consequences in glycoviral gene delivery. *Journal of the American Chemical Society*. 2003;125(28):8465-75.
259. Aoyama Y, Kanamori T, Nakai T, Sasaki T, Horiuchi S, Sando S, et al. Artificial viruses and their application to gene delivery. Size-controlled gene coating with glycocluster nanoparticles. *Journal of the American Chemical Society*. 2003;125(12):3455-7.
260. Rettig L, Haen SP, Bittermann AG, von Boehmer L, Curioni A, Krämer SD, et al. Particle size and activation threshold: a new dimension of danger signalling. *Blood*. 2010;blood-2009-11-247817.
261. Glass JJ, Li Y, De Rose R, Johnston AP, Czuba EI, Khor SY, et al. Thiol-Reactive Star Polymers Display Enhanced Association with Distinct Human Blood Components. *ACS applied materials & interfaces*. 2017;9(14):12182-94.
262. Glass JJ, Yuen D, Rae J, Johnston AP, Parton RG, Kent SJ, et al. Human immune cell targeting of protein nanoparticles–caveospheres. *Nanoscale*. 2016;8(15):8255-65.

**Chapter 2: Elucidating the Influences of Size, Surface Chemistry,
and Dynamic Flow on Cellular Association of Nanoparticles
Made by Polymerization-Induced Self-Assembly**

Elucidating the Influences of Size, Surface Chemistry, and Dynamic Flow on Cellular Association of Nanoparticles Made by Polymerization-Induced Self-Assembly

Song Yang Khor, Mai N. Vu, Emily H. Pilkington, Angus P. R. Johnston, Michael R. Whittaker, John F. Quinn, Nghia P. Truong,* and Thomas P. Davis*

The size and surface chemistry of nanoparticles dictate their interactions with biological systems. However, it remains unclear how these key physicochemical properties affect the cellular association of nanoparticles under dynamic flow conditions encountered in human vascular networks. Here, the facile synthesis of novel fluorescent nanoparticles with tunable sizes and surface chemistries and their association with primary human umbilical vein endothelial cells (HUVECs) is reported. First, a one-pot polymerization-induced self-assembly (PISA) methodology is developed to covalently incorporate a commercially available fluorescent dye into the nanoparticle core and tune nanoparticle size and surface chemistry. To characterize cellular association under flow, HUVECs are cultured onto the surface of a synthetic microvascular network embedded in a microfluidic device (SynVivo, INC). Interestingly, increasing the size of carboxylic acid-functionalized nanoparticles leads to higher cellular association under static conditions but lower cellular association under flow conditions, whereas increasing the size of tertiary amine-decorated nanoparticles results in a higher level of cellular association, under both static and flow conditions. These findings provide new insights into the interactions between polymeric nanomaterials and endothelial cells. Altogether, this work establishes innovative methods for the facile synthesis and biological characterization of polymeric nanomaterials for various potential applications.

effects.^[1,2] The encapsulation of drugs and imaging agents inside the core of nanomaterials has been shown to improve drug efficacy and imaging contrast by enhancing in vivo solubility, stability, and targeting.^[3,4] This encapsulation also reduces peripheral toxicity and cardiotoxicity that would otherwise be encountered during the circulation of these compounds around the cardiovascular system.^[5] Moreover, antibodies covalently attached to the surface of nanoparticles are able to trigger immune responses against bacteria, viruses, and cancer cells more effectively than free antibodies.^[6] In cardiovascular diseases, nanoparticles decorated with targeting ligands have been increasingly exploited for the delivery of therapeutics to the vascular wall (i.e., endothelial cells).^[7]

For the above clinical applications, nanomaterials circulate in the human vascular network before reaching their targets (e.g., cancer cells, immune cells, or blood clots).^[8] As such, investigating and understanding the complex nano-bio interactions between nanomaterials and bio-

logical systems inside vascular networks (e.g., endothelial cell adhesion) are critical for designing nanoparticles with desired properties for these applications.^[9] For instance, nanoparticles carrying anticancer drugs are expected to have a minimal off-target association with healthy endothelial cells before reaching tumors.^[10] On the other hand, specific association between nanomaterials and endothelial cells may be beneficial for use in cardiovascular diseases.^[9] Despite these potential benefits, the interactions between nanomaterials and endothelial cells under flow conditions in vascular networks remain poorly characterized due to a lack of suitable models.^[11]

A major challenge in the in vitro characterization of interactions between nanomaterials and endothelial cells is to mimic dynamic flow conditions and complex microenvironments that exist within in vivo vascular networks.^[12,13] Traditional approaches for studying nano-bio interactions typically involve incubating nanoparticles with cells under static conditions (e.g., in a well-plate), which clearly fails to model dynamic flow conditions in the vascular network.^[14] Considerable efforts

1. Introduction

Polymeric nanomaterials hold great potential for improving the diagnosis and treatment of diseases with reduced off-target

S. Y. Khor, M. N. Vu, E. H. Pilkington, Dr. A. P. R. Johnston, Dr. M. R. Whittaker, Dr. J. F. Quinn, Dr. N. P. Truong, Prof. T. P. Davis
ARC Centre of Excellence in Convergent Bio-Nano Science and Technology
Monash Institute of Pharmaceutical Sciences
Monash University
381 Royal Parade, Parkville, VIC 3052, Australia
E-mail: nghia.truong@monash.edu; thomas.p.davis@monash.edu
E. H. Pilkington, Prof. T. P. Davis
Department of Chemistry
University of Warwick
Gibbet Hill, Coventry CV47AL, UK

 The ORCID identification number(s) for the author(s) of this article can be found under <https://doi.org/10.1002/smll.201801702>.

DOI: 10.1002/smll.201801702

have been made to develop reliable methods for evaluating cellular associations of nanomaterials under realistic flow conditions. For example, Langer and co-workers have developed a simple microfluidic device lined with cells as a tool for determining parameters that affect cellular interaction of nanoparticles under flow conditions.^[15] This device was prepared by using electrical tape to attach a polydimethylsiloxane (PDMS) mould onto a glass slide to create a single, straight microchannel (54 × 900 μm). Samuel et al. have employed a more complex microfluidic device with multichannels to evaluate cellular uptake of silica particles into endothelial cells.^[16] This work highlighted that shear stress and surface chemistry are critical parameters for nanoparticle uptake by endothelial cells.^[16] To date, the majority of studies in nano–bio interactions under flow conditions employ microfluidic devices with simple straight microchannels, which do not adequately reflect the complex geometry and dynamic shear rates found in vascular networks.

Recent advances in computer-aided lithography have enabled the manufacture of microfluidic devices with vascular network mimicking channels. In particular, Prabhakarandian et al. have successfully developed physiologically realistic synthetic microvascular networks (SMNs) for modeling cell–cell and particle–cell interactions in the microvasculature.^[17,18] These SMNs not only possess a complex geometry similar to microvasculature but also can mimic various shear rates observed in vivo.^[19,20] Mitragotri and co-workers have employed these SMNs to explore the effects of nanoparticle shape and flow on targeting antibody-coated nanoparticles to lung and brain endothelium.^[21,22] Moreover, variants of the SMN have been developed which incorporate both a SMN and a tumor region, thus allowing rapid screening of cancer drug delivery systems.^[23,24] So far, these realistic SMNs have been employed to investigate the effect of only single physicochemical property of polymeric nanomaterials (e.g., size or surface chemistry alone) on nano–bio interactions under flow conditions. As such, we still do not understand how the nano–bio interactions in vascular networks will change with systematic variation of multiple nanoparticle physicochemical properties (e.g., both size and surface chemistry). In order to gain such understanding, it is necessary to reproducibly synthesize a comprehensive library of fluorescently labeled polymeric nanoparticles with various surface chemistries and similar size, as well as various sizes and identical surface chemistry.^[25]

We have recently developed several reversible addition-fragmentation chain transfer (RAFT) emulsion polymerization techniques that can be used to synthesize nanoparticles with tunable size, shape, and surface chemistry via either polymerization-induced self-assembly (PISA) or temperature-induced morphological transformation.^[26–30] Emulsion polymerization is an environmentally and industrially friendly technique that can be used to reproducibly yield large-scale, concentrated nanoparticle suspensions in water.^[31,32] Significantly, PISA can be employed to prepare nanoparticles with various sizes (diameters) and identical surface chemistry by using a single macromolecular chain transfer agent (macro-CTA) and different amounts of a hydrophobic monomer (i.e., styrene).^[33] The diameters of these PISA nanoparticles could be predetermined before the polymerization, thus allowing the reproducible

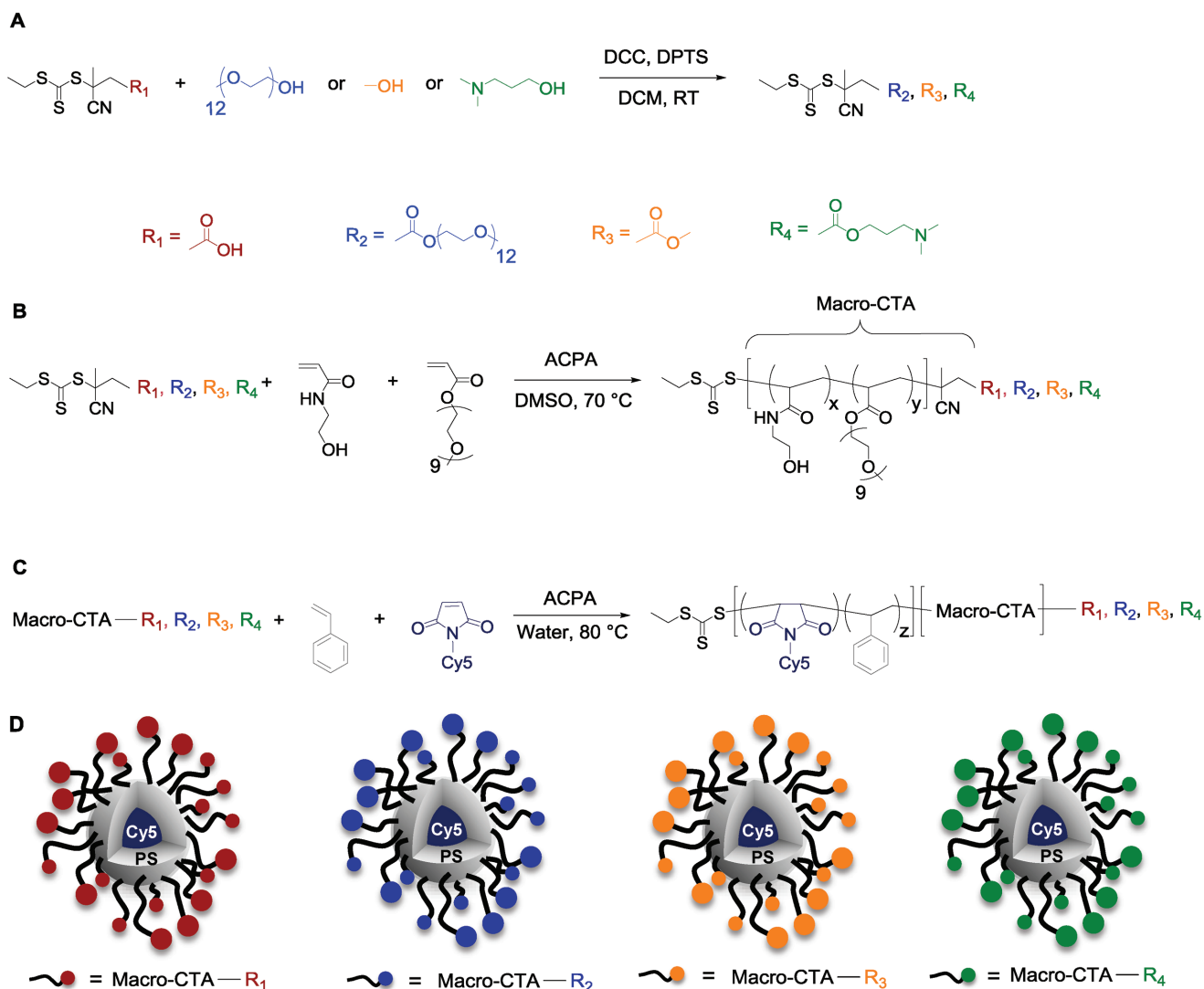
production of nanoparticles with the desired size. However, modification of the macro-CTA end group typically resulted in a change in the morphology of PISA nanoparticles (from sphere to worm and vesicle).^[34] As such, it remains challenging to prepare spherical nanoparticles with different surface chemistries and similar size via the PISA technique. In addition, the core of PISA nanoparticles has not been labeled with a commercially available fluorescent dye, thus limiting their applications in nano–bio interaction studies.

To address these synthesis challenges, we developed a PISA formulation for the production of fluorescently labeled spherical nanoparticles that have the same size and various surface chemistries as well as identical surface chemistry and different sizes. This PISA technique allowed the facile preparation of a library of 12 nanoparticles (4 surface chemistries × 3 sizes). These nanoparticles were fluorescently labeled with a commercially available Cyanine5 maleimide (Cy5-maleimide, Lumiprobe) to allow the subsequent studies of nano–bio interactions. To characterize the association of these nanoparticles with endothelial cells under flow conditions, human umbilical vein endothelial cells (HUVECs) were cultured under cell medium flow in vascular network microchannels of a microfluidic chip (SynVivo). After the HUVECs became confluent, fluorescently labeled nanoparticles were injected into the vascular network channels using a syringe pump. Subsequently, the HUVECs were collected and analyzed using flow cytometry and confocal microscopy. Interestingly, data obtained revealed for the first time the interplay of size, surface chemistry and flow conditions in the cellular association of PISA nanoparticles.

2. Results and Discussion

2.1. Synthesis of PISA Nanoparticles Having Various Surface Chemistries and a Predetermined Diameter

First, we modified the carboxylic acid group of 4-cyano-4-(ethylthiocarbonothioylthio) pentanoic acid (ECT) with methanol, dimethylamino-1-propanol, and poly(ethylene glycol) methyl ether (PEG) (Scheme 1A) to produce three new CTAs with different functional groups (methyl ester (Me), tertiary amine ester (TA), and PEG, respectively). ¹H nuclear magnetic resonance (NMR) spectra (Figure S1, Supporting Information) confirm the successful synthesis of these CTAs. Four CTAs (including ECT) were subsequently employed in RAFT solution polymerization of poly(ethylene glycol) methyl ether acrylate (PEGA) and N-hydroxyethyl acrylamide (HEAA) using ACPA as a radical initiator (Scheme 1B). It is worth noting that a low 4,4'-Azobis(4-cyanopentanoic acid) (ACPA)/CTA ratio (5 mol% instead of 10%) was judiciously selected to produce well-defined macro-CTAs with high end-group fidelity.^[34] In this work, the high end-group fidelity of macro-CTAs plays an important role because these end groups introduce different surface chemistries (a premodification approach). After purification, well-defined macro-CTAs with four different end groups were obtained. In contrast to the different end groups, these macro-CTAs exhibit similar compositions and molecular weights (Table S1, Supporting Information), which is expected to facilitate reproducible access to PISA nanoparticles with



Scheme 1. A) Modification of the ECT; B) RAFT solution polymerization of HEAA and PEGA; C) aqueous RAFT emulsion polymerization of styrene and Cy5-maleimide; D) schematic representation of particles with different end-groups formed via PISA.

predetermined sizes.^[33] That said, the difference in macro-CTA end group has been found to affect the morphology of nanoparticles obtained by the PISA technique.^[34] As such, it is challenging to prepare spherical nanoparticles with different surface chemistries using PISA technique.

To address this challenge, a low ACPA/macro-CTA ratio (12 mol%) was chosen for RAFT emulsion polymerization of styrene. In our previous work, when employing a macro-CTA terminated with a methyl ester group, it has been demonstrated that this low ACPA/macro-CTA ratio resulted in a reduced number of polymer chains aggregating during the initial phase of the PISA process and the formation of PISA nanoparticles having a spherical morphology.^[34] In this work, we hypothesized that using this low ratio of ACPA/macro-CTA (12 mol%) would also lead to only spherical PISA nanoparticles, regardless of macro-CTAs having four different end groups. To test this hypothesis, four emulsion polymerizations of styrene using 12 mol% of ACPA/macro-CTA ratio and macro-CTAs

with carboxylic acid (COOH), Me, TA, and PEG end groups were conducted. After the emulsion polymerizations, the morphology of nanoparticles was characterized by transmission electron microscopy (TEM). Figure S4 (Supporting Information) shows that all nanoparticles with different surface chemistries exhibited the same spherical shape and relatively similar size, regardless of macro-CTA end groups. This supports our hypothesis and demonstrates for the first time that PISA technique, in addition to its well-known capacity to tune particles size and shape, can also be used to prepare spherical nanoparticles with various surface chemistries and predetermined particle sizes.

2.2. A Novel PISA Method to Label Nanoparticles with a Commercially Available Fluorescent Dye

To label PISA nanoparticles with fluorescent dyes, there are several techniques available in the literature. For instance,

Armes and co-workers have developed a postmodification method to label the surfaces of PISA nanoparticles with rhodamine dyes using thiol chemistry.^[35] The presence of rhodamine dyes on the surface may affect the cellular association of PISA nanoparticles and therefore, this approach is not suitable for this study. To label the core of PISA nanoparticles with fluorescent dyes, Clavier and co-workers synthesized a family of boron-dipyrromethene (BODIPY) monomers.^[36] This method can covalently attach fluorescent dyes in the core of PISA nanoparticles during emulsion polymerization. However, these BODIPY monomers are not commercially available and this method is limited to a small number of fluorescent dyes. To develop a more facile and versatile technique, we selected Cy5-maleimide as a representative for a large family of commercially available fluorescent dyes having a maleimide functional group. It has been shown that *N*-substituted maleimides rapidly insert into growing polystyrene chains allowing the precise incorporation of *N*-substituted maleimide units in these polymers.^[37,38] As such, we hypothesized that *N*-substituted Cy5-maleimide dye could rapidly copolymerize with styrene during the PISA process, even in the presence of a high excess of styrene (Scheme 1C). To verify this hypothesis, Cy5-maleimide in styrene was added after 4 h emulsion polymerization of styrene (when the solution became turbid indicating PISA nanoparticles formed). After another 2 h of polymerization followed by purification by dialysis, the polymer product was characterized by SEC coupled with refractive index (RI) and UV-Vis detectors. SEC traces from RI and UV-Vis

detectors in Figure S5 (Supporting Information) revealed two peaks at a relatively similar retention time at approximately 26 min, suggesting that the Cy5 dye had been covalently incorporated into the polystyrene chains (the core of PISA nanoparticles). This PISA method (the addition of maleimide dyes during PISA process) paves the way for the facile and versatile labeling of PISA nanoparticles with commercially available fluorescent dyes.

We employed this newly developed PISA method to prepare a library of 12 fluorescently labeled nanoparticles for nanobio interaction studies (Figure 1). The nanoparticle library consists of three sizes (small: ≈ 40 nm; medium: ≈ 70 nm; and large: ≈ 130 nm) and four surface chemistries (carboxylic acid: COOH; tertiary amine: TA; methyl ester: Me.; and PEG). The sizes of nanoparticles were precisely determined before the polymerization by targeting different molecular weights (Figures S6–S9, Supporting Information).^[33] This allows us to produce PISA nanoparticles with relatively similar sizes (see TEM images in Figure 1) and low dispersity (below 0.2, see dynamic light scattering (DLS) data in Tables S2 to S5, Supporting Information) even though four different macroCTAs were used. The surface chemistries of nanoparticles were changed by modifying the CTAs as discussed above. It should be noted that altering the surface chemistries of the nanoparticles did not result in any appreciable differences in zeta potential (Tables S2–S5, Supporting Information). Nonetheless, this premodification approach allows us to estimate the percentage of functional groups available on the surface

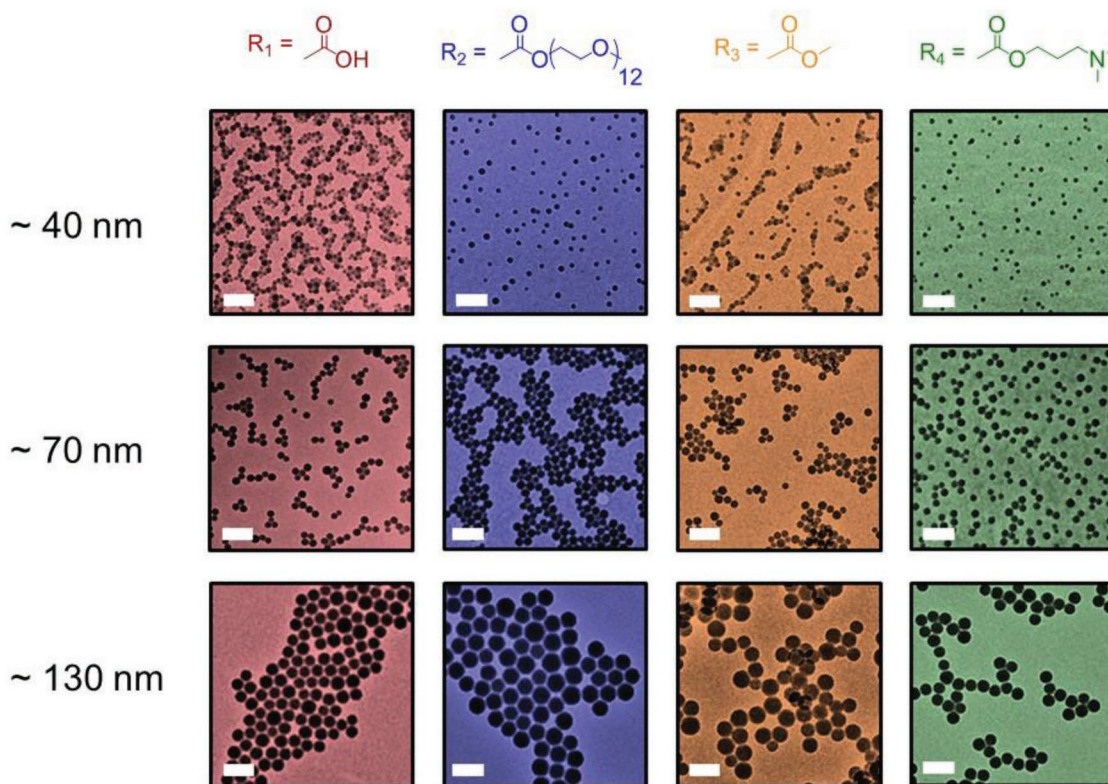


Figure 1. TEM images of the nanoparticles obtained by RAFT aqueous emulsion polymerization of styrene with (red) P(HEAA-*co*-PEGA)-COOH, (blue) P(HEAA-*co*-PEGA)-N(CH₃)₂, (green) P(HEAA-*co*-PEGA)-Me, and (yellow) P(HEAA-*co*-PEGA)-PEG, at 80 °C for 6 h. All scale bars represent 200 nm.

of PISA nanoparticles as previously described.^[34] Significantly, all nanoparticles have been successfully labeled with Cy5 dyes (Figure S11, Supporting Information). Altogether, we have synthesized the first library of fluorescently labeled, spherical PISA nanoparticles that have tunable sizes and surface chemistries.

2.3. Toxicity of Macro-CTAs and PISA Nanoparticles

After polymerization, the macro-CTAs were precipitated to remove unreacted monomer and then extensively dried in a vacuum oven to remove trace amounts of organic solvent. The nanoparticles were dialyzed against MiliQ water for 48 h to remove unreacted styrene monomer confirmed via the absence of styrene vinyl peaks on the ¹H NMR spectrum (Figure S2, Supporting Information). Before the nano–bio interaction studies, the toxicity of all macro-CTAs and nanoparticles was investigated. We used AlamarBlue assays for characterization of cell viability of HUVECs because the fluorescent emission of AlamarBlue reagents (610 nm) does not overlap with that of Cy5 dye (680 nm) attached in the styrenic core of PISA nanoparticles. Cell viability data in Figure 2 suggest that all macro-CTAs and nanoparticles are well-tolerated, even at high concentrations up to 1 mg mL⁻¹. Only small- and medium-size nanoparticles with tertiary amine groups on the surface (S4 and M4) and medium-size nanoparticles with Me and PEG surface (M2 and M3) exhibited slight toxicity (cell viability reduced to approximately 80%), which may be related to high level of cellular associations of these nanoparticles (see data and discussion below). To minimize the potential impact of toxicity on understanding nano–bio interactions, we used

nanoparticle concentrations in the range 10–200 µg mL⁻¹ for all subsequent cellular association studies in both static and flow conditions.

2.4. Preparation of Synthetic Microvascular Networks in a Microfluidic Device

One of the major challenges in the preparation of the SMN is the formation of a confluent and intact lumen of HUVECs in PDMS microchannels of a microfluidic device (SynVivo, see Figure 3A). To address this challenge, these microchannels were first coated with Matrigel, a “glue” for attachment of HUVECs onto the PDMS surface. This step was conducted under cold conditions (all reagents and the microfluidic chips were stored in the fridge and kept in an ice bath during the coating) to minimize the polymerization of Matrigel and the formation of clumps. That said, we found that some clumps still formed, but could be removed by extensive washing with endothelial cell growth medium (EGM). It is worth noting that prior removal of any Matrigel clump is important for the subsequent formation of a complete and confluent layer of HUVECs inside the microchannels. After coating with Matrigel, HUVECs (2.5 × 10⁷ cells mL⁻¹) were slowly injected until they covered approximately 90% of the surface of the microchannels (see Figure S10, Supporting Information). The chip was then placed in an incubator (37 °C, 5% CO₂) for 1 h to allow cells to attach to the Matrigel-coated microchannel surface. Subsequently, fresh EGM at 37 °C was injected into the microchannel at a flow rate of 0.1 µL min⁻¹. After 24 h, a complete and confluent layer of HUVECs was observed by both bright field and

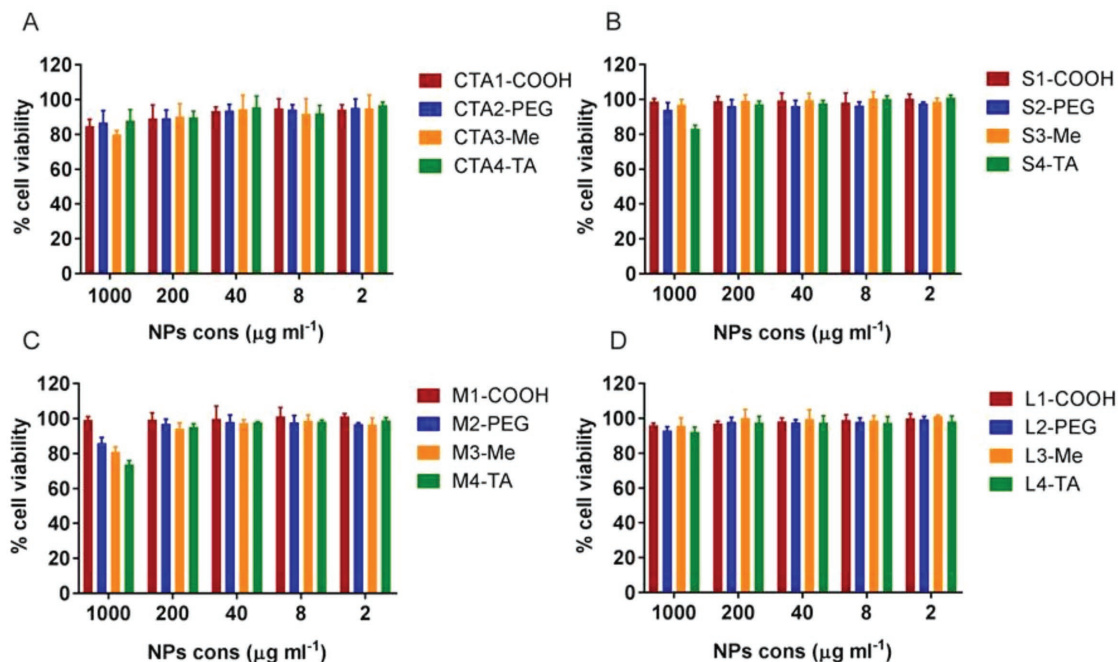


Figure 2. Evaluation of cytotoxicity to HUVECs after 48 h for A) macro-CTAs, B) small particles, C) intermediate particles, and D) large particles under static conditions using AlamarBlue assay. Data are shown as mean ± SD (*n* = 3).

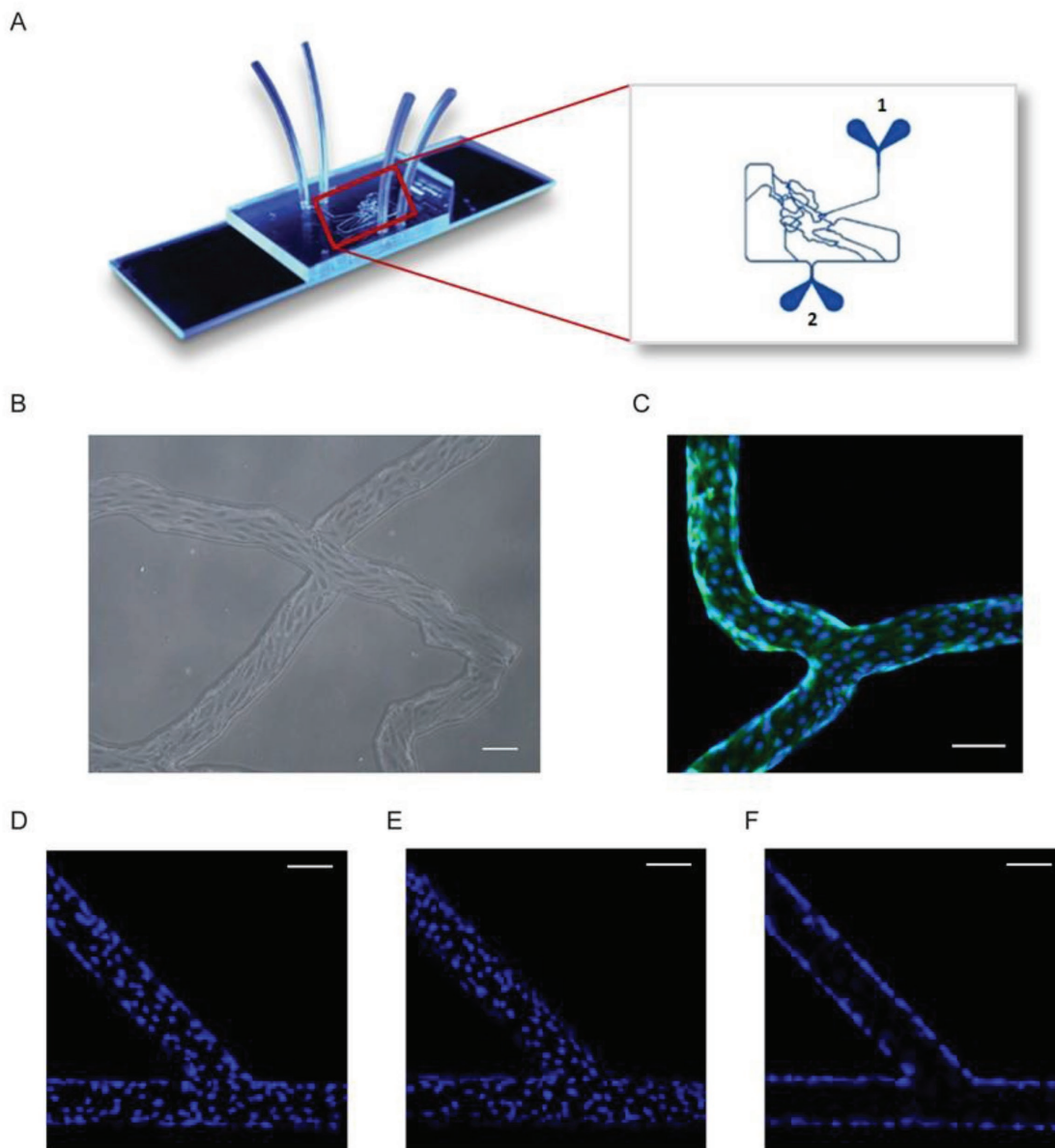


Figure 3. A) Model synthetic microvascular network: 1) inlet port where cell growth media with or without nanoparticles is injected into the system and 2) outlet port where perfusate from the system is collected. Adapted with permission from SynVivo, Inc., <http://www.synvivobio.com/microfluidic-chips/> (accessed: July 2018). B) Bright field and C) confocal images of a confluent layer of HUVECs in flow channels. Cells were stained with Calcein AM (cytoplasm: green channel) and Hoechst 33342 (nucleus: blue channel). Nucleus of HUVECs stained with Hoechst 33342 was imaged D) at the bottom, E) at the top, and F) on the sides of the vascular pipeline. Scale bars = 100 μm .

confocal microscopy (Figure 3B,C). It has been demonstrated that endothelial cells cultured under such flow conditions have similar morphology and function to that observed *in vivo*.^[23,39] To further verify the complete formation of a 3D lumen of HUVECs on the top, bottom, and side of the microchannels, an Eclipse TiE Microscope with a Nikon A1R Confocal was utilized to acquire a 3D Z-stack of the synthetic vessels. Figure 3D–F show images of the cell nucleus stained with Hoechst 33342 (a stain that emits blue fluorescence when bound to dsDNA in the cell nucleus) when focused at the bottom, at the top, and on the sides of microchannels, respectively. These images confirm the formation

of a complete lumen of HUVECs under flow conditions and suggest that the microfluidic chip is ready for use as a SMN (Video S1, Supporting Information).

2.5. Effects of Dynamic Flow Conditions on PISA Nanoparticles with Different Surface Chemistries

After the microfluidic chip was successfully coated with HUVECs, nanoparticle suspension in EGM (at 37 °C) was introduced into the SMN at a flow rate of 1.0 $\mu\text{L min}^{-1}$. This flow rate was selected to create a physiological shear rate range

(from ≈ 30 to ≈ 240 s⁻¹) found in vivo.^[19,23] After 4 h, chilled 4-(2-hydroxyethyl)-1-piperazineethanesulfonic acid (HEPES) buffered saline solution (HBSS) was injected to remove non-associated nanoparticles from the microchannels before HUVECs were collected for analysis by flow cytometry. The concentration of nanoparticles in all studies was kept constant at approximate 1×10^{11} particles mL⁻¹ (measured by Nanosight) to ensure the same number of nanoparticles were interacting with HUVECs in each experiment. We also performed cellular association studies under static conditions (where PISA nanoparticles were incubated with HUVECs in 48-well plates) at the same concentration to ensure that data obtained under static and flow conditions were comparable.

Figure 4 shows the median fluorescence intensity (MFI) of Cy5 dye detected by flow cytometry, which indicates the level of PISA nanoparticles (medium size ≈ 70 nm) associated with HUVECs. The fluorescence intensity of all nanoparticles was slightly different (Figure S11, Supporting Information) and, therefore, these MFI values in Figure 4 were normalized to the same fluorescent intensity per nanoparticle. Data in Figure 4 demonstrated that the level of nanoparticles associated with HUVECs in flow conditions was significantly reduced when compared to static conditions. Specifically, for COOH-, PEG-, Me-, and TA-functionalized particles, the MFI values were decreased 4.27 ($P < 0.01$), 6.07 ($P < 0.0001$), 6.37 ($P < 0.001$), and 7.01 ($P < 0.001$) fold, respectively. The decreased association between nanoparticles and HUVECs under flow conditions may be related to the reduced exposure of these nanoparticles to cells even though the same number of particles had been introduced.^[10] In flow conditions, spherical nanoparticles tend to follow the cell medium streamlines when passing through the SMN; while in static conditions, all nanoparticles have a tendency to settle on the cell surfaces due to gravity.^[40] That said, the trend of association between HUVECs and PISA nanoparticles of different surface chemistries (i.e., COOH < PEG < Me < TA) is similar when comparing

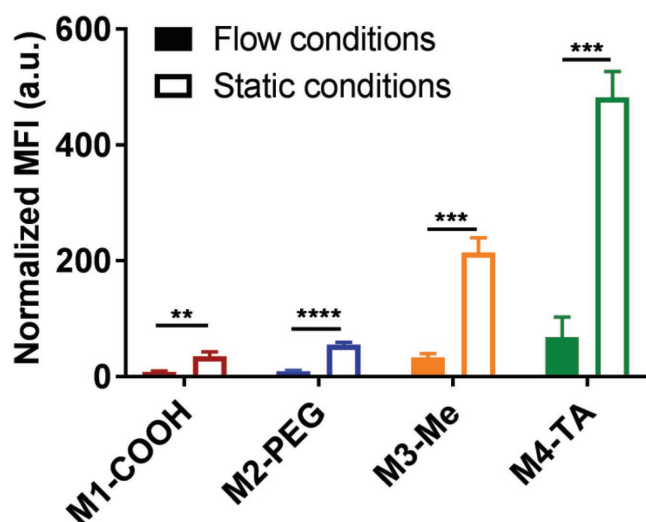


Figure 4. Cellular association of four different end-group particles with HUVECs under static and flow conditions as measured by flow cytometry. Data are presented as mean \pm SD ($n = 3$); ** $P < 0.01$, *** $P < 0.001$, **** $P < 0.0001$ (pair *t*-test).

between static and flow conditions. This result suggested that studying nano–bio interactions of these PISA nanoparticles under static conditions may be still useful to predict interaction trends but cannot provide quantitative information on the level of cellular association under flow conditions.

Furthermore, under static and flow conditions, nanoparticles that possessed TA-terminated groups exhibited enhanced cellular association compared to COOH-functionalized nanomaterials. This result is consistent with previous studies and may be related to the adsorption of different proteins from the cell medium onto the nanoparticle surface forming a protein corona.^[41–44] Further work is needed to comprehensively investigate the protein corona of these PISA particles in the presence of cell media, serum, and plasma. In the present study, we proceeded to further investigate the effect of dynamic flow conditions on the two types of PISA nanoparticles that exhibited the highest and lowest level of cellular associations (M4-TA and M1-COOH, respectively).

2.6. Effects of Dynamic Flow Conditions on PISA Nanoparticles with Different Sizes

In this study, we first investigated how dynamic flow conditions affected the degree of cellular association of TA-functionalized nanoparticles with various sizes. Figure 5 shows that under both static and flow conditions, an increase in particle size led to an enhanced cellular association between TA-functionalized nanoparticles and HUVECs. Similar to the results for varying surface chemistry, data obtained in static condition could be used to predict the trend in cellular association as a function of particle size under flow conditions for TA-decorated nanoparticles. That said, the level of cellular association under flow conditions was significantly lower than was observed under static conditions, which may also be related to the reduced exposure as discussed above.

To observe the cellular association of TA-functionalized particles with HUVECs, cells were further stained with Hoechst 33342 and then imaged by a Nikon confocal microscope. Confocal microscopy images in Figure 6 showed that large nanoparticles (130 nm) associated with HUVECs to a greater extent

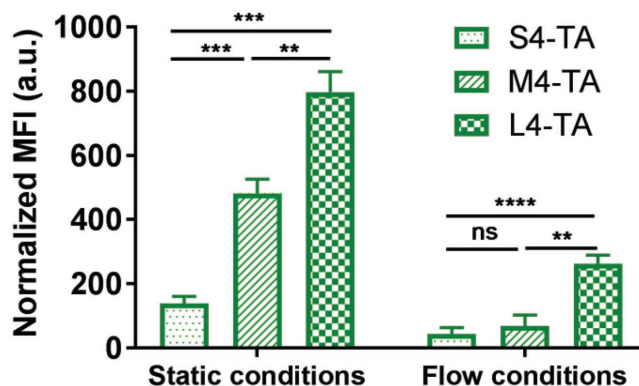


Figure 5. Cellular association of amine-functionalized particles having three different sizes with HUVECs under static and flow conditions as measured by flow cytometry. Data are presented as mean \pm SD ($n = 3$), ** $P < 0.01$, *** $P < 0.001$, **** $P < 0.0001$, ns $P > 0.05$ (pair *t*-test).

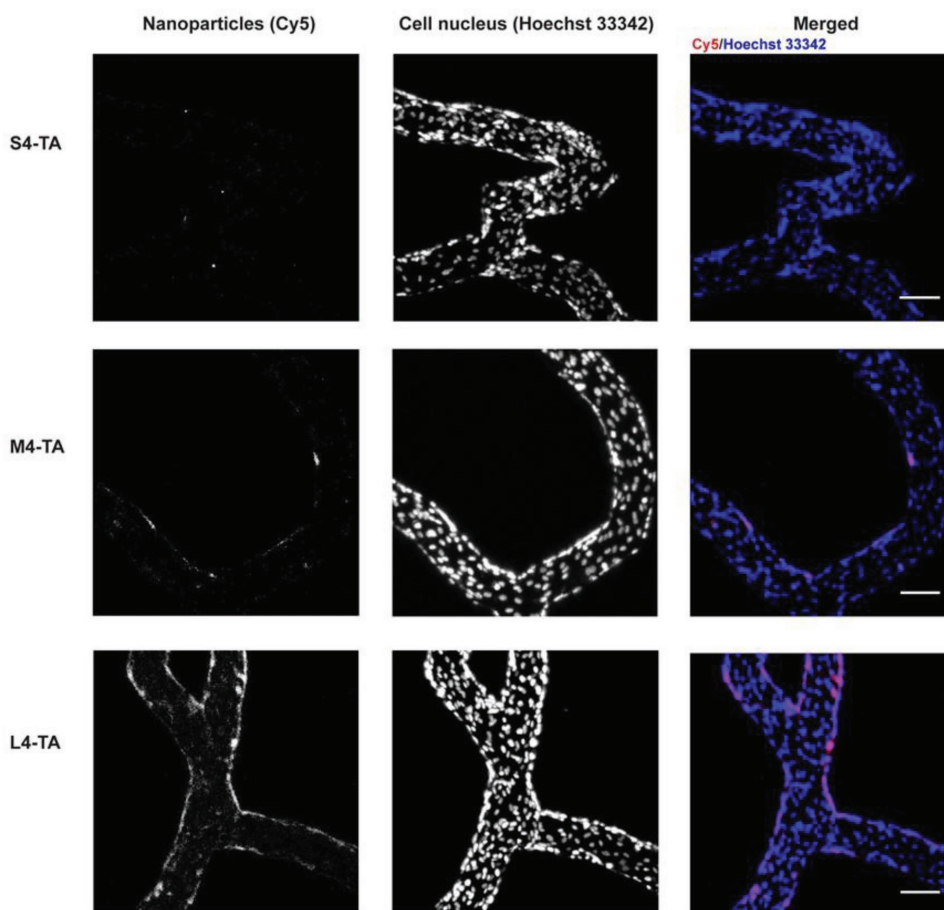


Figure 6. Images of tertiary amine-functionalized particles with three different sizes associated with HUVECs in the synthetic vascular network. Scale bars = 100 μm .

than medium and small particles (70 and 40 nm), which is consistent with data obtained by flow cytometry (Figure 5). It has been shown that large nanoparticles exhibit a higher tendency to tumble out of the general circulation and scavenge along vascular walls than smaller nanomaterials.^[9,45,46] This tendency may increase the exposure of large nanoparticles with TA-tagged groups to endothelial cells and as a result, increase cellular association. From Figure 6, it is unclear whether these nanoparticles are internalized into the cells or merely bound to the cell surface. To further interrogate this, we collected HUVECs, stained the cells with Calcein AM and Hoechst 33342 and acquired Z-stack images of these cells using a high-resolution confocal microscopy. Images in Figure 7 and Figure S13 (Supporting Information) suggest that TA-functionalized particles may be internalized by HUVECs. That said, additional characterization (e.g., using a specific hybridization internalization probe) are needed to fully confirm the cellular uptake of these particles.^[47]

Next, the cellular association of carboxylic acid-decorated nanoparticles with three different sizes was studied. Figure 8 shows that, under static conditions, the larger nanoparticles had a higher degree of cellular association than did the smaller particles (a similar trend to that observed for TA-functionalized nanoparticles). Interestingly, this trend is reversed under

flow conditions. Small carboxylic acid-decorated nanoparticles exhibited the highest level of cellular association (approximately ninefold higher than medium and large nanoparticles). As such, for carboxylic acid-decorated nanoparticles, data obtained in the static assay cannot be used to predict the trend in cellular associations under flow conditions. The decreased cellular association of medium and large nanoparticles decorated with carboxylic acid may be related to the effect of a strong drag force induced by the fluidic flow.^[48] It has been postulated that drag force of the fluidic flow on large nanoparticles is higher than that on small particles and therefore, large nanoparticles are detached from cell surfaces more than small counterparts.^[49,50] In the other words, the low drag force of fluidic flow exerted on the 40 nm nanoparticles with carboxylic acid surfaces is not strong enough to detach these particles from the cell surface whereas the high drag force on medium and large nanoparticles is sufficient to detach these particles from HUVECs (Figure S14, Supporting Information). For TA-functionalized nanoparticles, the effect of drag force (even on large nanoparticles) is negligible compared to their strong adhesive force with HUVECs and hence, the flow conditions cannot reverse the trend of cellular associations. In addition, the cellular uptake of carboxylic acid-, PEG-, and methyl- functionalized nanoparticles was observed by confocal microscopy (Figure 9;

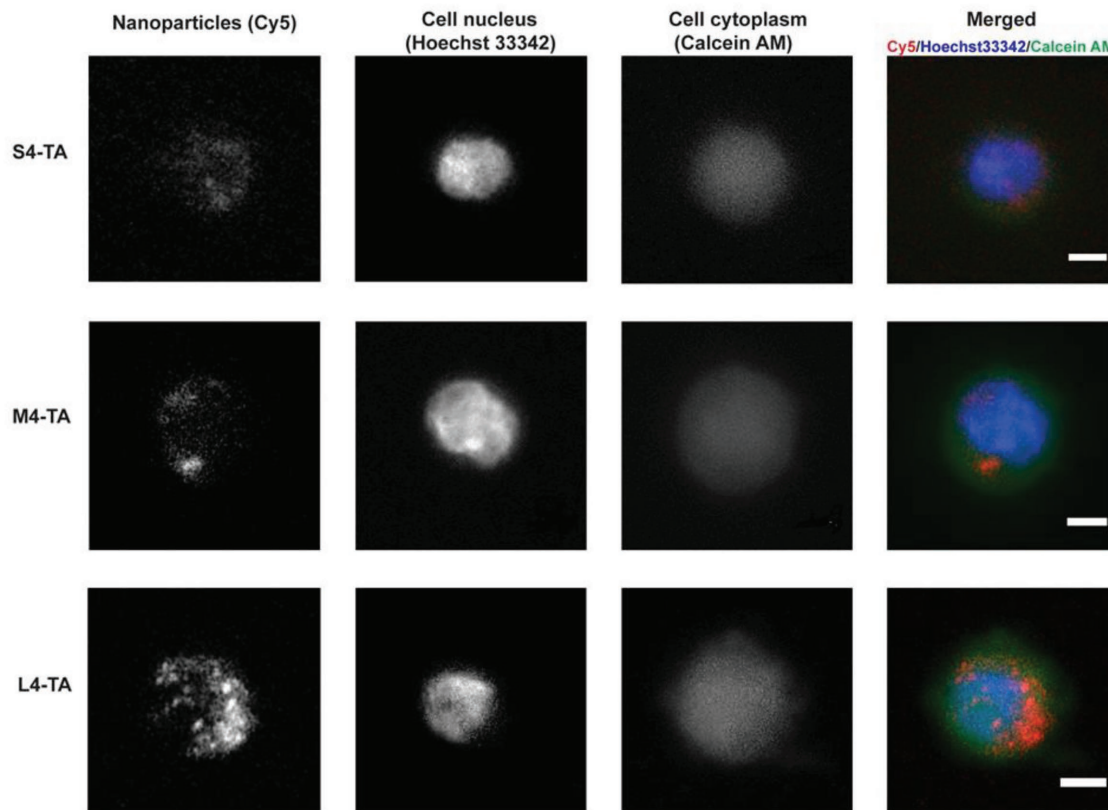


Figure 7. Images of tertiary amine-functionalized particles with three different sizes internalized into HUVECs under flow conditions. The cells were harvested from the vascular network, mounted onto coverslips, and imaged using a Nikon A1R confocal microscope. Scale bars = 5 μm .

Figures S12 and S15, Supporting Information). Taken together, these results clearly indicate that the effect of flow conditions on cellular associations is strongly dependent not only on the particle size but also the particle surface chemistry.

3. Conclusion

We have successfully developed a facile PISA method to label the core of nanoparticles with a commercially available fluorescent dye. This method simply exploits the rapidly polymerizable maleimide moiety commonly found in commercially available

functional dyes. As such, this versatile method has great potential to be widely used for the reproducible preparation of large-scale, concentrated, and fluorescently labeled nanoparticles. By using a low ratio of radical initiator/macro-CTA ratio (12 mol%), the PISA nanoparticles remains a spherical shape regardless of the end group, which allows the synthesis of a library of PISA nanoparticles having various sizes and identical surface chemistry as well as different surface chemistries and similar size. This library has enabled comprehensive investigation of the interplay of particle size, surface chemistry, and flow conditions on particle associations with endothelial cells. Under both static and flow conditions, nanoparticles functionalized with TA groups associated with HUVECs more than particles with PEG, methyl ester, and carboxylate surfaces. In contrast, carboxylic acid group decorated nanoparticles bind relatively weakly to HUVECs and as such, larger-sized particles (130 and 70 nm) are strongly affected by the drag force leading to removal from cell surfaces. We also found that assays under static conditions failed to predict behavior under flow for particles that bind weakly with HUVECs (i.e., for particles with COOH surfaces). Altogether, the synthesis and biological characterization methods developed in this work enable improved characterization of the nano-bio interactions of nanomaterials under flow conditions, and pave the way for future studies that will employ human blood as the mobile phase to more accurately mimic the human vascular network. Diverse particle parameters (such as size, shape, surface chemistry, rigidity, and targeting ligands) will also be studied to provide optimum nanoparticle designs

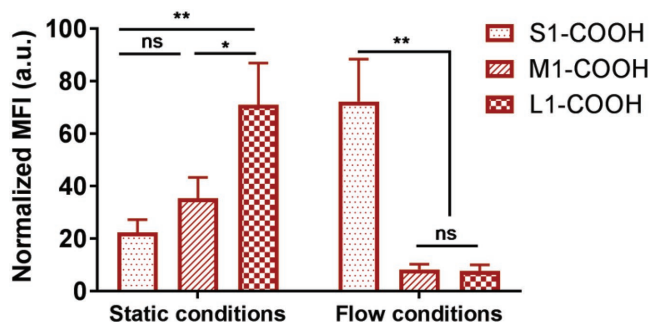


Figure 8. Cellular association between carboxylic acid-functionalized particles with three different sizes and HUVECs under static and flow conditions as measured by flow cytometry. Data are presented as mean \pm SD ($n = 3$); * $P < 0.05$, ** $P < 0.01$, ns $P > 0.05$ (pair t -test).

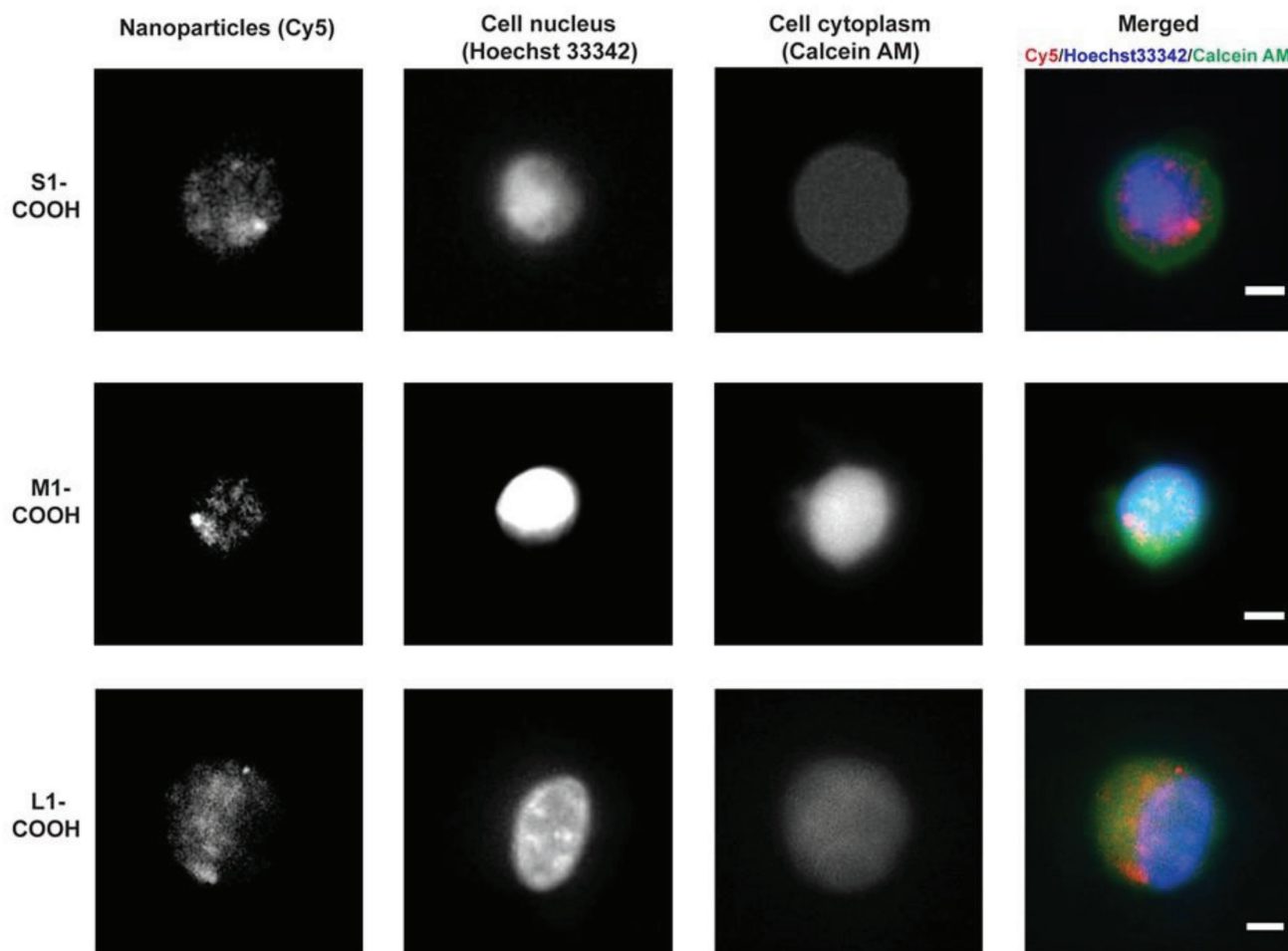


Figure 9. Images of carboxylic acid-functionalized particles with three different sizes internalized into HUVECs under flow conditions. The cells were harvested from the vascular network, mounted onto coverslips, and imaged using a Nikon A1R confocal microscope. Scale bars = 5 μm .

for potential applications in drug delivery, immunotherapy, and cardiovascular disease treatments.

4. Experimental Section

Materials: Ethanethiol (97%), carbon disulfide (>99.9%), p-toluenesulfonyl chloride (>99%), dimethyl sulfoxide (>99.9%, anhydrous), dicyclohexylcarbodiimide (DCC), 4-dimethylaminopyridine (DMAP), trimethylamine (>99%), methanol (99%, anhydrous grade), 3-dimethylamino-1-propanol (TA, 99%), PEG (average $M_n = 550$), and p-toluenesulfonic acid monohydrate (>98.5%) were purchased from Sigma-Aldrich and used as received. Cy5-maleimide was purchased from Lumiprobe and used as received. PEGA (average $M_n = 480 \text{ g mol}^{-1}$; Sigma-Aldrich), HEAA (97%, Sigma-Aldrich), and styrene (>99%, Sigma-Aldrich) were passed through a column of basic alumina (activity I) to remove inhibitor before use. ACPA (98%, Alfa Aesar) was recrystallized twice in methanol before use. MiliQ water (resistivity > 18.2 $\text{M}\Omega \text{ cm}^{-1}$) was produced by a Millipore MiliQ Academic Water Purification System. All other chemicals and solvents used were of at least analytical grade and used as received.

Synthesis of CTAs: ECT-COOH was synthesized as previously described.^[33] Modification of ECT-COOH with methanol (ECT-Me) was carried out as previously described.^[34] Modification of ECT-COOH

with TA (ECT-TA) and PEG (ECT-PEG) was conducted as follows: ECT-COOH (1.00 g, 3.8 mmol), DMAP (0.112 g, 0.38 mmol), and dimethylamino-1-propanol (0.450 mL of 0.872 g mL^{-1} , 3.8 mmol) or PEG (3.1 g, 5.7 mmol) were dissolved in anhydrous dichloromethane (8.0 mL), and added to a 50 mL round bottom flask equipped with a magnetic stirring bar, which was cooled in an ice bath. DCC (1.18 g, 5.7 mmol) was dissolved in anhydrous dichloromethane (8.0 mL) and slowly added dropwise over 5 min under stirring. The reaction vessel was then brought out of the ice bath and allowed to warm up to room temperature. After stirring continuously for 16 h, the reaction mixture was filtered twice to remove dicyclohexyl urea. The filtrate was dried over magnesium sulfate before purification by column chromatography on silica gel. To purify ECT-TA, gradient solvent mixtures were used: petroleum benzene (boiling range 60–80 $^{\circ}\text{C}$):ethyl acetate (3:2 gradually changed to 1:2), and subsequently petroleum benzene (boiling range 60–80 $^{\circ}\text{C}$):ethyl acetate (1:1 with 5 v/v % triethylamine). After complete removal of residual solvents, a dark orange oil was obtained (0.823 g, 62% yield). To purify ECT-PEG, different gradient solvent mixtures were used: petroleum benzene:ethyl acetate (3:2 slowly changed to 1:2) and subsequently acetone. After complete removal of residual solvents, an orange oil was obtained (1.588 g, 51% yield). Characterization of the four CTAs by NMR spectroscopy is provided in Figure S1 (Supporting Information).

Synthesis of Macro-CTAs: P(PEGA-co-HEAA)-COOH, P(PEGA-co-HEAA)-TA, P(HEAA-co-PEGA)-Me, and P(PEGA-co-HEAA)-PEG

were synthesized as follows: ECT/ECT-TA/ECT-Me/ECT-PEG (120 mg/160 mg/126 mg/368 mg, 4.58×10^{-4} mol), PEGA (7.00 g, 1.46×10^{-2} mol), HEAA (2.10 g, 1.83×10^{-2} mol), ACPA (6 mg, 2.28×10^{-5} mol) and DMSO (48 mL, anhydrous) were added to a 50 mL round bottom flask equipped with a stirrer bar. The flask was sealed with a rubber septum and sparged with nitrogen for 1 h at room temperature. After polymerization for 4 h in an oil bath at 70 °C, the flask was cooled in an ice bath and exposed to air. Aliquots (50 μ L) of the crude reactions were sampled for ^1H NMR and SEC analysis to determine PEGA and HEAA conversion, and polydispersity index. The crude reactions were dialyzed against acetone (1 L) using a dialysis membrane (MWCO = 3.5 kDa) for 3 h, to exchange the DMSO. The polymers were recovered via precipitation from acetone into a large excess of diethyl ether (300 mL) and dried under high vacuum for 48 h. Characterizations of the four macro-CTAs were provided in the supporting information (Table S1 and Figure S3, Supporting Information).

Synthesis of Fluorescently Labeled Nanoparticles: A typical emulsion polymerization of styrene and Cy5 maleimide was carried out as follows: macro-CTA (86 mg, 5.5×10^{-6} mol) was added to a 25 mL glass bottle equipped with a stirrer bar. ACPA (1.0 mg, 3.5×10^{-6} mol) was dissolved in MilliQ water (20 mL) by stirring for 30 min. A portion (4 mL) of that ACPA solution (3.5×10^{-4} mol L $^{-1}$) was mixed with the macro-CTA in the glass bottle and sealed with a rubber septum. Styrene (1 mL) was added to a 2 mL glass bottle and also sealed with a rubber septum. Both glass bottles were sparged with nitrogen for 25 min at room temperature. After that, an aliquot of deoxygenated styrene (400 μ L) was added to the 25 mL glass bottle drop-wise via a gas-tight syringe. The reactants were purged for a further 5 min before heating in an oil bath preheated to 80 °C (stirring at 300 rpm). While polymerizing, Cy5 maleimide (1.0 mg, 1.6×10^{-6} mol) was added to 1 mL of styrene and stirred for 30 min in the dark at room temperature. The Cy5 maleimide/styrene mixture was then filtered through a 0.45 μ m polytetrafluoroethylene (PTFE) filter and then sealed with a rubber septum before sparging with nitrogen for 10 min. An aliquot (50 μ L) of the Cy5 maleimide/styrene mixture was then added to the emulsion polymerization at 4 h via a gas-tight syringe. The polymerization was then allowed to continue for another 2 h before cooling the reaction in an ice bath and opening to the air. An aliquot (50 μ L) of the crude mixture was sampled for SEC and ^1H NMR analysis. The reaction mixture was dialyzed against MilliQ water for 48 h using a dialysis membrane (MWCO = 12 kDa) and stored in the fridge (4 °C) and in the dark to prevent photobleaching. The fluorescence signal of each nanoparticle was characterized by fluorescence spectrophotometry (Figure S11, Supporting Information).

Characterizations of CTAs, Macro-CTAs, and Nanoparticles: ^1H NMR spectroscopy: all ^1H NMR spectra were obtained in deuterated chloroform (RAFT agents), deuterated DMSO (macro-CTAs) or a mixture of deuterated acetone and deuterated chloroform in a 9:1 ratio (emulsion polymerizations) on a Bruker Avance III 400 MHz spectrometer. Size exclusion chromatography (SEC): Analyses of polymer solutions were performed using a Shimadzu modular system comprising a DGU-12A degasser, an SIL-20AD automatic injector, a 5.0 μ m bead-size guard column (50 \times 7.8 mm) followed by three KF-805L columns (300 \times 8 mm, bead size: 10 μ m, pore size maximum: 5000 Å), a SPD-20A ultraviolet detector (the absorbance was set at 646 nm to detect Cy5), and an RID-10A differential refractive-index detector. A CTO-20A oven was used to maintain the columns at 40 °C. The eluent was *N,N*-dimethylacetamide (HPLC grade, with 0.03% w/v LiBr) with a flow rate set at 1 mL min $^{-1}$ using an LC-20AD pump. Calibration was done using commercial narrow molecular weight distribution polystyrene (PSTY) standards with a molecular weight range of 500 to 2×10^6 g mol $^{-1}$. All polymer samples were passed through a 0.45 μ m PTFE filter prior to injection. TEM: an aliquot (5 μ L) of 0.1 wt% latex solution (diluted with MilliQ water) was deposited on a Formvar-coated copper grid (GSCu100F-50, Proscitech) and was left to dry overnight in the air and at room temperature. TEM imaging was performed using a Tecnai F20 transmission electron microscope at an accelerating

voltage of 200 kV at ambient temperature. DLS: DLS measurements were performed using a Malvern Zetasizer Nano Series running DLS software and operating a 4 mW He-Ne laser at 633 nm. The analysis was performed at an angle of 173°. The sample RI was set at 1.59 for polystyrene. The dispersant viscosity and RI were set to 0.89 Ns m $^{-2}$ and 1.33, respectively. The number of nanoparticles per 1 mL was measured using a NanoSight NS300 (Malvern). The measurements were carried out with nanoparticle solutions (0.1 μ g mL $^{-1}$) at room temperature with manual shutter and gain adjustments. SEC, ^1H NMR, TEM, and DLS data for all nanoparticles are reported in the Supporting Information (COOH: Table S2, Figure S6; PEG: Table S3, Figure S7; Me: Table S4, Figure S8; TA: Table S5, Figure S9).

Cell Viability Assay: Cell viability studies were conducted in the presence of macro-CTAs and nanoparticles using the AlamarBlue assays. HUVECs (Lonza) were seeded onto 96-well plates at a cell density of 5000 cells per well in 100 μ L of EGM (Lonza). The cells were then incubated at 37 °C, 5% CO $_2$ for 24 h. Subsequently, the medium was removed and replenished with 100 μ L of fresh medium along with different concentrations of the polymers. After 48 h incubation, the cells were washed twice with chilled HBSS (Sigma-Aldrich) before being incubated with 10% (v/v) AlamarBlue reagent in EGM for 4 h at 37 °C, 5% CO $_2$. Fluorescence was measured at an excitation wavelength of 510 nm and an emission wavelength of 610 nm using a ClarioStar microplate reader. The experiments were performed in triplicate, and relative cell viability was calculated as the percentage viable compared to control cells in EGM without the addition of polymers and nanoparticles.

Culture of HUVECs in Synthetic Microvascular Networks under Cell Medium Flow: Before seeding HUVECs into the microvascular network device/chip (SynVivo, SMN1-D001), Matrigel (In Vitro Technologies) was used to coat microchannels inside the chip. First, Matrigel (1/10 in chilled EGM) was injected into the device in cold conditions. After that, the chip was placed in a fridge at 4 °C for 1 h and then at 37 °C, 5% CO $_2$ in an incubator before a flow of fresh EGM was perfused through the chip to wash out unreacted Matrigel and gel clumps. Next, HUVECs (2.5×10^7 cells mL $^{-1}$) were gently injected into the network until reaching 90% confluence (see Figure S10, Supporting Information) before clamping the inlet and outlet ports. The device was then incubated (37 °C, 5% CO $_2$) for around 1 h for cell attachment before cell medium was changed. After that, a flow of fresh medium was perfused through the chip at the rate of 0.1 μ L min $^{-1}$ for 20 h using a syringe pump (Harvard Apparatus, Holliston MA).

Cell Association under Static Conditions: HUVECs were seeded at 40 000 cells per well in 48-well plates, incubated for 22 h at 37 °C, 5% CO $_2$. 240 μ L of nanoparticles in EGM were added to the cells and incubated for 4 h. The cells were then washed three times with chilled HBSS and collected after treating with trypsin/EDTA (Lonza). After centrifugation at 300 g for 5 min, cells were resuspended in 300 μ L of 1×10^{-3} M propidium iodide (PI, Life Technologies) solution in HBSS, and analyzed by flow cytometry using a FACSCanto II (BD Biosciences, San Jose, CA).

Cell Association under Flow Conditions: Nanoparticles in EGM were injected into the chip via a 1 mL syringe connected with Tygon tubing (0.02"ID \times 0.06"OD, SynVivo). The flow of nanoparticles (in EGM) was perfused from the inlet port through the chip for 4 h at 1.0 μ L min $^{-1}$ using a syringe pump. At the end of the experiments, 1 mL of chilled HBSS was used to wash out nonassociated particles. For quantifying cellular association using flow cytometry, HUVECs were treated with chilled trypsin/EDTA followed by incubating in a fridge at 4 °C for 5 min before harvesting. After that, the HUVECs were collected by centrifuging at 300 g for 5 min at 4 °C, and resuspended in 300 μ L of 1×10^{-3} M PI in HBSS. Cellular association of nanoparticles was then analyzed by flow cytometry (FACSCanto II from BD Biosciences, San Jose, CA). For live cell imaging, a solution of 1×10^{-3} M Calcein AM (Sigma-Aldrich) and 0.3×10^{-3} M Hoechst 33342 (Sigma-Aldrich) in HBSS was perfused through the chip for 15 min at 5 μ L min $^{-1}$. After that, the device was incubated for another 10 min before acquiring images using a confocal microscope.

Supporting Information

Supporting Information is available from the Wiley Online Library or from the author.

Acknowledgements

S.Y.K. and M.N.V. contributed equally to this work. Electron microscopy was performed at the Bio21 Advanced Microscopy Facility, The University of Melbourne. This work was carried out within the Australian Research Council (ARC) Centre of Excellence in Convergent Bio-Nano Science and Technology (Project No. CE140100036). The authors would like to thank Mr. Cameron Nowell for his technical support on confocal microscopy. S.Y.K. and E.H.P. acknowledge the financial support from the Australian Government Research Training Program Scholarship. M.N.V. acknowledges the financial support of Vietnamese Government and the Faculty of Pharmacy and Pharmaceutical Sciences, Monash University. N.P.T. acknowledges the award of a DECRA Fellowship from the ARC (DE180100076). J.F.Q. acknowledges receipt of a Future Fellowship from the ARC (FT170100144). T.P.D. is grateful for the award of an Australian Laureate Fellowship from the ARC (FL140100052).

Conflict of Interest

The authors declare no conflict of interest.

Keywords

cellular association, dynamic flow, PISA, size, surface chemistry

Received: May 3, 2018

Revised: June 10, 2018

Published online: July 25, 2018

- [1] M. E. Davis, Z. Chen, D. M. Shin, *Nat. Rev. Drug Discovery* **2008**, *7*, 771.
- [2] D. Peer, J. M. Karp, S. Hong, O. C. Farokhzad, R. Margalit, R. Langer, *Nat. Nanotechnol.* **2007**, *2*, 751.
- [3] N. P. Truong, J. F. Quinn, M. R. Whittaker, T. P. Davis, *Polym. Chem.* **2016**, *7*, 4295.
- [4] N. P. Truong, W. Y. Gu, I. Prasadam, Z. F. Jia, R. Crawford, Y. Xiao, M. J. Monteiro, *Nat. Commun.* **2013**, *4*, 1902.
- [5] C. J. Cheng, G. T. Tietjen, J. K. Saucier-Sawyer, W. M. Saltzman, *Nat. Rev. Drug Discovery* **2015**, *14*, 239.
- [6] H. F. Yuan, W. Jiang, C. A. von Roemeling, Y. Q. Qie, X. J. Liu, Y. X. Chen, Y. F. Wang, R. E. Wharen, K. Yun, G. J. Bu, K. L. Knutson, B. Y. S. Kim, *Nat. Nanotechnol.* **2017**, *12*, 763.
- [7] M. E. Lobatto, V. Fuster, Z. A. Fayad, W. J. M. Mulder, *Nat. Rev. Drug Discovery* **2011**, *10*, 835.
- [8] C. Li, *Nat. Mater.* **2014**, *13*, 110.
- [9] H. T. Ta, N. P. Truong, A. K. Whittaker, T. P. Davis, K. Peter, *Expert Opin. Drug Delivery* **2018**, *15*, 33.
- [10] N. P. Truong, M. R. Whittaker, C. W. Mak, T. P. Davis, *Expert Opin. Drug Delivery* **2015**, *12*, 129.
- [11] S.-Y. Lee, M. Ferrari, P. Decuzzi, *J. Biomech.* **2009**, *42*, 1885.
- [12] R. Toy, P. M. Peiris, K. B. Ghaghada, E. Karathanasis, *Nanomedicine* **2014**, *9*, 121.
- [13] H. J. Hsieh, C. A. Liu, B. Huang, A. H. H. Tseng, D. L. Wang, *J. Biomed. Sci.* **2014**, *21*, 3.
- [14] M. Bjornmalm, M. Faria, X. Chen, J. W. Cui, F. Caruso, *Langmuir* **2016**, *32*, 10995.
- [15] O. C. Farokhzad, A. Khademhosseini, S. Y. Yon, A. Hermann, J. J. Cheng, C. Chin, A. Kiselyuk, B. Tepy, G. Eng, R. Langer, *Anal. Chem.* **2005**, *77*, 5453.
- [16] S. P. Samuel, N. Jain, F. O'Dowd, T. Paul, D. Kashanin, V. A. Gerard, Y. K. Gun'ko, A. Prina-Mello, Y. Volkov, *Int. J. Nanomed.* **2012**, *7*, 2943.
- [17] B. Prabhakarpanid, M. C. Shen, K. Pant, M. F. Kiani, *Microvasc. Res.* **2011**, *82*, 210.
- [18] G. Lamberti, Y. Tang, B. Prabhakarpanid, Y. Wang, K. Pant, M. F. Kiani, B. Wang, *Microvasc. Res.* **2013**, *89*, 107.
- [19] B. Prabhakarpanid, K. Pant, R. C. Scott, C. B. Pattillo, D. Irimia, M. F. Kiani, S. Sundaram, *Biomed. Microdevices* **2008**, *10*, 585.
- [20] J. M. Rosano, N. Tousi, R. C. Scott, B. Krynska, V. Rizzo, B. Prabhakarpanid, K. Pant, S. Sundaram, M. F. Kiani, *Biomed. Microdevices* **2009**, *11*, 1051.
- [21] P. Kolhar, A. C. Anselmo, V. Gupta, K. Pant, B. Prabhakarpanid, E. Ruoslahti, S. Mitragotri, *Proc. Natl. Acad. Sci. USA* **2013**, *110*, 10753.
- [22] N. Doshi, B. Prabhakarpanid, A. Rea-Ramsey, K. Pant, S. Sundaram, S. Mitragotri, *J. Controlled Release* **2010**, *146*, 196.
- [23] Y. Tang, F. Soroush, J. B. Sheffield, B. Wang, B. Prabhakarpanid, M. F. Kiani, *Sci. Rep.* **2017**, *7*, 9359.
- [24] B. Prabhakarpanid, M. C. Shen, J. B. Nichols, C. J. Garson, I. R. Mills, M. M. Matar, J. G. Fewell, K. Pant, *J. Controlled Release* **2015**, *201*, 49.
- [25] N. P. Truong, J. F. Quinn, M. V. Dussert, N. B. T. Sousa, M. R. Whittaker, T. P. Davis, *ACS Macro Lett.* **2015**, *4*, 381.
- [26] N. P. Truong, C. Zhang, T. A. H. Nguyen, A. Anastasaki, M. W. Schulze, J. F. Quinn, A. K. Whittaker, C. J. Hawker, M. R. Whittaker, T. P. Davis, *ACS Macro Lett.* **2018**, *7*, 159.
- [27] L. Esser, N. P. Truong, B. Karagoz, B. A. Moffat, C. Boyer, J. F. Quinn, M. R. Whittaker, T. P. Davis, *Polym. Chem.* **2016**, *7*, 7325.
- [28] N. P. Truong, M. R. Whittaker, A. Anastasaki, D. M. Haddleton, J. F. Quinn, T. P. Davis, *Polym. Chem.* **2016**, *7*, 430.
- [29] N. P. Truong, J. F. Quinn, A. Anastasaki, D. M. Haddleton, M. R. Whittaker, T. P. Davis, *Chem. Commun.* **2016**, *52*, 4497.
- [30] S. Kaga, N. P. Truong, L. Esser, D. Senyschyn, A. Sanyal, R. Sanyal, J. F. Quinn, T. P. Davis, L. M. Kaminskas, M. R. Whittaker, *Biomacromolecules* **2017**, *18*, 3963.
- [31] N. G. Engelis, A. Anastasaki, G. Nurumbetov, N. P. Truong, V. Nikolaou, A. Shegiwal, M. R. Whittaker, T. P. Davis, D. M. Haddleton, *Nat. Chem.* **2017**, *9*, 171.
- [32] N. P. Truong, J. F. Quinn, A. Anastasaki, M. Rolland, M. Vu, D. Haddleton, M. R. Whittaker, T. P. Davis, *Polym. Chem.* **2017**, *8*, 1353.
- [33] N. P. Truong, M. V. Dussert, M. R. Whittaker, J. F. Quinn, T. P. Davis, *Polym. Chem.* **2015**, *6*, 3865.
- [34] S. Y. Khor, N. P. Truong, J. F. Quinn, M. R. Whittaker, T. P. Davis, *ACS Macro Lett.* **2017**, *6*, 1013.
- [35] J. Rosselgong, A. Blanazs, P. Chambon, M. Williams, M. Semsarilar, J. Madsen, G. Battaglia, S. P. Armes, *ACS Macro Lett.* **2012**, *1*, 1041.
- [36] C. Grazon, J. Rieger, R. Meallet-Renault, B. Charleux, G. Clavier, *Macromolecules* **2013**, *46*, 5167.
- [37] M. Zamfir, J. F. Lutz, *Nat. Commun.* **2012**, *3*, 1138.
- [38] B. V. K. J. Schmidt, N. Fechner, J. Falkenhagen, J. F. Lutz, *Nat. Chem.* **2011**, *3*, 234.
- [39] C. Freese, L. Anspach, R. C. Deller, S. J. Richards, M. I. Gibson, C. J. Kirkpatrick, R. E. Unger, *Biomater. Sci.* **2017**, *5*, 707.
- [40] J. W. Cui, M. Faria, M. Bjornmalm, Y. Ju, T. Suma, S. T. Gunawan, J. J. Richardson, H. Heidar, S. Bals, E. J. Crampin, F. Caruso, *Langmuir* **2016**, *32*, 12394.

- [41] N. P. Truong, Z. Jia, M. Burges, N. A. McMillan, M. J. Monteiro, *Biomacromolecules* **2011**, *12*, 1876.
- [42] N. P. Truong, Z. F. Jia, M. Burgess, L. Payne, N. A. J. McMillan, M. J. Monteiro, *Biomacromolecules* **2011**, *12*, 3540.
- [43] M. S. Ehrenberg, A. E. Friedman, J. N. Finkelstein, G. Oberdorster, J. L. McGrath, *Biomaterials* **2009**, *30*, 603.
- [44] N. Faucheux, R. Schweiss, K. Lutzow, C. Werner, T. Groth, *Biomaterials* **2004**, *25*, 2721.
- [45] E. C. Eckstein, A. W. Tilles, F. J. Millero, *Microvasc. Res.* **1988**, *36*, 31.
- [46] T. R. Lee, M. Choi, A. M. Kopacz, S. H. Yun, W. K. Liu, P. Decuzzi, *Sci. Rep.* **2013**, *3*, 2079.
- [47] H. Y. Liu, A. P. R. Johnston, *Angew. Chem. Int. Ed.* **2013**, *52*, 5744.
- [48] J. F. Tan, S. Shah, A. Thomas, H. D. Ou-Yang, Y. L. Liu, *Microfluid. Nanofluid.* **2013**, *14*, 77.
- [49] C. Fillafer, G. Ratzinger, J. Neumann, Z. Guttenberg, S. Dissauer, I. K. Lichtscheidl, M. Wirth, F. Gabor, M. F. Schneider, *Lab Chip* **2009**, *9*, 2782.
- [50] V. R. S. Patil, C. J. Campbell, Y. H. Yun, S. M. Slack, D. J. Goetz, *Biophys. J.* **2001**, *80*, 1733.



Supporting Information

for *Small*, DOI: 10.1002/smll.201801702

Elucidating the Influences of Size, Surface Chemistry, and Dynamic Flow on Cellular Association of Nanoparticles Made by Polymerization-Induced Self-Assembly

Song Yang Khor, Mai N. Vu, Emily H. Pilkington, Angus P. R. Johnston, Michael R. Whittaker, John F. Quinn, Nghia P. Truong, and Thomas P. Davis**

Supporting Information

Elucidating the influences of size, surface chemistry and dynamic flow on cellular association of nanoparticles made by polymerization-induced self-assembly

Song Yang Khor[‡], Mai N. Vu[‡], Emily H. Pilkington, Angus P.R. Johnston, Michael R. Whittaker, John F. Quinn, Nghia P. Truong*, and Thomas P. Davis*

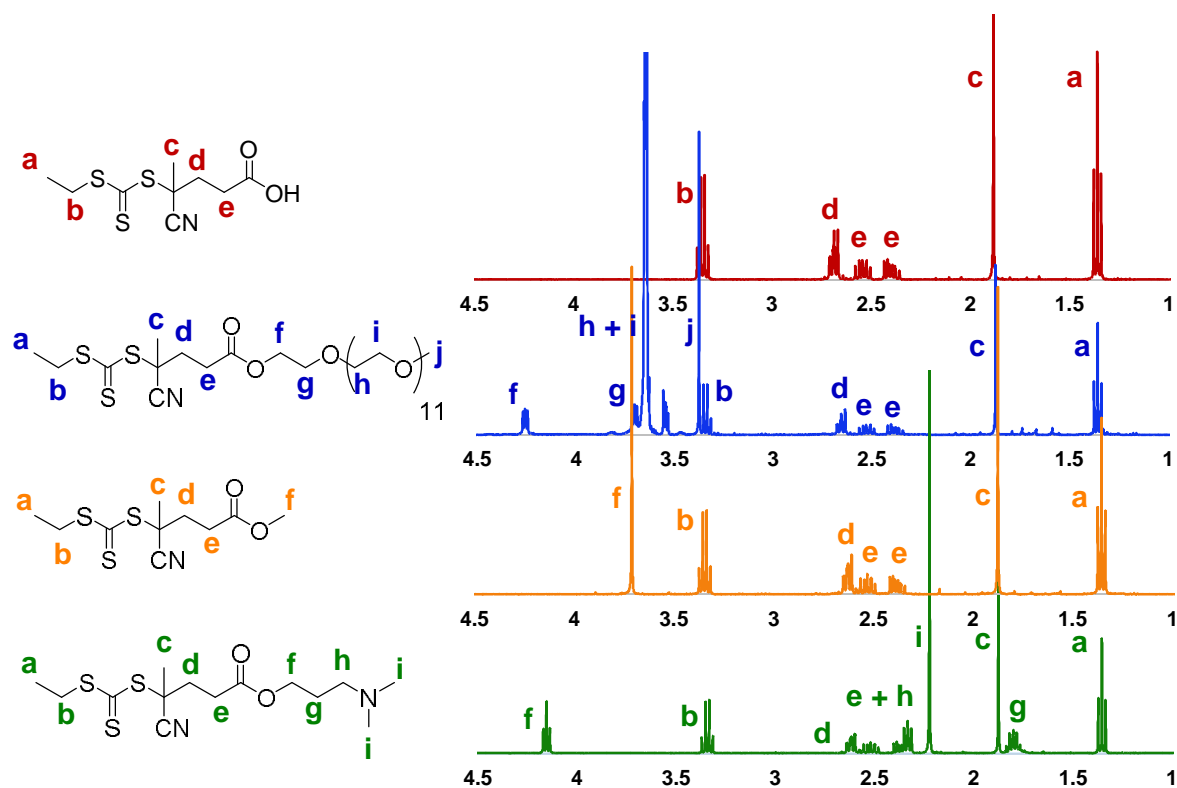


Figure S1. ^1H NMR spectrum of ECT-COOH (red), ECT-PEG (blue), ECT-Me (yellow), and ECT-TA (green) in chloroform- d_6 .

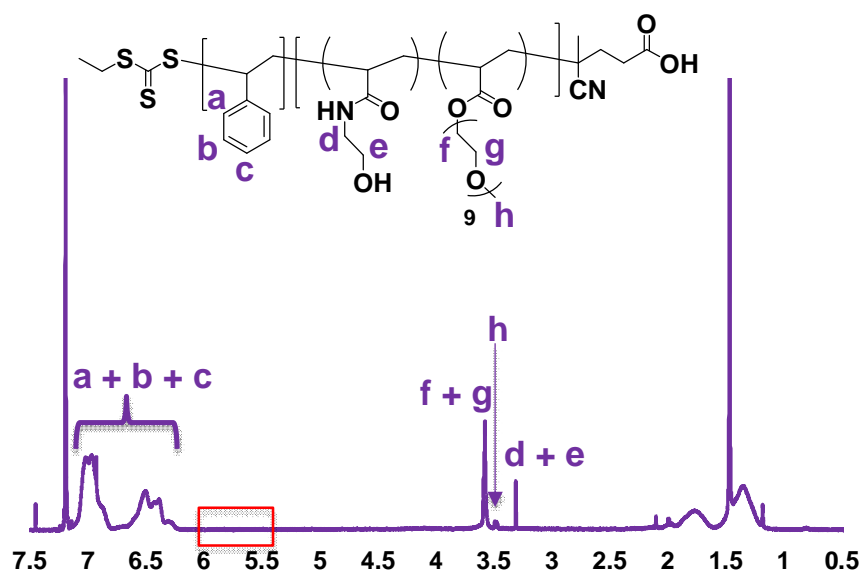


Figure S2. ¹H NMR spectrum of P(PEGA-*co*-HEAA)-*b*-P(STY)-COOH in acetone-*d*₆ and chloroform-*d*₃ (9:1 ratio). The red box highlights to absence of vinyl proton peaks at 5.7 ppm.

Table S1. (SEC, ^1H NMR data for P(HEAA-*co*-PEGA)-COOH, P(HEAA-*co*-PEGA)-N(CH₃)₂, P(HEAA-*co*-PEGA)-Me, and P(HEAA-*co*-PEGA)-PEG macro-CTAs, synthesised by RAFT solution polymerization of HEAA and PEGA at 70 °C in DMSO for 4 h using ACPA as the initiator.)

RAFT agent	RAFT : HEAA : PEGA : ACPA	SEC ^{a)}		^1H NMR				$M_{n, \text{NMR}}^{\text{f)}$ (g/mol)
		PDI	M_n (g/mol)	Conversion (%)		DP		
				HEAA ^{b)}	PEGA ^{c)}	HEAA ^{d)}	PEGA ^{e)}	
ECT		1.21	16500	63	81	25	26	15700
ECT-PEG	20 : 800 : 640 : 1	1.27	16000	60	79	24	25	15600
ECT-Me		1.22	17700	65	81	26	26	15700
ECT-TA		1.25	17100	60	75	24	24	14700

^{a)} SEC measurements were carried out in DMAC + 0.03 wt% of LiBr solution, and using PSTY standards for calibration; ^{b)} HEAA conversion was calculated by integrating the area of a peak at 5.5 ppm ($I_{5.5}$) and the area of peaks from 4.5 to 5.0 ppm ($I_{4.5-5.0}$), and applying the following equation: HEAA conversion (%) = $100 - (I_{5.5}/I_{4.5-5.0} \times 100)$; ^{c)} PEGA conversion was calculated by integrating the area of a peak at 5.9 ppm ($I_{5.9}$) and the area of peaks from 3.9 to 4.2 ppm ($I_{3.9-4.2}$), and applying the following equation: PEGA conversion (%) = $100 - (I_{5.9}/I_{3.9-4.2} \times 2 \times 100)$; ^{d)} The degree of polymerization of HEAA was derived using the following equation: HEAA degree of polymerization = (HEAA conversion/100) \times ([HEAA]/[RAFT]); ^{e)} The degree of polymerization of PEGA was derived using the following equation: PEGA degree of polymerization = (PEGA conversion/100) \times ([PEGA]/[RAFT]); ^{f)} The $M_{n, \text{NMR}}$ was calculated by the following equation: $(\text{DP}_{\text{HEAA}} \times 115) + (\text{DP}_{\text{PEGA}} \times 480) + 263$ (ECT)/806 (ECT-PEG)/277 (ECT-Me)/349 (ECT-TA).

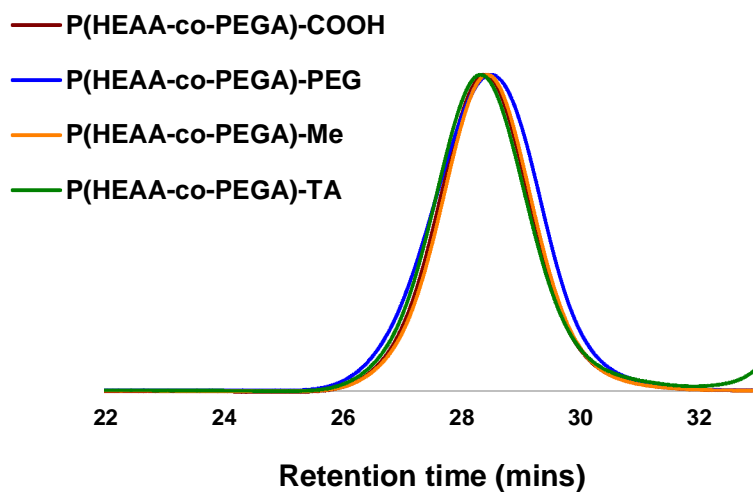


Figure S3. SEC traces for P(HEAA-*co*-PEGA)-COOH (red), P(HEAA-*co*-PEGA)-PEG (blue), P(HEAA-*co*-PEGA)-Me (yellow), and P(HEAA-*co*-PEGA)-TA (green) macro-CTA synthesized by RAFT solution polymerization of HEAA and PEGA in DMSO at 70 °C using ACPA as an initiator.

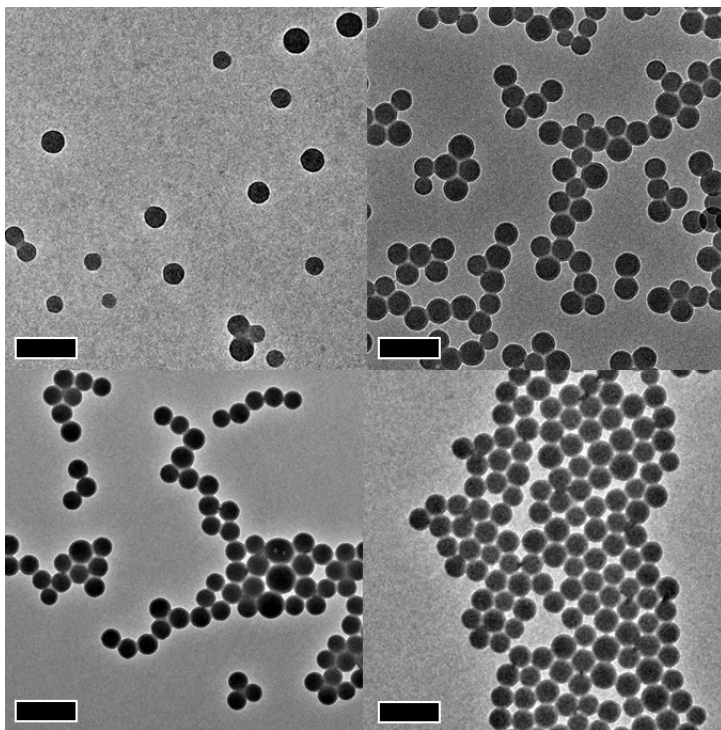


Figure S4. TEM image of the particles formed by RAFT aqueous emulsion polymerization of styrene with (A) P(HEAA-*co*-PEGA)-COOH, (B) P(HEAA-*co*-PEGA)-PEG, (C) P(HEAA-*co*-PEGA)-Me, and (D) P(HEAA-*co*-PEGA)-TA, at 80 °C for 6 h. All scale bars represent 200 nm.

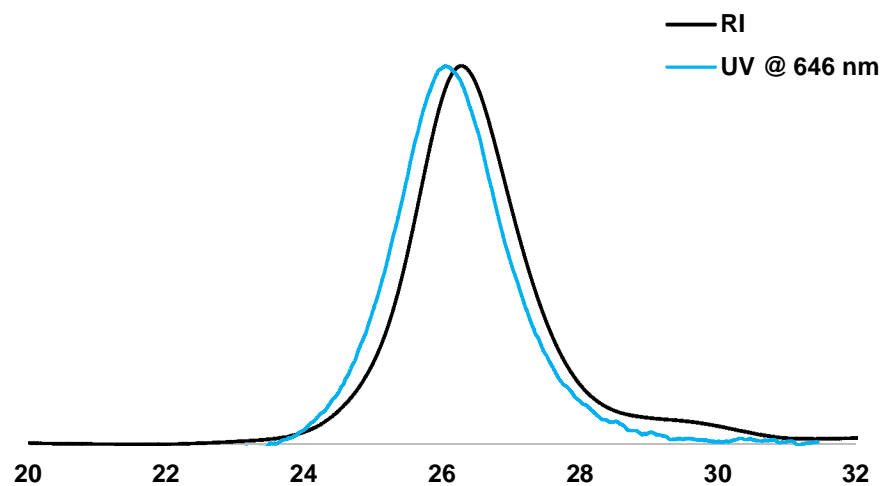


Figure S5. RI (black) and UV (blue) SEC traces for RAFT aqueous emulsion polymerization of styrene with Cy5-maleimide injected after 4 h emulsion polymerization of styrene, followed by another 2 h of polymerization.

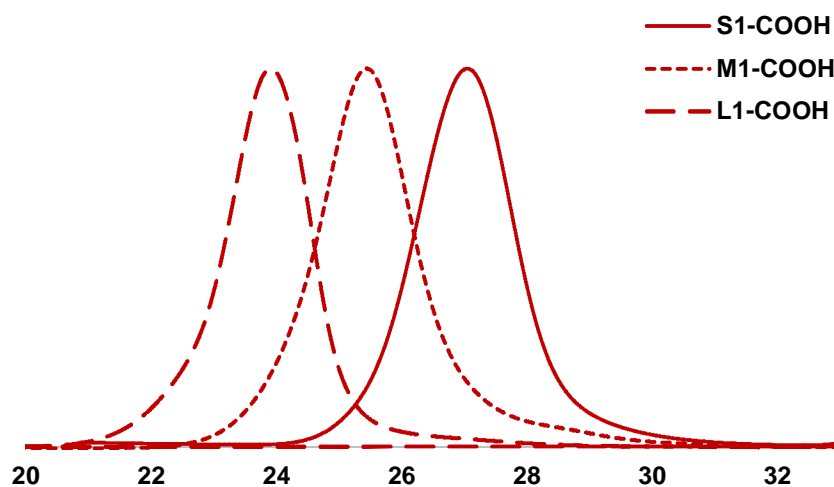


Figure S6. SEC traces for S1-COOH (solid line), M1-COOH (short dash-line), and L1-COOH (long dash-line) synthesized by RAFT aqueous emulsion polymerization of styrene at 80 °C using ACPA as an initiator.

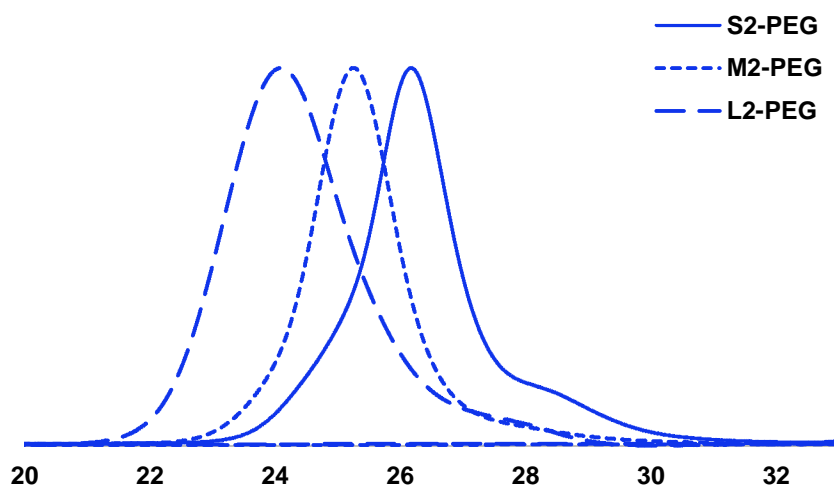


Figure S7. SEC traces for S2-PEG (solid line), M2-PEG (short dash-line), and L2-PEG (long dash-line) synthesized by RAFT aqueous emulsion polymerization of styrene at 80 °C using ACPA as an initiator.

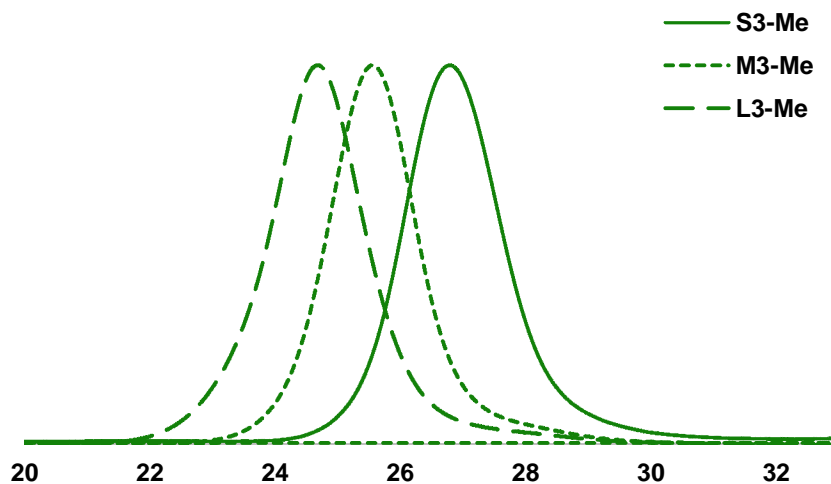


Figure S8. SEC traces for S3-Me (solid line), M3-Me (short dash-line), and L3-Me (long dash-line) synthesized by RAFT aqueous emulsion polymerization of styrene at 80 °C using ACPA as an initiator.

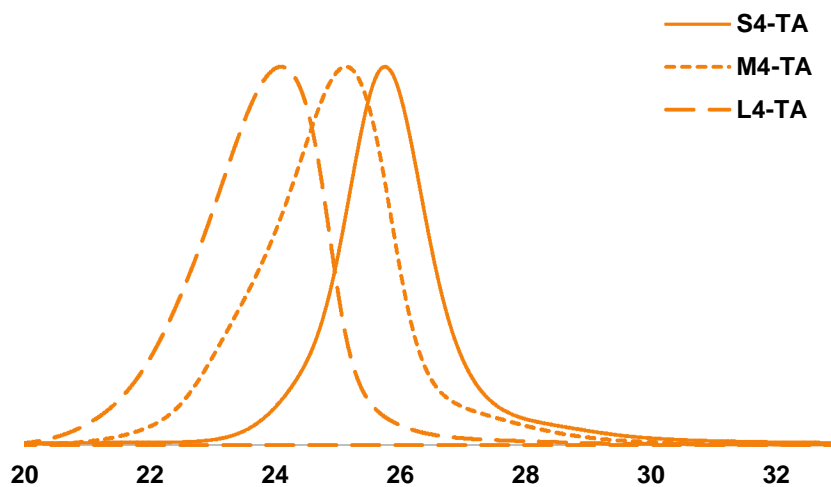


Figure S9. SEC traces for S4-TA (solid line), M4-TA (short dash-line), and L4-TA (long dash-line) synthesized by RAFT aqueous emulsion polymerization of styrene at 80 °C using ACPA as an initiator.

Table S2. SEC, ¹H NMR, TEM, and DLS data for RAFT aqueous emulsion polymerization of styrene with P(HEAA-*co*-PEGA)-COOH at 80 °C for 6 h using ACPA as the initiator.

Polymer code	Macro-CTA : Styrene : ACPA	SEC ^{a)}		¹ H NMR		TEM	DLS ^{e)}		
		PDI	M _n (g/mol)	Conv. ^{b)} (%)	M _{n,(th)} ^{c)}	D _{TEM} ^{d)} (nm)	D _h (nm)	PSD	ζ (mV)
S1-COOH	1:334:0.3	1.38	38200	97	49200	36±9	36±8	0.180	-14±1.2
M1-COOH	1:636:0.3	1.40	65900	96	79100	74±6	77±4	0.105	-12±0.5
L1-COOH	1:973:0.3	1.41	114800	96	112900	132±14	141±6	0.035	-13±0.6

^{a)} SEC measurements were carried out in DMAC + 0.03 wt% of LiBr solution, and using PSTY standards for calibration; ^{b)} Styrene conversion was calculated by integrating the area of a peak at 5.7 ppm (I_{5.7}) and the area of peaks from 6.3 to 7.5 ppm (I_{6.3-7.5}), and applying the following equation: styrene conversion (%) = 100 – (I_{5.7}/I_{6.3-7.5} × 5 × 100); ^{c)} The M_n(th) was calculated by the following equation: (styrene conversion/100) × ([styrene]/[macro-CTA]) + 16500; ^{d)} D_{TEM} was calculated by ImageJ; ^{e)} Dynamic light scattering measurements were performed at 25 °C with the reported values averaged over 5 consecutive measurements.

Table S3. SEC, ¹H NMR, TEM, and DLS data for RAFT aqueous emulsion polymerization of styrene with P(HEAA-*co*-PEGA)-PEG at 80 °C for 6 h using ACPA as the initiator.

Polymer code	Macro-CTA : Styrene : ACPA	SEC ^{a)}		¹ H NMR		TEM	DLS ^{e)}		
		PDI	M _n (g/mol)	Conv. ^{b)} (%)	M _{n,(th)} ^{c)}	D _{TEM} ^{d)} (nm)	D _h (nm)	PSD	ζ (mV)
S2-PEG	1:340:0.3	1.42	39300	90	47600	39±12	40±5	0.250	-11±2.1
M2-PEG	1:716:0.3	1.59	60000	92	77300	70±9	75±3	0.143	-9±0.7
L2-PEG	1:1250:0.3	1.66	118500	99	124000	142±8	138±3	0.162	-10±0.8

^{a)} SEC measurements were carried out in DMAC + 0.03 wt% of LiBr solution, and using PSTY standards for calibration; ^{b)} Styrene conversion was calculated by integrating the area of a peak at 5.7 ppm (I_{5.7}) and the area of peaks from 6.3 to 7.5 ppm (I_{6.3-7.5}), and applying the following equation: styrene conversion (%) = 100 – (I_{5.7}/I_{6.3-7.5} × 5 × 100); ^{c)} The M_n(th) was calculated by the following equation: (styrene conversion/100) × ([styrene]/[macro-CTA]) + 16500; ^{d)} D_{TEM} was calculated by ImageJ; ^{e)} Dynamic light scattering measurements were performed at 25 °C with the reported values averaged over 5 consecutive measurements.

Table S4. SEC, ¹H NMR, TEM, and DLS data for RAFT aqueous emulsion polymerization of styrene with P(HEAA-*co*-PEGA)-Me at 80 °C for 6 h using ACPA as the initiator.

Polymer code	Macro-CTA : Styrene : ACPA	SEC ^{a)}		¹ H NMR		TEM	DLS ^{e)}		
		PDI	M _n (g/mol)	Conv. ^{b)} (%)	M _{n,(th)} ^{c)}	D _{TEM} ^{d)} (nm)	D _h (nm)	PSD	ζ (mV)
S3-Me	1:318:0.15	1.28	33400	99	48500	34±10	39±8	0.111	-1.5±0.1
M3-Me	1:636:0.15	1.33	73600	97	79900	75±3	78±2	0.039	-1.8±0.2
L3-Me	1:980:0.15	1.38	113800	94	111700	139±11	138±1	0.015	-1.2±0.6

^{a)} SEC measurements were carried out in DMAC + 0.03 wt% of LiBr solution, and using PSTY standards for calibration; ^{b)} Styrene conversion was calculated by integrating the area of a peak at 5.7 ppm (I_{5.7}) and the area of peaks from 6.3 to 7.5 ppm (I_{6.3-7.5}), and applying the following equation: styrene conversion (%) = 100 – (I_{5.7}/I_{6.3-7.5} × 5 × 100); ^{c)} The M_n(th) was calculated by the following equation: (styrene conversion/100) × ([styrene]/[macro-CTA]) + 16500; ^{d)} D_{TEM} was calculated by ImageJ; ^{e)} Dynamic light scattering measurements were performed at 25 °C with the reported values averaged over 5 consecutive measurements.

Table S5. SEC, ¹H NMR, TEM, and DLS data for RAFT aqueous emulsion polymerization of styrene with P(HEAA-*co*-PEGA)-TA at 80 °C for 6 h using ACPA as the initiator.

Polymer code	Macro-CTA : Styrene : ACPA	SEC ^{a)}		¹ H NMR		TEM	DLS ^{e)}		
		PDI	M _n (g/mol)	Conv. ^{b)} (%)	M _{n,(th)} ^{c)}	D _{TEM} ^{d)} (nm)	D _h (nm)	PSD	ζ (mV)
S4-TA	1:450:0.3	1.44	51400	96	62600	35±3	35±3	0.188	-6±0.1
M4-TA	1:800:0.3	1.61	69900	94	95900	73±6	77±4	0.069	-6±0.2
L4-TA	1:1220:0.3	1.52	158700	92	134500	133±6	145±2	0.082	-5±0.1

^{a)} SEC measurements were carried out in DMAC + 0.03 wt% of LiBr solution, and using PSTY standards for calibration; ^{b)} Styrene conversion was calculated by integrating the area of a peak at 5.7 ppm (I_{5.7}) and the area of peaks from 6.3 to 7.5 ppm (I_{6.3-7.5}), and applying the following equation: styrene conversion (%) = 100 – (I_{5.7}/I_{6.3-7.5} × 5 × 100); ^{c)} The M_n(th) was calculated by the following equation: (styrene conversion/100) × ([styrene]/[macro-CTA]) + 16500; ^{d)} D_{TEM} was calculated by ImageJ; ^{e)} Dynamic light scattering measurements were performed at 25 °C with the reported values averaged over 5 consecutive measurements.



Figure S10. A bright field image of HUVECs in the synthetic microvascular networks right after seeding, presenting around 90% confluent coated of the cells over the channels. Scale bar = 100 μm .

Video S1. Formation of the complete and intact lumen of HUVECs in the synthetic microvascular network. Cells were stained with Calcein AM (green) and Hoechst 33342 (blue).

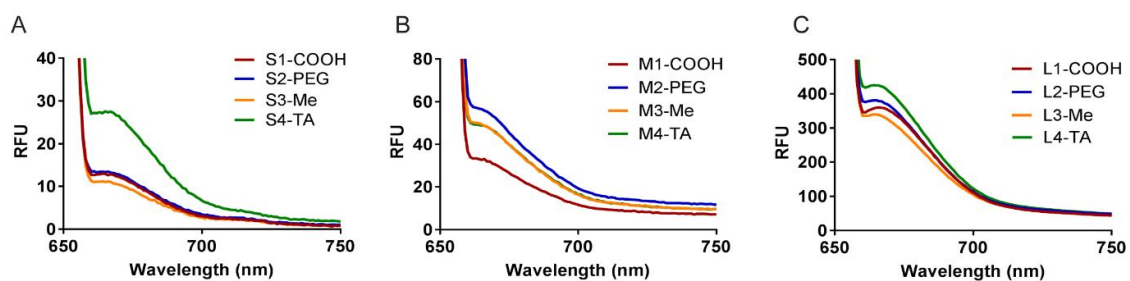


Figure S11. Fluorescence measurement for an equivalent number of nanoparticles using a fluorescence spectrophotometry with the excitation of 635 nm: (A) small particles, (B) intermediate particles, and (C) large particles.

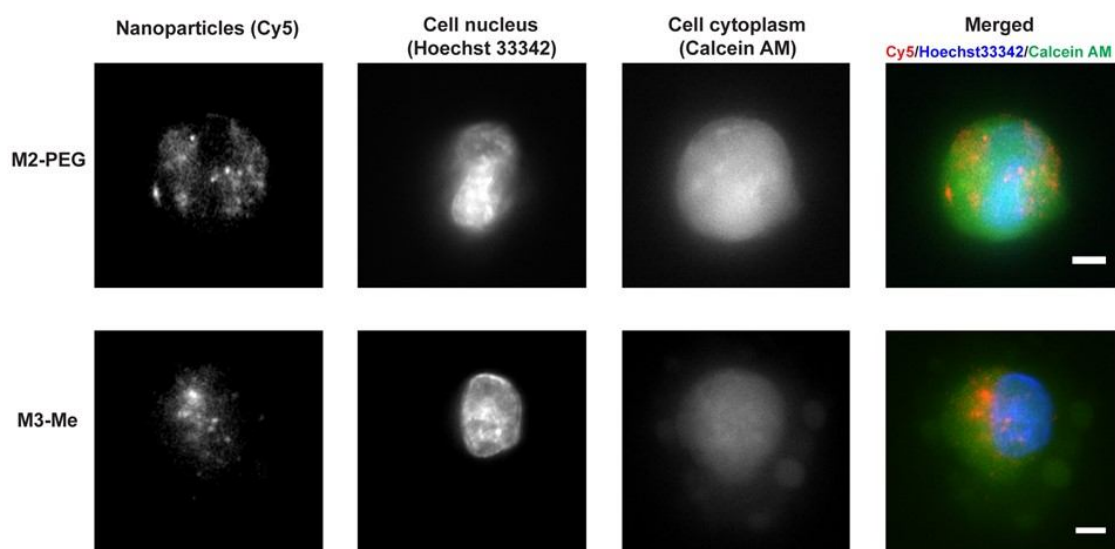


Figure S12. Images of intermediate-sized particles with PEG and methyl surface groups internalized into HUVECs under flow conditions. The cells were harvested from the vascular network, mounted onto coverslips, and imaged using a Nikon A1R confocal microscope.

Scale bars = 5 μm .

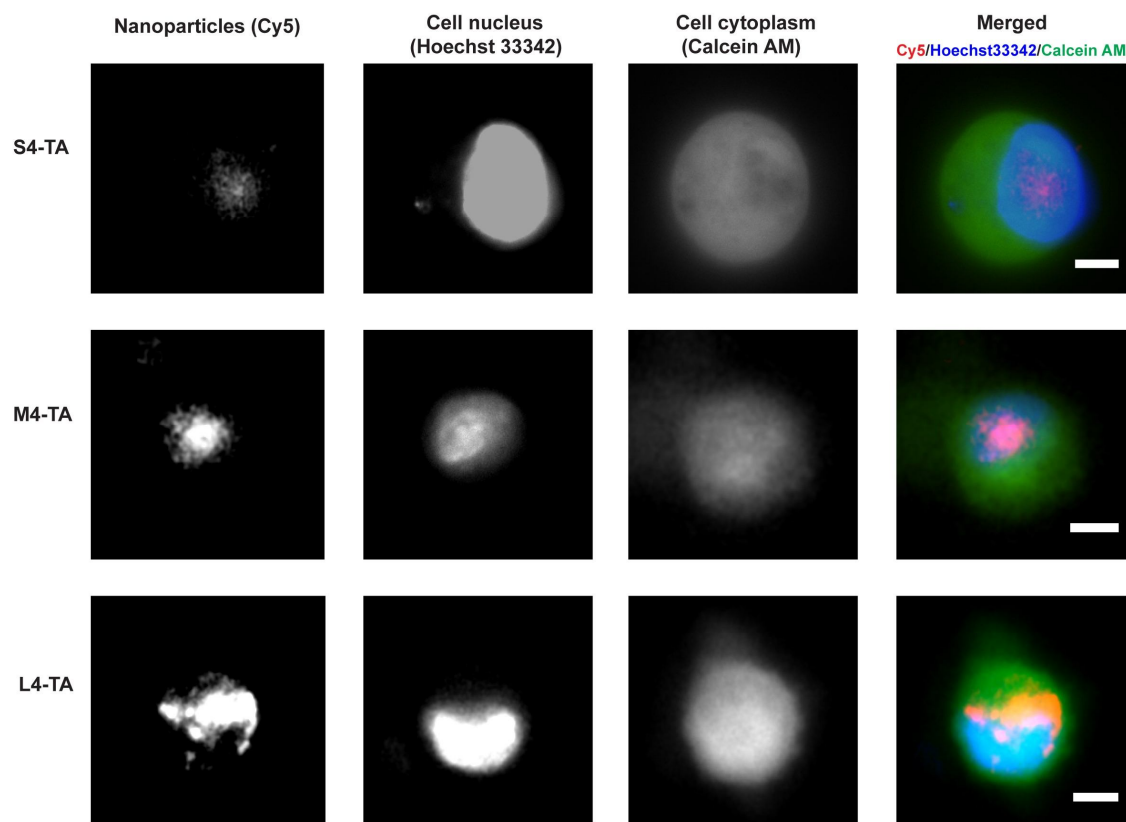


Figure S13. Images of tertiary amine-functionalized particles with three different sizes internalized into HUVECs under flow conditions. The cells were harvested from the vascular network, mounted onto coverslips, and imaged using a Nikon A1R confocal microscope. Scale bars = 5 μm .

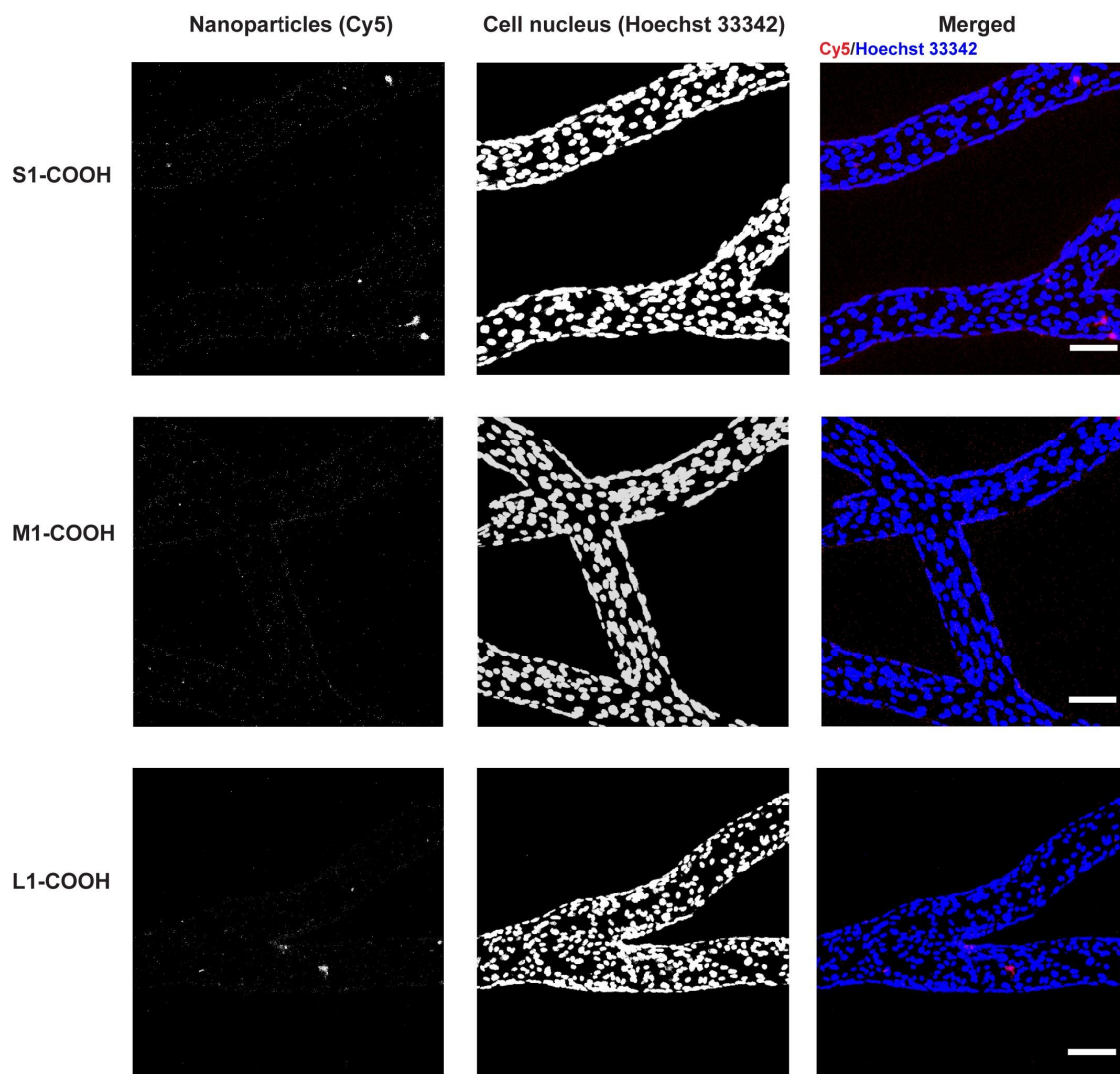


Figure S14. Images of carboxylic acid-functionalized particles with three different sizes associated with HUVECs in the synthetic vascular network. Scale bars = 100 μm .

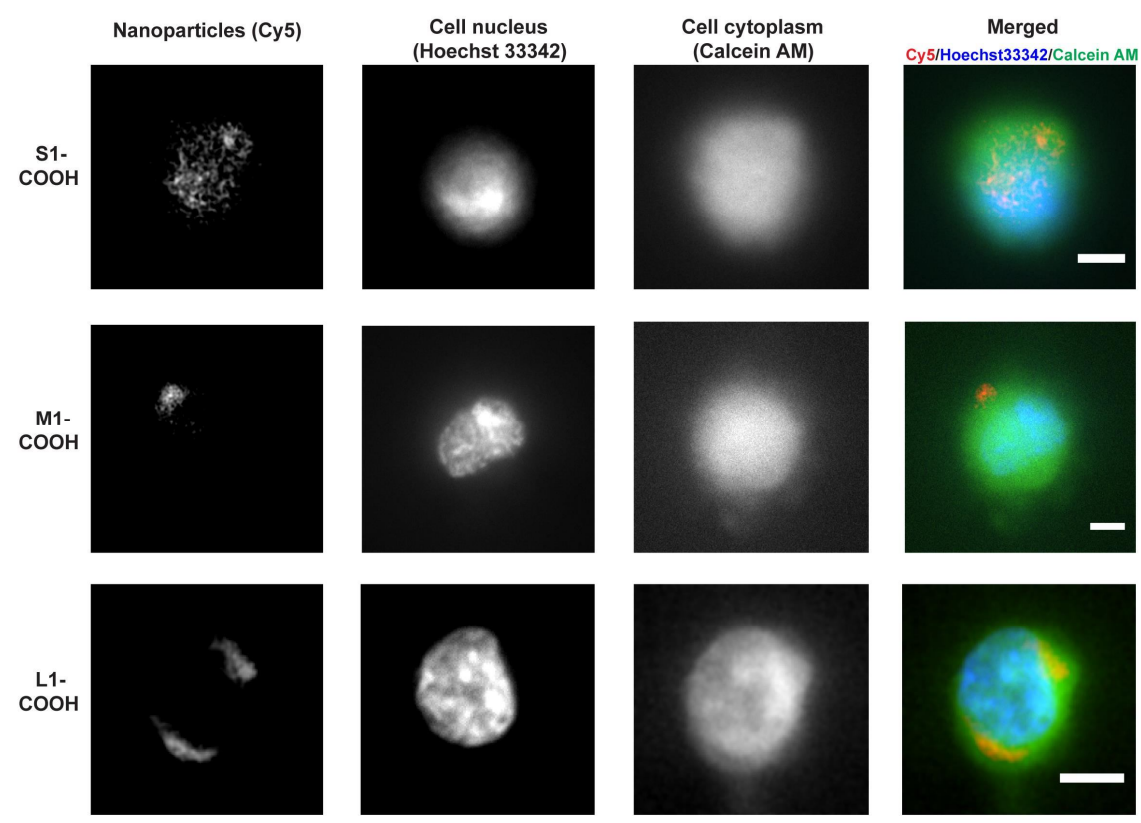


Figure S15. Images of carboxylic acid-functionalized particles with three different sizes internalized into HUVECs under flow conditions. The cells were harvested from the vascular network, mounted onto coverslips, and imaged using a Nikon A1R confocal microscope. Scale bars 5 μm .

**Chapter 3: Nanoparticle Size and Surface Chemistry Dictates the
Abundance of Linear Fibrinogen Proteins in the Protein Corona
When Exposed to Human Plasma**

1. Introduction

Due to the diversity of their physicochemical properties, polymeric nanomaterials have the potential to improve conventional treatment and diagnosis of human diseases; specifically in applications such as drug delivery, imaging, and vaccines (1). However, along with the increased multiplicity of physicochemical properties, there is a myriad of biological interactions that occur following the exposure of such nanomaterials to complex biological milieu such as blood. Understanding the relationship between a nanomaterial's physicochemical properties and their biological interactions is critical in producing the desired physiological effect thereafter intravenous administration to the body.

Following introduction into a biological fluid (e.g. intravenous administration of nanomaterials), a nanomaterial is rapidly rendered by proteins, lipids, and saccharides to form a "corona" (2, 3). The formation of proteins on a nanomaterial's surface is largely driven by hydrogen bonding, van der Waals forces, electrostatic and hydrophobic interactions (4). Typically, a "soft" corona is formed from proteins of high abundance, followed by displacement by proteins of high affinity according to the Vroman effect (5). The protein corona has been shown to decrease the surface energy of the nanomaterial while increasing their solubility and biocompatibility (4, 6). Yet, it has been recognized that protein corona formation on nanomaterials also promotes undesired outcomes. For example, protein corona formation may trigger biological events that lead to protein misfolding and aggregation at the surface. As a result of this protein conformational change, an immune response may be produced by the host to eliminate the circulating nanomaterial. Furthermore, protein corona formation may conceal the desired chemical or biological features of the engineered nanomaterial. Critically, the aforementioned biological interactions directly impact the clinical efficacy of nanomaterials, thus impacting their overall translational value. Therefore, investigating and understanding the protein corona of nanoparticles, especially *in vivo*, has

become one of the major foci of nanomedicine research as it defines the biological identity of the circulating nanomaterial and ultimately determines their biological fate (7).

To date, the relationship between a nanomaterial's physicochemical properties and their protein coronae has been extensively investigated (8-10). More recently, there has been particular interest in the interplay of two or more nanoparticle physicochemical properties on their protein coronae. Typically, such studies involve the synthesis of nanomaterials with well-defined physicochemical properties (such as size, surface chemistry, and morphology), followed by incubation of said nanomaterials in a serum or other biological fluid, and then proteomic quantification. For example, Parak and colleagues synthesized 5 nm gold nanoparticles with several surface modifications that systematically altered the colloidal stability of the nanoparticles (11). The gold nanoparticles were incubated with murine serum or bronchoalveolar lavage fluid, the proteins on each type of nanoparticle was isolated and then analyzed by liquid chromatography-tandem mass spectrometry (LC-MS)/MS. This study revealed that nanoparticle surface modification correlated with protein corona composition. Furthermore, discrepancies in the protein corona size and composition were found dependent on the biological media and duration of exposure. Another such study was conducted by Walkey *et al.* wherein characterizations of the protein corona of 105 surface-modified gold nanoparticles were carried out (12). The bioinformatics-style approach employed by Walkey *et al.* showed that hyaluronan-binding proteins acted as mediators for nanoparticle cellular interactions. Using label-free LC-MS/MS, Walkey *et al.* also showed that differences in the nanoparticle size and poly(ethylene glycol) grafting density affected the adsorption of proteins in human serum, which correlated with nanoparticle uptake by a macrophage cell line (13).

Herein, the objective of this thesis chapter is to characterize the protein corona of a library of polystyrene nanoparticles with varying sizes and surface chemistries in human serum. A total of 12 types of polystyrene nanoparticles (three sizes; 40 nm, 70 nm, 130 nm × 4 surface

chemistries; carboxylate, methyl-ester, poly(ethylene glycol), tertiary-amine) was produced from a previously published synthetic protocol (14). Specifically, a library of well-defined and biocompatible polystyrene nanoparticles (three sizes × four surface chemistries) were synthesized via polymerization-induced self-assembly (PISA) under reversible addition-fragmentation chain transfer (RAFT) aqueous emulsion polymerization conditions. The choice of such surface chemistries was made to represent some of the common chemical groups found on nanoparticles in nanomedicinal applications. Furthermore, the size of each was tuned to produce 3 distinct sizes. Subsequently, the proteins forming the protein corona on the nanoparticles after exposure to human plasma were isolated and analyzed with LC-MS/MS via a previously established label-free quantification protocol (15, 16). The results demonstrated that the nanoparticles i) possessed similar number of proteins and proportion of proteins in the corona, ii) serotransferrin and immunoglobulin heavy constant gamma 1 are enriched in the corona of all nanoparticles, and iii) only the TA-terminated nanoparticles show size-dependent association with fibrinogen proteins and alpha-2-macroglobulins.

2. Materials and methods

2.1 Materials

A library of well-defined polystyrene nanoparticles were made using a previously established protocol (14). Briefly, the carboxylic acid (COOH) group of a 4-cyano-4-(ethylthiocarbonothioylthio) pentanoic acid (ECT) was modified with methanol, dimethylamino-1-propanol, and poly(ethylene glycol) methyl ether (PEG) to produce chain transfer agents (CTAs) with R groups bearing the desired functional groups (methyl ester (Me), tertiary amine ester (TA), and PEG (with a methoxy group as the terminus). All 4 CTAs (COOH, Me, TA, and PEG) were employed in a series of reversible addition fragmentation chain transfer (RAFT) solution polymerization of poly(ethylene glycol) methyl ether acrylate

(PEGA) and *N*-hydroxyethyl acrylamide (HEAA) with 4,4'-azobis(4-cyanopentanoic acid) (ACPA) as the radical initiator. Furthermore, by conducting the polymerizations under similar conditions, 4 macro-CTAs with different end groups of similar PEGA and HEAA composition and molecular weights were obtained. These 4 macro-CTAs were then used for a series of RAFT aqueous emulsion polymerizations of styrene with ACPA as the radical initiator. Unlike our prior study (14), wherein Cyanine5 maleimide (Cy5-maleimide) was added during each RAFT aqueous emulsion polymerization process, the polymerizations carried out in this study were allowed to proceed without addition of Cy5-maleimide. A label-free quantification protocol was employed in this study, eliminating any potential interference from the fluorophores. Nonetheless, a library of well-defined polystyrene nanoparticles was obtained (Table 1).

2.2 Dynamic light scattering and zeta potential

A Malvern Zetasizer Nano Series operating a 4 mW He-Ne laser at 633 nm was used to perform dynamic light scattering (DLS) measurements on the nanoparticles. All measurements were performed at an incident angle of 173° for the light source. For polystyrene nanoparticles, the sample refractive index (RI) was set at 1.59. The dispersant viscosity and RI were fixed at 0.89 Ns m^{-2} and 1.33, respectively.

2.3 Collection and processing of human plasma

Blood was collected from 4 healthy human donors after obtaining informed consent in agreement with the University of Melbourne Human ethics approval No. 1443420 and the Australian National Health and Medical Research Council Statement on Ethical Conduct in Human Research. The blood from each donor was collected by venipuncture into Vacuette (Greiner Bio-One) collection tubes that contained sodium heparin and inverted 5 times.

Centrifugation of the blood samples at 950g, 12 min and low brake was carried out to obtain the plasma, and the resulting plasma was gathered and stored at -20 °C until use.

2.4 Protein corona formation and isolation

All 12 nanoparticles were made up in 0.01 M phosphate-buffered saline (PBS) solution to a concentration of 1 mg/mL and then mixed with human plasma to make a final concentration of 0.1 mg/mL in a 1 mL suspension. The nanoparticle/plasma mixtures were incubated on a shaker with the temperature set at 37 °C for 16 h. Following incubation, the nanoparticle/plasma mixtures were placed onto a 0.7 M sucrose cushion solution and then mixed well. The samples were centrifuged at 16 300 g for 30 min at ambient temperature to isolate the nanoparticle-protein “hard” corona from the remaining plasma. After centrifugation, the supernatant was removed, and the nanoparticle-protein pellets were washed three times with 0.01 M PBS. After the washes, 5% β-mercaptoethanol (Sigma-Aldrich; 50 μL) in 4× reducing loading dye was added to each sample, and the mixture incubated at 95 °C for 5 min. The samples were centrifuged for 3 min at 21 100 g and 4 °C, and the supernatant (20 μL) of each sample was resolved with a pre-cast 1D PAGE gel (Mini-PROTEAN TGX, Bio-Rad Laboratories). The gel was run in a reducing buffer mix, made to 1× from a 10× premixed electrophoresis buffer (25 mM Tris, 192 mM glycine, 0.1% SDS, pH 8.3, BioRad), at 200 V/0.04 A/8 W for 5 min. The protein gel was incubated in Instant Blue stain (Expedion Ltd) for 30 min on a shaker in order to fix and visualize the protein bands. The Instant Blue stain solution was discarded and replaced with Mili-Q water to destain the gel for 1 h (with fresh Mili-Q water every 20 min).

2.5 In-gel proteolytic digestion, plasma control sample preparation, LC-MS/MS analysis and label-free quantification

The whole region of the gel containing the resolved proteins was removed and subjected to an in-gel trypsin digestion procedure as described previously (15). Accordingly, the peptides were extracted, dried extensively in a Speed-Vac, and stored at -20 °C until use. For LC-MS/MS analysis, each sample was reconstituted in 20 µL of 2% acetonitrile (CAN), 0.1% formic acid and then LC-MS/MS data acquisition was carried out using nano-LC coupled to a Q-Exactive Hybrid Quadrupole-Orbitrap Mass Spectrometer (ThermoFisher) as previously described (17). For label-free proteomics analysis, the LC gradient was set to 65 min using a gradient that reached 25% CAN after 20 min, then 35% after 35 min, 45% after 49 min, 50% after 51 min, and finally 90% after 57 min. MaxQuant software (v1.6.0.1) was used to identify peptide sequences and protein identity by matching the human protein database (*Homo sapiens* annotated proteins downloaded from Uniprot) concatenated with reversed copies of all sequences and further supplemented with frequently observed contaminants (e.g. human keratin and porcine trypsin). Finally, label-free quantification of identified proteins was performed as previously described (15).

2.6 Method of protein hit filtering and significance

Each experiment was conducted in quadruplicate to assess reproducibility. Proteins that were detected in at least three out of the four replicates with an LFQ intensity > 0 were included for further analyses (Tables 2-4; Figure 2). The LFQ intensity was used to approximate the relative protein abundance between different types of polystyrene nanoparticles and intensity was used to represent the protein abundance for each type of polystyrene nanoparticle (Figure 3). A student's *t* test was carried out to evaluate the significance of differences observed across the nanoparticles, with *p* values of 0.05 or less considered significant.

3. Results and Discussion

To simultaneously test the effects of nanoparticle size and surface chemistry on the protein corona of nanoparticles, a published protocol for label-free quantitative LC-MS/MS proteomics was employed (15) and modified for use with these polystyrene cored nanoparticles. The nanoparticles used in this study were synthesized from PISA formulation, based on a published protocol (14).

3.1 Synthesis of PISA Nanoparticles with Various Surface Chemistries and Sizes

Compared with conventional self-assembly techniques, PISA is a powerful technique for the synthesis of polymeric nanomaterials with desired physicochemical properties (18-20). The synthesis of PISA nanoparticles with tunable size, surface chemistry, and shape have been demonstrated by prior studies (21-23). Significantly, PISA formulations carried out under RAFT emulsion polymerization conditions are considered to be environmentally and industrially-friendly due to the reproducible and facile production of concentrated nanoparticle suspensions in water (24, 25). A previous work (found in Chapter 2) detailed the development of a RAFT aqueous emulsion polymerization technique that could be used to produce well-defined polystyrene nanoparticles with tunable size, and surface chemistry (14). Here, we employed a similar protocol to produce a library of polystyrene nanoparticles with COOH, Me, TA, and PEG surface chemistries, and predetermined diameters, to investigate the effects of size and surface chemistry on the protein corona of nanoparticles incubated in human serum. Firstly, the 4 macro-CTAs bearing COOH, Me, TA, and PEG surface chemistries from Chapter 2 were used for a series of RAFT aqueous emulsion polymerizations of styrene. Similar to the reaction conditions outlined in Chapter 2, a low ratio of ACPA to macro-CTA was kept because it provided facile access to well-defined spherical nanoparticles. Furthermore, similar feed ratios of styrene to macro-CTAs were used to target similar nanoparticle diameters to those

found in the prior study (Chapter 2) (14). It should be noted that no Cy5 maleimide was added to the emulsion polymerization for this study. From the TEM and DLS data in Table 1, it was observed that the diameters of nanoparticles synthesized for this study were similar to those found in the prior study in Chapter 2. The similarity in diameter between the Cy5 and non-Cy5 polystyrene nanoparticles demonstrate the reproducibility of the PISA formulations. Interestingly, the nanoparticles synthesized herein appeared to exhibit a more narrow size distribution (PSD < 0.100; Table 1) in comparison with the Cy5 nanoparticles in Chapter 2 (PSD from 0.015 to 0.250). The addition of Cy5 maleimide to the emulsion polymerization in Chapter 2 resulted in an increase in the particle size distribution. Nonetheless, the nanoparticles synthesized across both studies were well-defined in terms of particle size distribution.

3.2 Summary of the human protein coronae

Based on the methodology for protein hit filtering (detailed in the respective section 2.6), a total of 183, 186, and 189 proteins were positively identified (i.e. present in at least two or more replicates) for polystyrene nanoparticles in the small (~40 nm), medium (~70 nm), and large (~130 nm) size range, respectively. Figure 1 shows Venn diagrams for all 12 nanoparticles tested (segmented by their size range). Overall, the 12 nanoparticles in each of their respective size ranges shared a significant proportion of the proteins identified; 78% for small nanoparticles, 77% for medium nanoparticles, and 76% for large nanoparticles. For each size range, only a relatively small proportion of proteins were unique to each surface chemistry (Figure 1). For example, out of the 183 proteins identified, only 8, 3, 2, and 3 proteins were uniquely associated with COOH, PEG, TA, and Me-terminated nanoparticles respectively.

The top ten abundant proteins found associated with the nanoparticles, as well as those found in the plasma control are listed in Table 2, Table 3, and Table 4. Within each size range, tested, there is a diversity of 14 proteins found within the list of top ten abundant proteins associated with each nanoparticle. Furthermore, of the top ten abundant proteins in the plasma

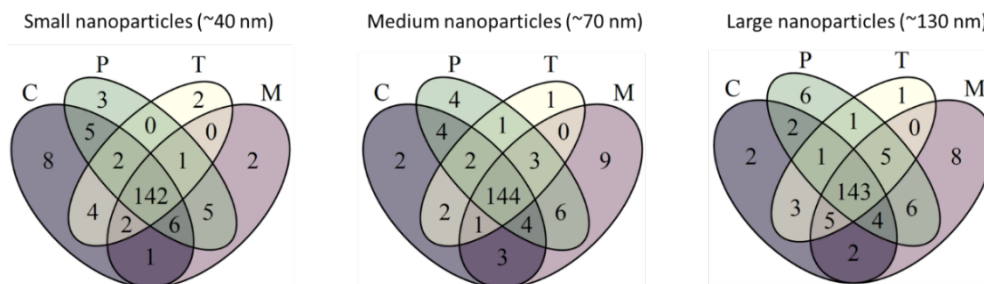


Figure 1. Venn diagrams showing the distribution of proteins associated with nanoparticles after incubation with human plasma.

control sample, only two proteins were absent in the list of top ten abundant proteins associated with each nanoparticle. Interestingly, while human serum albumin ranks as the most abundant protein in human plasma, it is not found within the lists of the top ten abundant proteins associated with the nanoparticles tested herein. With regards to other studies on protein corona, human serum albumin is commonly found on the surface of nanoparticles incubated in plasma. For instance, Tenzer *et al.* incubated silica and polystyrene nanoparticles in human plasma and obtained quantitative time-resolved profiles of human plasma coronas (26). Indeed, Tenzer *et al.*'s work showed that serum albumin ranked as the most abundant protein associated with negatively and positively charged polystyrene nanoparticles after 0.5 min of plasma exposure. However, the data in Tenzer *et al.*'s also showed that while human serum albumin (gene name: ALBU) was increased in abundance up to 5 min of plasma exposure, the normalized abundance of human serum albumin decreased with prolonged plasma exposure up to the measured time period of 120 min. Furthermore, several studies have found that the protein corona of a nanoparticle changes its composition over time (27-29). In fact, Dell'Orco *et al.* demonstrated that shortly after introduction into the blood, a nanoparticle will be rapidly rendered by serum albumin (28). Over time, the serum albumin will be replaced by less abundant proteins that

possess a higher association rate constant and lower dissociation rate constant (30). In this study, the nanoparticles were incubated in human plasma for a period of 16 h. Based on observations (28, 30) that show the substitution of serum albumin with other proteins over time, it is plausible that an amount of serum albumin that formed initially was replaced by other proteins (listed in Tables 2-4) over the 16 h that the nanoparticles in this study were incubated.

Table 1 TEM and DLS data for RAFT aqueous emulsion polymerization of styrene with P(HEAA-*co*-PEGA) macro-CTAs bearing COOH, Me, PEG, and TA R groups, at 80 °C for 6 h using ACPA as the radical initiator.

Surface chemistry	Polymer code	TEM ^a		DLS ^b	
		D _{TEM} (nm)	D _h (nm)	PSD	ζ (mV)
COOH	csd	38±12	38±8	0.097	-16±1.2
	cmd	72±4	77±4	0.062	-14±0.8
	clد	138±11	145±6	0.055	-11±0.9
Me	msd	35±10	40±7	0.052	-1.0±0.2
	mmd	73±3	75±4	0.027	-1.4±0.4
	mld	135±11	139±4	0.023	-1.1±0.3
PEG	psd	33±9	37±7	0.089	-10±1.1
	pmd	72±7	74±4	0.065	-11±0.7
	plد	140±11	144±5	0.042	-11±0.8
TA	tsd	35±9	37±5	0.068	-5±0.3
	tmd	75±8	78±4	0.043	-4±0.5
	tld	136±8	140±12	0.041	-5±0.2

^a D_{TEM} was calculated by ImageJ. ^b Dynamic light scattering measurements were performed at 25 °C with the reported values averaged over 5 consecutive measurements.

Table 2. Top ten most abundant proteins associated with small nanoparticles with COOH, PEG, TA, and Me surface chemistries incubated in human plasma

No.	CSD	PSD	TSD	MSD	Plasma
1	Ig heavy constant gamma 1	Alpha 2 macroglobulin	Fibrinogen beta chain	Serotransferrin	Serum albumin
2	Fibrinogen beta chain	Ig heavy constant gamma 1	Fibrinogen gamma chain	Ig heavy constant gamma 1	Ig heavy constant gamma 1
3	Serotransferrin	Serotransferrin	Fibrinogen alpha chain	Alpha 2 macroglobulin	Fibrinogen beta chain
4	Complement C3	Fibrinogen beta chain	Ig heavy constant gamma 1	Fibrinogen beta chain	Complement C3
5	Apolipoprotein B	Complement C3	Serotransferrin	Complement C3	Serotransferrin
6	Fibrinogen gamma chain	Apolipoprotein B	Alpha 2 macroglobulin	Fibrinogen alpha chain	Apolipoprotein A1
7	Fibrinogen alpha chain	Fibrinogen gamma chain	Complement C3	Fibrinogen gamma chain	Alpha-1-antitrypsin
8	Alpha 2 macroglobulin	Fibrinogen alpha chain	Apolipoprotein B	Apolipoprotein B	Fibrinogen alpha chain
9	Ig heavy constant gamma 2	Haptoglobin	Fibronectin 1	Apolipoprotein A1	Haptoglobin
10	Haptoglobin	Ig heavy constant gamma 2	Immunoglobulin Kappa Constant	Immunoglobulin Kappa Constant	Alpha-2-macroglobulin

Table 3. Top ten most abundant proteins associated with medium nanoparticles with COOH, PEG, TA, and Me surface chemistries incubated in human plasma

No.	CMD	PMD	TMD	MMD	Plasma
1	Ig heavy constant gamma 1	Ig heavy constant gamma 1	Ig heavy constant gamma 1	Alpha 2 macroglobulin	Serum albumin
2	Serotransferrin	Alpha 2 macroglobulin	Serotransferrin	Ig heavy constant gamma 1	Ig heavy constant gamma 1
3	Complement C3	Serotransferrin	Fibrinogen beta chain	Transferrin	Fibrinogen beta chain
4	Alpha 2 macroglobulin	Complement C3	Complement C3	Complement C3	Complement C3
5	Apolipoprotein B	Apolipoprotein B	Alpha 2 macroglobulin	Apolipoprotein B	Serotransferrin
6	Fibrinogen beta chain	Fibrinogen beta chain	Fibrinogen gamma chain	Fibrinogen beta chain	Apolipoprotein A1
7	Ig heavy constant gamma 2	Immunoglobulin Kappa Constant	Fibrinogen alpha chain	Immunoglobulin Kappa Constant	Alpha-1-antitrypsin
8	Immunoglobulin Kappa Constant	Fibrinogen gamma chain	Apolipoprotein B	Fibrinogen gamma chain	Fibrinogen alpha chain
9	Haptoglobin	Haptoglobin	Ig heavy constant gamma 2	Apolipoprotein A1	Haptoglobin
10	Fibrinogen gamma chain	Fibrinogen alpha chain	Serpin family A member 1	Haptoglobin	Alpha-2-macroglobulin

Table 4. Top ten most abundant proteins associated with large nanoparticles with COOH, PEG, TA, and Me surface chemistries incubated in human plasma

No.	CLD	PLD	TLD	MLD	Plasma
1	Ig heavy constant gamma 1	Ig heavy constant gamma 1	Ig heavy constant gamma 1	Serotransferrin	Serum albumin
2	Apolipoprotein B	Serotransferrin	Serotransferrin	Ig heavy constant gamma 1	Ig heavy constant gamma 1
3	Complement C3	Alpha 2 macroglobulin	Alpha 2 macroglobulin	Alpha 2 macroglobulin	Fibrinogen beta chain
4	Fibrinogen beta chain	Complement C3	Apolipoprotein B	Complement C3	Complement C3
5	Serotransferrin	Fibrinogen beta chain	Complement C3	Apolipoprotein B	Serotransferrin
6	Alpha 2 macroglobulin	Apolipoprotein B	Fibrinogen beta chain	Fibrinogen beta chain	Apolipoprotein A1
7	Fibrinogen gamma chain	Fibrinogen gamma chain	Immunoglobulin Kappa Constant	Fibrinogen gamma chain	Alpha-1-antitrypsin
8	Fibrinogen alpha chain	Fibrinogen alpha chain	Fibrinogen gamma chain	Immunoglobulin Kappa Constant	Fibrinogen alpha chain
9	Haptoglobin	Immunoglobulin Kappa Constant	Haptoglobin	Fibrinogen alpha chain	Haptoglobin
10	Ig heavy constant gamma 2	Haptoglobin	Apolipoprotein A1	Apolipoprotein A1	Alpha-2-macroglobulin

Furthermore, nanoparticles that comprise of PEG species of various molecular weights and conformations repulse globular proteins such as serum albumin (31, 32). Thus, it is plausible that the PEGylated composition of the polystyrene nanoparticles used in this study could be more resistant to human serum albumin adsorption, indicating their potential for drug delivery and targeting.

To gain a holistic perspective on the protein-binding profile of each nanoparticle, the proteins were grouped according to their abundance (LFQ % threshold) beginning from 0.01% up to 1.00% of total LFQ against the number of proteins within each threshold (Figure 2a) and proportion out of total proteins (Figure 2b). From Figures 2a&2b, it is observed that all 12 nanoparticles shared a similar count of proteins that were present at least 0.01%, 0.05%, 0.10%, 0.20%, 0.30%, 0.40%, 0.50%, and 1.00% of the LFQ threshold. Figure 2a illustrates that only a small fraction (10 to 12 proteins) found at least 1.00% of the LFQ threshold for all nanoparticles. Figure 2b illustrates that proteins that make up 0.01% to 0.05% of LFQ threshold represent up to 28% of all proteins whereas higher abundance proteins that make up at least 1.00% of LFQ threshold only represent 3% of the proteins on the protein corona of all nanoparticles. In short, this data revealed the similarity in protein-binding profile between polystyrene cored nanoparticles of various sizes and surface chemistries after 24 h of incubation in human plasma. This similarity in protein-binding profile between polystyrene nanoparticles of various sizes and surface chemistries stands in contrast to other studies that have revealed the protein-binding profile of other nanoparticles. For example, Zhang *et al.* reported the plasma-binding profiles of polystyrene cored nanoparticles that were incubated in human plasma and found that distinctive protein-binding profiles existed based on the incubation time, size, and surface chemistry of the nanoparticles (33). Furthermore, two studies by Tenzer *et al.* also reported that distinctive protein-binding profiles were achieved between nanoparticles with various surface chemistries (26, 34). Upon inspection of the aforementioned

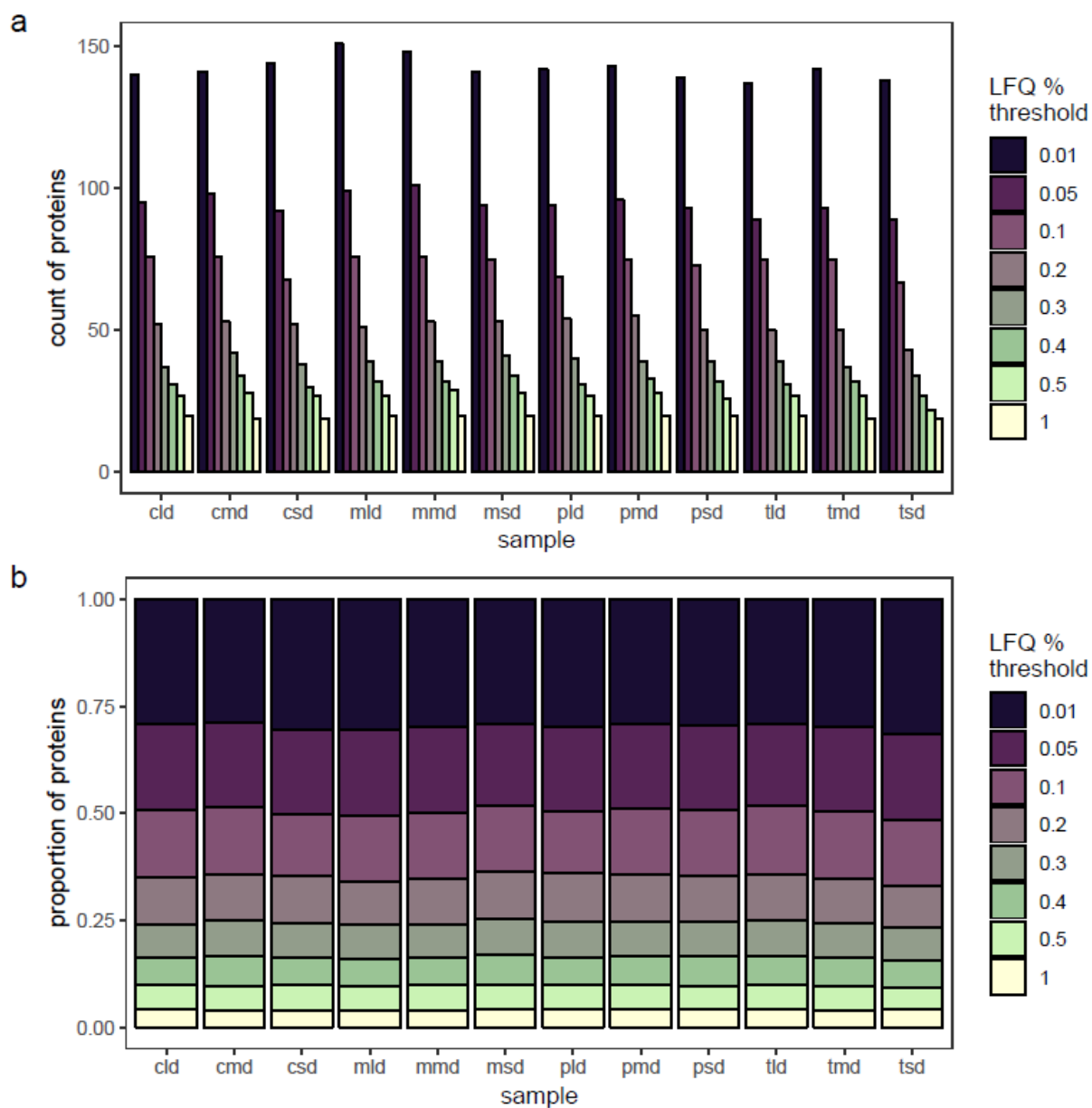


Figure 2. (A) Count of proteins found at 0.01%, 0.05%, 0.1%, 0.2%, 0.3%, 0.4%, 0.5%, and 1.0% of LFMQ threshold found in the protein corona of nanoparticles of various sizes and surface chemistries. (B) Proportion of proteins found at 0.01%, 0.05%, 0.1%, 0.2%, 0.3%, 0.4%, 0.5%, and 1.0% of LFMQ threshold found in the protein corona of nanoparticles of various sizes and surface chemistries.

studies, it was noted that the incubation times (up to 2 h) were substantially shorter than the incubation time of 16 h used in this study. Moreover, previous studies have shown that the protein corona dynamically changes in composition over time due to continuous protein association and dissociation events controlled predominantly by the Vroman effect (26, 29, 33, 34). Therefore, it can be said that a plasma exposure time of at least 16 h resulted in the formation of similar plasma-binding profiles for polystyrene cored nanoparticles regardless of size and surface chemistry.

3.3 Serotransferrin and immunoglobulin proteins are highly enriched in the protein corona

Figure 3a depicts the most abundant proteins identified in the hard corona of the nanoparticles. Proteins such as serotransferrin (TF), immunoglobulin heavy constant gamma 1 (IGHG1), alpha-2-macroglobulin (A2M), fibrinogen alpha chain (FGA), fibrinogen beta chain (FGB), and fibrinogen gamma chain proteins (FGG) represent the most enriched proteins found on the nanoparticles; an observation consistent with the appearance of such proteins within the lists of abundant proteins in Tables 2-4. TF is commonly found enriched in the protein corona of nanoparticles (26, 35-37). As an iron carrier, TF plays a critical role in maintaining iron homeostasis in the body (38). Furthermore, TF is internalized by a specific interaction with its cognate receptor on the cell membrane (39) and has been explored as a potential target for therapeutic agents (40-42). A study carried out by Salvati *et al.* found that the adsorption of proteins on a transferrin-functionalized nanoparticle surface in a biological environment resulted in a loss of specificity in targeting (41). Thus, instead of pre-functionalizing the nanoparticle with TF, the enrichment of proteins such as TF in the protein corona of the polystyrene nanoparticles of various sizes and surface chemistries could enhance their uptake by its cognate receptors. However, it is not explicitly clear i) which nanoparticle parameters were responsible for the enrichment of TF in the nanoparticles herein and ii) the spatial location

of the TF in the protein corona. As such, further experiments need to be carried out to reliably apply such nanoparticles for TF receptor targeting applications.

Similarly, IGHG1 is commonly found to be abundant in the protein corona of nanoparticles (43-46). The binding of immunoglobulins to complement receptors on specific types of immune cells (particularly macrophages) has been known to trigger particle phagocytosis (47-49). However, while it is reasonable to expect that nanoparticles with a high content of immunoglobulins in their corona will be subjected to a higher degree of non-specific immune cell association and subsequent clearance, there is evidence in the literature that suggests that other proteins found in the corona of nanoparticles have a larger role to play with respect to phagocytotic clearance. For example, the work by Saha *et al.* studied the proteome association of gold nanoparticles in human serum and found that immunoglobulins and apolipoproteins were the major proteins found in the coronae of all gold nanoparticles (43). Saha *et al.* presented statistical evidence that coronal proteins with functions relating to the complement, lipoprotein, and coagulation pathways possessed a highly positive correlation with macrophage uptake. Conversely, the presence of immunoglobulins in the corona mostly resulted in a negative correlation with macrophage uptake (43). While immunoglobulins were abundant in the corona, significant competition and reorganization of protein moieties of lower abundance (e.g., complement factors and coagulation) in the corona eventually led to macrophage recognition. Thus, the mere abundance of IGHG1 in the protein corona of the nanoparticles here does translate to high non-specific clearance *in vivo*.

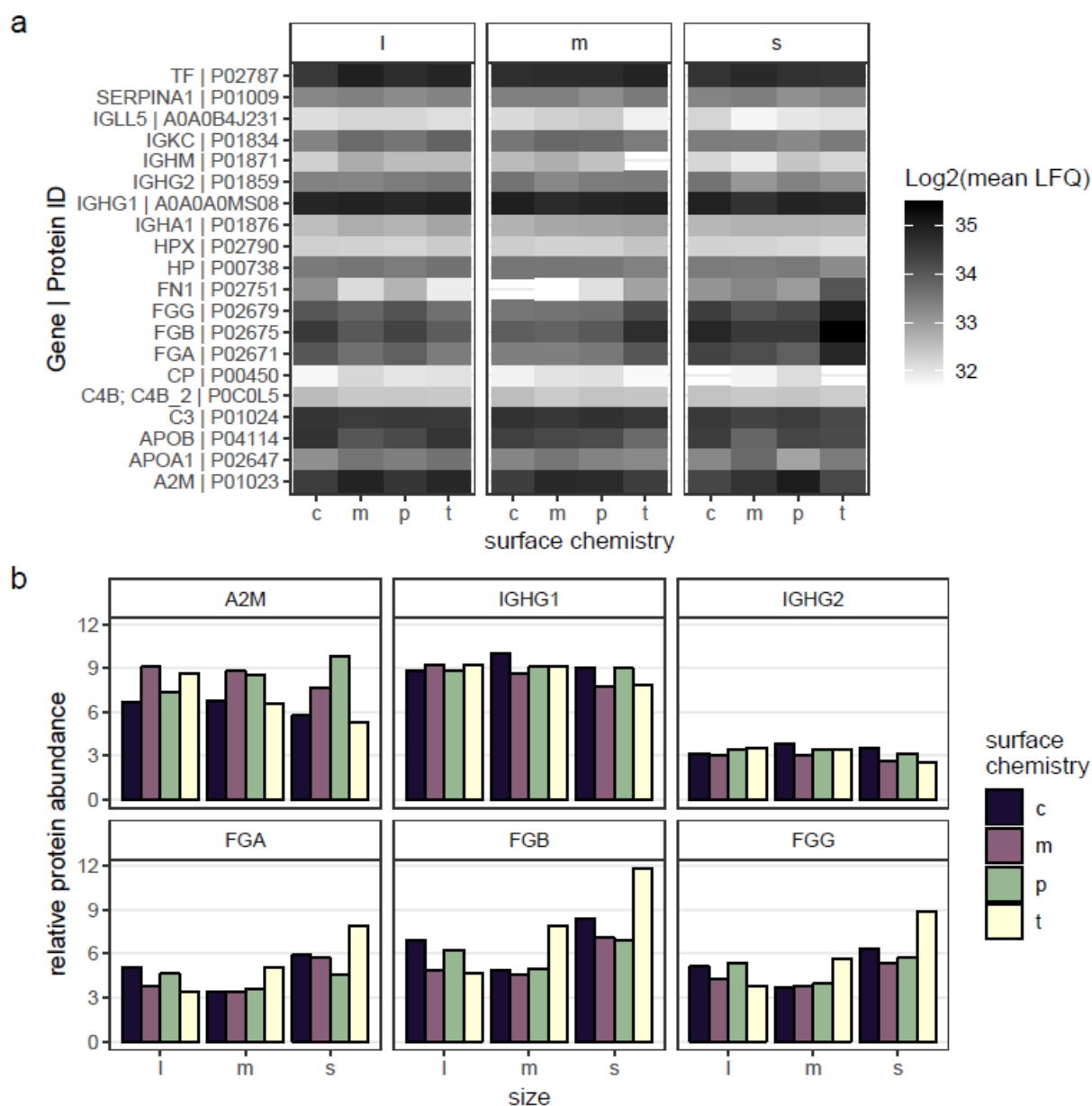


Figure 3. (A) Heat map of the most abundant proteins in the protein corona of polystyrene nanoparticles synthesized via PISA bearing 4 different surface chemistries (c = COOH, m = Me, p = PEG, t = TA) with 3 sizes of each surface chemistry (s = ~40 nm, m = ~70 nm, and l = ~130 nm). Proteins that constituted at least 1% of the protein corona are displayed. (B) Relative protein abundance of alpha-2-macroglobulin (A2M), Ig heavy constant gamma 1 (IGHG1), Ig heavy constant gamma 2 (IGHG2), fibrinogen alpha chain (FGA), fibrinogen (FGB), and fibrinogen gamma chain (FGG) in the protein corona of polystyrene nanoparticles synthesized via PISA bearing 4 different surface chemistries (c = COOH, m = Me, p = PEG, t = TA) with 3 sizes of each surface chemistry (s = ~40 nm, m = ~70 nm, and l = ~130 nm).

3.4 Nanoparticle surface chemistry and size dictate fibrinogen association

Although TF and IGHG1 were found to be highly enriched among other proteins (Figure 3a), the enrichment levels between nanoparticles were similar. From the protein abundance heat map in Figure 3a, there appeared to be a size- and surface chemistry-dependent effect for nanoparticle association with fibrinogen (fibrinogen alpha chain (FGA), fibrinogen beta chain (FGB), and fibrinogen gamma chain (FGG)). Fibrinogen plays a major role in the formation of blood clots, which in turn are formed through the polymerization of thrombin-truncated fibrinogen molecules termed fibrins (30). The structure of fibrinogen has been described as an elongated and sigmoidal structure, consisting of pairs of α , β , and γ chains that contain 562, 461, and 411 amino acid residues respectively (50, 51). A seminal study conducted by the Minchin group found that anionic gold nanoparticles bound and induced unfolding of fibrinogen, leading to a biological cascade that resulted in the release of inflammatory cytokines (52). Curiously, the study also found that not all nanoparticles that bound fibrinogen demonstrated this effect. In fact, when completely bound to fibrinogen, the 20 nm gold nanoparticles did not induce cytokine release whereas the 5 nm gold nanoparticle promoted an inflammatory response when bound to fibrinogen (52). To facilitate comparisons of intercorona abundance, the relative protein abundance value (RPA) of each type of the proteins identified in Figure 3a was derived based on the mean LFQ (Log₂ scale) of the protein. From Figure 3b, it was observed that TA-terminated nanoparticle association with FGG, FGB, and FGA displayed a size-dependent effect. In particular, FGG, FGB, and FGA association increased as TA-terminated nanoparticle size increased. COOH-, Me-, and PEG-terminated nanoparticles did not display a similar size-dependent effect for association with FGG, FGB, and FGA proteins. Interestingly, examination of the RPA values for association of TA-terminated nanoparticles with alpha-2-macroglobulin (A2M) revealed that there was an inverse relationship between nanoparticle size and A2M association. That is, as TA nanoparticle size

increased, nanoparticle association with A2M decreased relative to other abundant proteins in the corona. Initially, it was postulated that this contrast in protein association behavior could be linked to the protein morphology (e.g. the linear morphology of fibrinogen versus the globular morphology of A2M). Yet, TA-terminated nanoparticle association with globular proteins such as IGHG1 and IGHG2 did not display any appreciable size-dependent effect, much less an inverse size-dependent relationship. Several investigations have already showed that size plays a significant role in protein corona formation. Therefore, while it is still plausible that the globular morphology of A2M contributed to the inverse size-dependent relationship, it appears that other underlying factor/s relating to A2M were most likely responsible for the inverse size-dependent relationship observed herein.

4. Conclusion

In this thesis chapter, a quantitative and qualitative analysis of the protein corona of polystyrene nanoparticles synthesized via PISA was carried out. The protein corona was formed in a clinically relevant environment; human plasma from healthy donors. The primary objective of this study was to simultaneously examine the effects of nanoparticle size and surface chemistry on the protein corona composition. Firstly, well-defined polystyrene nanoparticles were formed via a previously established protocol (14). The nanoparticles possessed diameters and ζ -potentials that were similar to their Cy5-labelled counterparts in the previous study, demonstrating the repeatability of such PISA formulations. Then, the library of nanoparticles of 4 surface chemistries (COOH, Me, PEG, TA) with 3 sizes (~40 nm, ~70 nm, ~130 nm) of each surface chemistry was incubated in human plasma for 16 h, followed by in-gel proteolytic, LC-MS/MS analysis, and label-free quantification. In summary, the data enclosed in this chapter has revealed that the protein corona of nanoparticles incubated in human serum for 16 h i) possessed a substantially similar composition regardless of size or surface chemistry and ii) was enriched in TF and IGHG1 proteins. Finally, TA-terminated

nanoparticles displayed a size-dependent association with linear fibrinogen proteins and an inverse size-dependent association with the A2M protein. While the exact factor/s that contributed to the above observations require further examination, this study has characterized the protein coronae of representative polymeric nanoparticles with changing size and surface chemistry. The data presented herein is expected to guide the rational design of nanoparticles for biomedical applications.

5. References

1. Dai Q, Bertleff-Zieschang N, Braunger JA, Björnmalm M, Cortez-Jugo C, Caruso F. Particle targeting in complex biological media. *Advanced healthcare materials*. 2018;7(1):1700575.
2. Monopoli MP, Åberg C, Salvati A, Dawson KA. Biomolecular coronas provide the biological identity of nanosized materials. *Nature nanotechnology*. 2012;7(12):779.
3. Cedervall T, Lynch I, Lindman S, Berggård T, Thulin E, Nilsson H, et al. Understanding the nanoparticle–protein corona using methods to quantify exchange rates and affinities of proteins for nanoparticles. *Proceedings of the National Academy of Sciences*. 2007;104(7):2050-5.
4. Lynch I, Dawson KA. Protein-nanoparticle interactions. *Nano today*. 2008;3(1-2):40-7.
5. Vroman L. Effect of adsorbed proteins on the wettability of hydrophilic and hydrophobic solids. *Nature*. 1962;196(4853):476.
6. Ding F, Radic S, Chen R, Chen P, Geitner NK, Brown JM, et al. Direct observation of a single nanoparticle–ubiquitin corona formation. *Nanoscale*. 2013;5(19):9162-9.
7. Ke PC, Lin S, Parak WJ, Davis TP, Caruso F. A decade of the protein corona. *ACS nano*. 2017;11(12):11773-6.
8. Docter D, Westmeier D, Markiewicz M, Stolte S, Knauer S, Stauber R. The nanoparticle biomolecule corona: lessons learned–challenge accepted? *Chemical Society Reviews*. 2015;44(17):6094-121.
9. Van Hong Nguyen B-JL. Protein corona: a new approach for nanomedicine design. *International journal of nanomedicine*. 2017;12:3137.
10. Mahmoudi M. Debugging nano–bio interfaces: systematic strategies to accelerate clinical translation of nanotechnologies. *Trends in biotechnology*. 2018.

11. Johnston BD, Kreyling WG, Pfeiffer C, Schäffler M, Sarioglu H, Ristig S, et al. Colloidal Stability and Surface Chemistry Are Key Factors for the Composition of the Protein Corona of Inorganic Gold Nanoparticles. *Advanced Functional Materials*. 2017;27(42):1701956.
12. Walkey CD, Olsen JB, Song F, Liu R, Guo H, Olsen DWH, et al. Protein corona fingerprinting predicts the cellular interaction of gold and silver nanoparticles. *ACS nano*. 2014;8(3):2439-55.
13. Walkey CD, Olsen JB, Guo H, Emili A, Chan WC. Nanoparticle size and surface chemistry determine serum protein adsorption and macrophage uptake. *Journal of the American Chemical Society*. 2012;134(4):2139-47.
14. Khor SY, Vu MN, Pilkington EH, Johnston AP, Whittaker MR, Quinn JF, et al. Elucidating the Influences of Size, Surface Chemistry, and Dynamic Flow on Cellular Association of Nanoparticles Made by Polymerization-Induced Self-Assembly. *Small*. 2018;14(34):1801702.
15. Wang M, Siddiqui G, Gustafsson OJ, Käkinen A, Javed I, Voelcker NH, et al. Plasma Proteome Association and Catalytic Activity of Stealth Polymer-Grafted Iron Oxide Nanoparticles. *Small*. 2017;13(36):1701528.
16. Wang M, Gustafsson OJ, Siddiqui G, Javed I, Kelly HG, Blin T, et al. Human plasma proteome association and cytotoxicity of nano-graphene oxide grafted with stealth polyethylene glycol and poly (2-ethyl-2-oxazoline). *Nanoscale*. 2018.
17. Siddiqui G, Srivastava A, Russell AS, Creek DJ. Multi-omics based identification of specific biochemical changes associated with PfKelch13-mutant artemisinin-resistant *Plasmodium falciparum*. *The Journal of infectious diseases*. 2017;215(9):1435-44.

18. Warren NJ, Armes SP. Polymerization-induced self-assembly of block copolymer nano-objects via RAFT aqueous dispersion polymerization. *Journal of the American Chemical Society*. 2014;136(29):10174-85.
19. Charleux B, Delaittre G, Rieger J, D'Agosto F. Polymerization-induced self-assembly: from soluble macromolecules to block copolymer nano-objects in one step. *Macromolecules*. 2012;45(17):6753-65.
20. Khor SY, Quinn JF, Whittaker MR, Truong NP, Davis TP. Controlling Nanomaterial Size and Shape for Biomedical Applications via Polymerization-Induced Self-Assembly. *Macromolecular rapid communications*. 2018:1800438.
21. Li Y, Armes SP. RAFT synthesis of sterically stabilized methacrylic nanolatexes and vesicles by aqueous dispersion polymerization. *Angewandte Chemie International Edition*. 2010;49(24):4042-6.
22. Zhang W, D'Agosto F, Dugas P-Y, Rieger J, Charleux B. RAFT-mediated one-pot aqueous emulsion polymerization of methyl methacrylate in presence of poly (methacrylic acid-co-poly (ethylene oxide) methacrylate) trithiocarbonate macromolecular chain transfer agent. *Polymer*. 2013;54(8):2011-9.
23. Zhang W, D'Agosto F, Boyron O, Rieger J, Charleux B. Toward a better understanding of the parameters that lead to the formation of nonspherical polystyrene particles via RAFT-mediated one-pot aqueous emulsion polymerization. *Macromolecules*. 2012;45(10):4075-84.
24. Engelis NG, Anastasaki A, Nurumbetov G, Truong NP, Nikolaou V, Shegiwal A, et al. Sequence-controlled methacrylic multiblock copolymers via sulfur-free RAFT emulsion polymerization. *Nature chemistry*. 2017;9(2):171.
25. Truong NP, Quinn JF, Anastasaki A, Rolland M, Vu MN, Haddleton DM, et al. Surfactant-free RAFT emulsion polymerization using a novel biocompatible thermoresponsive polymer. *Polymer Chemistry*. 2017;8(8):1353-63.

26. Tenzer S, Docter D, Kuharev J, Musyanovych A, Fetz V, Hecht R, et al. Rapid formation of plasma protein corona critically affects nanoparticle pathophysiology. *Nature nanotechnology*. 2013;8(10):772.
27. Lundqvist M, Stigler J, Cedervall T, Berggård T, Flanagan MB, Lynch I, et al. The evolution of the protein corona around nanoparticles: a test study. *ACS nano*. 2011;5(9):7503-9.
28. Dell'Orco D, Lundqvist M, Oslakovic C, Cedervall T, Linse S. Modeling the time evolution of the nanoparticle-protein corona in a body fluid. *PloS one*. 2010;5(6):e10949.
29. Casals E, Pfaller T, Duschl A, Oostingh GJ, Puntès V. Time evolution of the nanoparticle protein corona. *ACS nano*. 2010;4(7):3623-32.
30. Pelaz B, del Pino P, Maffre P, Hartmann R, Gallego M, Rivera-Fernandez S, et al. Surface functionalization of nanoparticles with polyethylene glycol: effects on protein adsorption and cellular uptake. *ACS nano*. 2015;9(7):6996-7008.
31. Jin J, Han Y, Zhang C, Liu J, Jiang W, Yin J, et al. Effect of grafted PEG chain conformation on albumin and lysozyme adsorption: A combined study using QCM-D and DPI. *Colloids and Surfaces B: Biointerfaces*. 2015;136:838-44.
32. Ostuni E, Chapman RG, Holmlin RE, Takayama S, Whitesides GM. A survey of structure–property relationships of surfaces that resist the adsorption of protein. *Langmuir*. 2001;17(18):5605-20.
33. Zhang H, Burnum KE, Luna ML, Petritis BO, Kim JS, Qian WJ, et al. Quantitative proteomics analysis of adsorbed plasma proteins classifies nanoparticles with different surface properties and size. *Proteomics*. 2011;11(23):4569-77.
34. Tenzer S, Docter D, Rosfa S, Wlodarski A, Kuharev Jr, Rekić A, et al. Nanoparticle size is a critical physicochemical determinant of the human blood plasma corona: a comprehensive quantitative proteomic analysis. *ACS nano*. 2011;5(9):7155-67.

35. Sakulkhu U, Mahmoudi M, Maurizi L, Salaklang J, Hofmann H. Protein corona composition of superparamagnetic iron oxide nanoparticles with various physico-chemical properties and coatings. *Scientific reports*. 2014;4:5020.
36. Sempf K, Arrey T, Gelperina S, Schorge T, Meyer B, Karas M, et al. Adsorption of plasma proteins on uncoated PLGA nanoparticles. *European Journal of Pharmaceutics and Biopharmaceutics*. 2013;85(1):53-60.
37. Koshkina O, Westmeier D, Lang T, Bantz C, Hahlbrock A, Würth C, et al. Tuning the Surface of Nanoparticles: Impact of Poly (2-ethyl-2-oxazoline) on Protein Adsorption in Serum and Cellular Uptake. *Macromolecular bioscience*. 2016;16(9):1287-300.
38. Jiang X, Weise S, Hafner M, Röcker C, Zhang F, Parak WJ, et al. Quantitative analysis of the protein corona on FePt nanoparticles formed by transferrin binding. *Journal of The Royal Society Interface*. 2009;7(suppl_1):S5-S13.
39. Ciechanover A, Schwartz A, Dautry-Varsat A, Lodish H. Kinetics of internalization and recycling of transferrin and the transferrin receptor in a human hepatoma cell line. Effect of lysosomotropic agents. *Journal of Biological Chemistry*. 1983;258(16):9681-9.
40. Choi CHJ, Alabi CA, Webster P, Davis ME. Mechanism of active targeting in solid tumors with transferrin-containing gold nanoparticles. *Proceedings of the National Academy of Sciences*. 2010;107(3):1235-40.
41. Salvati A, Pitek AS, Monopoli MP, Prapainop K, Bombelli FB, Hristov DR, et al. Transferrin-functionalized nanoparticles lose their targeting capabilities when a biomolecule corona adsorbs on the surface. *Nature nanotechnology*. 2013;8(2):137.
42. Wang J, Tian S, Petros RA, Napier ME, DeSimone JM. The complex role of multivalency in nanoparticles targeting the transferrin receptor for cancer therapies. *Journal of the American chemical society*. 2010;132(32):11306-13.

43. Saha K, Rahimi M, Yazdani M, Kim ST, Moyano DF, Hou S, et al. Regulation of macrophage recognition through the interplay of nanoparticle surface functionality and protein corona. *ACS nano*. 2016;10(4):4421-30.
44. Monopoli MP, Walczyk D, Campbell A, Elia G, Lynch I, Baldelli Bombelli F, et al. Physical– chemical aspects of protein corona: relevance to in vitro and in vivo biological impacts of nanoparticles. *Journal of the American Chemical Society*. 2011;133(8):2525-34.
45. Lara S, Alnasser F, Polo E, Garry D, Lo Giudice MC, Hristov DR, et al. Identification of receptor binding to the biomolecular corona of nanoparticles. *ACS nano*. 2017;11(2):1884-93.
46. Kratz F, Elsadek B. Clinical impact of serum proteins on drug delivery. *Journal of Controlled Release*. 2012;161(2):429-45.
47. Le Cabec V, Carréno S, Moisan A, Bordier C, Maridonneau-Parini I. Complement receptor 3 (CD11b/CD18) mediates type I and type II phagocytosis during nonopsonic and opsonic phagocytosis, respectively. *The Journal of Immunology*. 2002;169(4):2003-9.
48. Daéron M. Fc receptor biology. *Annual review of immunology*. 1997;15(1):203-34.
49. Swanson JA, Hoppe AD. The coordination of signaling during Fc receptor-mediated phagocytosis. *Journal of leukocyte biology*. 2004;76(6):1093-103.
50. Kollman JM, Pandi L, Sawaya MR, Riley M, Doolittle RF. Crystal structure of human fibrinogen. *Biochemistry*. 2009;48(18):3877-86.
51. Hall CE, Slayter HS. The fibrinogen molecule: its size, shape, and mode of polymerization. *The Journal of Cell Biology*. 1959;5(1):11-27.
52. Deng ZJ, Liang M, Monteiro M, Toth I, Minchin RF. Nanoparticle-induced unfolding of fibrinogen promotes Mac-1 receptor activation and inflammation. *Nature nanotechnology*. 2011;6(1):39.

Chapter 4: Nanoparticle Size and Surface Chemistry Influences

Phagocytic Cell Association in Whole Human Blood

4.1 Introduction

Polymeric nanomaterials possess substantial clinical potential because of their versatility in physical and chemical design (1, 2). This versatility of polymeric nanomaterials allows them to be designed to overcome clinical hurdles that preclude conventional medicines from becoming viable clinical therapies. As examples, polymeric nanomaterials can be loaded with therapeutic cargo such as hydrophobic drugs, nucleic acids, and proteins to inhibit premature degradation of the agent, improve circulation time, and ultimately improve clinical efficacy (3, 4). Further interesting examples of the clinical use of polymeric nanomaterials include MRI contrast agents (5), theragnostic tools (6), and vaccines (7).

Many of the aforementioned nanomaterial applications will involve the intravenous administration of nanomaterials, wherein the human blood represents the first point of biological contact. Human blood contains phagocytic and nonphagocytic white blood cells (WBC) that act as an initial immunological response to foreign bodies and help mediate their rapid subsequent clearance from the body (8). Phagocytic WBC also avidly target circulating nanoparticles for clearance from the body in a similar fashion to pathogens. This provides a significant challenge for the clinical translation of nanoparticles in that the rapid sequestration and clearance of nanoparticles by WBCs can adversely affect their clinical efficacy. Furthermore, the association of nanoparticles with WBCs can also present opportunities to exploit nanoparticles for drug delivery applications. As such, understanding the complex interactions between polymeric nanomaterials and the immune system is critical for designing nanomaterials with the desired clinical outcome after intravenous administration.

To date, there have been numerous studies that investigate the impact of nanomaterial physicochemical properties such as size and surface chemistry on their biological behaviour (9-11). For instance, the Rotello group synthesized a library of 2, 4, and 6 nm cationic, anionic, and neutral gold nanoparticles, and evaluated their uptake by human cervical carcinoma (HeLa)

cell line (12). The authors found that contrasting behaviour was observed in that cellular uptake decreased with increased zwitterionic and anionic particle size, while cellular uptake increased with increasing cationic particle size. Another study by Walkey *et al.* found that nanoparticle size and surface PEG density of gold nanoparticles correlates with adsorption of serum proteins and their uptake by a macrophage cell line (13). In addition, He *et al.* investigated the effect of size and surface charge of polystyrene nanoparticles on murine macrophage uptake and *in vivo* biodistribution (14). The study suggested that small changes in nanoparticle size and surface charges could result in significant changes to the macrophage cell line uptake and tumour accumulation profile. Although helpful, most studies on nanoparticle association with immune cells to date have been restricted to immortalized cell lines or rodent models as a model of the interactions between nanomaterials and various biological systems. There remains a relatively poor understanding of how nanomaterials interact with primary human systems, specifically whole blood.

Investigating the interactions between nanomaterials and WBCs in the complex and competitive environment of primary human blood has rarely been undertaken. This represents a gap in knowledge considering that blood is the first organ nanomaterials encounter when they are intravenously administered. The phagocytic WBCs include granulocytes and monocytes which act in the primary defence against infection and are vital components of the innate immune system. Another phagocytic cell population is dendritic cells, which are principally involved in the initiation of the adaptive immune response, commonly known as antigen presentation. Dendritic cells take up and process pathogens and vaccines for presentation to the adaptive immune system (B cells and T cells), which produce antibody and cell-mediated immune responses (15). Non-phagocytic WBC populations in the blood include the lymphocytic populations of B cells, T cell and NK cells. T and B cells respond to specific pathogens via their T and B cell receptors. Natural Killer (NK) cells are innate immune cells

that destroy cells which are infected by viruses or malformed into cancerous cells. All WBC populations have specific receptors that allow their ready identification via application of fluorescent antibodies and flow cytometry.

To better understand the factors that govern nanoparticle interactions with blood immune cells, our collaborators at the University of Melbourne developed a whole human blood assay (16, 17). This allowed the group to study WBC targeting by functionalized nanomaterials (18), using particle chemistry to inhibit the clearance of nanomaterials by phagocytic blood cells (19), and using nanoparticles to activate blood dendritic cells for vaccination purposes (20). The results of such studies contribute to a fundamental understanding of the immunological interactions of the respective nanomaterials for future clinical use. Nonetheless, previous studies have only investigated the biological impact of modifying a single physicochemical parameter (e.g., surface charge, presence/absence of targeting ligands etc.). It is not known how changing multiple nanoparticle characteristics will influence particle association with human immune cells. Recent advances in RAFT polymerization techniques have enabled polymeric nanomaterials to be more readily synthesized with highly tunable and varied physicochemical properties (described in Chapter 2 of this thesis). Therefore, it is a primary objective of the present study to investigate the effect of systematic variation of multiple nanomaterial physicochemical properties (e.g., both size and surface chemistry) on nanomaterial association with WBCs in whole human blood.

Herein, we evaluated a library of fluorescently-labelled polystyrene nanoparticles with 4 separate surface chemistries and 3 predetermined particle sizes in a human whole blood assay for particle association with 6 WBC populations; neutrophils, monocytes, B cells, T cells, NK cells, and DCs (Scheme 1), using a previously published protocol (16, 17). The nanoparticles were previously assembled via polymerization- induced self-assembly (PISA) using reversible addition-fragmentation chain transfer (RAFT) emulsion polymerization conditions (21). The

results of our study showed that 1) size and surface chemistry significantly affected nanoparticle association with phagocytic WBCs (neutrophils and monocytes), 2) WBC populations were affected by size or surface chemistry, or size and surface chemistry, and 3) size was a more significant determinant of nanoparticle association with WBCs than the chemistries we studied.

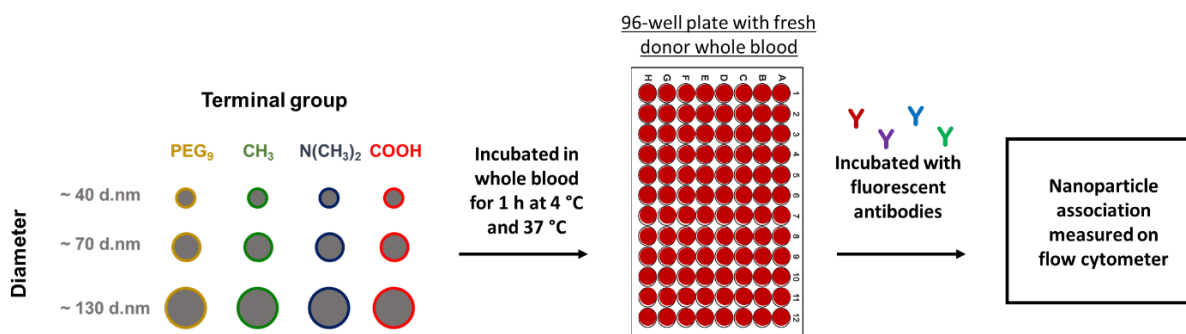
4.2 Experimental Section

4.2.1 Nanoparticle Synthesis

A library of Cyanine 5(Cy5)-labelled polystyrene nanoparticles was obtained via PISA under RAFT aqueous emulsion polymerization condition as previously described (21).

4.2.1.1 Materials

Carbon disulphide (>99.9%), ethanethiol (97%), dimethyl sulfoxide (>99.9%, anhydrous), p-toluenesulfonyl chloride (>99%), dicyclohexylcarbodiimide (DCC), trimethylamine (>99%, anhydrous grade), 4-dimethylaminopyridine (DMAP), methanol (99%, anhydrous grade), 3-dimethylamino-1-propanol (TA, 99%), PEG (average $M_n = 550 \text{ g mol}^{-1}$), and p-toluenesulfonic acid monohydrate (>98.5%) were acquired from Sigma Aldrich and used as received. Poly(ethylene glycol) methyl ether acrylate (PEGA, average $M_n = 480 \text{ g mol}^{-1}$, Sigma Aldrich), hydroxyethyl acrylate (HEAA; 97%, Sigma Aldrich), and styrene (>99%, Sigma Aldrich) were put through a column of basic alumina (activity I) to remove inhibitor before use. Cy5-maleimide was purchased from Lumiprobe and used according to manufacturer's instructions. ACPA (98%, Alfa Aesar) was recrystallized twice in methanol before use. MilliQ water (resistivity $> 18.2 \text{ M}\Omega \text{ cm}^{-1}$) was produced by a Millipore MilliQ Academic Water Purification System. All other reagents and solvents used were at least analytical grade.



Scheme 1. Summary of nanoparticle library of different surface chemistries and similar sizes, and different sizes and similar surface chemistries. Fluorescent nanoparticles were incubated in whole human blood at 4 °C and 37 °C for 1 hour. The WBC populations were then phenotyped with fluorescent antibodies to study which WBC populations associated with the nanoparticles. Cells were analyzed on a flow cytometer.

4.2.1.2 *Synthesis of Cy5-labelled nanoparticles*

Briefly, 4-cyano-4-(ethylthiocarbonothioylthio) pentanoic acid (ECT) was modified with methanol (Me), 3-dimethylamino-1-propanol (TA), and PEG (average $M_n = 550$) to obtain 4 CTAs with carboxylic acid (COOH), poly(ethylene glycol) (PEG), methyl (Me), and tertiary amine (TA) R groups as per previously published studies (22, 23). After that, a succession of RAFT solution polymerizations of PEGA and HEAA with each of the 4 CTAs was carried out. From these polymerization reactions, 4 macro-CTAs with similar degree of polymerization (DP) of PEGA (DP = 24-26) and HEAA (DP = 24-26) and molecular weights were obtained (Table S1, Supporting Information). Finally, a series of RAFT aqueous emulsion polymerizations of styrene with each of the 4 macro-CTAs was carried. RAFT aqueous emulsion polymerizations were carried out with varying feed ratios of styrene:macro-CTA using each of the 4 macro-CTAs. This technique allowed systematic variation of the final nanoparticle diameter and, importantly, resulted in the synthesis of polystyrene nanoparticles with different end groups/similar size and different size/similar end group (Table S1, Supporting Information). Significantly, an aliquot of Cy5 maleimide/styrene was introduced during the RAFT aqueous emulsion polymerizations of styrene to obtain fluorescent nanoparticles for flow cytometric analysis.

4.2.2 Measurement of nanoparticle fluorescence intensity

The fluorescence intensity of each nanoparticle was quantified in units of molecules of equivalent soluble fluorochrome (MESF). The MESF value discloses that a sample labelled with a fluorochrome possesses the same fluorescence intensity as an equivalent number of molecules of the fluorochrome free in a solution under the same experimental conditions (24). A Cy5 MESF bead kit (Bangs Laboratories) was used to establish calibration curves (MESF v Channel value) on the flow cytometer. Following Cy5 MESF calibration, the flow cytometer

was configured to enhance acquisition and counting of submicron particles; this was enabled by a proprietary light detection module called Ghost Detect Module™. Nanoparticles were diluted in PBS (100 µg/mL, and then analyzed on the flow cytometer).

4.2.3 Blood Acquisition

Blood was collected from healthy human volunteers after obtaining informed consent in accordance with the University of Melbourne Human ethics approval 1443420 and the Australian National Health and Medical Research Council Statement on Ethical Conduct in Human Research. For the WBC association and PBMC association studies, blood was drawn by venepuncture into Vacuette collection tubes (Greiner Bio-One) containing sodium heparin. The tubes were inverted 5 times to mix the blood with the anti-coagulant. All blood samples were studied within 1 h of collection.

4.2.4 High-Throughput Screening (HTS) Assay for Particle Association with WBC Populations

The association between our library of Cy5-labelled polystyrene nanoparticles and WBCs in whole blood was carried out as described previously (16-18, 20). Freshly acquired human blood (100 µL) was deposited into 1.5 mL wells of 96-well plates (Nunc™ 96-Well Polypropylene DeepWell™ Storage Plates, Thermo Fisher). The plates were then covered and incubated on ice (4°C) or in a 37 °C waterbath for 1 h to bring the plates to their respective temperatures. After this, nanoparticles (diluted in PBS) were added to the respective wells on the plates and incubated at ice (4°C) or in a 37 °C waterbath for 1 h, before placing both plates on ice. Next, RBCs were lysed 3× with Pharm Lyse buffer (BD Biosciences) at 15× the volume of blood for each round of lysing. Cells were washed 2× with PBS with centrifugation (500 G, 5 min, 4 °C) between each round of washing. Cells were then phenotyped on ice for 1 h using titrated concentrations of antibodies against CD66b (BV421, G10F5), CD45 (V500, H130k),

CD19 (BV650, HIB19), CD14 (APC-H7, MΦP9), CD3 (AF800, SP34-2), Lin-1 (FITC), HLA-DR (PerCP Cy5.5, L243), and CD56 (PE, B159). The gating tree to identify the phagocytic populations is shown in Figure 1. All antibodies were obtained from BD Biosciences and used as received. Furthermore, cells were washed twice in cold (4°C) FACS wash buffer (FWB, WB; 1×PBS consisting of 0.5% w/v bovine serum albumin (Sigma Aldrich) and 2 mM EDTA pH 8 (Ambion)), fixed with 1% formaldehyde in MilliQ water, and analysed on a High Throughput Sampler (HTS; BD Biosciences) coupled to a flow cytometer (LSRFortessa, BD Biosciences). The resultant data was analysed on FlowJo v10 and graphed using GraphPad Prism v7.

4.2.5 HTS Assay for Association with Peripheral Blood Mononuclear Cells

To study the interactions of nanoparticles with WBC populations in the absence of human plasma, red blood cells, neutrophils and platelets, we fractionated whole blood into peripheral blood mononuclear cells (PBMC). Firstly, fresh whole blood from each of the donors was fractionated through Ficoll Paque (PLUS) (GE Healthcare Life Sciences) density gradient centrifugation. PBMC from each donor was isolated from the fractionated blood by aspirating the buffy coat layer. Isolated PBMCs were made up to 3× the original volume with PBS. Nanoparticles were added to PBMC (100 µL) and then incubated at 37 °C for 1 h, before placing on ice. Then, the cells were phenotyped on ice as above for 1 h using titrated concentrations of antibodies against CD66b (BV421, G10F5), CD45 (V500, H130k), CD19 (BV650, HIB19), CD14 (APC-H7, MΦP9), CD3 (AF800, SP34-2), and CD56 (PE, B159). After this, cells were washed twice in cold (4°C) FWB, fixed with formaldehyde, and analysed on an HTS (BD Biosciences) coupled to a flow cytometer (LSRFortessa, BD Biosciences). The resultant data was analysed on FlowJo v10 and graphed using GraphPad Prism 7.

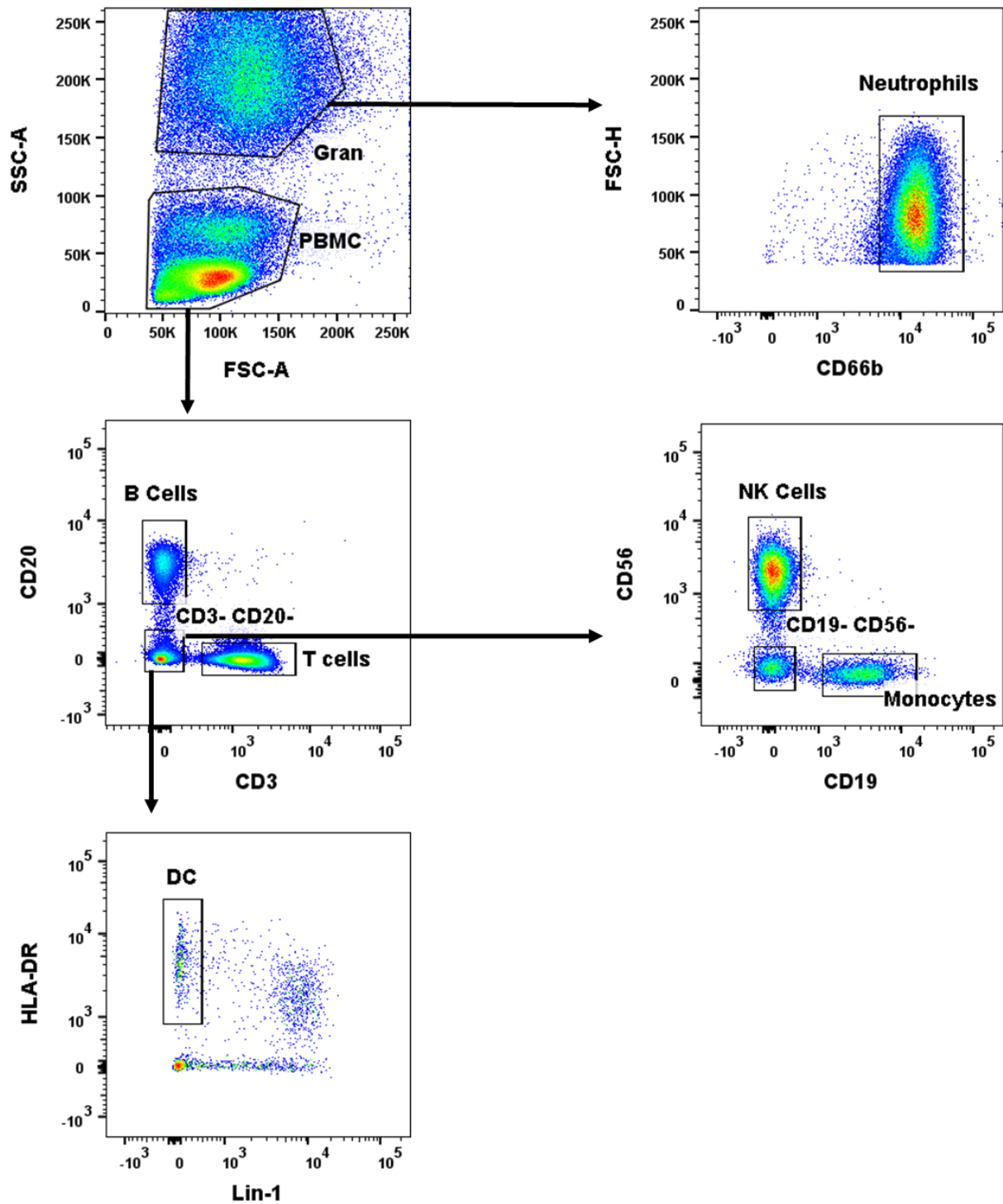


Figure 1. Cy5-labelled polystyrene nanoparticles with various sizes and surface chemistries were incubated in fresh blood for 1 h, at 37 °C. The association with primary human blood cells was examined by flow cytometry according to the representative gating tree above.

4.2.6 Statistical Analyses

WBC association results post-compensation were analysed using Wilcoxon nonparametric two-tailed matched pairs signed rank test (GraphPad v7). A p value of <0.005 was considered to be significant.

4.2.7 Multiple Linear Regression Analyses

Multiple linear regression analysis for association of the nanoparticle library with each of the WBC populations was carried out against several variates of the nanoparticle's physicochemical properties; polydispersity index (PDI; from size exclusion chromatography), nanoparticle number average, particle size distribution and zeta potential from the DLS (DLS_D and ZP respectively), nanoparticle diameter from the TEM (TEM_D), and number of macro-CTA per nanoparticle (N_{MCTA}; derived using equation from previous study (22)). To differentiate the nanoparticle end groups (COOH, PEG, Me, and TA), the partition coefficient value (mLogP) was estimated from a training set of experimentally measured partition coefficients containing the most common elements (H, C, O, S, N, and halogens) (25). The aforementioned variables are summarized in Table 1. Each of the variates were modelled and the response models were cropped by excluding statistically non-significant variates considering a significance level of $p = 0.05$. Such variates were systematically removed until only statistically significant variates remained (Table 2).

4.3 Results

4.3.1 Nanoparticle Synthesis and Characterization

The physicochemical properties of polymeric nanomaterials are highly tunable and may be controlled in a facile manner. This leads to the possibility of bespoke polymeric nanomaterials for desired applications. For instance, RAFT agents are typically modified via their R group to conjugate small molecule therapeutic agents or proteins. In an example, Davis

and colleagues synthesized an amine-functional RAFT linear polymer via the polymerization of poly(*N*-(2-hydroxypropyl) methacrylamide) (PHPMA) with a thiazolidine-2-thione RAFT agent; followed by conjugation with lysozyme (26). In another case, a RAFT agent was synthesized to possess a pendent pyridyldisulfide functional group located in its core (27). The centrally located pyridyldisulfide group was exploited for bovine serum albumin (BSA) conjugation, with the central position of the BSA designed to shield it from premature proteolytic cleavage.

Due to the diversity of polymeric nanomaterial physicochemical properties, it is essential to understand the biological impact of simultaneous change in multiple physicochemical properties. To that end, we synthesized a library of 12 core-confined Cy5-labelled polystyrene nanoparticles with four end groups (COOH, PEG, Me, and TA) and 3 sizes for each of the end groups (~30 nm (S-suffix), ~70nm (M-suffix), and ~130nm (L-suffix); Scheme 1). It should be noted that the confinement of Cy5 to the nanoparticle core removes any potential effect of fluorophore interaction with WBC. The diversity in end group was achieved through the use of well-defined macro-CTAs with high end-group fidelity (23). The deployment of macro-CTAs with various end groups for RAFT aqueous emulsion polymerization of styrene introduces different surface chemistries to the resultant polystyrene nanoparticles (a so-called premodification approach). Furthermore, the use of macro-CTAs composed of PEGA and HEAA for RAFT aqueous emulsion polymerization of styrene has been shown to result in the ultrafast synthesis of nanoparticles with i) narrow distribution of molecular weights of particle sizes, ii) no use of organic solvents, and iii) high solids content. Importantly, the diameter of the nanoparticles could be precisely controlled through systematic variation of the macro-CTA:styrene ratio. This principle was applied to obtain well-defined nanoparticles with different surface chemistries but similar sizes (Table S1).

4.3.2 Quantification of nanoparticle fluorescence intensity via Cy5 MESF beads

Flow cytometry has been routinely used to quantify cellular association with nanoparticles made from silica (28, 29), gold (30, 31), chitosan (14), polystyrene (32), and inorganic (33) material. However, the use of flow cytometry to quantify the relative fluorescence intensity of nanoparticles has not been undertaken to our knowledge. The quantification of fluorescence intensity for each of the nanoparticles tested was used to normalize the differences in fluorescence intensity between each nanoparticle; enabling the comparison of WBC association.

A Cy5 MESF bead kit was used to establish calibration curves of MESF against channel value on the Stratadigm S100 EXI flow cytometer. Although fluorescence labelling and subsequent conversion to MESF can be easily characterized by flow cytometry, it has been a challenge for conventional flow cytometry to detect particles smaller than 200 nm in diameter (34, 35). Nonetheless, flow cytometers such as the Stratadigm S100 EXI possess a light detection module that can be calibrated to measure the fluorescence of any sample without the presence of cells (i.e. submicron particles). This feature was exploited to detect the presence of our nanoparticles which range in size from ~30 nm to ~130 nm. Nanoparticles were diluted in PBS to replicate the state they would be in when added to the whole blood assay, and then run on the Stratadigm S100 EXI with the “Ghost” light detection module activated. Forward scatter (FSC) and side scatter (SSC) logarithmic scale plots were obtained for each nanoparticle, in addition to adjunct FSC and SSC histograms for each plot. In Figure 2, we observed that the flow cytometer appeared to distinguish the presence of nanoparticles from the concurrent increase in FSC and SSC in comparison to the PBS-only sample. In addition, the increase in nanoparticle diameter was accompanied by shifts in the SSC histograms. Conversely, there were no significant shifts in FSC histograms. This observation is consistent with prior studies.

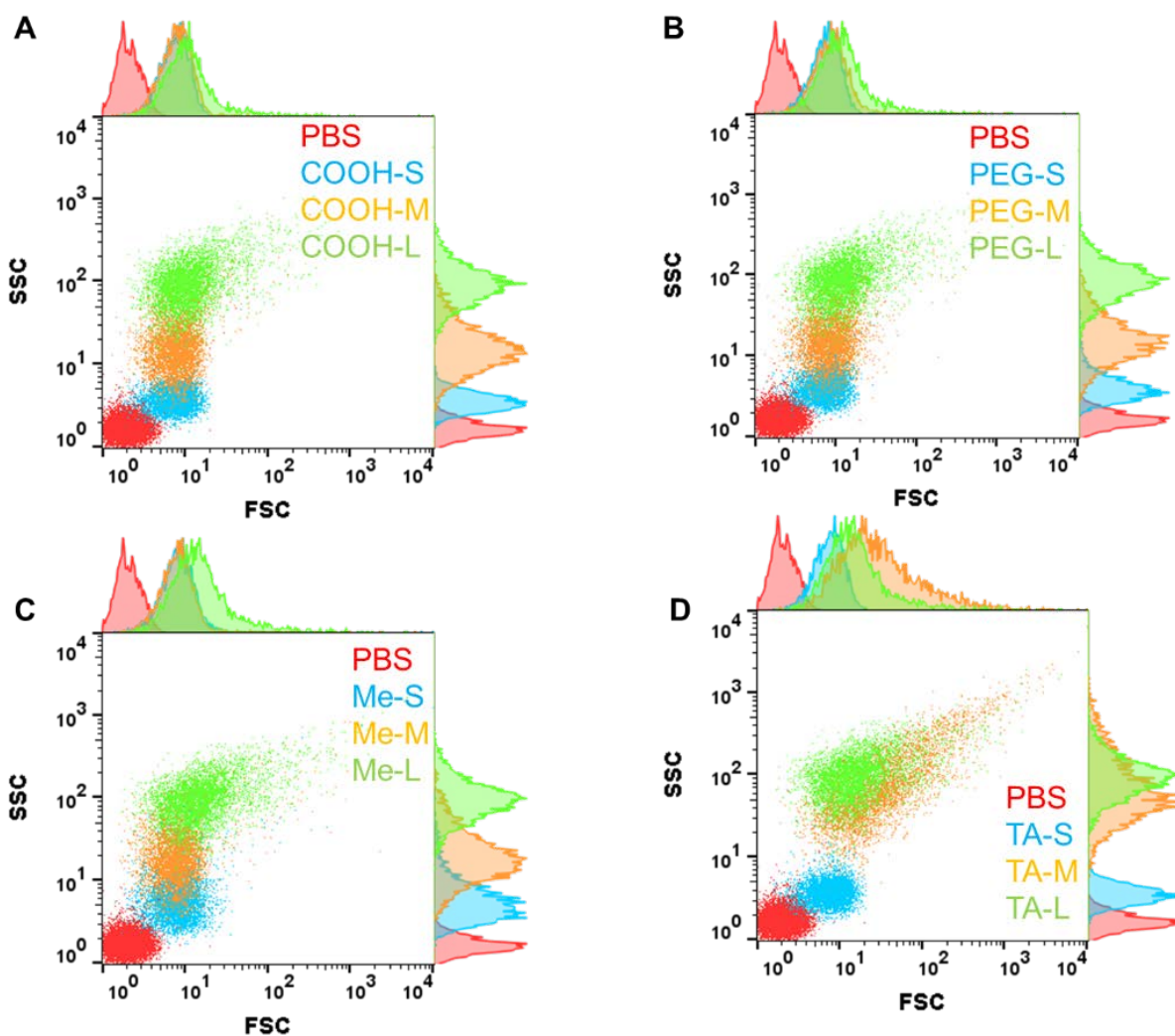


Figure 2. SSC versus FSC scatter plot with adjunct histograms of nanoparticles of different surface chemistries and similar sizes. The nanoparticles with (A) COOH, (B) PEG, (C) Me, and (D) TA surface groups and 3 sizes of each surface group were dispersed in PBS at 100 $\mu\text{g}/\text{mL}$ and then analyzed on a Stratadigm S100 EXI with a light detection module. that observed concurrent increases in SSC with the size of submicron particles (36, 37).

Furthermore, it was observed that the scatter plot of the TA-M nanoparticles showed the possibility that the TA-M nanoparticles had aggregated, resulting in a broad distribution of nanoparticle size over the FSC and SSC region (Figure 2D). The aggregation of TA-M nanoparticles was a surprising observation and the exact cause is unknown without further

investigation. Nonetheless, due to the aggregation of TA-M nanoparticles in PBS, blood association data from the TA-M nanoparticles was excluded from further analysis.

After confirming that the flow cytometer could detect our nanoparticles, we analyzed the fluorescence intensity of each nanoparticle. Based on the histograms from the 642 nm (Cy5 excitation) channel, the nanoparticle channel values were input into the MESF v channel value calibration curve to obtain the MESF value for each nanoparticle.

4.3.3 Analysis of nanoparticle-WBC association data

The clinical application of polymeric nanomaterials will, in some cases, involve intravenous injection of nanomaterials. After intravenous administration, nanoparticles encounter a diversity of circulating cells that are not well-characterized by current studies using immortalized cell-lines or rodents. In particular, characterizing the association of nanoparticles with WBCs in human blood is essential for the successful clinical translation of polymeric nanomaterials. Therefore, we have used a whole blood assay model to investigate the effect of both size and surface chemistry on nanoparticle association with WBCs. So far, nanoparticle association with blood cells in fresh human blood from healthy donors has been found to be influenced by the presence of surface thiol reactive groups on star polymers (17), and the surface charge of hyperbranched polymers (16). Herein, we aim to contribute to the growing body of knowledge of nanoparticle association with human blood cells in fresh blood by investigating the influence of nanoparticle size and surface chemistry on WBC association. A gating tree that was used to identify the WBC populations is shown in Figure 1. After isolating the Cy5 signal for each WBC populations, the level of association for each nanoparticle was indicated by the median fluorescence intensity (MFI) per cell.

To minimise experimental differences and enable better size versus surface chemistry comparisons, the entire library of nanoparticles was studied in the same assay. In addition, each

nanoparticle within the same assay was tested against 4 donors at both 4 °C and 37 °C. After the high throughput assays were carried out, the entire data-set was analyzed from several perspectives. By examining the data set as a whole, it was apparent that the nanoparticle association with WBCs at 4 °C was modest relative to nanoparticle association with WBCs at 37 °C. This observation was consistent with previous similar studies (16, 17), therefore the nanoparticle association data at 4 °C was not shown. Furthermore, based on the unexpected aggregation behaviour of the ~70 nm TA-terminated nanoparticles, the entire ~70 nm nanoparticle series was excluded from analysis. Nonetheless, with the nanoparticle association at 37 °C for the 30 nm and 130 nm nanoparticles, we firstly examined the differences according to MFI across different surface chemistries but the same size range (Figure 3 and 4) to study the effect of varying surface chemistry on nanoparticle association with WBCs. Then, we kept the surface chemistry constant (COOH; Figure 5, Me; Figure 6, PEG; Figure 7) to study the effect of nanoparticle size on WBC association. Nanoparticle association was also tested in the absence of plasma protein (Figure 8 and Figure 9). Finally, statistical analysis was carried out on the entire data set to study the effect of both size and surface chemistry on WBC association (Table 1 and Table 2).

4.3.4 TA Surface Chemistry Enhances Association with Phagocytic WBC Population

Immediately apparent from nanoparticle association at 37 °C was the preferential association of nanoparticles with neutrophils, monocytes, and B cells over dendritic cells, NK cells, and T cells. Nonetheless, statistically significant differences in MFI between nanoparticles with different surface chemistries and within a similar size range were observed across all WBC populations. For nanoparticles in the ~30 nm size range with different surface chemistries (Figure 3), statistically significant differences in MFI between the nanoparticles was observed for neutrophils, monocytes, B cells, DC, NK cells, and T cells. TA-terminated nanoparticles showed statistically significantly higher neutrophil, monocyte, and B cell

association compared to the COOH-terminated 30 nm nanoparticles. Conversely, PEG and Me-terminated ~30 nm nanoparticles showed lower association with neutrophils, monocytes and B cells compared to

TA-terminated nanoparticles (Figure 3). Interestingly, this trend was reversed when association for TA-terminated nanoparticles with DC, NK cells, and T cells were the lowest compared to the other surface chemistries. Furthermore, association with Me-terminated nanoparticles with these cell populations were significantly higher than other surface chemistries.

Next, we compared the effect of the 4 different surface chemistry using the larger 130 nm particle set. Compared with the 30 nm particle set, the MFIs for the 130 nm particle set were higher, indicating higher nanoparticle association. Interestingly, for nanoparticles in the ~130 nm size range (Figure 4), TA-terminated nanoparticles show significantly higher MFI for NK cells and T cells compared to Me-terminated nanoparticles. There appears to be a size-dependent effect on nanoparticle association with NK cells and T cells rather than a surface chemistry effect; this will be discussed later. In summary, comparison of nanoparticle association across the ~30 nm and ~130 nm nanoparticle size range suggests higher nonspecific clearance for TA-terminated nanoparticle and lower nonspecific clearance for PEG and Me-terminated nanoparticles.

4.3.4 Phagocytic and Nonphagocytic Cell Association Increases as Nanoparticle Size Increases

For COOH and TA-terminated nanoparticles, MFI increased significantly as size increased for neutrophils, monocytes, NK cells, and T cells. No significant differences in association were observed for B cells and DC cells. An increase in PEG-terminated nanoparticle size also led to an increase in cellular association. However, this association

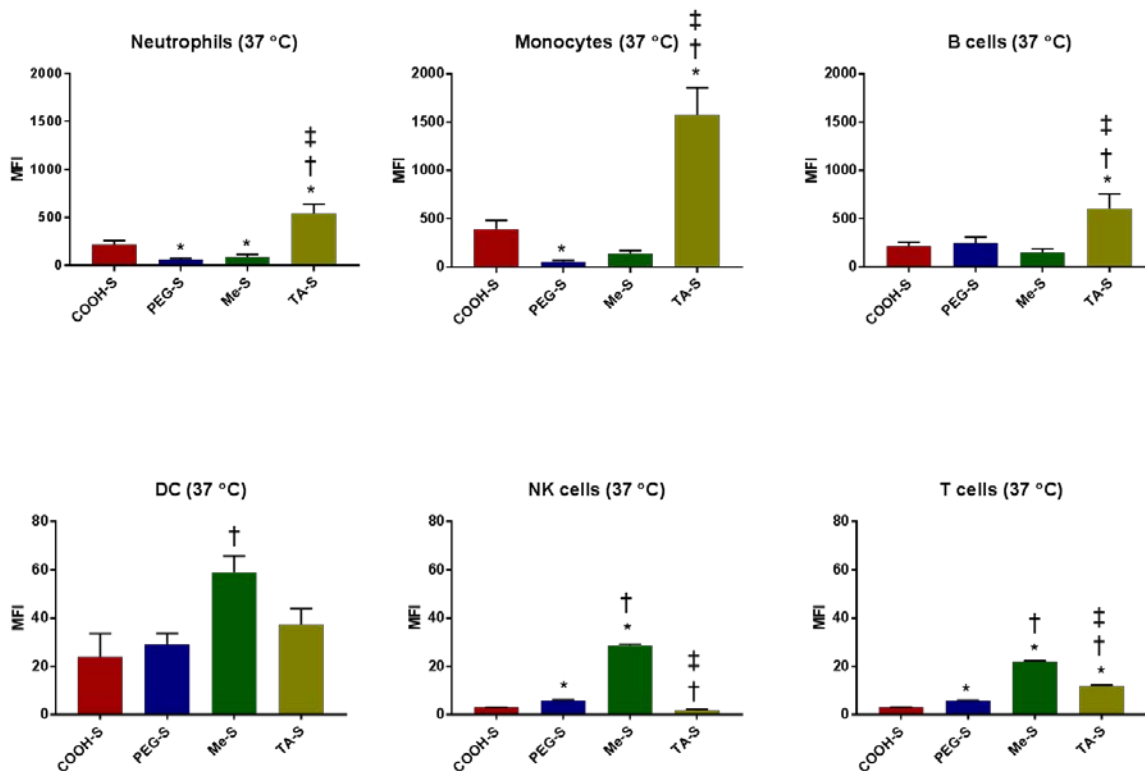


Figure 3. ~30 nm TA-terminated nanoparticles display enhanced association with neutrophils, monocytes, and B cells over ~30 nm nanoparticles with other surface chemistries in whole human blood. Nanoparticles with COOH, PEG, Me, and TA surface groups were incubated with fresh human blood at 100 $\mu\text{g}/\text{mL}$ for 1 h at 37 °C. The red blood cells were lysed and washed before phenotyping with fluorescent antibodies on ice. WBC association with Cy5-labeled nanoparticles was determined by flow cytometry and characterized by median fluorescence intensity (MFI). Note that the scales for the upper and lower rows are distinct from each other to accommodate the differences in nanoparticle association. All nanoparticles were tested with 4 individual donors. The errors bars represent standard deviation. * $p < 0.05$; COOH versus PEG or Me or TA, † < 0.05 ; PEG versus COOH or Me or TA, and ‡ < 0.05 ; Me versus COOH or PEG or TA.

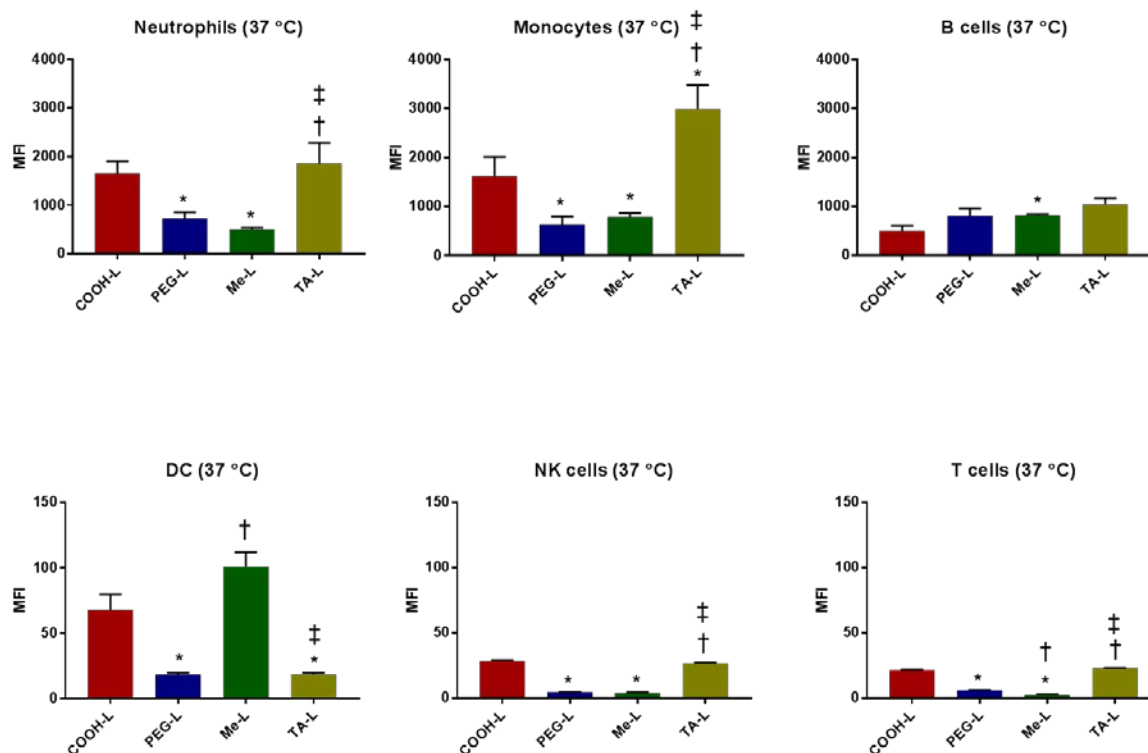


Figure 4. ~130 nm TA-terminated nanoparticles display enhanced association with neutrophils, monocytes, NK cells, and T cells over ~130 nm nanoparticles with other surface chemistries in whole human blood. Nanoparticles with COOH, PEG, Me, and TA surface groups were incubated with fresh human blood at 100 $\mu\text{g}/\text{mL}$ for 1 h at 4 or 37 $^{\circ}\text{C}$. The red blood cells were lysed and washed before phenotyping with fluorescent antibodies on ice. WBC association with Cy5-labeled nanoparticles was determined by flow cytometry and characterized by median fluorescence intensity (MFI). Note that the scales for the upper and lower rows are distinct from each other to accommodate the differences in nanoparticle association. All nanoparticles were tested with 4 individual donors. The errors bars represent standard deviation. * $p < 0.05$; COOH versus PEG or Me or TA, † < 0.05 ; PEG versus COOH or Me or TA, and ‡ < 0.05 ; Me versus COOH or PEG or TA.

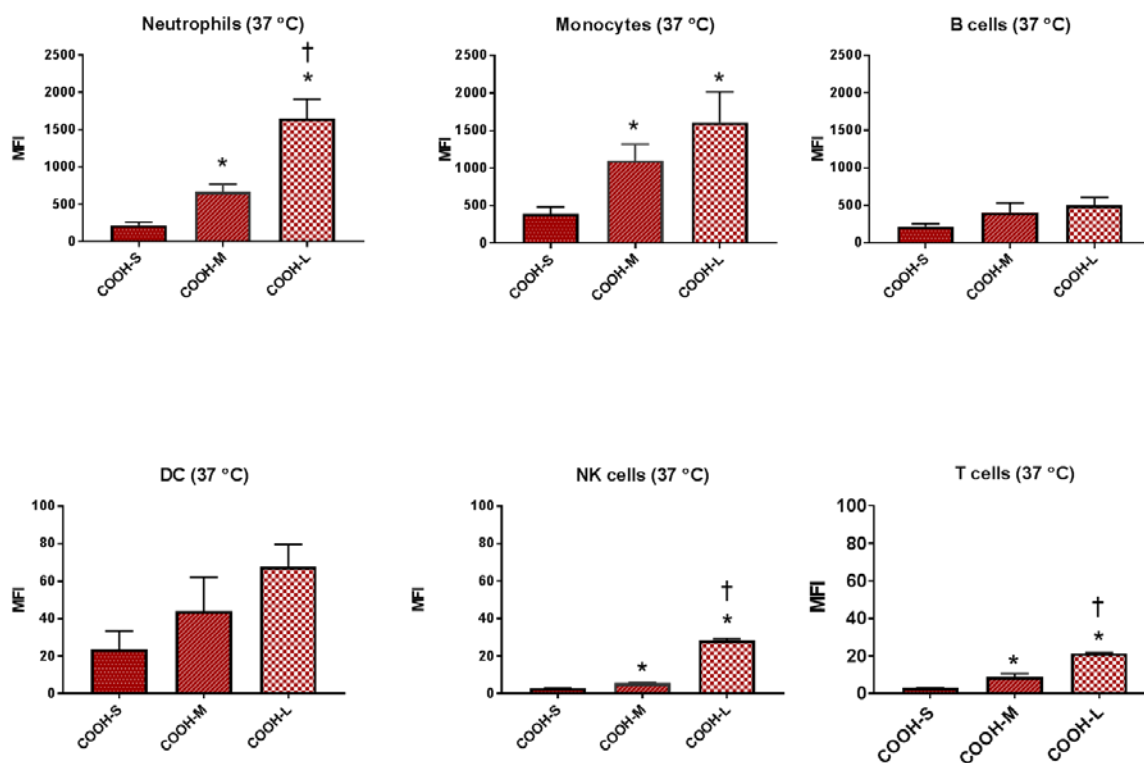


Figure 5. COOH-terminated nanoparticles display increasing association with WBCs as size increases. Nanoparticles with COOH surface groups were incubated with fresh human blood at 100 $\mu\text{g}/\text{mL}$ for 1 h at 4 or 37 $^{\circ}\text{C}$. The red blood cells were lysed and washed before phenotyping with fluorescent antibodies on ice. WBC association with Cy5-labeled nanoparticles was determined by flow cytometry and characterized by median fluorescence intensity (MFI). Note that the scales for the upper and lower rows are distinct from each other to accommodate the differences in nanoparticle association. All nanoparticles were tested with 4 individual donors. The errors bars represent standard deviation. * $p < 0.05$; COOH versus PEG or Me or TA, † < 0.05 ; PEG versus COOH or Me or TA, and ‡ < 0.05 ; Me versus COOH or PEG or TA.

plateaus after the intermediate (~70 nm) size, with no statistically significance when comparing ~70 nm and ~130 nm nanoparticles for association with neutrophils, monocytes, and B cells (Figure 5). It appears that at ~70 nm in size, PEG-terminated nanoparticles reach a point of diminishing association with neutrophils, monocytes, and B cells (Figure 6). Taken together, the association results show that smaller COOH, TA, and PEG-terminated nanoparticles have potential to reduce nanoparticle-immune cell interaction. We anticipate that these differences in *ex vivo* blood cell association would translate to differences in clearance and targeting *in vivo*, although this needs to be formally tested. Similarly, the use of larger COOH, TA, and PEG-terminated nanoparticles may be more suited for applications that rely on the recruitment of neutrophils, monocytes, NK cells, and T cells. As an example, Kang and coworkers have designed neutrophil-mimicking nanoparticles by decorating the surface of poly(D,L-lactic-co-glycolic acid) nanoparticles with inflammatory neutrophil membrane (38). In another example, Xuan *et al.* synthesized cell membrane-enveloped mesoporous silica nanoparticles with properties such as large size (~50 nm), and high chemical stability to increase phagocytosis by cells such as monocytes (39). The presence of targeting moieties on the nanoparticle surface was shown to enable increased association with tumour endothelium. For Me-terminated nanoparticles (Figure 7), the association with neutrophils, monocytes, and B cells increased as their size-increased. Interestingly, Me-terminated nanoparticle association with T cells and NK cell population decreased with the increase in size. Both NK cells and T cells are lymphocytic cells that make up the adaptive immune system. This observation suggests that smaller Me-terminated nanoparticles are more suitable for applications that rely on the association of nanoparticles with NK cells and T cells. For example, several groups have investigated the modification of nanoparticle surface chemistry for attachment to the surface of reprogrammed T lymphocytes (40) and transplanted T cells (41). To the best of our knowledge, there has yet to be a nanoparticle-based system that exploits the potential physiological effect of NK cell

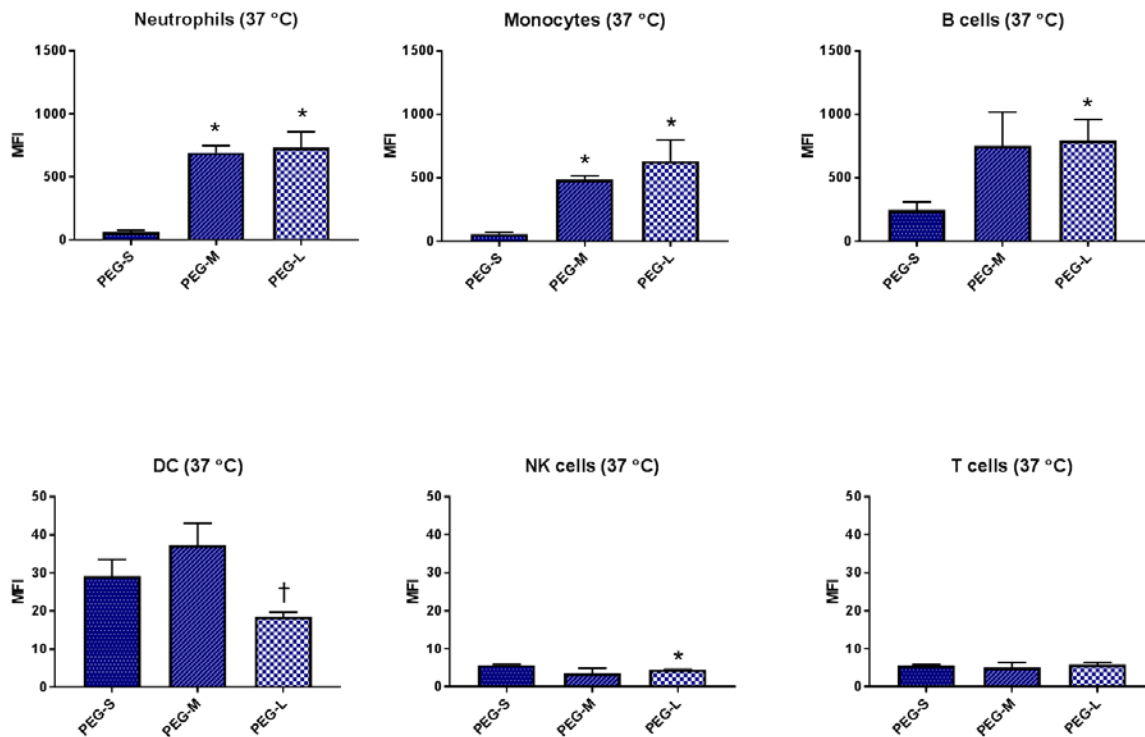


Figure 6. PEG-terminated nanoparticles display increasing association with WBCs until ~70 nm. Nanoparticles with PEG surface groups were incubated with fresh human blood at 100 $\mu\text{g}/\text{mL}$ for 1 h at 4 or 37 $^{\circ}\text{C}$. The red blood cells were lysed and washed before phenotyping with fluorescent antibodies on ice. WBC association with Cy5-labeled nanoparticles was determined by flow cytometry and characterized by median fluorescence intensity (MFI). Note that the scales for the upper and lower rows are distinct from each other to accommodate the differences in nanoparticle association. All nanoparticles were tested with 4 individual donors. The errors bars represent standard deviation. * $p < 0.05$; COOH versus PEG or Me or TA, † $p < 0.05$; PEG versus COOH or Me or TA, and ‡ $p < 0.05$; Me versus COOH or PEG or TA.

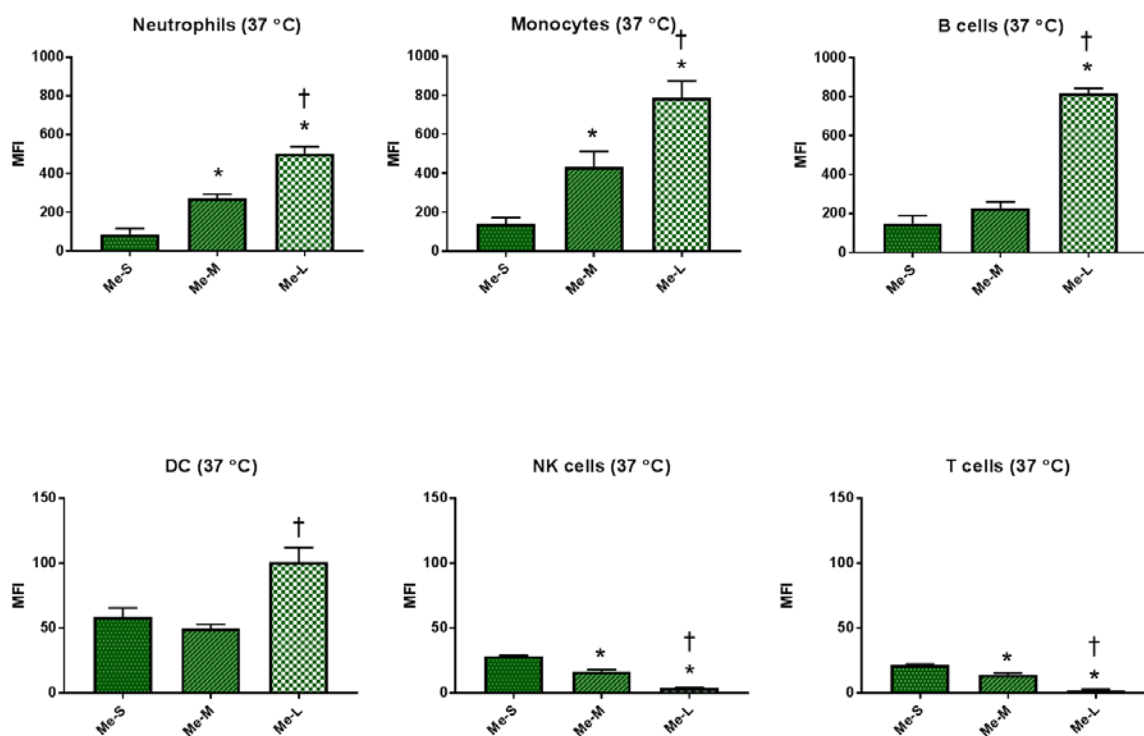


Figure 7. Me-terminated nanoparticles display similar MFI to PEG-terminated nanoparticles; indicating a stealthy characteristic in vivo. Nanoparticles with Me surface groups were incubated with fresh human blood at 100 $\mu\text{g}/\text{mL}$ for 1 h at 4 or 37 $^{\circ}\text{C}$. The red blood cells were lysed and washed before phenotyping with fluorescent antibodies on ice. WBC association with Cy5-labeled nanoparticles was determined by flow cytometry and characterized by median fluorescence intensity (MFI). Note that the scales for the upper and lower rows are distinct from each other to accommodate the differences in nanoparticle association. All nanoparticles were tested with 4 individual donors. The errors bars represent standard deviation. * $p < 0.05$; COOH versus PEG or Me or TA, † < 0.05 ; PEG versus COOH or Me or TA, and ‡ < 0.05 ; Me versus COOH or PEG or TA.

association. In comparison with T cell-based therapies, NK cell therapies are largely limited to pre-clinical studies (42). Overall, the Me-terminated nanoparticles displayed a similar level of immune cell association compared with the PEG-terminated nanoparticles. That is, both Me- and PEG-terminated nanoparticles substantially exhibited lower immune-cell association compared with COOH- and TA-terminated nanoparticles.

4.3.5 Blood proteins affects immune cell association with COOH- and PEG-terminated Nanoparticles

It is well established that phagocytic association of nanoparticles is influenced by the formation of a protein corona (43, 44). To investigate the effect of protein corona formation in this study, we fractionated whole blood through Ficoll Paque density gradient to obtain a buffy coat layer that contains mostly PBMCs (T cells, B cells, NK cells, and monocytes) except granulocytes, dendritic cells, red blood cells, platelets, and proteins. After aspirating the buffy coat from the fractionated whole blood, the nanoparticle library was incubated with the buffy coat for 1 hr at 37 °C, and the results analyzed on flow cytometer.

Based on the small nanoparticle dataset, we observed that the incubation of small nanoparticles with the PBMCs resulted in an increased association of T cells, B cells, NK cells, and monocytes with the COOH- and PEG-terminated nanoparticles (Figure 8). The increased association of PBMCs with anionic nanoparticles that were terminated with COOH groups was reflected in a prior study that investigated association of anionic hyperbranched nanoparticles with PBMCs (16). There were no appreciable changes in PBMC association with the Me-terminated nanoparticles. Furthermore, TA-terminated nanoparticles showed increased association with T cells in the absence of plasma proteins but showed decreased association with B cells. With the PEG-terminated nanoparticles, we observed an increase in PBMC association, which could lead to increased non-specific uptake and subsequent bodily clearance

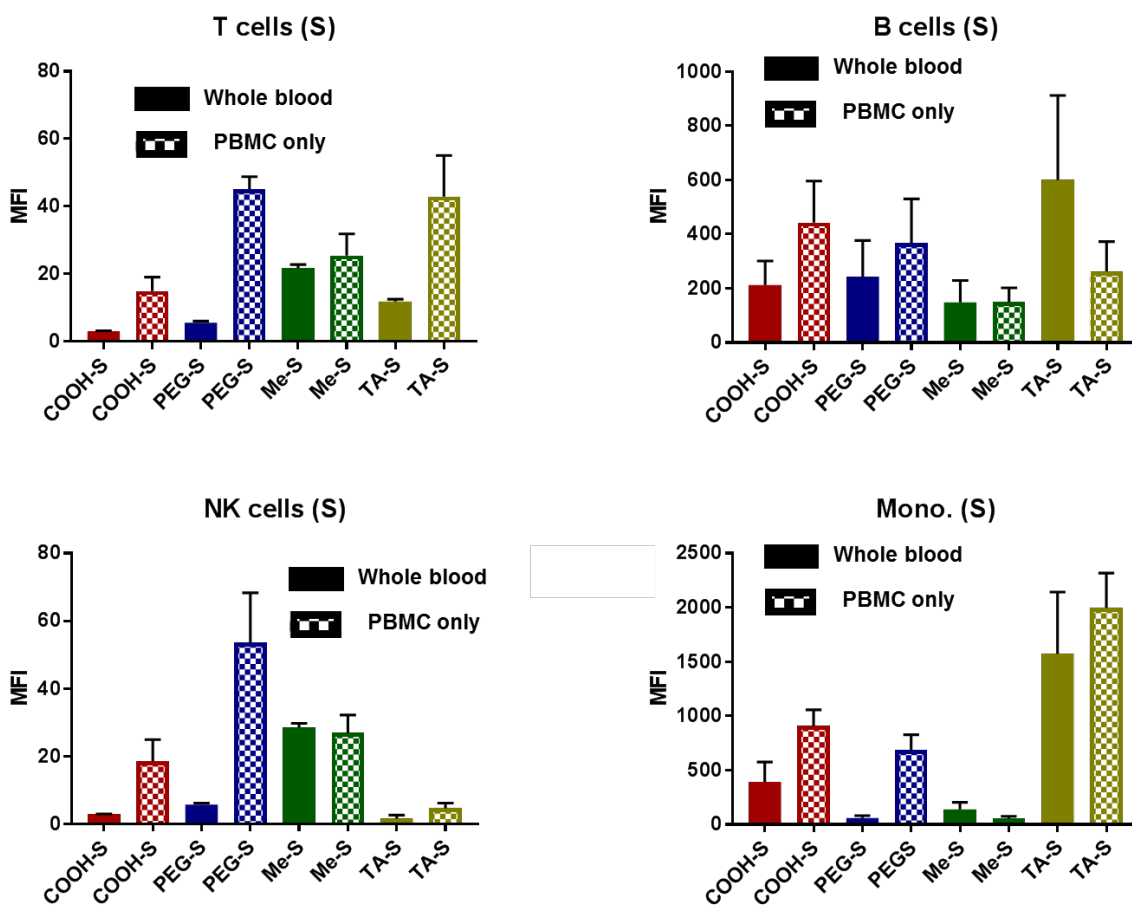


Figure 8. Anionic and PEGylated nanoparticles show increased PBMC association in the absence of blood plasma proteins. Whole blood was fractionated to obtain a buffy coat, wherein nanoparticles were incubated in the buffy coat which is substantially made up of PBMCs. All nanoparticles were tested with 4 individual donors. The error bars represent standard deviation.

(45). However, there is literature evidence that showed that polystyrene nanoparticles modified with PEG or poly(ethyl ethylene phosphate) and exposed to plasma proteins display low immune cell uptake (46).

Remarkably, Wurm and colleagues showed that cellular uptake increased in the absence of plasma proteins, showing that certain plasma proteins (such as clusterin) are necessary to inhibit non-specific cellular uptake (46). Likewise, our data also showed a similar behaviour in that cellular association increased in the absence of plasma proteins.

When the nanoparticle size was increased, nanoparticle association for the COOH- and PEG-terminated nanoparticles increased albeit modestly in comparison with their smaller counterparts (Figure 9). Similarly, there were no appreciable changes in nanoparticle association for Me- and TA-terminated nanoparticles. This result suggests that the increase in nanoparticle size could also cause an increase in proteins such as clusterin that inhibit non-specific cellular uptake.

4.3.6 Phagocytic Association with Nanoparticles is Strongly Predicted by Nanoparticle Size and Surface Chemistry

Multiple Linear Regression (MLR) analysis was carried out based on previous works that modelled the relationship of experimental factors and biological/chemical responses (47, 48). The main objective of our MLR analysis was to conduct a holistic comparison of the physicochemical properties of the 11 nanoparticles against their WBC association and determine which experimental factors are statistically significant in this data set. It should be noted that unlike previous studies, the statistical modelling carried out in this work is not intended to predict nanoparticle association with WBCs beyond the current data set. No simulations were carried out for this study because of the relatively small data set. Rather, MLR analysis in the context of this study was carried out primarily to determine the coefficient of

statistically significant ($p < 0.05$) experimental factors (PDI, TEM_D , Z average, zeta potential, particle size distribution (PSD), and MLogP). A positive MLR coefficient predicts that the

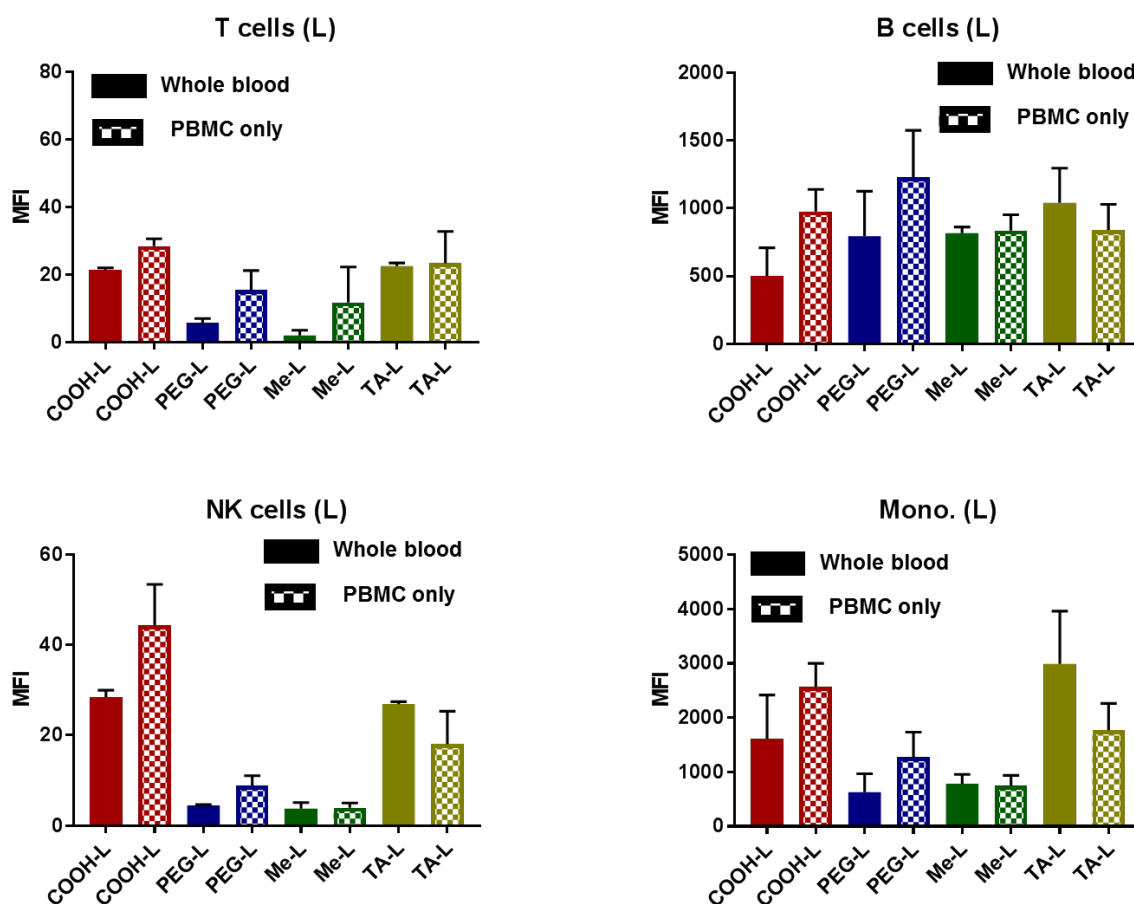


Figure 9. The effect of blood plasma protein on PBMC association for larger nanoparticles (~130 nm) is attenuated in comparison with their smaller nanoparticle counterparts (~30 nm). Whole blood was fractionated to obtain a buffy coat, wherein nanoparticles were incubated in the buffy coat which is substantially made up of PBMCs. All nanoparticles were tested with 4 individual donors. The error bars represent standard deviation.

experimental factor promotes nanoparticle association and a negative MLR predicts an decrease in nanoparticle association.

MLR analysis was carried out according to the experimental factors and biological responses disclosed herein (Table 1). After an MLR response was obtained, statistically insignificant experimental factors ($p > 0.05$) were systematically eliminated from the model one-by-one until none remained. Based on this methodology, we obtained statistically significant results for nanoparticle association with neutrophils and monocytes. Other cellular populations (B cells, DC, NK cells, and T cells) were not statistically significantly affected by the sum and individual experimental factors. For the neutrophil model, the surface chemistry of nanoparticles (as modelled by their MLogP) was the most significant factor in their association with neutrophils. Specifically, this meant that for a unit change in MLogP value (i.e. from the lowest MlogP value; PEG to the highest MlogP value; TA) together with other experimental factors kept constant, neutrophil association increased by 192 MFI units. Comparatively, for a unit change in nanoparticle size, nanoparticle association is predicted to increase by 68 and 61 MFI units respectively (Table 2). Likewise, our monocyte model indicated that nanoparticle size and end group also significantly affected monocyte association as a whole (Table 2).

Table 1 Experimental factors and corresponding response values

NP	Experimental factors						Association (MFI)					
	PDI	TEM _D (nm)	Z Ave (nm)	Zeta Potential (mV)	MLogP	PSD	Neutrophils	Monocytes	DC	B cells	NK cells	T cells
COOH-S	1.38	36	36	-14	-0.386	0.18	219	392	24	213	3	3
COOH-M	1.4	74	77	-12	-0.386	0.105	671	1102	44	406	6	9
COOH-L	1.41	132	141	-13	-0.386	0.035	1648	1610	68	502	28	21
PEG-S	1.42	39	40	-11	-2.523	0.25	65	59	29	244	6	6
PEG-M	1.59	70	75	-9	-2.523	0.143	694	487	37	753	4	5
PEG-L	1.66	142	138	-10	-2.523	0.162	732	630	19	795	5	6
Me-S	1.28	34	39	-1.5	0.133	0.111	86	141	59	149	29	22
Me-M	1.33	75	78	-1.8	0.133	0.039	272	433	50	228	17	14
Me-L	1.38	139	138	-1.2	0.133	0.015	501	787	101	818	4	2
TA-S	1.44	35	35	-6	0.891	0.188	547	1574	37	600	2	12
TA-L	1.52	133	145	-5	0.891	0.082	1854	2995	19	1042	27	23

Table 2 Coefficients of experimental factors against nanoparticle-cell association

Coefficients	Neutrophils	Monocytes
PDI	-	-
TEM _D (nm)	61.0	70.0
Z Ave (nm)	68.0	80.0
Zeta Potential (mV)	-35.0	-
MLogP	192	593
PSD	-	-

4.4 Conclusion

The results in this thesis chapter demonstrate that i) PEG and Me-terminated nanoparticles are less-likely to be phagocytosed by blood monocytes and neutrophils when compared to COOH- and , ii) larger nanoparticles are more strongly associated with immune cells than smaller nanoparticles, iii) COOH and PEG-decorated nanoparticle association with PBMCs increase in the absence of plasma proteins, and iv) size is a statistically more significant effector of WBC association with nanoparticle in comparison with nanoparticle surface chemistry. The data enclosed in this thesis chapter is expected to aid the clinical translation of nanoparticles because of the characterization of nano-bio interactions of nanoparticles in human whole blood. Future studies could expand on other physicochemical properties such as morphology, stiffness, and targeting ligands to provide optimum nanoparticle designs for potential applications such as drug delivery, immunotherapy, and imaging.

4.5 References

1. Zhang L, Gu F, Chan J, Wang A, Langer R, Farokhzad O. Nanoparticles in medicine: therapeutic applications and developments. *Clinical pharmacology & therapeutics*. 2008;83(5):761-9.
2. Peer D, Karp JM, Hong S, Farokhzad OC, Margalit R, Langer R. Nanocarriers as an emerging platform for cancer therapy. *Nature nanotechnology*. 2007;2(12):751.
3. Truong NP, Gu W, Prasadam I, Jia Z, Crawford R, Xiao Y, et al. An influenza virus-inspired polymer system for the timed release of siRNA. *Nature communications*. 2013;4:1902.
4. Elsabahy M, Wooley KL. Design of polymeric nanoparticles for biomedical delivery applications. *Chemical Society Reviews*. 2012;41(7):2545-61.
5. Lee N, Hyeon T. Designed synthesis of uniformly sized iron oxide nanoparticles for efficient magnetic resonance imaging contrast agents. *Chemical Society Reviews*. 2012;41(7):2575-89.
6. Lee D-E, Koo H, Sun I-C, Ryu JH, Kim K, Kwon IC. Multifunctional nanoparticles for multimodal imaging and theragnosis. *Chemical Society Reviews*. 2012;41(7):2656-72.
7. Fang RH, Hu C-MJ, Luk BT, Gao W, Copp JA, Tai Y, et al. Cancer cell membrane-coated nanoparticles for anticancer vaccination and drug delivery. *Nano letters*. 2014;14(4):2181-8.
8. Matsui H, Ito T, Ohnishi S. Phagocytosis by macrophages. III. Effects of heat-labile opsonin and poly (L-lysine). *Journal of cell science*. 1983;59(1):133-43.
9. Zhu M, Nie G, Meng H, Xia T, Nel A, Zhao Y. Physicochemical properties determine nanomaterial cellular uptake, transport, and fate. *Accounts of chemical research*. 2012;46(3):622-31.

10. Behzadi S, Serpooshan V, Tao W, Hamaly MA, Alkawareek MY, Dreaden EC, et al. Cellular uptake of nanoparticles: journey inside the cell. *Chemical Society Reviews*. 2017;46(14):4218-44.
11. Pelaz B, Charron G, Pfeiffer C, Zhao Y, De La Fuente JM, Liang XJ, et al. Interfacing engineered nanoparticles with biological systems: anticipating adverse nano–bio interactions. *Small*. 2013;9(9-10):1573-84.
12. Jiang Y, Huo S, Mizuhara T, Das R, Lee Y-W, Hou S, et al. The interplay of size and surface functionality on the cellular uptake of sub-10 nm gold nanoparticles. *ACS nano*. 2015;9(10):9986-93.
13. Walkey CD, Olsen JB, Guo H, Emili A, Chan WC. Nanoparticle size and surface chemistry determine serum protein adsorption and macrophage uptake. *Journal of the American Chemical Society*. 2012;134(4):2139-47.
14. He C, Hu Y, Yin L, Tang C, Yin C. Effects of particle size and surface charge on cellular uptake and biodistribution of polymeric nanoparticles. *Biomaterials*. 2010;31(13):3657-66.
15. Reuter A, Panozza SE, Macri C, Dumont C, Li J, Liu H, et al. Criteria for dendritic cell receptor selection for efficient antibody-targeted vaccination. *The Journal of Immunology*. 2015:1402535.
16. Glass JJ, Chen L, Alcantara S, Crampin EJ, Thurecht KJ, De Rose R, et al. Charge Has a Marked Influence on Hyperbranched Polymer Nanoparticle Association in Whole Human Blood. *ACS Macro Letters*. 2017;6(6):586-92.
17. Glass JJ, Li Y, De Rose R, Johnston AP, Czuba EI, Khor SY, et al. Thiol-Reactive Star Polymers Display Enhanced Association with Distinct Human Blood Components. *ACS applied materials & interfaces*. 2017;9(14):12182-94.

18. Glass JJ, Kent SJ, De Rose R. Enhancing dendritic cell activation and HIV vaccine effectiveness through nanoparticle vaccination. *Expert review of vaccines*. 2016;15(6):719-29.
19. Cui J, De Rose R, Alt K, Alcantara S, Paterson BM, Liang K, et al. Engineering poly (ethylene glycol) particles for improved biodistribution. *ACS nano*. 2015;9(2):1571-80.
20. De Rose R, Zelikin AN, Johnston AP, Sexton A, Chong SF, Cortez C, et al. Binding, internalization, and antigen presentation of vaccine-loaded nanoengineered capsules in blood. *Advanced Materials*. 2008;20(24):4698-703.
21. Khor SY, Vu MN, Pilkington EH, Johnston AP, Whittaker MR, Quinn JF, et al. Elucidating the Influences of Size, Surface Chemistry, and Dynamic Flow on Cellular Association of Nanoparticles Made by Polymerization-Induced Self-Assembly. *Small*. 2018;14(34):1801702.
22. Truong NP, Dussert MV, Whittaker MR, Quinn JF, Davis TP. Rapid synthesis of ultrahigh molecular weight and low polydispersity polystyrene diblock copolymers by RAFT-mediated emulsion polymerization. *Polymer Chemistry*. 2015;6(20):3865-74.
23. Khor SY, Truong NP, Quinn JF, Whittaker MR, Davis TP. Polymerization-induced self-assembly: The effect of end group and initiator concentration on morphology of nanoparticles prepared via RAFT aqueous emulsion polymerization. *ACS Macro Letters*. 2017;6(9):1013-9.
24. Schwartz A, Gaigalas AK, Wang L, Marti GE, Vogt RF, Fernandez-Repollet E. Formalization of the MESF unit of fluorescence intensity. *Cytometry Part B: Clinical Cytometry: The Journal of the International Society for Analytical Cytology*. 2004;57(1):1-6.
25. Moriguchi I, HIRONO S, LIU Q, NAKAGOME I, MATSUSHITA Y. Simple method of calculating octanol/water partition coefficient. *Chemical and pharmaceutical bulletin*. 1992;40(1):127-30.

26. Tao L, Liu J, Xu J, Davis TP. Synthesis and bioactivity of poly (HPMA)–lysozyme conjugates: the use of novel thiazolidine-2-thione coupling chemistry. *Organic & biomolecular chemistry*. 2009;7(17):3481-5.
27. Tao L, Liu J, Davis TP. Branched Polymer– Protein Conjugates Made From Mid-Chain-Functional P (HPMA). *Biomacromolecules*. 2009;10(10):2847-51.
28. Lesniak A, Fenaroli F, Monopoli MP, Åberg C, Dawson KA, Salvati A. Effects of the presence or absence of a protein corona on silica nanoparticle uptake and impact on cells. *ACS nano*. 2012;6(7):5845-57.
29. Herd H, Daum N, Jones AT, Huwer H, Ghandehari H, Lehr C-M. Nanoparticle geometry and surface orientation influence mode of cellular uptake. *ACS nano*. 2013;7(3):1961-73.
30. Atukorale PU, Yang Y-S, Bekdemir A, Carney RP, Silva PJ, Watson N, et al. Influence of the glycocalyx and plasma membrane composition on amphiphilic gold nanoparticle association with erythrocytes. *Nanoscale*. 2015;7(26):11420-32.
31. Bartneck M, Keul HA, Singh S, Czaja K, Bornemann J, Bockstaller M, et al. Rapid uptake of gold nanorods by primary human blood phagocytes and immunomodulatory effects of surface chemistry. *ACS nano*. 2010;4(6):3073-86.
32. Rodriguez PL, Harada T, Christian DA, Pantano DA, Tsai RK, Discher DE. Minimal "Self" peptides that inhibit phagocytic clearance and enhance delivery of nanoparticles. *Science*. 2013;339(6122):971-5.
33. Toduka Y, Toyooka T, Ibuki Y. Flow cytometric evaluation of nanoparticles using side-scattered light and reactive oxygen species-mediated fluorescence–correlation with genotoxicity. *Environmental science & technology*. 2012;46(14):7629-36.
34. Van der Pol E, Coumans F, Grootemaat A, Gardiner C, Sargent I, Harrison P, et al. Particle size distribution of exosomes and microvesicles determined by transmission electron

microscopy, flow cytometry, nanoparticle tracking analysis, and resistive pulse sensing. *Journal of Thrombosis and Haemostasis*. 2014;12(7):1182-92.

35. Zhu S, Ma L, Wang S, Chen C, Zhang W, Yang L, et al. Light-scattering detection below the level of single fluorescent molecules for high-resolution characterization of functional nanoparticles. *ACS nano*. 2014;8(10):10998-1006.

36. Zucker RM, Ortenzio JN, Boyes WK. Characterization, detection, and counting of metal nanoparticles using flow cytometry. *Cytometry Part A*. 2016;89(2):169-83.

37. Konokhova AI, Chernova DN, Strokotov DI, Karpenko AA, Chernyshev AV, Maltsev VP, et al. Light-scattering gating and characterization of plasma microparticles. *Journal of biomedical optics*. 2016;21(11):115003.

38. Kang T, Zhu Q, Wei D, Feng J, Yao J, Jiang T, et al. Nanoparticles coated with neutrophil membranes can effectively treat cancer metastasis. *ACS nano*. 2017;11(2):1397-411.

39. Xuan M, Shao J, Dai L, He Q, Li J. Macrophage cell membrane camouflaged mesoporous silica nanocapsules for in vivo cancer therapy. *Advanced healthcare materials*. 2015;4(11):1645-52.

40. Huang B, Abraham WD, Zheng Y, López SCB, Luo SS, Irvine DJ. Active targeting of chemotherapy to disseminated tumors using nanoparticle-carrying T cells. *Science translational medicine*. 2015;7(291):291ra94-ra94.

41. Stephan MT, Moon JJ, Um SH, Bershteyn A, Irvine DJ. Therapeutic cell engineering with surface-conjugated synthetic nanoparticles. *Nature medicine*. 2010;16(9):1035.

42. Guillerey C, Huntington ND, Smyth MJ. Targeting natural killer cells in cancer immunotherapy. *Nature immunology*. 2016;17(9):1025.

43. Monopoli MP, Åberg C, Salvati A, Dawson KA. Biomolecular coronas provide the biological identity of nanosized materials. *Nature nanotechnology*. 2012;7(12):779.

44. Tenzer S, Docter D, Kuharev J, Musyanovych A, Fetz V, Hecht R, et al. Rapid formation of plasma protein corona critically affects nanoparticle pathophysiology. *Nature nanotechnology*. 2013;8(10):772.
45. Yang Q, Jones SW, Parker CL, Zamboni WC, Bear JE, Lai SK. Evading immune cell uptake and clearance requires PEG grafting at densities substantially exceeding the minimum for brush conformation. *Molecular pharmaceutics*. 2014;11(4):1250-8.
46. Schöttler S, Becker G, Winzen S, Steinbach T, Mohr K, Landfester K, et al. Protein adsorption is required for stealth effect of poly (ethylene glycol)-and poly (phosphoester)-coated nanocarriers. *Nature nanotechnology*. 2016;11(4):372.
47. Sainz V, Peres C, Ciman T, Rodrigues C, Viana A, Afonso C, et al. Optimization of protein loaded PLGA nanoparticle manufacturing parameters following a quality-by-design approach. *RSC Advances*. 2016;6(106):104502-12.
48. Le TC, Yan B, Winkler DA. Robust prediction of personalized cell recognition from a cancer population by a dual targeting nanoparticle library. *Advanced Functional Materials*. 2015;25(44):6927-35.

**Chapter 5: Polymerization-Induced Self-Assembly: The Effect of
End Group and Initiator Concentration on Morphology of
Nanoparticles Prepared via RAFT Aqueous Emulsion
Polymerization**

Polymerization-Induced Self-Assembly: The Effect of End Group and Initiator Concentration on Morphology of Nanoparticles Prepared via RAFT Aqueous Emulsion Polymerization

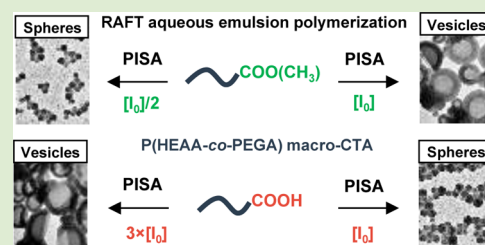
Song Yang Khor,[†] Nghia P. Truong,[†] John F. Quinn,[†] Michael R. Whittaker,^{*,†} and Thomas P. Davis^{*,†,‡}

[†]ARC Centre of Excellence in Convergent Bio-Nano Science and Technology, Monash Institute of Pharmaceutical Sciences, Monash University, Parkville, Melbourne, Victoria 3052, Australia

[‡]Department of Chemistry, University of Warwick, Coventry CV4 7AL, United Kingdom

Supporting Information

ABSTRACT: Polymerization-induced self-assembly (PISA) is a widely used technique for the synthesis of nanoparticles with various morphologies including spheres, worms, and vesicles. The development of a PISA formulation based on reversible addition–fragmentation chain transfer (RAFT) aqueous emulsion polymerization offers considerable advantages such as enhanced rate of polymerization, high conversion and environmentally friendly conditions. However, this formulation has typically produced spheres as opposed to worms and vesicles. Herein, we report the formation of vesicle morphology by increasing the RAFT end-group hydrophobicity of the macromolecular chain transfer agent or manipulating the radical initiator concentration used in the aqueous emulsion polymerization PISA formulation. Additionally, decreasing the molecular weight of the hydrophobic polystyrene domain in these vesicles leads to the formation of worms. This work demonstrates that RAFT end-group hydrophobicity and radical initiator concentration are key parameters which can be exploited to enable access to sphere, worm, and vesicle morphologies via the RAFT aqueous emulsion polymerization.



Amphiphilic block copolymer nanoparticles with different morphologies have attracted increasing attention in recent years due to their diverse applications in catalysis, coatings, nanoreactors, imaging, tissue engineering, and drug delivery.^{1–4} Traditionally, spheres, worms, and vesicles have been prepared by the self-assembly of block copolymers in selective solvents.^{5,6} However, this conventional self-assembly technique is usually time-consuming and is generally performed in dilute solution (<2 wt %).⁷ The development of an alternative self-assembly strategy, so-called polymerization-induced self-assembly (PISA), has allowed block copolymer synthesis and self-assembly to be combined in one step.^{8,9} Therefore, PISA has recently become a widely used synthesis technique for the facile preparation of soft functional nanoparticles in relatively concentrated solutions.^{10–12}

In PISA, macromolecular chain transfer agents (macro-CTAs) are typically employed in reversible addition–fragmentation chain transfer (RAFT) dispersion or emulsion polymerizations.^{13–16} During the chain extension of the macro-CTA, the growing amphiphilic block copolymer chains self-assemble in situ into spherical micelles.^{17,18} These micelles subsequently transform into worms and vesicles as the polymerization of the second block continues.^{19,20} This transformation has been widely observed during RAFT dispersion polymerizations, in which the monomers are soluble in the continuous phase.^{21–23} However, in RAFT emulsion

polymerizations of solvophobic monomers (e.g., styrene as a water-immiscible monomer), it has been increasingly recognized that only spherical micelles can be obtained.²⁴ Access to the complete suite of sphere, worm, and vesicle morphologies has not been achieved in the majority of PISA formulations based on RAFT aqueous emulsion polymerizations.^{25–28} The lack of worm and vesicle morphologies limits the scope and application of this particular formulation of PISA.²⁴

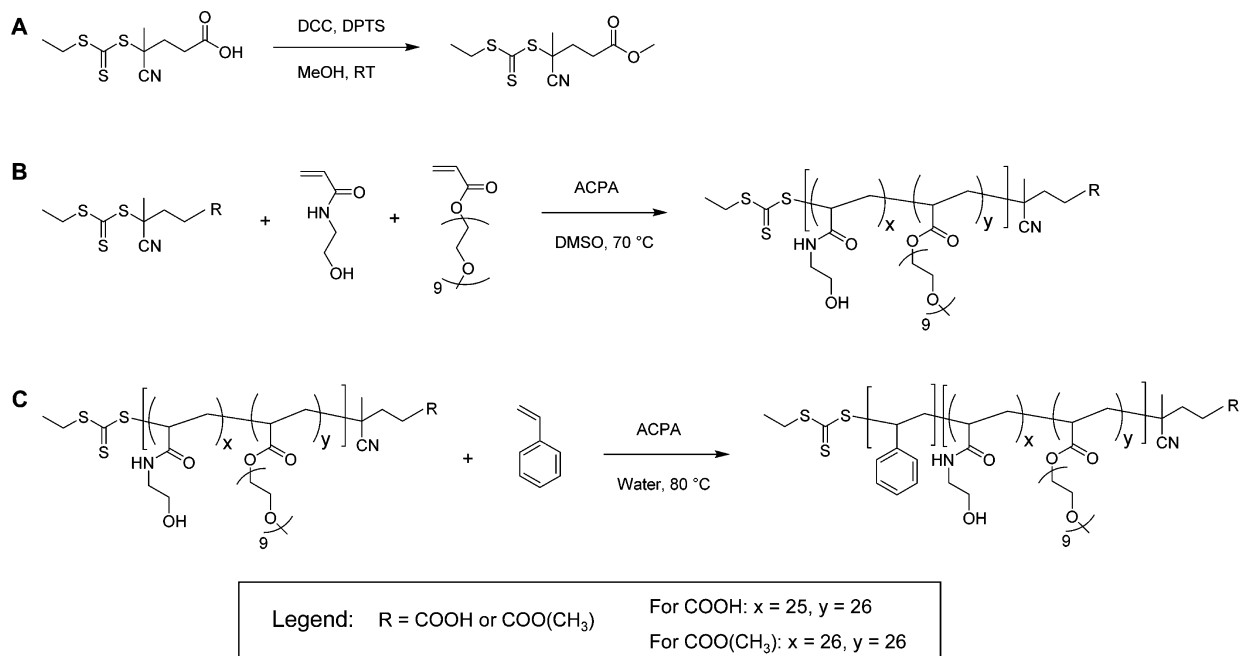
Considerable efforts have been made in order to overcome this limitation by developing specific macro-CTAs for RAFT aqueous emulsion polymerizations. Charleux and co-workers prepared polystyrene spheres, worms, and vesicles by using a specific macro-CTA composed of acrylic acid (AA) and poly(ethylene glycol) methyl ether acrylate (PEGA) units.^{29–31} Truong et al. have recently developed biocompatible thermoresponsive macro-CTAs that allowed the controlled RAFT aqueous emulsion polymerizations of styrene as well as various methacrylates, and subsequently applied these latexes for preparing nanoparticles with tunable morphologies and core properties.^{32,33} Although these significant studies demonstrate that worms and vesicles can be prepared via RAFT aqueous emulsion polymerization, it remains unclear why the majority

Received: August 7, 2017

Accepted: August 28, 2017

Published: August 31, 2017

Scheme 1. (A) Modification of ECT with Methanol; (B) RAFT Polymerization of HEAA and PEGA in the Presence of ECT or ECT-Me in DMSO at 70 °C; (C) Aqueous RAFT Emulsion Polymerization of Styrene Using P(HEAA-co-PEGA)-COOH or P(HEAA-co-PEGA)-Me macro-CTA at 80 °C



of other RAFT aqueous emulsion polymerizations often lead to only spherical nanoparticles. For instance, using a water-miscible macro-CTA comprised *N*-hydroxyethyl acrylamide (HEAA) and PEGA in RAFT aqueous emulsion polymerization of styrene led to only spherical nanoparticles, even when the molecular weight of the polystyrene core and the solids content were in the range expected to facilitate worm and vesicle morphologies.²⁸

Toward addressing this challenging question, the groups of D'Agosto and Armes have recently investigated the effects of macro-CTA topology and monomer solubility, respectively, on the evolution of kinetically trapped spheres to other morphologies. It has been found that the presence of PEGA hydrophilic side-chains close to the hydrophobic polystyrene segment promoted the morphology transformation from sphere to vesicle.³⁴ In addition, the use of water-immiscible 2-hydroxybutyl methacrylate for the core-forming block allowed access to an unusual "monkey nut" morphology.³⁵ These works reveal that certain parameters of the RAFT emulsion polymerizations are important to the transformation of spheres to other morphologies. However, the typical worm-like morphology obtained via the PISA technique remained absent when manipulating either the macro-CTA topology or the monomer solubility.^{34,35} Therefore, further research is required to identify other critical parameters in the RAFT aqueous emulsion polymerizations that allow comprehensive access to sphere, worm, and vesicle morphologies.²⁴

In the traditional solution self-assembly technique, the hydrophobicity of the polymer end-group has been identified as a critical parameter in dictating final nanoparticle morphology.³⁶ For example, Du and co-workers reported that the incorporation of a tiny terminal alkynyl group in poly(*N*-isopropylacrylamide) and poly[oligo(ethylene glycol) methacrylate] homopolymers facilitated the self-assembly of hydrophilic polymers and dictated the final morphology of self-assembled nanoparticles.³⁷ However, the effect of this

parameter on the morphology of PISA nanoparticles obtained by RAFT aqueous emulsion polymerization has never been fully investigated although the modification of the end group is relatively simple.^{38–40}

Herein, we studied the effect of macro-CTA end-group hydrophobicity (manipulated through RAFT agent design), on the morphology of nanoparticles formed by PISA using RAFT aqueous emulsion polymerization. Subsequently, we discovered that radical initiator concentration also has a significant effect on the morphology of these PISA nanoparticles. To study these effects, the carboxylic acid end-group of a RAFT agent was first modified to produce a methyl ester-terminated RAFT agent (Scheme 1A). Both RAFT agents were then used for the polymerization of HEAA and PEGA to produce macro-CTAs with carboxylic acid and methyl ester end-groups (Scheme 1B). Next, we conducted a series of aqueous emulsion polymerizations of styrene using both macro-CTAs (Scheme 1C) and studied the morphology of the PISA nanoparticles formed. To the best of our knowledge, this is the first report demonstrating that end-group hydrophobicity and initiator concentration can be used to access to spherical, filamentous, and vesicular nanoparticles via RAFT aqueous emulsion polymerization.

To increase the hydrophobicity of the polymer end-group, the carboxylic acid functional group of 4-cyano-4-(ethylthiocarbonothioylthio)pentanoic acid (ECT) was methylated to produce ECT-Me (Scheme 1A). In this modification, methanol was used as both reactant and solvent. ¹H NMR spectrum in Figure S1B showed a singlet peak belonging to methyl protons adjacent to the ester group at 3.71 ppm (f), confirming a successful methylation reaction. ECT and ECT-Me were then used for the polymerization of HEAA and PEGA via RAFT solution polymerization (Scheme 1B) to yield macro-CTAs with different end-groups, P(HEAA-co-PEGA)-COOH and P(HEAA-co-PEGA)-Me. ¹H NMR was used to calculate the degree of polymerization (DP) of HEAA and PEGA units (Figure S2). By using identical polymerization conditions, two

well-defined macro-CTAs with relatively narrow molecular weight distributions (Figure S3), similar molecular weight, and repeating units were prepared (Table S1), thus, enabling the effect of end-group hydrophobicity on the morphology of PISA nanoparticles to be elucidated.

Subsequently, RAFT aqueous emulsion polymerizations of styrene with P(HEAA-co-PEGA)-COOH and P(HEAA-co-PEGA)-Me were carried out for 6 h at 80 °C. Both reactions reached very high conversions (>90%) and two diblock copolymers with relatively similar repeating units and molecular weights were obtained (Figures S4 and S5 and Table S2). Transmission electron microscopy (TEM) analysis showed that the RAFT aqueous emulsion polymerization of styrene with P(HEAA-co-PEGA)-COOH macro-CTA, even in protonated form at pH below the pK_a (Figure S6), produced only spherical nanoparticles (Figure 1A). This result is consistent with the

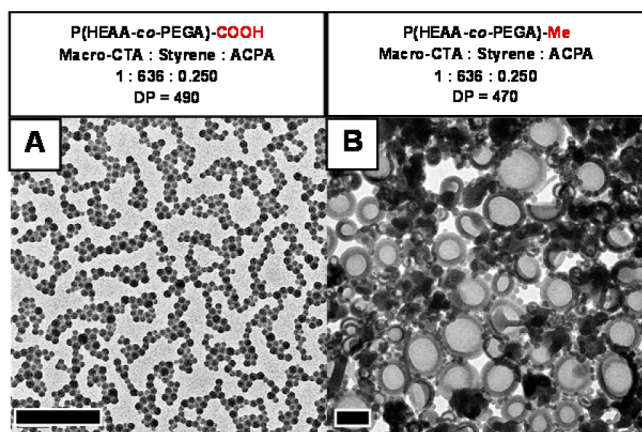


Figure 1. TEM images of the particles formed by RAFT aqueous emulsion polymerization of styrene with (A) P(HEAA-co-PEGA)-COOH and (B) P(HEAA-co-PEGA)-Me, at 80 °C for 6 h. All scale bars represent 500 nm.

outcome of our previous study.²³ Interestingly, the TEM image in Figure 1B revealed that the use of P(HEAA-co-PEGA)-Me macro-CTA under otherwise identical conditions led to the formation of vesicle morphology (Figure 1B). This result demonstrates for the first time that the hydrophobicity of macro-CTA end-groups could change the morphology of nanoparticles prepared by RAFT aqueous emulsion polymer-

izations. It is important to note that an acid radical initiator, 4,4-azobis(4-cyanopentanoic acid) (ACPA), was used in both solution polymerizations (i.e., to make P(HEAA-co-PEGA)-Me macro-CTA) and in the emulsion polymerization (to prepare vesicles). As a result, based on theoretical calculation using eq 1, there is possibly up to 18% of carboxylic acid end-group (%) presented on the surface of the vesicles formed.⁴¹ That said, the presence of methyl ester end-group was sufficient to promote the formation of vesicle morphology, which could not be accessed by using P(HEAA-co-PEGA)-COOH as the macro-CTA.

$$\% = \frac{[I]_0(1 - e^{-k_d t})2f\left(1 - \frac{f_c}{2}\right)}{[\text{macro-CTA}]_0 + [I]_0(1 - e^{-k_d t})2f\left(1 - \frac{f_c}{2}\right)} \quad (1)$$

where $[\text{macro-CTA}]_0$ and $[I]_0$ are the initial concentrations of chain transfer agent and initiator, respectively; $k_d = Ae^{-E_a/RT}$ is the rate constant for initiator decomposition (values of $2.2289 \times 10^{-5} \text{ s}^{-1}$ and $9.2082 \times 10^{-5} \text{ s}^{-1}$ were estimated for the decomposition at 70 and 80 °C based on A (frequency factor) = $1.2461 \times 10^{17} \text{ s}^{-1}$, R (gas constant) = $8.314 \text{ J mol}^{-1} \text{ K}^{-1}$ and E_a (activation energy) = $142800 \text{ J mol}^{-1}$);⁴¹ t is the polymerization time; f is the efficiency of a radical initiator (a value of 0.6 was used in this study); and f_c is the coupling factor (a value of 0 was used in this study).⁴²

The formation of vesicles observed when using the P(HEAA-co-PEGA)-Me macro-CTA could be due to an increase in the critical packing parameter (p) and the number of chains aggregated in one particle (N_a). First, the methyl ester end-group could reduce the effective interfacial area of the formed particles (a), resulting in an increase in p (see eq 2). Second, using P(HEAA-co-PEGA)-Me may facilitate the self-assembly of amphiphilic polymer chains formed during the polymerization leading to a higher number of chains aggregated in one particle (N_a) than using P(HEAA-co-PEGA)-COOH. Both the increase in p and N_a have been previously shown to favor the generation of vesicle morphology rather than spheres.^{43,44} To provide further insight, we hypothesized that reversing the change of p and N_a caused by the methyl ester end-group would lead to the formation of other morphologies. Specifically, we postulated that (i) reducing p by targeting lower molecular weights of polystyrene block would form worms and spheres (as typically found in RAFT dispersion polymerizations)⁴⁵ and

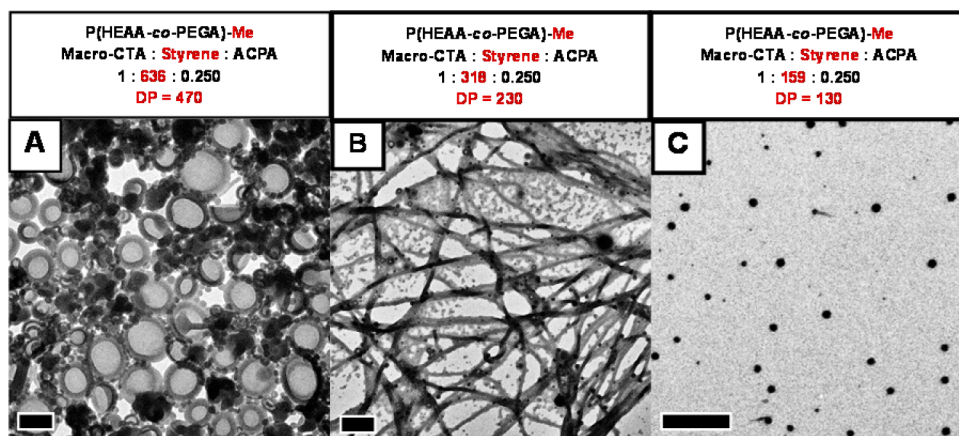


Figure 2. TEM images of particles formed by RAFT aqueous emulsion polymerization of styrene using P(HEAA-co-PEGA)-Me macro-CTA with various styrene: macro-CTA feed ratios (A) 636:1, (B) 318:1, and (C) 159:1. All scale bars represent 500 nm.

(ii) using lower radical initiator concentration would decrease the number of amphiphilic polymer chains forming and aggregating, thus, resulting in a lower N_a that could facilitate spherical morphology found when using the P(HEAA-co-PEGA)-COOH macro-CTA.

$$p = v/al \quad (2)$$

where p is the critical packing parameter; v is the volume of hydrophobic chains; a is an effective interfacial area at the hydrophobic–water interface; and l is the length of hydrophobic chains.

To test the first hypothesis, two more RAFT aqueous emulsion polymerizations using P(HEAA-co-PEGA)-Me as the macro-CTA were conducted. In these two polymerizations, the volume of styrene was reduced by a factor of 2 and 4 in order to reduce the molecular weights of polystyrene (Table S3). In PISA, it has been well-known that decreasing molecular weights of solvophobic polymers constituting the core of nanoparticles usually results in lower p and morphology change from vesicle ($1/2 < p < 1$) to worm ($1/3 < p < 1/2$) and sphere ($p < 1/3$).^{11,44} After 6 h of polymerizations, a similar conversion was reached and, as expected, lower molecular weights of amphiphilic block copolymer were obtained (Table S3; Figure S7). Significantly, the TEM images in Figure 2 revealed worm and sphere morphologies for latexes of lower molecular weight polystyrene particles. These results confirmed our first hypothesis and suggested that the critical packing parameter theory goes some way toward explaining nanoparticle morphology obtained by the PISA technique. In addition, chemical modifications of macro-CTA end-group could become a new tool for the manipulation of nanoparticle morphology.

Next, we tested the second hypothesis by performing RAFT aqueous emulsion polymerization of styrene using P(HEAA-co-PEGA)-Me as the macro-CTA and reducing the concentration of the radical initiator by half (Table S4; Figure S9). Incredibly, we observed the change from vesicles back to spheres (Figure 3) when simply decreasing the radical initiator concentration in the emulsion polymerization. This result not only shed light on the PISA process via RAFT aqueous emulsion polymerizations, but also provided a facile method to synthesize nanoparticles with tunable morphologies. It should be noted that the

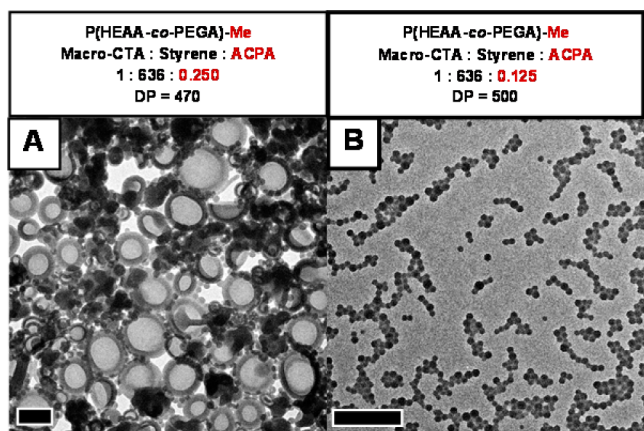


Figure 3. TEM images of particles formed by RAFT aqueous emulsion polymerization of styrene with P(HEAA-co-PEGA)-Me at 80 °C for 6 h with macro-CTA: ACPA feed ratios (A) 1:0.250 and (B) 1:0.125. All scale bars represent 500 nm.

repeating unit of polystyrene was relatively similar, even when a lower amount of the ACPA was used. Therefore, as a result of the reducing radical initiator concentration, the number of polymer chains growing and aggregating (N_a) was decreased and, hence, spheres were produced, although the total number of polymer chains in the solution was unchanged.

Although the formation of spheres at low N_a and vesicles at high N_a is well-known for traditional solution self-assembly, it has not been applied for the PISA method.^{43,46} Moreover, in PISA formulations, other parameters such as molecular weight, solids content, macro-CTA topology, and monomer solubility also interplay with the N_a in the generation of nonspherical morphologies. As such, further work on the overall understanding of all these parameters would be highly desirable. In the current study focusing on the effect of macro-CTA end-groups and initiator concentration, it would be interesting to investigate whether increasing the initiator concentration of RAFT emulsion polymerization using the carboxylic acid end-group macro-CTA could also lead to different morphologies aside from spheres.

P(HEAA-co-PEGA)-COOH macro-CTA was therefore used for the next two RAFT aqueous emulsion polymerizations (Table S5; Figure S8). In these polymerizations, the ACPA concentration was doubled and tripled to increase the number of simultaneously growing and aggregating chains (assuming the number of terminated chains remain the same), which would be expected to form vesicles instead of spheres. Indeed, TEM images (Figure 4) confirmed these expected morphologies. This result demonstrated for the first time that vesicle morphology was achieved by solely tuning the radical initiator concentration from a PISA formulation that otherwise only yielded spherical nanoparticles. Compared to other ways to target nonspherical morphologies such as macro-CTA-hydrophile topology, monomer solubility and end-group modification, this novel strategy does not affect the chemical composition of the final nanoparticles, which is very important in some applications such as drug delivery. That said, the worm morphology was still not clearly observed in Figure 4B.

In pursuit of the worm morphology using P(HEAA-co-PEGA)-COOH, we conducted a series of emulsion polymerizations of styrene with lower amounts of monomer (Table S6). TEM images (Figure 5) showed that as the amount of styrene decreased, a lower polystyrene molecular weight was obtained (Figure S10) and the morphology changed accordingly. When the amount of styrene added was halved, the TEM images showed mainly the worm morphology (Figure 5C). Changing the pH of worm latex did not affect the worm morphology (Figures S11 and S12). It is worth noting that a comprehensive study of the phase diagram by changing the molecular weights of macro-CTAs and polystyrene is required in order to obtain pure worms. Further decrease in the amount of styrene added produced spheres (Figure 5D). The morphological change from vesicle to worm and then to sphere aligns with the decrease in p discussed above.

In conclusion, we have demonstrated for the first time that macro-CTA end-group hydrophobicity and radical initiator concentration are critical parameters that allow comprehensive access to sphere, worm, and vesicle morphology of PISA nanoparticles synthesized via RAFT aqueous emulsion polymerization. In particular, increasing the end-group hydrophobicity by substituting the carboxylic acid end-group with a methyl ester group led to the formation of vesicles. Remarkably, altering the radical initiator concentration also resulted in a

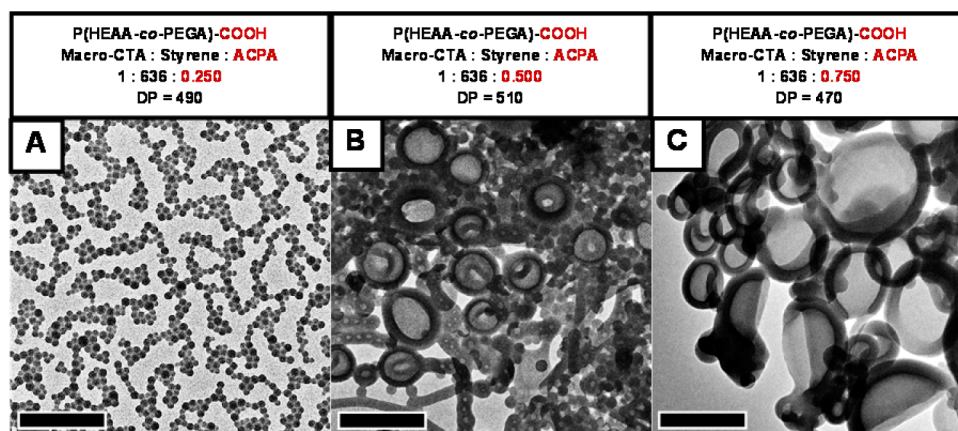


Figure 4. TEM images of particles formed by RAFT aqueous emulsion polymerization of styrene using P(HEAA-co-PEGA)-COOH macro-CTA with macro-CTA: ACPA ratio (A) 1:0.250, (B) 1:0.500, and (C) 1:0.750. All scale bars represent 500 nm.

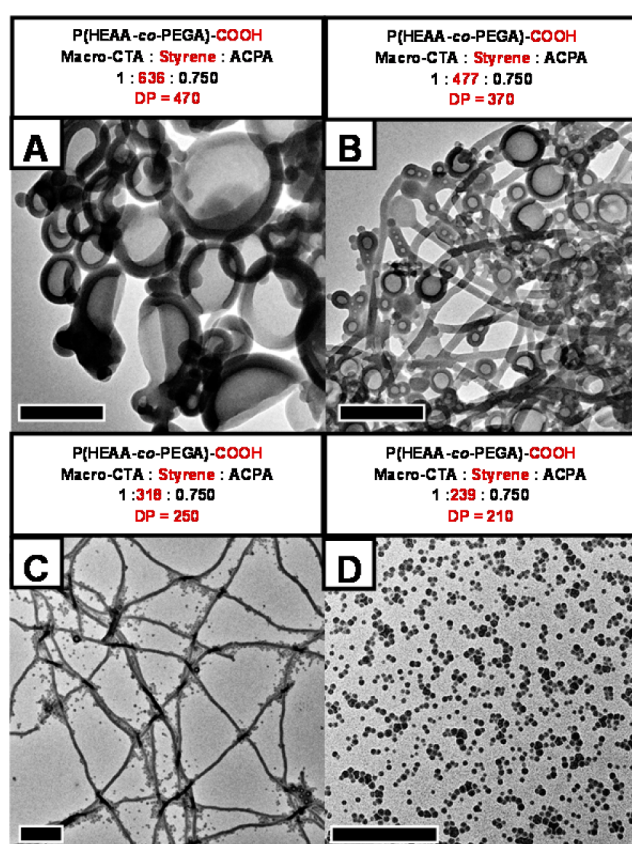


Figure 5. TEM images of particles formed by RAFT aqueous emulsion polymerization of styrene with P(HEAA-co-PEGA)-COOH macro-CTA at 80 °C with styrene: macro-CTA feed ratio (A) 636:1, (B) 477:1, (C) 318:1, and (D) 238:1. All scale bars represent 500 nm.

morphological change between spheres and vesicles. Worm morphology could also be obtained when the molecular weight of the polystyrene block constituting the PISA nanoparticles was decreased. Altogether, this work adds significant knowledge to the field of controlling nanoparticle morphology via RAFT aqueous emulsion polymerization and provides an environmentally friendly technique for the synthesis of nanomaterials with tunable shapes.

■ ASSOCIATED CONTENT

Supporting Information

The Supporting Information is available free of charge on the ACS Publications website at DOI: [10.1021/acsmacrolett.7b00583](https://doi.org/10.1021/acsmacrolett.7b00583).

Experimental details and supporting figures and tables (PDF).

■ AUTHOR INFORMATION

Corresponding Authors

*E-mail: michael.whittaker@monash.edu.

*E-mail: thomas.p.davis@monash.edu.

ORCID

Song Yang Khor: 0000-0003-2437-3218

Nghia P. Truong: 0000-0001-9900-2644

John F. Quinn: 0000-0002-4593-1170

Michael R. Whittaker: 0000-0001-5706-3932

Thomas P. Davis: 0000-0003-2581-4986

Author Contributions

The manuscript was written through contributions of all authors. All authors have given approval to the final version of the manuscript.

Notes

The authors declare no competing financial interest.

■ ACKNOWLEDGMENTS

Electron microscopy was performed at the Bio21 Advanced Microscopy Facility, The University of Melbourne. This work was carried out within the Australian Research Council (ARC) Centre of Excellence in Convergent Bio-Nano Science and Technology (Project No. CE140100036). S.Y.K. acknowledges the financial support from the Australian Government Research Training Program Scholarship. N.P.T. acknowledges the Honourable Geoffrey Connard AM Early Career Researcher Award. J.F.Q. acknowledges receipt of a Future Fellowship from the ARC (FT170100144). T.P.D. is grateful for the award of an Australian Laureate Fellowship from the ARC.

■ REFERENCES

- (1) Truong, N. P.; Whittaker, M. R.; Mak, C. W.; Davis, T. P. The importance of nanoparticle shape in cancer drug delivery. *Expert Opin. Drug Delivery* **2015**, *12*, 129.

- (2) Canton, I.; Warren, N. J.; Chahal, A.; Amps, K.; Wood, A.; Weightman, R.; Wang, E.; Moore, H.; Armes, S. P. Mucin-Inspired Thermoresponsive Synthetic Hydrogels Induce Stasis in Human Pluripotent Stem Cells and Human Embryos. *ACS Cent. Sci.* **2016**, *2*, 65.
- (3) Ta, H. T.; Truong, N. P.; Whittaker, A. K.; Davis, T. P.; Peter, K. The effects of particle size, shape, density and flow characteristics on particle margination to vascular walls in cardiovascular diseases. *Expert Opin. Drug Delivery* **2017**, *1*, na.
- (4) Truong, N. P.; Gu, W. Y.; Prasadam, I.; Jia, Z. F.; Crawford, R.; Xiao, Y.; Monteiro, M. J. An influenza virus-inspired polymer system for the timed release of siRNA. *Nat. Commun.* **2013**, *4*, 1902.
- (5) Zhang, L.; Eisenberg, A. Multiple Morphologies of "Crew-Cut" Aggregates of Polystyrene-*b*-poly(acrylic acid) Block Copolymers. *Science* **1995**, *268*, 1728.
- (6) Zhang, L. F.; Yu, K.; Eisenberg, A. Ion-induced morphological changes in "crew-cut" aggregates of amphiphilic block copolymers. *Science* **1996**, *272*, 1777.
- (7) Fielding, L. A.; Lane, J. A.; Derry, M. J.; Mykhaylyk, O. O.; Armes, S. P. Thermo-responsive Diblock Copolymer Worm Gels in Non-polar Solvents. *J. Am. Chem. Soc.* **2014**, *136*, 5790.
- (8) Charleux, B.; Delaître, G.; Rieger, J.; D'Agosto, F. Polymerization-Induced Self-Assembly: From Soluble Macromolecules to Block Copolymer Nano-Objects in One Step. *Macromolecules* **2012**, *45*, 6753.
- (9) Tan, J.; Sun, H.; Yu, M.; Sumerlin, B. S.; Zhang, L. Photo-PISA: Shedding Light on Polymerization-Induced Self-Assembly. *ACS Macro Lett.* **2015**, *4*, 1249.
- (10) Wan, W. M.; Hong, C. Y.; Pan, C. Y. One-pot synthesis of nanomaterials via RAFT polymerization induced self-assembly and morphology transition. *Chem. Commun.* **2009**, 5883.
- (11) Warren, N. J.; Armes, S. P. Polymerization-Induced Self-Assembly of Block Copolymer Nano-objects via RAFT Aqueous Dispersion Polymerization. *J. Am. Chem. Soc.* **2014**, *136*, 10174.
- (12) Tan, J. B.; Huang, C. D.; Liu, D. D.; Li, X. L.; He, J.; Xu, Q.; Zhang, L. Polymerization-Induced Self-Assembly of Homopolymer and Diblock Copolymer: A Facile Approach for Preparing Polymer Nano-Objects with Higher-Order Morphologies. *ACS Macro Lett.* **2017**, *6*, 298.
- (13) Truong, N. P.; Quinn, J. F.; Whittaker, M. R.; Davis, T. P. Polymeric filomicelles and nanoworms: two decades of synthesis and application. *Polym. Chem.* **2016**, *7*, 4295.
- (14) Zhang, B. H.; Lv, X. Q.; An, Z. S. Modular Monomers with Tunable Solubility: Synthesis of Highly Incompatible Block Copolymer Nano-Objects via RAFT Aqueous Dispersion Polymerization. *ACS Macro Lett.* **2017**, *6*, 224.
- (15) Gao, P.; Cao, H.; Ding, Y.; Cai, M.; Cui, Z. G.; Lu, X. H.; Cai, Y. L. Synthesis of Hydrogen-Bonded Pore-Switchable Cylindrical Vesicles via Visible-Light-Mediated RAFT Room-Temperature Aqueous Dispersion Polymerization. *ACS Macro Lett.* **2016**, *5*, 1327.
- (16) Wang, X.; Figg, C. A.; Lv, X. Q.; Yang, Y. Q.; Sumerlin, B. S.; An, Z. S. Star Architecture Promoting Morphological Transitions during Polymerization-Induced Self-Assembly. *ACS Macro Lett.* **2017**, *6*, 337.
- (17) Yeow, J.; Xu, J. T.; Boyer, C. Polymerization-Induced Self-Assembly Using Visible Light Mediated Photoinduced Electron Transfer-Reversible Addition-Fragmentation Chain Transfer Polymerization. *ACS Macro Lett.* **2015**, *4*, 984.
- (18) Zhou, W.; Qu, Q. W.; Xu, Y. Y.; An, Z. S. Aqueous Polymerization-Induced Self-Assembly for the Synthesis of Ketone-Functionalized Nano-Objects with Low Polydispersity. *ACS Macro Lett.* **2015**, *4*, 495.
- (19) Esser, L.; Truong, N. P.; Karagoz, B.; Moffat, B. A.; Boyer, C.; Quinn, J. F.; Whittaker, M. R.; Davis, T. P. Gadolinium-functionalized nanoparticles for application as magnetic resonance imaging contrast agents via polymerization-induced self-assembly. *Polym. Chem.* **2016**, *7*, 7325.
- (20) Qu, Q. W.; Liu, G. Y.; Lv, X. Q.; Zhang, B. H.; An, Z. S. In Situ Cross-Linking of Vesicles in Polymerization-Induced Self Assembly. *ACS Macro Lett.* **2016**, *5*, 316.
- (21) Derry, M. J.; Fielding, L. A.; Armes, S. P. Polymerization-induced self-assembly of block copolymer nanoparticles via RAFT non-aqueous dispersion polymerization. *Prog. Polym. Sci.* **2016**, *52*, 1.
- (22) Sugihara, S.; Blanazs, A.; Armes, S. P.; Ryan, A. J.; Lewis, A. L. Aqueous Dispersion Polymerization: A New Paradigm for in Situ Block Copolymer Self-Assembly in Concentrated Solution. *J. Am. Chem. Soc.* **2011**, *133*, 15707.
- (23) Zhu, A. Q.; Lv, X. Q.; Shen, L. L.; Zhang, B. H.; An, Z. S. Polymerization-Induced Cooperative Assembly of Block Copolymer and Homopolymer via RAFT Dispersion Polymerization. *ACS Macro Lett.* **2017**, *6*, 304.
- (24) Canning, S. L.; Smith, G. N.; Armes, S. P. A Critical Appraisal of RAFT-Mediated Polymerization-Induced Self-Assembly. *Macromolecules* **2016**, *49*, 1985.
- (25) Cunningham, V. J.; Alswieleh, A. M.; Thompson, K. L.; Williams, M.; Leggett, G. J.; Armes, S. P.; Musa, O. M. Poly(glycerol monomethacrylate)-Poly(benzyl methacrylate) Diblock Copolymer Nanoparticles via RAFT Emulsion Polymerization: Synthesis, Characterization, and Interfacial Activity. *Macromolecules* **2014**, *47*, 5613.
- (26) Rieger, J.; Zhang, W. J.; Stoffelbach, F.; Charleux, B. Surfactant-Free RAFT Emulsion Polymerization Using Poly(N,N-dimethylacrylamide) Trithiocarbonate Macromolecular Chain Transfer Agents. *Macromolecules* **2010**, *43*, 6302.
- (27) Chaduc, I.; Girod, M.; Antoine, R.; Charleux, B.; D'Agosto, F.; Lansalot, M. Batch Emulsion Polymerization Mediated by Poly(methacrylic acid) MacroRAFT Agents: One-Pot Synthesis of Self-Stabilized Particles. *Macromolecules* **2012**, *45*, 5881.
- (28) Truong, N. P.; Dussert, M. V.; Whittaker, M. R.; Quinn, J. F.; Davis, T. P. Rapid synthesis of ultrahigh molecular weight and low polydispersity polystyrene diblock copolymers by RAFT-mediated emulsion polymerization. *Polym. Chem.* **2015**, *6*, 3865.
- (29) Boisse, S.; Rieger, J.; Belal, K.; Di-Cicco, A.; Beaunier, P.; Li, M. H.; Charleux, B. Amphiphilic block copolymer nano-fibers via RAFT-mediated polymerization in aqueous dispersed system. *Chem. Commun.* **2010**, *46*, 1950.
- (30) Zhang, W. J.; D'Agosto, F.; Boyron, O.; Rieger, J.; Charleux, B. Toward Better Understanding of the Parameters that Lead to the Formation of Nonspherical Polystyrene Particles via RAFT-Mediated One-Pot Aqueous Emulsion Polymerization. *Macromolecules* **2012**, *45*, 4075.
- (31) Chaduc, I.; Crepet, A.; Boyron, O.; Charleux, B.; D'Agosto, F.; Lansalot, M. Effect of the pH on the RAFT Polymerization of Acrylic Acid in Water. Application to the Synthesis of Poly(acrylic acid)-Stabilized Polystyrene Particles by RAFT Emulsion Polymerization. *Macromolecules* **2013**, *46*, 6013.
- (32) Truong, N. P.; Quinn, J. F.; Anastasaki, A.; Haddleton, D. M.; Whittaker, M. R.; Davis, T. P. Facile access to thermoresponsive filomicelles with tuneable cores. *Chem. Commun.* **2016**, *52*, 4497.
- (33) Truong, N. P.; Quinn, J. F.; Anastasaki, A.; Rolland, M.; Vu, M.; Haddleton, D.; Whittaker, M. R.; Davis, T. P. Surfactant-free RAFT emulsion polymerization using a novel biocompatible thermoresponsive polymer. *Polym. Chem.* **2017**, *8*, 1353.
- (34) de la Haye, J. L.; Zhang, X. W.; Chaduc, I.; Brunel, F.; Lansalot, M.; D'Agosto, F. The Effect of Hydrophile Topology in RAFT-Mediated Polymerization-Induced Self-Assembly. *Angew. Chem., Int. Ed.* **2016**, *55*, 3739.
- (35) Cockram, A. A.; Neal, T. J.; Derry, M. J.; Mykhaylyk, O. O.; Williams, N. S. J.; Murray, M. W.; Emmett, S. N.; Armes, S. P. Effect of Monomer Solubility on the Evolution of Copolymer Morphology during Polymerization-Induced Self-Assembly in Aqueous Solution. *Macromolecules* **2017**, *50*, 796.
- (36) Du, J. Z.; Willcock, H.; Patterson, J. P.; Portman, I.; O'Reilly, R. K. Self-Assembly of Hydrophilic Homopolymers: A Matter of RAFT End Groups. *Small* **2011**, *7*, 2070.

(37) Liu, T. T.; Tian, W.; Zhu, Y. Q.; Bai, Y.; Yan, H. X.; Du, J. Z. How does a tiny terminal alkynyl end group drive fully hydrophilic homopolymers to self-assemble into multicompartiment vesicles and flower-like complex particles? *Polym. Chem.* **2014**, *5*, 5077.

(38) Carmean, R. N.; Figg, C. A.; Scheutz, G. M.; Kubo, T.; Sumerlin, B. S. Catalyst-Free Photoinduced End-Group Removal of Thiocarbonylthio Functionality. *ACS Macro Lett.* **2017**, *6*, 185.

(39) Altintas, O.; Josse, T.; Abbasi, M.; De Winter, J.; Trouillet, V.; Gerbaux, P.; Wilhelm, M.; Barner-Kowollik, C. ATRP-based polymers with modular ligation points under thermal and thermomechanical stress. *Polym. Chem.* **2015**, *6*, 2854.

(40) Gutekunst, W. R.; Anastasaki, A.; Lunn, D. J.; Truong, N. P.; Whitfield, R.; Jones, G. R.; Treat, N. J.; Abdilla, A.; Barton, B. E.; Clark, P. G.; Haddleton, D. M.; Davis, T. P.; Hawker, C. J. Practical Chain-End Reduction of Polymers Obtained with ATRP. *Macromol. Chem. Phys.* **2017**, 1700107.

(41) Matyjaszewski, K.; Davis, T. P. *Handbook of Radical Polymerization*; Wiley, 2002.

(42) Gody, G.; Maschmeyer, T.; Zetterlund, P. B.; Perrier, S. Exploitation of the Degenerative Transfer Mechanism in RAFT Polymerization for Synthesis of Polymer of High Livingness at Full Monomer Conversion. *Macromolecules* **2014**, *47*, 639.

(43) Truong, N. P.; Quinn, J. F.; Dussert, M. V.; Sousa, N. B. T.; Whittaker, M. R.; Davis, T. P. Reproducible Access to Tunable Morphologies via the Self-Assembly of an Amphiphilic Diblock Copolymer in Water. *ACS Macro Lett.* **2015**, *4*, 381.

(44) Truong, N. P.; Whittaker, M. R.; Anastasaki, A.; Haddleton, D. M.; Quinn, J. F.; Davis, T. P. Facile production of nanoaggregates with tuneable morphologies from thermoresponsive P(DEGMA-co-HPMA). *Polym. Chem.* **2016**, *7*, 430.

(45) Lovett, J. R.; Warren, N. J.; Ratcliffe, L. P. D.; Kocik, M. K.; Armes, S. P. pH-Responsive Non-Ionic Diblock Copolymers: Ionization of Carboxylic Acid End-Groups Induces an Order-Order Morphological Transition. *Angew. Chem., Int. Ed.* **2015**, *54*, 1279.

(46) Mai, Y.; Eisenberg, A. Self-assembly of block copolymers. *Chem. Soc. Rev.* **2012**, *41*, 5969.

Supporting information

Polymerization-Induced Self-Assembly: The Effect of End Group and Initiator Concentration on Morphology of Nanoparticles Prepared via RAFT Aqueous Emulsion Polymerization

Song Yang Khor[†], Nghia P. Truong[†], John F. Quinn[†], Michael R. Whittaker^{*†}, and Thomas P. Davis^{*†‡}

[†]ARC Centre of Excellence in Convergent Bio-Nano Science & Technology, Monash Institute of Pharmaceutical Sciences, Monash University, Parkville, Melbourne, Victoria 3052, Australia.

[‡] Department of Chemistry, University of Warwick, Coventry CV4 7AL, UK.

Materials

Ethaneithiol (97%), carbon disulfide (>99.9%), p-toluenesulfonyl chloride (>99%), dimethyl sulfoxide (>99.9%, anhydrous), dicyclohexylcarbodiimide (DCC), 4-dimethylaminopyridine (DMAP), methanol (99%, anhydrous grade), and p-toluenesulfonic acid monohydrate (>98.5%) were acquired from Sigma Aldrich and used as received. Potassium hydroxide (pellet, AR grade) was purchased from ChemSupply and used as received. Poly(ethylene glycol) methyl ether acrylate average Mn ~ 480 (PEGA, Sigma-Aldrich), N-hydroxyethyl acrylamide (HEAA, 97%, Sigma-Aldrich) and styrene (>99%, Sigma-Aldrich) were passed through a column of basic alumina (activity I) to remove inhibitor prior to use. 4, 4'-Azobis(4-cyanopentanoic acid) (ACPA, 98%, Alfa Aesar) was recrystallized twice in methanol prior to use. MilliQ water (resistivity >18.2 MΩ cm⁻¹) was generated using a Millipore MilliQ Academic Water Purification System. All other chemicals and solvents used were of at least analytical grade and used as received.

Synthesis of chain transfer agent (CTA), 4-cyano-4-(ethylthiocarbonothioylthio) pentanoic acid (ECT).

ECT was synthesised as previously described.¹

Methylation of ECT

4-(dimethylamino)pyridinium 4-toluenesulfonate (DPTS) was synthesised according to literature.² ECT (1.00 g, 3.8 mmol) and DPTS (0.112 g, 0.38 mmol) were dissolved in anhydrous methanol (8.0 mL), and added to a 50 mL round bottom flask, which was placed in an ice bath. Separately, DCC (1.18 g, 5.7 mmol) was dissolved in anhydrous methanol (8.0 mL) and added dropwise over 5 min under stirring. Then, the flask was brought out of ice and allowed to warm up to 23 °C. After stirring continuously for 16 h, the reaction mixture was filtered twice to remove dicyclohexyl urea. The filtrate was dried over magnesium sulfate before purification by column chromatography on silica gel using a gradient solvent mixture of petroleum benzine (boiling range 60-80 °C) : ethyl acetate (3 : 2 slowly changed to 1 : 2). After complete removal of residual solvents, an orange oil was obtained (0.788 g, 79% yield). ¹H NMR (CDCl₃) ppm: 3.71 (s, 3H, -CH₃), 3,34 (q, 2H, CH₃-CH₂-), 2.68 – 2.32 (m, 4H, -CH₂-CH₂-), 1.88 (s, 3H, -C-CH₃), 1.36 (t, 2H, CH₃-CH₂-).

Synthesis of P(PEGA-*co*-HEAA)-COOH and P(HEAA-*co*-PEGA)-Me macro-chain transfer agents (macro-CTAs)

A 50 mL round bottom flask equipped with a stirrer bar was charged with ECT/ECT-Me (120 mg/126 mg, 4.56×10^{-4} mol), PEGA (7.00 g, 1.46×10^{-2} mol), HEAA (2.10 g, 1.83×10^{-2} mol), ACPA (6 mg, 2.28×10^{-5} mol) and DMSO (48 mL, anhydrous). The flask was sealed with a rubber septum and deoxygenated by nitrogen purging for 1 h at ambient temperature. The flask was immersed in a preheated oil bath at 70 °C. After 4 h, the polymerization was quenched by plunging the flask in an ice bath and exposing the reaction mixture to air. An aliquot (50 µL) of the crude reaction mixture was sampled for ¹H NMR analysis to determine PEGA and HEAA conversion. The crude reaction mixture was then dialysed against acetone (1 L), using a dialysis membrane with molecular weight cut-off 3.5 kDa, for 3 h to replace the DMSO. The polymer was recovered by precipitating three times from acetone into a large excess of diethyl ether (300 mL). After drying under high vacuum for 48 h, a sticky yellow solid was obtained.

RAFT emulsion polymerization of styrene in water with P(HEAA-*co*-PEGA)-COOH or P(HEAA-*co*-PEGA)-Me macro-CTAs

A typical emulsion polymerization was carried out as follows: macro-CTA (86 mg, 5.5×10^{-6} mol) was added to a 25 mL glass vial equipped with a stirrer bar. ACPA (2.0 mg, 7.0×10^{-6} mol) was dissolved in MiliQ water (20 mL) by stirring for 30 min. An aliquot (4 mL) of the

ACPA solution ($3.5 \times 10^{-4} \text{ mol L}^{-1}$) was added to the macro-CTA and the glass vial was sealed with a rubber septum (for emulsion polymerizations conducted above the pK_a of P(HEAA-*co*-PEGA)-COOH macro-CTA, the pH of the reaction solution was adjusted by addition of NaOH). Styrene (1 mL) was added into a 2 mL glass vial and then sealed with a rubber septum. Both glass vials were deoxygenated by nitrogen purging for 25 min at ambient temperature. After 25 min of nitrogen purging, an aliquot of deoxygenated styrene (400 μL) was added into the 25 mL vial drop-wise via a gas-tight syringe. The reaction mixture was subsequently purged with nitrogen for a further 5 min before placing the vial in an oil bath preheated to 80 °C and stirring at 300 RPM. During the polymerization, samples were periodically withdrawn using a gas-tight syringe for a kinetics study and were characterized by ^1H NMR and TEM. After 6 h, the polymerization was quenched by immersing the polymerization vessel in an ice bath and opening to air. Aliquots (50 μL) of the crude reaction mixture were sampled to determine styrene conversion (^1H NMR), molecular weight (SEC), and particle morphology (TEM).

Characterization

^1H NMR spectroscopy

All ^1H NMR spectra were recorded in either deuterated DMSO (for macro-CTAs) or a mixture of deuterated acetone and deuterated chloroform in a 9 : 1 ratio (for emulsion polymerizations) on a Bruker Advance III 400 MHz spectrometer.

Size exclusion chromatography (SEC)

Analyses of polymer solutions were performed using a Shimadzu modular system comprising a DGU-12A degasser, an SIL-20AD automatic injector, a 5.0 μm bead-size guard column (50 x 7.8 mm) followed by three KF-805L columns (300 x 8 mm, bead size: 10 μm , pore size maximum: 5000 Å), a SPD-20A ultraviolet detector, and an RID-10A differential refractive-index detector. A CTO-20A oven was used to maintain the columns at 40 °C. The eluent was *N,N*-dimethylacetamide (HPLC grade, with 0.03 % w/v LiBr) with a flow rate set at 1 mL min^{-1} using a LC-20AD pump. Calibration was achieved using commercial narrow molecular weight distribution polystyrene (PSTY) standards with a molecular weight range of 500 to $2 \times 10^6 \text{ g mol}^{-1}$. All polymer samples were pushed through 0.45 μm filters prior to injection.

Transmission electron microscopy (TEM)

TEM imaging was performed using a Tecnai F20 transmission electron microscope at an accelerating voltage of 200 kV at ambient temperature. An aliquot (5 μ L) of 0.1 wt% latex solution (diluted with MiliQ water) was deposited on a Formvar coated copper grid (GSCu100F-50, Proscitech) and was allowed to dry overnight in air and at ambient temperature.

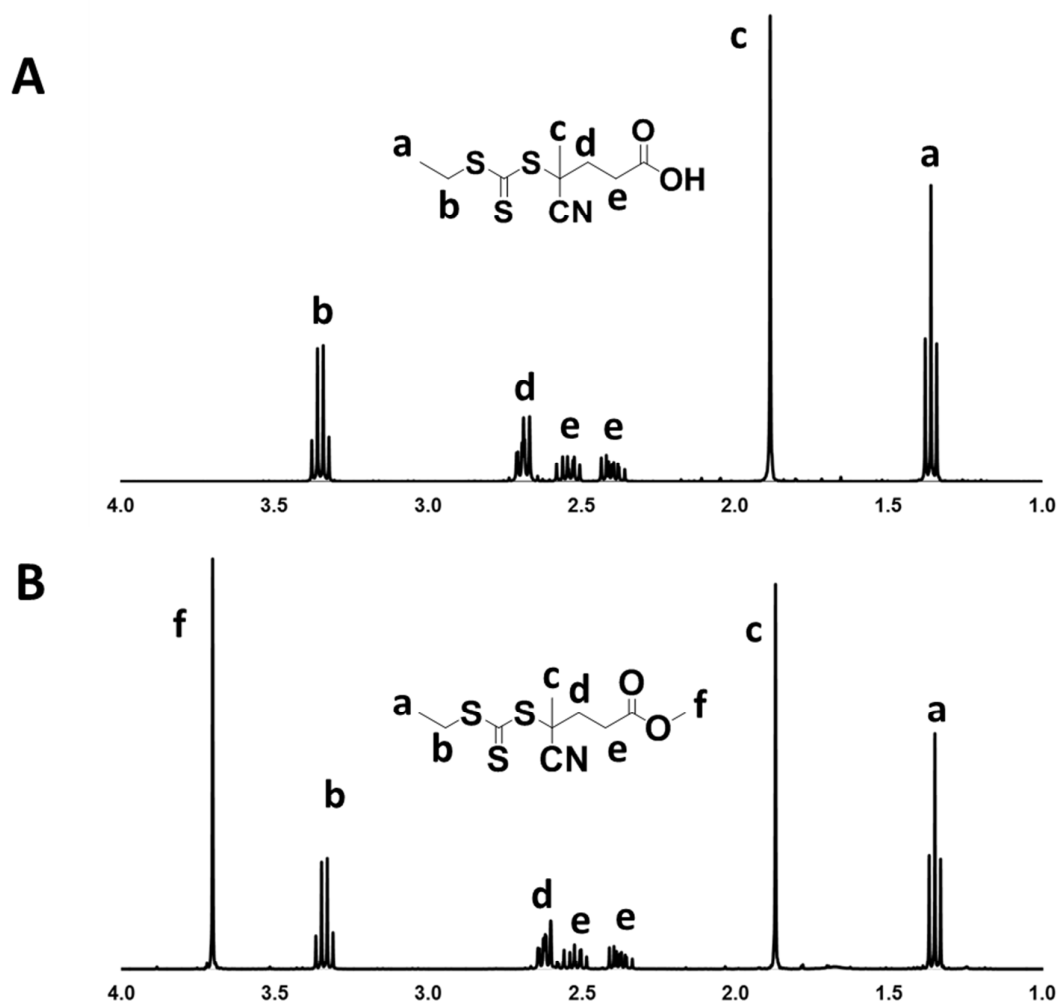


Figure S1. ^1H NMR spectrum of a) ECT, and b) ECT (Me) in chloroform- d_6 .

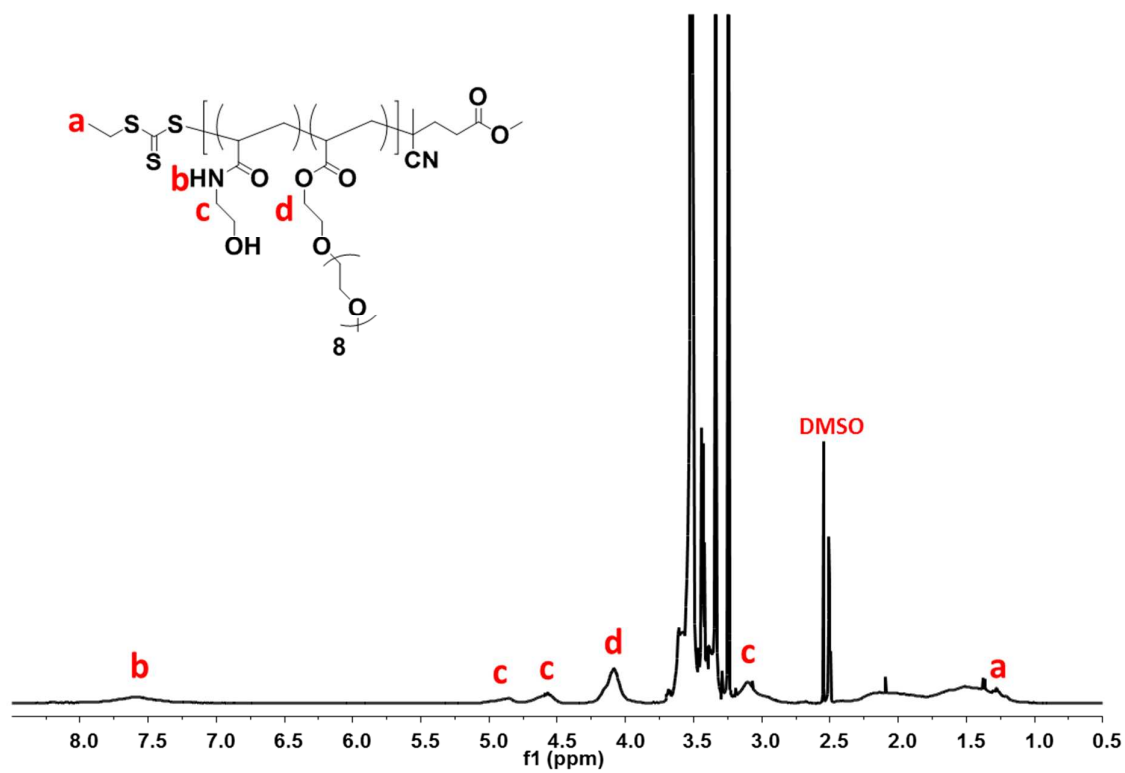


Figure S2. ^1H NMR spectrum of P(HEAA-co-PEGA)-Me macro-CTA, recorded in DMSO-d_6 .

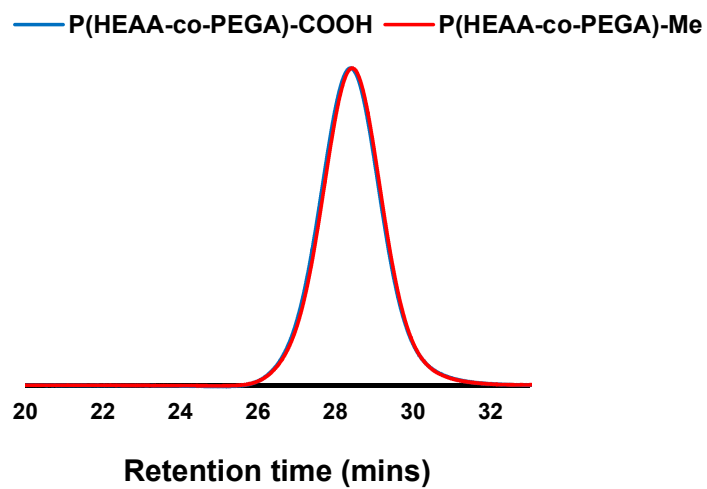


Figure S3. SEC traces for P(HEAA-*co*-PEGA)-COOH (blue) and P(HEAA-*co*-PEGA)-Me (red) macro-CTA synthesized by RAFT solution polymerization of HEAA and PEGA in DMSO at 70 °C using ACPA as an initiator.

Table S1. SEC, ¹H NMR data for P(HEAA-*co*-PEGA)-COOH and P(HEAA-*co*-PEGA)-Me macro-CTAs, synthesised by RAFT solution polymerization of HEAA and PEGA at 70 °C in DMSO for 4 h using ACPA as the initiator.

RAFT agent	RAFT : HEAA : PEGA : ACPA	SEC ^a		¹ H NMR				
				Conversion (%)		DP		M _{n,NMR} ^f (g/mol)
		PDI	M _n (g/mol)	HEAA ^b	PEGA ^c	HEAA ^d	PEGA ^e	
ECT	20 : 800 : 640 : 1	1.21	16500	63	81	25	26	15600
ECT-Me		1.22	17100	65	81	26	26	15700

^a SEC measurements were carried out in DMAC + 0.03 wt% of LiBr solution, and using PSTY standards for calibration. ^b HEAA conversion was calculated by integrating the area of a peak at 5.5 ppm ($I_{5.5}$) and the area of peaks from 4.5 to 5.0 ppm ($I_{4.5-5.0}$), and applying the following equation: HEAA conversion (%) = $100 - (I_{5.5}/I_{4.5-5.0} \times 100)$. ^c PEGA conversion was calculated by integrating the area of a peak at 5.9 ppm ($I_{5.9}$) and the area of peaks from 3.9 to 4.2 ppm ($I_{3.9-4.2}$), and applying the following equation: PEGA conversion (%) = $100 - (I_{5.9}/I_{3.9-4.2} \times 2 \times 100)$. ^d The degree of polymerization of HEAA was derived using the following equation: HEAA degree of polymerization = (HEAA conversion/100) × ([HEAA]/[RAFT]). ^e The degree of polymerization of PEGA was derived using the following equation: PEGA degree of polymerization = (PEGA conversion/100) × ([PEGA]/[RAFT]). ^f The M_{n,NMR} was calculated by the following equation: (DP_{HEAA} × 115) + (DP_{PEGA} × 480) + (263 (COOH) or 277 (COO(CH₃))).

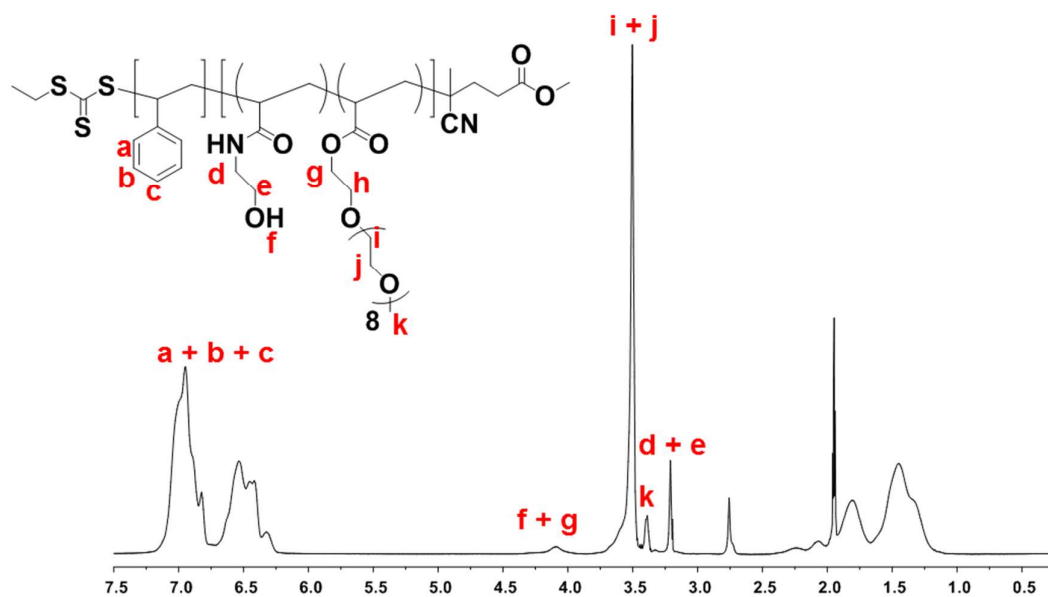


Figure S4. ^1H NMR spectrum of P(HEAA-*co*-PEGA)-*b*-P(STY)-Me in acetone- d_6 and chloroform- d_6 (9:1 ratio).

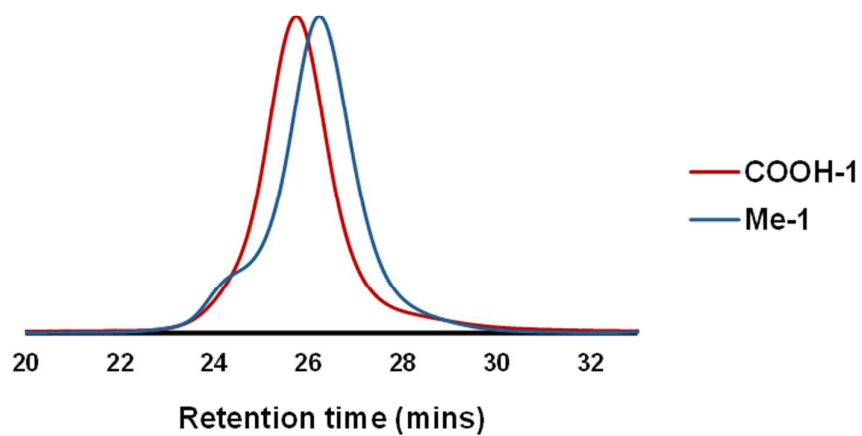


Figure S5. SEC traces for RAFT aqueous emulsion polymerization of styrene with P(HEAA-*co*-PEGA)-COOH (red) and P(HEAA-*co*-PEGA)-Me (blue) (experiments COOH-1 and Me-1 respectively).

Table S2. SEC, ^1H NMR, and TEM data for RAFT aqueous emulsion polymerization of styrene with P(HEAA-*co*-PEGA)-COOH and P(HEAA-*co*-PEGA)-Me macro-CTA at 80 °C for 6 h using ACPA as the initiator.

Polymer code	Macro-CTA : Styrene : ACPA	SEC ^a			^1H NMR				TEM
		PDI	M _n ^a (g/mol)	M _p ^b (g/mol)	Conv. ^c (%)	M _{n, (th)} ^d (g/mol)	DP _{NMR} ^e	M _{n, NMR} ^f	Morphology
COOH-1	1 : 636 : 0.250	1.38	58100	77700	93	77100	497	67400	Sphere
Me-1		1.40	56500	61900	95	77900	470	64600	Vesicle

^a SEC data measurements were carried out in DMAC + 0.03 wt% of LiBr solution, and using PSTY standards for calibration. ^b M_p was acquired from the SEC software by measuring the molecular weight (MW) at the peak of the SEC trace. ^c Styrene conversion was calculated by integrating the area of a peak at 5.7 ppm (I_{5.7}) and the area of peaks from 6.3 to 7.5 ppm (I_{6.3-7.5}), and applying the following equation: styrene conversion (%) = 100 – (I_{5.7}/I_{6.3-7.5} × 5 × 100). ^d The M_{n, (th)} was calculated by the following equation: (styrene conversion/100) × ([styrene]/[macro-CTA]) + (15600 (COOH) or 15700 (COO(CH₃))). ^e The degree of polymerization of styrene was derived by integrating the area of peaks belonging to the phenyl ring protons of styrene from 6.3 to 7.5 ppm (I_{styrene}) over the area of peaks belonging to protons in the HEAA ethyl group, protons belonging to the repeating ethylene glycol units, and end methyl group from 3.1 to 4.5 ppm (I_{HEAA + PEGA + Me}), and applied in the following equation: DP_{styrene} = (I_{styrene}/I_{HEAA + PEGA}) × (1121/5). ^f M_{n, NMR} was calculated by the following equation: M_{n, NMR} = (DP_{styrene} × 104) + (15600 for COOH or 15700 for COO(CH₃)).

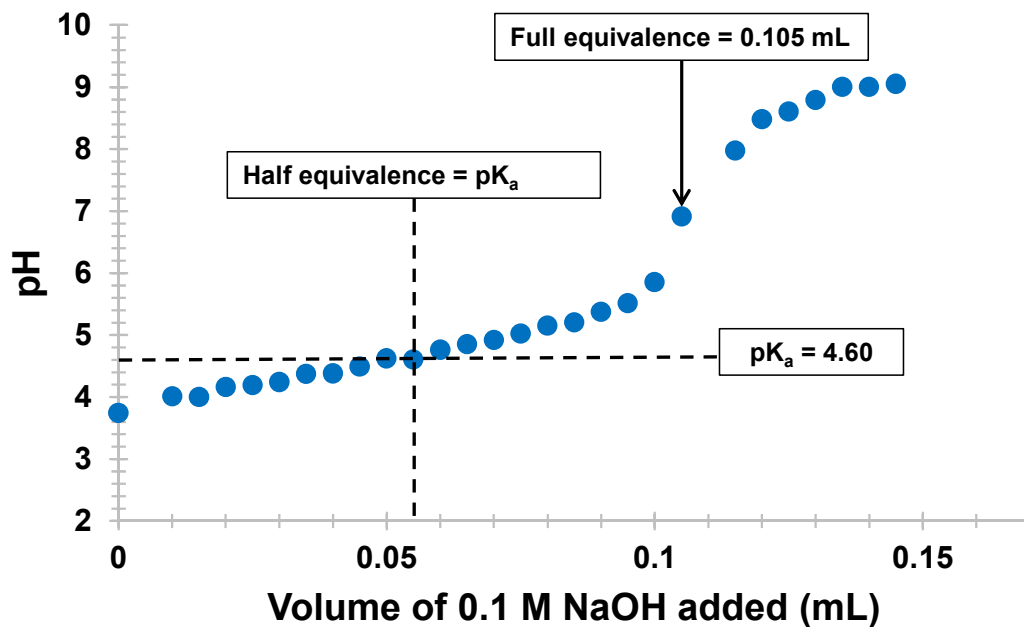


Figure S6. Titration of 0.1 M P(HEAA-co-PEGA)-COOH macro-CTA with 0.1 M NaOH.

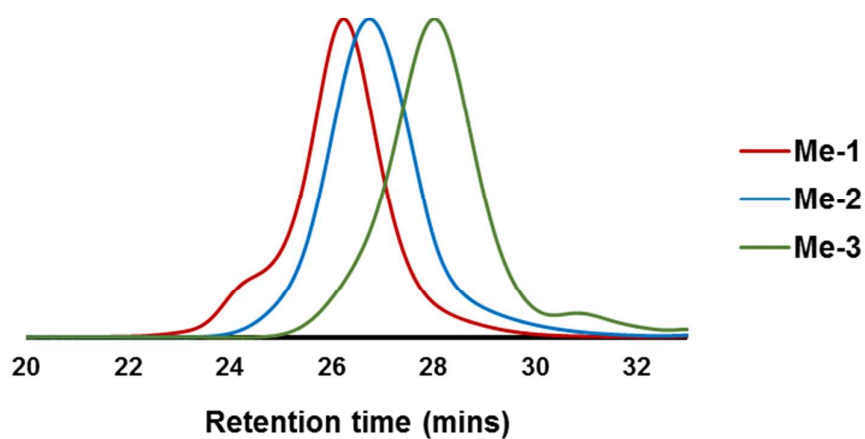


Figure S7. SEC traces for RAFT aqueous emulsion polymerization of styrene with P(HEAA-co-PEGA)-Me macro-CTA (experiments Me-1 to Me-3).

Table S3. SEC, ^1H NMR, and TEM data for RAFT aqueous emulsion polymerization of styrene with P(HEAA-*co*-PEGA)-Me macro-CTA at 80 °C for 6 h using ACPA as the initiator.

Polymer code	Macro-CTA : Styrene : ACPA	SEC ^a			^1H NMR				TEM
		PDI	M_n (g/mol)	M_p^b (g/mol)	Conv. ^c (%)	$M_{n(\text{th})}^d$ (g/mol)	DP_{NMR}^e	$M_{n,\text{NMR}}^f$	Morphology
Me-1	1 : 636 : 0.250	1.40	56500	61900	95	77900	470	64600	Vesicle
Me-2	1 : 318 : 0.250	1.37	34400	44200	94	46800	228	39500	Worm + Sphere
Me-3	1 : 159 : 0.250	1.19	22000	22400	94	31300	132	29500	Sphere

^a SEC data measurements were carried out in DMAC + 0.03 wt% of LiBr solution, and using PSTY standards for calibration. ^b M_p was acquired from the SEC software by measuring the molecular weight (MW) at the peak of the SEC trace. ^c Styrene conversion was calculated by integrating the area of a peak at 5.7 ppm ($I_{5.7}$) and the area of peaks from 6.3 to 7.5 ppm ($I_{6.3-7.5}$), and applying the following equation: styrene conversion (%) = 100 – ($I_{5.7}/I_{6.3-7.5} \times 5 \times 100$). ^d The $M_{n(\text{th})}$ was calculated by the following equation: (styrene conversion/100) × ([styrene]/[macro-CTA]) + 15700. ^e The degree of polymerization of styrene was derived by integrating the area of peaks belonging to the phenyl ring protons of styrene from 6.3 to 7.5 ppm (I_{styrene}) over the area of peaks belonging to protons in the HEAA ethyl group, protons belonging to the repeating ethylene glycol units, and end methyl group from 3.1 to 4.5 ppm ($I_{\text{HEAA} + \text{PEGA} + \text{Me}}$), and applied in the following equation: $DP_{\text{styrene}} = (I_{\text{styrene}}/I_{\text{HEAA} + \text{PEGA}}) \times (1121/5)$. ^f $M_{n,\text{NMR}}$ was calculated by the following equation: $M_{n,\text{NMR}} = (DP_{\text{styrene}} \times 104) + 15700$.

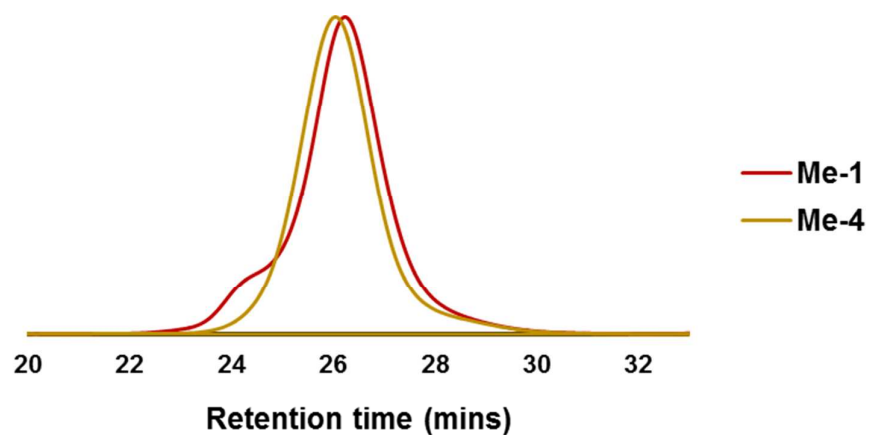


Figure S8. SEC traces for RAFT aqueous emulsion polymerization of styrene with P(HEAA-*co*-PEGA)-Me macro-CTA (experiments Me-1 and Me-4).

Table S4. SEC, ^1H NMR, and TEM data for RAFT aqueous emulsion polymerization of styrene with P(HEAA-*co*- PEGA)-Me macro-CTA at 80 °C for 6 h using ACPA as the initiator.

Polymer code	Macro-CTA : Styrene : ACPA	SEC ^a			^1H NMR				TEM
		PDI	M_n (g/mol)	M_p^b (g/mol)	Conv. ^c (%)	$M_{n(\text{th})}^d$ (g/mol)	DP_{NMR}^e	$M_{n,\text{NMR}}^f$	Morphology
Me-1	1 : 636 : 0.250	1.40	56500	61900	95	77900	470	64600	Vesicle
Me-4	1 : 636 : 0.125	1.39	57400	71200	97	79800	505	68200	Sphere

^a SEC data measurements were carried out in DMAC + 0.03 wt% of LiBr solution, and using PSTY standards for calibration. ^b M_p was acquired from the SEC software by measuring the molecular weight (MW) at the peak of the SEC trace. ^c Styrene conversion was calculated by integrating the area of a peak at 5.7 ppm ($I_{5.7}$) and the area of peaks from 6.3 to 7.5 ppm ($I_{6.3-7.5}$), and applying the following equation: styrene conversion (%) = $100 - (I_{5.7}/I_{6.3-7.5} \times 5 \times 100)$. ^d The $M_{n(\text{th})}$ was calculated by the following equation: (styrene conversion/100) \times ([styrene]/[macro-CTA]) + 15700. ^e The degree of polymerization of styrene was derived by integrating the area of peaks belonging to the phenyl ring protons of styrene from 6.3 to 7.5 ppm (I_{styrene}) over the area of peaks belonging to protons in the HEAA ethyl group, protons belonging to the repeating ethylene glycol units, and end methyl group from 3.1 to 4.5 ppm ($I_{\text{HEAA} + \text{PEGA} + \text{Me}}$), and applied in the following equation: $DP_{\text{styrene}} = (I_{\text{styrene}}/I_{\text{HEAA} + \text{PEGA}}) \times (1121/5)$. ^f $M_{n,\text{NMR}}$ was calculated by the following equation: $M_{n,\text{NMR}} = (DP_{\text{styrene}} \times 104) + 15700$.

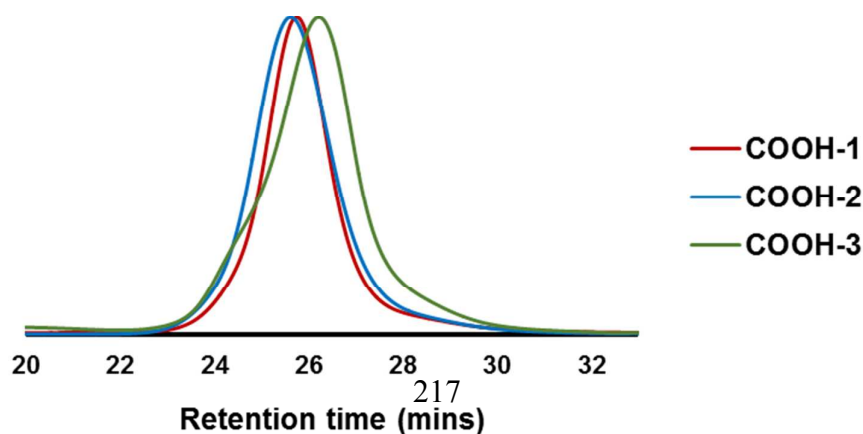


Figure S9. SEC traces for RAFT aqueous emulsion polymerization of styrene with P(HEAA-*co*-PEGA)-COOH macro-CTA (experiments COOH-1 to COOH-3).

Table S5. SEC, ^1H NMR, and TEM data for RAFT aqueous emulsion polymerization of styrene with P(HEAA-*co*-PEGA)-COOH macro-CTA at 80 °C for 6 h using ACPA as the initiator.

Polymer code	Macro-CTA : Styrene : ACPA	SEC ^a			^1H NMR				TEM
		PDI	M_n (g/mol)	M_p ^b (g/mol)	Conv. ^c (%)	$M_{n(\text{th})}$ ^d (g/mol)	DP_{NMR} ^e	$M_{n, \text{NMR}}$ ^f	Morphology
COOH-1	1 : 636 : 0.250	1.38	58100	77700	93	77100	497	67400	Sphere
COOH-2	1 : 636 : 0.500	1.47	59300	83000	97	79800	508	68500	Sphere + Vesicle + Worm
COOH-3	1 : 636 : 0.750	1.47	52700	60500	95	78500	467	64300	Vesicle

^a SEC data measurements were carried out in DMAC + 0.03 wt% of LiBr solution, and using PSTY standards for calibration. ^b M_p was acquired from the SEC software by measuring the molecular weight (MW) at the peak of the SEC trace. ^c Styrene conversion was calculated by integrating the area of a peak at 5.7 ppm ($I_{5.7}$) and the area of peaks from 6.3 to 7.5 ppm ($I_{6.3-7.5}$), and applying the following equation: styrene conversion (%) = $100 - (I_{5.7}/I_{6.3-7.5} \times 5 \times 100)$. ^d The $M_{n(\text{th})}$ was calculated by the following equation: (styrene conversion/100) \times ([styrene]/[macro-CTA]) + 15600. ^e The degree of polymerization of styrene was derived by integrating the area of peaks belonging to the phenyl ring protons of styrene from 6.3 to 7.5 ppm (I_{styrene}) over the area of peaks belonging to protons in the HEAA ethyl group and protons belonging to the repeating ethylene glycol units from 3.1 to 4.5 ppm ($I_{\text{HEAA} + \text{PEGA} + \text{Me}}$), and applied in the following equation: $DP_{\text{styrene}} = (I_{\text{styrene}}/I_{\text{HEAA} + \text{PEGA}}) \times (1118/5)$. ^f $M_{n, \text{NMR}}$ was calculated by the following equation: $M_{n(\text{th})} = (DP_{\text{styrene}} \times 104) + 15600$.

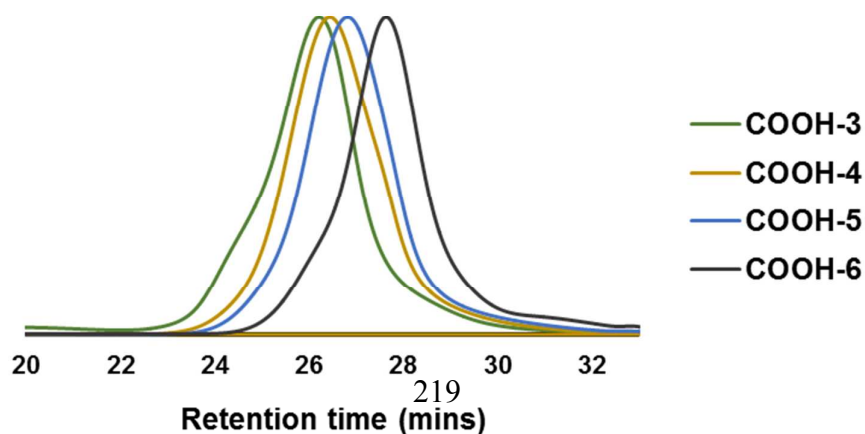


Figure S10. SEC traces for RAFT aqueous emulsion polymerization of styrene with P(HEAA-*co*-PEGA)-COOH macro-CTA (experiments COOH-3 to COOH-6).

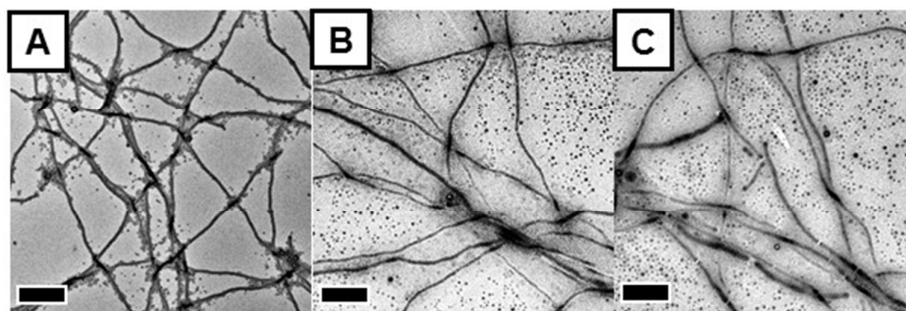


Figure S11. TEM images of particles from a latex solution of RAFT aqueous emulsion polymerization of styrene with P(HEAA-*co*-PEGA)-COOH macro-CTA, (A) before NaOH addition (pH = 4), (B) after NaOH addition (pH = 6), and (C) after returning the latex solution back to pH = 4 via HCl addition.

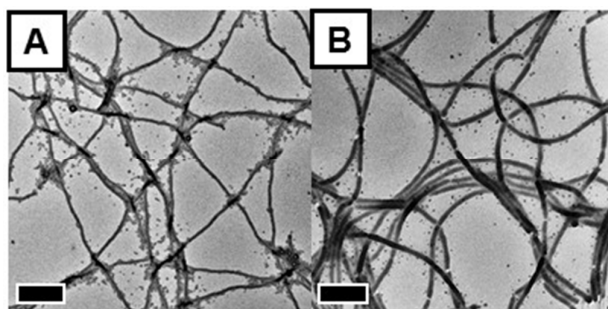


Figure S12. TEM images of particles formed from RAFT aqueous emulsion polymerization of styrene with P(HEAA-*co*-PEGA)-COOH macro-CTA conducted at, (A) pH = 4 (below the pK_a of the carboxylic acid end-group of the P(HEAA-*co*-PEGA)-COOH macro-CTA), and (B) pH = 7 (above the pK_a of the carboxylic acid end-group of the P(HEAA-*co*-PEGA)-COOH macro-CTA).

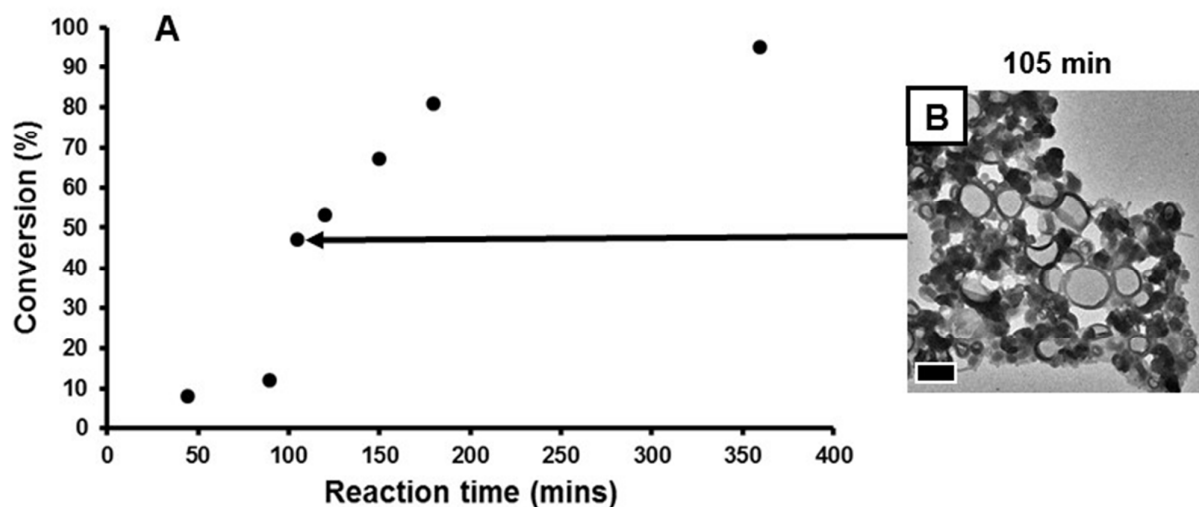


Figure S13. (A) Reaction time (min)s versus styrene conversion (%) of RAFT aqueous emulsion polymerization of styrene with P(HEAA-*co*-PEGA)-Me macro-CTA (experiment Me-1). (B) TEM image of particles formed at 105 min from RAFT aqueous emulsion polymerization of styrene with P(HEAA-*co*-PEGA)-Me macro-CTA. Scale bar represents 500 nm.

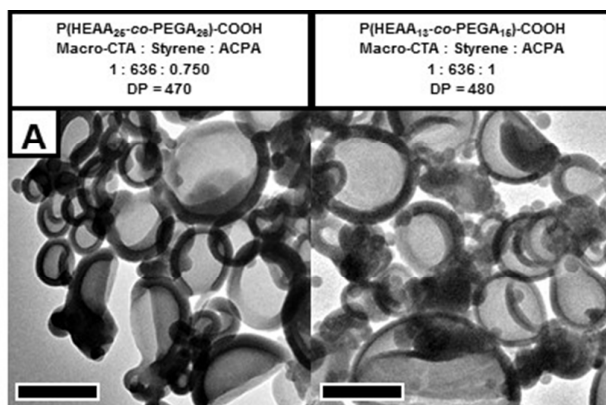


Figure S14. TEM images of particles formed from RAFT aqueous emulsion polymerization of styrene with, (A) P(HEAA₂₅-co-PEGA₂₆)-COOH macro-CTA ($M_n = 16500$ g/mol, PDI = 1.21), and (B) P(HEAA₁₃-co-PEGA₁₅)-COOH ($M_n = 8800$ g/mol, PDI = 1.15) macro-CTA.

Table S6. SEC, ^1H NMR, and TEM data for RAFT aqueous emulsion polymerization of styrene with P(HEAA-*co*-PEGA)-COOH macro-CTA at 80 °C for 6 h using ACPA as the initiator.

Polymer code	Macro-CTA : Styrene : ACPA	SEC ^a			^1H NMR				TEM
		PDI	M_n (g/mol)	M_p^b (g/mol)	Conv. ^c (%)	$M_{n(\text{th})}^d$ (g/mol)	DP_{NMR}^e	$M_{n, \text{NMR}}^f$	Morphology
COOH-3	1 : 636 : 0.750	1.47	52700	60500	95	78500	467	64300	Vesicle
COOH-4	1 : 477 : 0.750	1.50	42100	56900	98	64200	372	54100	Vesicle + Worm
COOH-5	1 : 318 : 0.750	1.47	32500	42800	98	48000	247	41300	Worm + Sphere
COOH-6	1 : 239 : 0.750	1.40	22700	27500	97	39700	208	37300	Sphere

^a SEC data measurements were carried out in DMAC + 0.03 wt% of LiBr solution, and using PSTY standards for calibration. ^b M_p was acquired from the SEC software by measuring the molecular weight (MW) at the peak of the SEC trace. ^c Styrene conversion was calculated by integrating the area of a peak at 5.7 ppm ($I_{5.7}$) and the area of peaks from 6.3 to 7.5 ppm ($I_{6.3-7.5}$), and applying the following equation: styrene conversion (%) = $100 - (I_{5.7}/I_{6.3-7.5} \times 5 \times 100)$. ^d The $M_{n(\text{th})}$ was calculated by the following equation: (styrene conversion/100) \times ([styrene]/[macro-CTA]) + 15600. ^e The degree of polymerization of styrene was derived by integrating the area of peaks belonging to the phenyl ring protons of styrene from 6.3 to 7.5 ppm (I_{styrene}) over the area of peaks belonging to protons in the HEAA ethyl group and protons belonging to the repeating ethylene glycol units from 3.1 to 4.5 ppm ($I_{\text{HEAA} + \text{PEGA} + \text{Me}}$), and applied in the following equation: $\text{DP}_{\text{styrene}} = (I_{\text{styrene}}/I_{\text{HEAA} + \text{PEGA}}) \times (1118/5)$. ^f $M_{n, \text{NMR}}$ was calculated by the following equation: $M_{n, \text{NMR}} = (\text{DP}_{\text{styrene}} \times 104) + 15600$.

References

- (1) Truong NP, Dussert MV, Whittaker MR, Quinn JF, Davis TP. Rapid synthesis of ultrahigh molecular weight and low polydispersity polystyrene diblock copolymers by RAFT-mediated emulsion polymerization. *Polymer Chemistry*. **2015**;6(20):3865-74.
- (2) Moore JS, Stupp SI. Room temperature polyesterification. *Macromolecules*. **1990**;23(1):65-70.

Chapter 6: Conclusion

6.1 Conclusion

The studies carried out in this thesis addressed two core concepts, i) the development of a nanoparticle platform via PISA that could access bespoke nanoparticles with controllable size (Chapter 2), surface chemistry (Chapter 2), and morphology (Chapter 5), and ii) the bio-nano interactions of a library of nanoparticles with various sizes and surface chemistries in dynamic flow conditions (Chapter 2), human plasma (Chapter 3), and whole human blood (Chapter 4). The development of a PISA nanoparticle platform that demonstrably produced nanoparticles of various sizes, surface chemistries, and morphologies is a potentially potent tool in adapting a single nanoparticle platform towards a multitude of diseases. The size of PISA nanoparticles could be tuned by varying the feed ratio of styrene to predetermine the resultant nanoparticle's diameter. PISA nanoparticles with various surface chemistries could be obtained via a premodification of the initial RAFT agent. To trigger morphological change in this PISA nanoparticle platform, macro-CTA end-group hydrophobicity and radical initiator concentration were revealed as novel experimental parameters that allowed comprehensive access to sphere, worm, and vesicle morphologies. Testing of the biological interactions of nanoparticle with several tuneable physicochemical properties in clinical relevant environments will guide the rational design of nanoparticles for clinical applications. As such, a matrix of nanoparticles with different sizes and surface chemistries was produced. Under flow conditions, tertiary amine-decorated nanoparticles displayed higher HUVECs association compared to the other surface chemistries. In contrast, carboxylate-terminated nanoparticles displayed lower binding to HUVECs with an increase in carboxylate-terminated nanoparticle leading to a further decrease in HUVECs binding due to increased drag force on the larger particles. A quantitative and qualitative analysis of the protein corona of nanoparticles with different sizes and surface chemistries revealed a highly similar protein corona composition. Furthermore, fibrinogen and alpha-2-macroglobulin association with tertiary amine-terminated

nanoparticles was size dependent. After incubation in whole human blood, PEG and methyl ester-decorated nanoparticles displayed decreased association with monocytes and neutrophils compared to other types of nanoparticles. Moreover, 130 nm nanoparticles were more strongly associated with immune cells compared with 30 nm nanoparticles. Based on the data arising from the RAFT aqueous emulsion polymerisation studies and the resultant bio-nano interaction studies, such nanoparticles may be synthesised through a predictable and rational approach and readily applied towards the field of medicine.

Appendix



Controlling Nanomaterial Size and Shape for Biomedical Applications via Polymerization-Induced Self-Assembly

Song Yang Khor, John F. Quinn, Michael R. Whittaker, Nghia P. Truong,*
and Thomas P. Davis*

Rapid developments in the polymerization-induced self-assembly (PISA) technique have paved the way for the environmentally friendly production of nanoparticles with tunable size and shape for a diverse range of applications. In this feature article, the biomedical applications of PISA nanoparticles and the substantial progress made in controlling their size and shape are highlighted. In addition to early investigations into drug delivery, applications such as medical imaging, tissue culture, and blood cryopreservation are also described. Various parameters for controlling the morphology of PISA nanoparticles are discussed, including the degree of polymerization of the macro-CTA and core-forming polymers, the concentration of macro-CTA and core-forming monomers, the solid content of the final products, the solution pH, the thermoresponsivity of the macro-CTA, the macro-CTA end group, and the initiator concentration. Finally, several limitations and challenges for the PISA technique that have been recently addressed, along with those that will require further efforts into the future, will be highlighted.

1. Introduction

Polymerization-induced self-assembly (PISA) is a useful technique for the concurrent synthesis of block copolymers and the production of polymeric nanomaterials.^[1–4] Compared with other self-assembly techniques, PISA allows the facile preparation of polymeric nanoparticles with tunable size and shape.^[5–8] The first literature example of PISA was reported by Ferguson et al. in 2002 as a novel approach to perform seeded emulsion polymerization in industry.^[9] In this example, acrylic acid (AA) was first polymerized to form a water-soluble macromolecular

chain transfer agent (macro-CTA), after which reversible addition-fragmentation chain transfer (RAFT) emulsion polymerization of butyl acrylate (BA) was carried out in the presence of this macro-CTA to produce a poly(AA)-*b*-poly(BA) (PAA-*b*-PBA) diblock copolymer. When the hydrophobic PBA block had reached a sufficient length, the diblock copolymer chains were no longer water-soluble and hence self-assembled into RAFT-containing seed particles for continued emulsion polymerization. This innovative approach for conducting aqueous RAFT emulsion polymerization does not require the preformation of seed particles by a solvent exchange method (acetone to water), thus overcoming a significant barrier to large-scale industrial manufacture. This approach was later termed PISA for the first time by Hashimoto and

colleagues, and while only spherical particles were obtained in the first report by Ferguson et al., the technique has since been employed to prepare polymeric nanoparticles with various sizes and shapes.^[10] Due to the initial development focusing on potential industrial application, PISA via RAFT emulsion polymerization is not only scalable but is also friendly to the environment (no use of organic solvents).^[11–14] That said, PISA did not attract wide interest when it was first reported, possibly due to the initial limitations in controlling particle size and shape.

Both the size and shape of nanoparticles are crucial factors that impact their properties and applications.^[15–19] For instance, the size and shape of PISA nanoparticles have been found to significantly affect their in vivo biodistribution.^[20] Although many applications have been proposed for PISA nano-objects including lubricants, pigment encapsulation, catalysis systems, coatings, and Pickering emulsifiers, their use in biomedical science is arguably the most exciting.^[21–27] Generally, the encapsulation of drugs and imaging agents inside the core of nanoparticles can improve drug efficacy and imaging contrast, as well as reduce peripheral toxicity and cardiotoxicity.^[28] In addition, PISA has recently been exploited to prepare so-called nanoworms, an emerging subclass of polymeric nanoparticles with a number of potentially beneficial physical properties such as high surface area and aspect ratio.^[29] Due to these unique properties, nanoworms have recently attracted considerable interest in a variety of different fields including catalysis,

S. Y. Khor, Dr. J. F. Quinn, Dr. M. R. Whittaker, Dr. N. P. Truong,
Prof. T. P. Davis
ARC Centre of Excellence in Convergent Bio-Nano Science
and Technology
Monash Institute of Pharmaceutical Sciences
Monash University
381 Royal Parade, Parkville, VIC 3052, Australia
E-mail: nghia.truong@monash.edu; thomas.p.davis@monash.edu
Prof. T. P. Davis
Department of Chemistry
University of Warwick
Gibbet Hill, Coventry CV47AL, UK

The ORCID identification number(s) for the author(s) of this article can be found under <https://doi.org/10.1002/marc.201800438>.

DOI: 10.1002/marc.201800438

material science, immunology, tissue engineering, and drug delivery.^[30–35] In addition to nanoworms, amphiphilic block copolymer vesicle structures or polymersomes have been commonly exploited for biomedical applications.^[36–38] Hence, this review will focus on the biomedical applications of spherical micelles, worm-like micelles, and vesicles.

In recent years, the increasing need for nanoparticles with tunable size and shape for various biomedical applications has stimulated significant efforts by polymer chemists to improve the PISA technique. From a simple methodology that could produce only spherical polystyrene nanoparticles, PISA has rapidly matured to become a powerful technique capable of producing a myriad of nanoparticle morphologies including worm, vesicle, lamella, etc.^[39,40] In this feature article, we do not aim to exhaustively account for every paper concerning the synthesis and application of PISA nor do we aim to critically analyze the PISA literature. Instead, we highlight studies that significantly advance the control of the particle size and shape, and the use of PISA particles in biomedical applications, and thereby tracing the interesting development of both synthesis and applications of PISA nanoparticles.

2. RAFT Dispersion Polymerization

2.1. Controlling Particle Shape

Prior to 2009, only spherical nanoparticles were successfully prepared using PISA. This was a consequence of the initial spherical morphology produced becoming locked due to the hydrophobic block generally being below its T_g , thus preventing further transition to worm or vesicle morphology. In order to promote morphological transitions, Pan and coworkers postulated that it would be necessary to improve the compatibility of the core-forming chains with the reaction media by significantly increasing the core-monomer feed ratio. The enhanced compatibility is required so that the growth rate of the core polymer chains is maintained after phase separation. To test this hypothesis, a RAFT dispersion polymerization of styrene was carried out in methanol using trithiocarbonate-terminated poly(4-vinylpyridine) as the macro-CTA.^[41] TEM images showed that at 2 h, spherical nanoparticles were obtained. However, at 24 h, various nanostructures such as doughnuts, lamellae, spherical nanoparticles, and vesicles were observed. This indicated that the transformation of the spherical nanoparticles into other morphologies was possible in this system. Further polymerizations were carried out by systematically varying the core monomer feed ratio and pure morphologies were obtained (spheres, nanotubes, large compound vesicles, and vesicles). This was the first study to demonstrate that the DP of the core polymer is directly correlated to the final nanoparticle morphology, thus differentiating PISA from traditional self-assembly where variation of the solubility parameter is exploited to obtain different nanoparticle morphologies.^[7]

In addition to core DP, the concentration of core-forming monomer also plays an important role in controlling the shape of PISA particles.^[42] In a follow-up study, Pan and coworkers conducted a series of RAFT dispersion polymerization of styrene in methanol in the presence of a poly(ethylene oxide)



Song Yang Khor is a Ph.D. candidate in pharmaceutical science at the Monash Institute of Pharmaceutical Sciences under the guidance of Prof. Thomas Davis, Dr. Michael Whittaker, Dr. John Quinn, and Prof. Stephen Kent. His Ph.D. thesis examines the synthesis of amphiphilic block copolymer nanoparticles via

polymerization-induced self-assembly (PISA) under reversible addition-fragmentation chain transfer (RAFT) emulsion polymerization conditions. Additionally, his Ph.D. research also investigates the biological interactions of PISA nanoparticles in human blood.



Nghia P. Truong obtained his bachelor and master degrees in chemistry from Vietnam National University – HoChi-Minh City (VNU-HCM) and received his Ph.D. in polymer chemistry from the University of Queensland, Australia. He is currently an ARC DECRA Fellow at the Faculty of Pharmacy and Pharmaceutical Sciences, Monash University.

His current research interests include engineering sequence-controlled, functional, and smart polymers and nanomaterials for applications in nanomedicine (e.g., drug and gene delivery, diagnostics, antibacterial materials) by using a variety of synthetic techniques including radical polymerization (RAFT, ATRP, SET-LRP, and CCTP), emulsion polymerization, self-assembly, polymerization-induced self-assembly, temperature-induced morphological transformation, and click chemistry.



Thomas P. Davis is the Monash–Warwick Professor of Medical Nanotechnology at Monash University in Melbourne, Australia. He also holds an appointment as professor of polymer nanotechnology at the Department of Chemistry at Warwick University, UK. Additionally, he is the director of the Australian Research Council (ARC) Centre of Excellence in

Convergent BioNano Science and Technology. Prof. Davis' research focuses on the application of polymer science and nanotechnology to therapeutic applications, and enhancing the fundamental understanding of how nanomaterials interact with biological systems.

(PEO) macro-CTA.^[43] The authors found that spherical micelles were formed first, with further polymerization of the polystyrene block producing nonspherical morphologies. The determining factors for the final copolymer morphology are both the chain length of the polystyrene block (relative to the PEO block) and the concentration of styrene in methanol. Using this methodology, spherical micelles, nanowires, and vesicles can all be prepared by simply changing the styrene feed ratio and concentration of styrene.

In 2012, Armes and colleagues demonstrated that copolymer concentration and corona degree of polymerization (DP) (DP of the macro-CTA or stabilizer) also affected the morphology of PISA nanoparticles.^[44,45] The authors carried out a series of RAFT aqueous dispersion polymerization of 2-hydroxypropyl methacrylate (HPMA) using poly(glycerol methacrylate) (PGMA) macro-CTA to construct phase diagrams that could provide reproducible access to desired morphologies. From the phase diagrams, the authors reported several interesting observations. Firstly, there is no dependence of morphology upon concentration when the DP of PGMA was sufficiently short (DP = 47 vs DP = 78, and DP = 112). In other words, at both 10 and 25 w/w%, the same core polymer DP will result in the same morphology. Nevertheless, spherical micelles, worms, and vesicles can be simply obtained by targeting the DP of the PHPMA block that gives the appropriate molecular curvature. For the PGMA DP of 78, the copolymer morphology was strongly dependent on the total solids concentration (Figure 1). This resulted in small regions in the phase diagram where it was possible to obtain pure worm or vesicle phase. Aside from these small areas, the copolymer morphologies were mostly mixed. Finally, for PGMA DP of 112, the phase diagram becomes dominated by spheres. The authors attribute this observation to the longer core-forming PHPMA block that was required to

sufficiently reduce the molecular curvature being significantly more dehydrated and hence less mobile, which precluded the in situ evolution of morphology from spheres to higher order morphologies. This hypothesis is supported by the observation that the addition of ethanol to the aqueous PISA formulation conducted using the longer macro-CTA allowed access to worms or vesicles. The addition of cosolvent solvates the core-forming PHPMA chains and hence increases their mobility to form higher order morphologies. Significantly, this study demonstrated that well-populated phase diagrams are vital to ensure reproducible targeting of pure phases, rather than mix phases.

The effects of core and corona DP on the shape of PISA particles are also significant for PISA in nonpolar solvents such as heptane. Fielding et al. conducted the first all-methacrylic *n*-alkane RAFT dispersion polymerization.^[46] In this study, a series of RAFT dispersion polymerizations of benzyl methacrylate (BzMA) with a poly(lauryl methacrylate) (PLMA) macro-CTA in *n*-heptane were carried out. The authors synthesized two PLMA macro-CTA (DP = 17 [short] and DP = 37 [long]). When using the long PLMA macro-CTA, only spherical nanoparticles were obtained regardless of the target DP of the PBzMA block. For these kinetically trapped nanoparticles, the authors suggest that the copolymer morphology cannot evolve because the PLMA block DP is sufficient to ensure effective steric stabilization, and hence prevent 1D fusion of spheres to form worms (a key step required for further vesicle formation). Nonetheless, the spherical nanoparticle diameter increased as the PBzMA block DP increased. When using the short PLMA macro-CTA, higher order morphologies were obtained. Specifically, pure worm and vesicle phases were obtained by systematically varying the PBzMA block DP and total solids content.

In 2012, Charleux and colleagues discovered that the addition of an organic solvent to water could be employed to

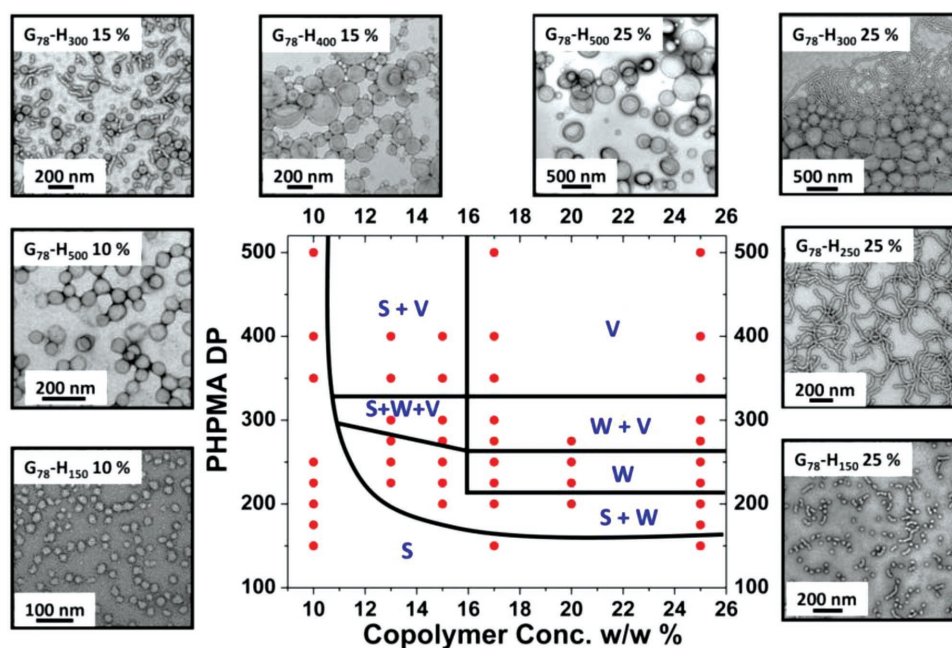


Figure 1. TEM images and the respective phase diagram for a series of RAFT aqueous dispersion polymerizations of HPMA in the presence of a P(GMA)₇₈ macro-CTA. Reproduced with permission.^[44] Copyright 2012, American Chemical Society.

control the final PISA morphology. Hydrophilic macro-CTA composed of 50 mol% MAA and 50 mol% PEOMA was used for the polymerization of BzMA in different media, ethanol–water or 1,4-dioxane–water mixtures.^[47] Depending on the solvent composition, the polymerization proceeded as a dispersion polymerization or emulsion polymerization. The authors found that for a given composition of the block copolymer, the final morphology depended strongly on the solvent composition. For example, the presence of ethanol favored the formation of nonspherical nanoparticles while the presence of water favored the formation of spherical nanoparticles. Interestingly, nonspherical nanoparticles were only obtained at high ethanol proportions whereas nonspherical nanoparticles could only be observed when the proportion of 1,4-dioxane was quite low (**Figure 2a,b**). At a given ethanol–water composition (95%/5% w/w), the increased length of the PBzMA core block changed the morphology from spheres to fibers and then to large spheres or vesicles. In conclusion, this work revealed that solvent composition can be used to promote morphology transitions irrespective of the copolymer composition.

The addition of a cosolvent (1,4-dioxane) to ethanol has also been found to increase the polymerization rate of styrene, the final conversion, and the particle shape. In this example,

polystyrene-based diblock copolymers were first synthesized via RAFT alcoholic dispersion polymerization. However, the reaction proceeded slowly and monomer conversion was incomplete (only 30–70% after 48 h at 80 °C). To address this, the authors investigated the use of a polystyrene-*alt*-*N*-phenylmaleimide, P(St-*alt*-NMI) core-forming block (with a poly(methacrylic acid) [PMAA] macro-CTA) to significantly increase the polymerization rate and also increase the final conversion.^[48] The alternating copolymerization of styrene and NMI has been shown to be highly efficient and rapid. In the initial experiments, the authors identified that carrying out the polymerization in ethanol led to gradual exclusion of the NMI comonomer from the cores of the growing micelles. This led exclusively to spherical nanoparticle morphology. Addition of 50% 1,4-dioxane as a cosolvent enabled the efficient synthesis of PMAA-P(St-*alt*-NMI) diblock copolymer nanoparticles. Intriguingly, while the typical spherical and worm-like morphology phases were observed, no vesicles were produced. Instead, a 2D lamellae morphology was obtained after the worm-like morphology phase. This effect was attributed to the relatively high T_g of the core-forming P(St-*alt*-NMI) block, which leads to rigid chains that are not flexible enough to form the more common vesicular morphology. Rheology studies confirmed that as the P(St-*alt*-NMI) block grows,

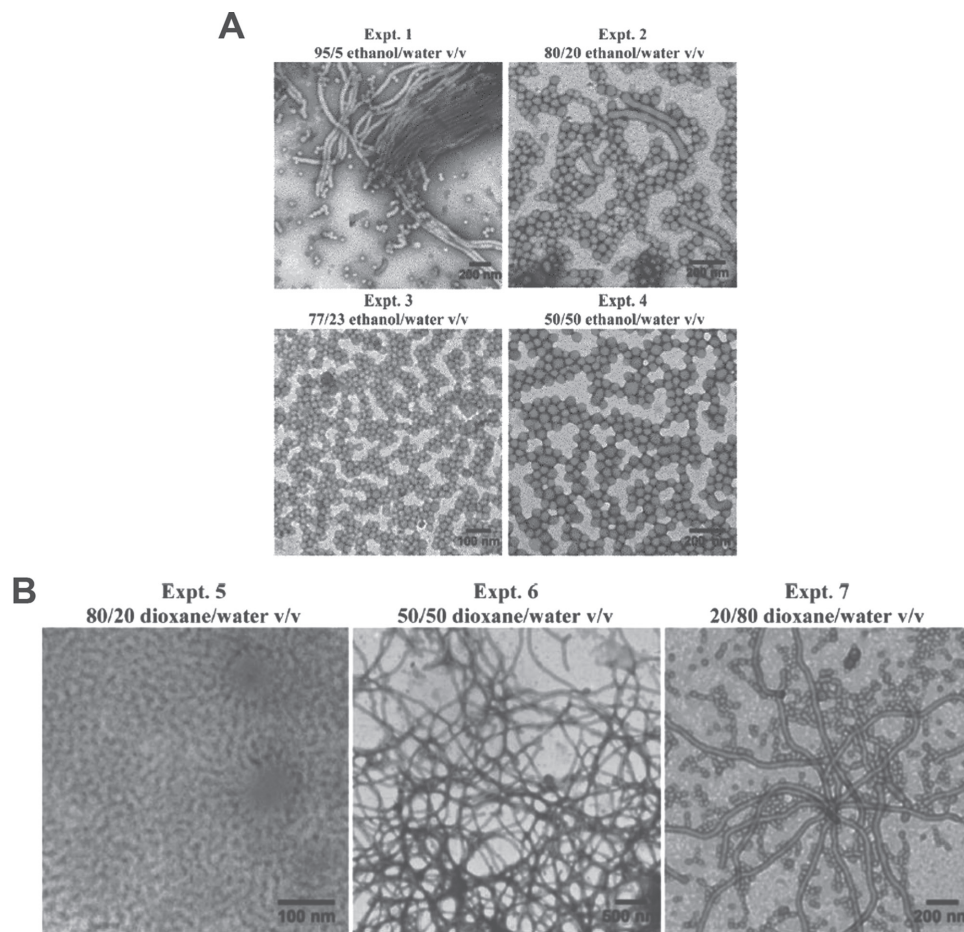


Figure 2. A) TEM images of the P(MAA-*co*-PEOMA)-*b*-P(BzMA) block copolymer nanoparticles synthesized in different ethanol–water volume ratios. Reproduced with permission.^[47] Copyright 2012, The Royal Society of Chemistry.

the relative brittleness of the gel increases. This result indicates that, at least in this case, the core P(St-*alt*-NMI) is responsible for the overall flexibility of the diblock copolymer nanoparticle.

In order to produce charged nanoparticles, polyelectrolytes can be employed as the stabilizing block.^[49–51] However, this approach has most often led to only spherical morphologies being obtained when using anionic polyelectrolytes.^[52] To overcome this limitation, an anionic polyelectrolytic stabilizing block based on poly(potassium 3-sulfopropyl methacrylate) (PKSPMA) was employed for systematically studying the effects of i) the diblock copolymer composition, ii) the overall solids content, and iii) added salt on the RAFT aqueous dispersion polymerization formulation.^[52–54] In the absence of salt, using the PKSPMA stabilizer resulted in ill-defined spherical nanoparticles as the DP of the core PHPMA polymer increased. Further, and contrary to previous RAFT aqueous dispersion polymerizations of HPMA, no worms or vesicles were observed when higher PHPMA DP was targeted. This effect was attributed to the strong polyelectrolyte nature of the PKSPMA block, which led to strong lateral repulsive electrostatic forces between the neighboring stabilizer chains and thus impeded their efficient self-assembly. To facilitate closer packing of the PKSPMA stabilizer chains, the authors added salt to the reaction for charge screening. Furthermore, to reduce the charge density within the corona layer, the authors copolymerized the KSPMA monomer with the nonionic 2-hydroxyethyl methacrylate (HEMA). By adding salt and using the stabilizing copolymer macro-CTA, the authors were able to obtain well-defined spherical nanoparticles with tunable diameters. A second strategy was also investigated to modulate the coronal charge density in these block copolymer nanoparticles. RAFT aqueous dispersion polymerization of HPMA was carried out using a binary mixture of two macro-CTAs. By systematically varying the proportion of PKSPMA and PGMA macro-CTAs, the overall zeta potential of the resultant block copolymers could be modulated. Moreover, this binary macro-CTA mixture strategy not only afforded control over the electrophoretic footprint of the nanoparticles but also enabled higher order morphologies such as vesicles to be accessed.

In a recent work, Wang et al. investigated the effect of polymer architecture on the morphology of diblock copolymers synthesized via PISA.^[55] A novel difunctional poly(ethylene glycol) (PEG)-based macro-CTA was synthesized. Both the mono- and bifunctionalized macro-CTAs were used for the RAFT aqueous dispersion polymerization of diacetone acrylamide (DAAM) to generate either linear PEG-PDAAM or star PEG-(PDAAM)₂ nanoparticles. This star architecture was shown to effectively promote morphological transitions to higher order morphologies (vesicle-like structures, no worms) at lower solids and DAAM DP compared to the linear PEG-based macro-CTA. This suggests that the star architecture increased the packing parameter and thus promoted morphological transitions during PISA conducted at high solids content.

An and coworkers have recently investigated the concurrent polymerization of macro-CTA and a CTA with the core-forming monomer.^[56] This polymerization technique results in a blend of block copolymer and homopolymer, and has therefore been termed polymerization-induced cooperative assembly (PICA). To carry out this synthesis, RAFT ethanolic dispersion polymerization of BzMA was mediated by both poly((*N,N'*-

dimethylamino)ethyl methacrylate) (PDMAEMA) macro-CTA and a small molecule CTA (i.e., both macro-CTA and CTA in the same pot). Under similar experimental conditions, the use of both PDAEMA macro-CTA and CTA resulted in short rods whereas the use of only the PDAEMA macro-CTA resulted in spheres. This result suggested that the new PICA process could promote morphological transitions by providing particles with increased packing parameter. When the CTA to macro-CTA ratio was increased (at the same target BzMA DP and solids), the morphology transitioned from fused spheres to largely perforated lamellae, to regular vesicles, and finally to distorted vesicles. Additionally, in PISA, it is known that higher solid content favors the formation of higher order morphologies (worms, vesicles, etc.). However, when the PICA synthesis was conducted over a range of solids from 10 to 20 wt%, the higher order morphologies persisted. These results demonstrate that CTA/macro-CTA ratio is another experimental parameter available to promote morphological transition.

Although RAFT-mediated PISA has been routinely achieved, almost all polymerizations are mediated by R-type macro-CTA (i.e., macro-CTA in which the leaving group R is the stabilizing block).^[57] As a result, the RAFT reactive group is inevitably located in the core of the polymer nanoparticles. To provide an alternative configuration, using a Z-type macro-CTA has been proposed.^[58] In this case, the stabilizing block is linked to the macro-CTA via the Z group, which ensures that the RAFT reactive group is at the center of the resultant block copolymer. Esterification of a RAFT agent with mPEG₄₅ yielded a Z-type macro-CTA, which was then used for a series of photoinitiated RAFT dispersion polymerization of *tert*-butyl acrylate (*t*BA) in ethanol/water (60/40 w/w). Systematic variation of the mean DP of the poly(*t*BA) (P*t*BA) block and the [*t*BA] was carried out to obtain block copolymers with different nanoparticle morphologies. Consistent with the literature, increasing the mean DP of P*t*BA at lower [*t*BA] (15 and 20% w/w) only led to the formation of spherical micelles. This is attributed to the reduced probability of sphere–sphere fusion that is necessary for worm formation. In contrast, higher order morphologies (worms and vesicles) were obtained at higher [*t*BA] (>25% w/w).

In addition to controlling the shape of PISA nanoparticles via the changing polymerization formulation, Armes and coworkers demonstrated that diblock copolymer displaying thermoresponsive character can be exploited to change the overall nanoparticle morphology.^[59,60] By conducting RAFT dispersion polymerizations of BzMA with a PLMA macro-CTA in *n*-dodecane, the authors were able to produce a range of sphere, worm, and vesicle phases by constructing a phase diagram with PLMA DP versus PBzMA DP. Curiously, the authors noticed that the worm phase forms a soft free-standing gel at ambient temperature. This gel formation was attributed to multiple worm–worm contacts. Heating the worm gel above 50 °C resulted in the onset of a worm-to-sphere transition. Concomitant degelation occurs as the sphere-to-sphere interactions are not as extensive as the worm-to-worm anisotropic interactions. Interestingly, this worm-to-sphere thermal transition is irreversible on heating a dilute solution (10% w/w) (**Figure 3**) but is reversible on heating a more concentrated dispersion (20% w/w), and as such the (ir)reversibility of the morphological transition can be considered concentration dependent. Furthermore, ¹H NMR

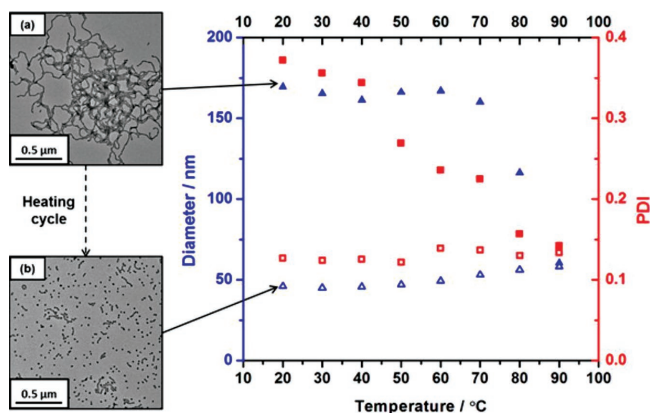


Figure 3. Dynamic light scattering (DLS) studies of dilute (10 wt%) dispersion of PLMA-*b*-PBzMA upon heating from 20 to 90 °C (closed symbols) and then cooled from 90 to 20 °C (open symbols). TEM inserts show the morphology of the P(LMA)-*b*-P(BzMA) block copolymer A) at the start and B) at the end of the heating cycle. Reproduced with permission.^[59] Copyright 2014, American Chemical Society.

studies provided confirmation that partial solvation of the core-forming block at an elevated temperature was sufficient enough to increase the copolymer curvature and hence induce a worm-to-sphere transition. In a similar work, PEG₁₁₃-*b*-PHPMA gels formed at above 10% w/w solids exhibit interesting thermoresponsive properties: heating the gel above its critical gelation temperature (i.e., to 40 °C) caused a worm-to-vesicle transition, resulting in degelation.^[60] Upon cooling the PEG₁₁₃-*b*-PHPMA vesicles to 2 °C overnight, the vesicles transitioned to spheres. Intriguingly, smaller vesicles were produced on warming to 50 °C. This thermal transition may also provide a convenient loading mechanism for the in situ encapsulation of proteins or antibodies.

Utilizing a RAFT aqueous dispersion polymerization formulation that produced a series of PGMA-*b*-PHPMA diblock copolymers, Lovett et al. exploited the thermo- and pH-responsive properties of this special diblock copolymer to produce profound morphological transitions.^[61,62] Switching the solution pH from 3.5 to 6.0 induced ionization of the terminal carboxylic acid on the PGMA stabilizer block, which increased its hydrophilic character. This resulted in a vesicle to sphere transition for the vesicles incorporating PHPMA₁₇₅ and a vesicle-to-worm transition for the vesicles incorporating PHPMA₂₀₀. However, if the DP of the PHPMA block is longer (225 or 250), no morphological transformation occurs. In regard to thermoresponsive behavior, only the PHPMA₁₇₅ vesicle underwent an order-order transition, with worms formed upon cooling to 5 °C. Subjecting the PGMA-*b*-PHPMA vesicles (regardless of PHPMA DP) to both pH switch and a temperature switch caused vesicle-to-sphere transition in each case. Altogether, the stimulus-responsive behavior of the PGMA-*b*-PHPMA vesicles depends primarily on the DP of the core-forming PHPMA block, although polymer end group is also implicated where potentially ionizable groups are incorporated at the chain terminus.

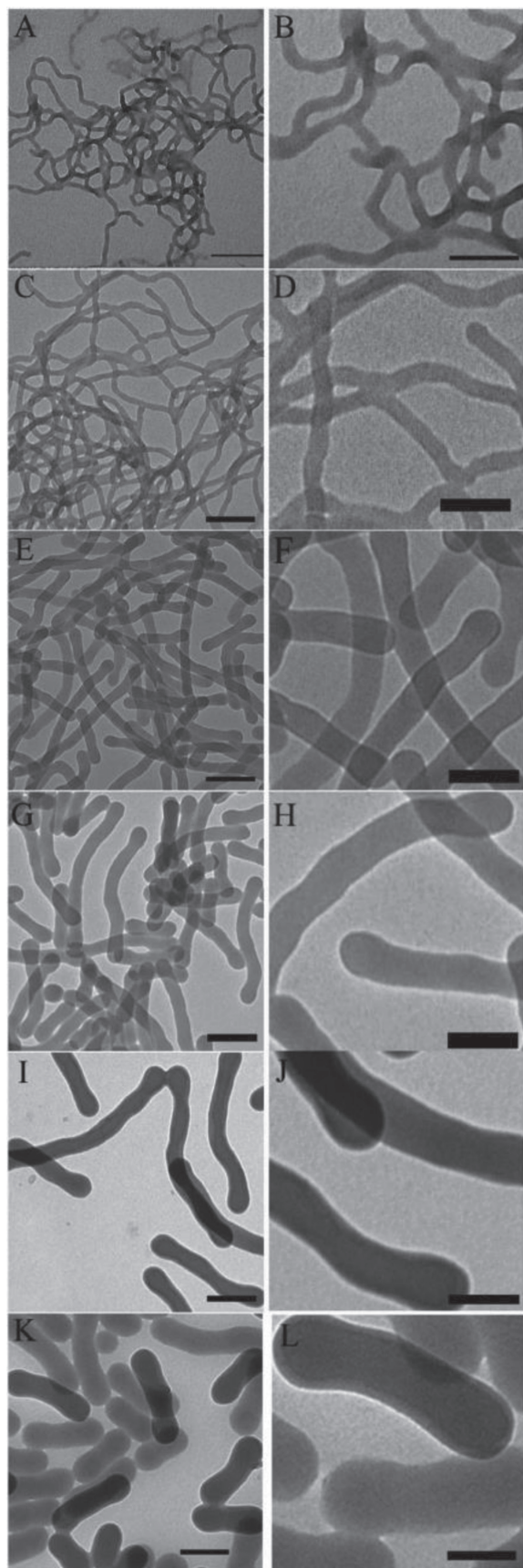
Another interesting experimental parameter to consider in controlling the shape of nanoparticles produced via RAFT dispersion polymerization is the choice of core-forming monomer. In a study by Chambon et al., PGMA-*b*-PHPMA

diblock copolymer vesicles were prepared and then used as precursors for chain extension with various monomers of differing aqueous solubility.^[63] When the PGMA-*b*-PHPMA diblock copolymer vesicles were chain-extended with HPMA, the resultant PGMA-*b*-PHPMA-*b*-PHPMA triblock copolymer chains formed smooth well-defined vesicles with membrane thickness of about 50–60 nm compared to the smooth well-defined PGMA-*b*-PHPMA vesicle membrane thickness of about 30–40 nm. Three other methacrylic monomers were investigated in this work; MMA, BzMA, and ethylene glycol dimethacrylate (EGDMA). For the PGMA-*b*-PHPMA-*b*-PMMA triblock copolymers, there is an increase in vesicle membrane thickness as the DP of PMMA increased. In addition, the vesicular morphology of PGMA-*b*-PHPMA-*b*-PMMA triblock copolymers was described as globular compared to the smooth PGMA-*b*-PHPMA diblock copolymer vesicles. When chain-extended with BzMA, the resultant PGMA-*b*-PHPMA-*b*-PBzMA triblock copolymers formed a distinctive framboidal morphology. Targeting longer PBzMA blocks led to significantly more pronounced globular features. This observation suggested that the globular features were formed from PBzMA chains. Finally, chain extension of PGMA-*b*-PHPMA diblock copolymer vesicles with EGDMA led to cross-linked vesicles with nano-scale domains within their membranes. In short, Chambon et al. showed that the vesicle morphology could be controlled via the choice of the third monomer.

2.2. Controlling Particle Size

Although spherical particles are commonly produced by PISA systems, controlling the diameter of PISA micelles was not demonstrated in early work.^[64–66] In 2010, Armes and coworkers reported the use of RAFT dispersion polymerization for the production of sterically stabilized micelles with a range of controlled diameters.^[67] To obtain such spherical micelles, a series of RAFT dispersion polymerizations of HPMA mediated by a PGMA macro-CTA were carried out. Systematic variation of the core PHPMA DP from 30 to 300 led to a monotonic increase in the mean micelle diameter from 26 to 105 nm. In addition, the authors discovered that targeting PHPMA DP 300 with a solids content of 20 wt% resulted in vesicles. To further demonstrate the utility of PISA via RAFT dispersion polymerization, Fielding and colleagues investigated the first all-methacrylic *n*-alkane-based formulation.^[46] This was accomplished via the RAFT dispersion polymerization of BzMA in the presence of a PLMA-based macro-CTA in *n*-heptane. Relatively long PLMA macro-CTAs could not form higher order morphologies. However, tuning the core PBzMA DP allowed access to a range of particle diameters. Specifically, as the core PBzMA DP increased from 100 to 900, the diameter of the spherical micelle increased from 41 to 139 nm. Since then, spherical micelles with well-controlled diameters have been obtained via adjusting the core DP.

To tune the diameter and length of worms, Zhang and colleagues used a PDMAEMA macro-CTA to mediate the RAFT dispersion polymerization of styrene in methanol and investigated the effect of PDMAEMA macro-CTA DP on the size of the resultant filament-like nanoparticles.^[68] Firstly, the authors



observed that the diameters of the filament-like nanoparticles increased as the DP of the PDMAEMA macro-CTA increased (Figure 4). In contrast, the apparent length of the filament-like nanoparticles appeared to decrease as PDMAEMA macro-CTA DP increased. In another study, Pei et al. found that changing the solids content of an identical poly(oligo(ethyleneglycol) methacrylate)-*b*-poly(3-phenylpropyl methacrylate) (POEGMA-*b*-PPMA) block copolymer could also alter the type of morphology, and in the case of worm-like particles, the cross-sectional diameter.^[69] For example, the 10 wt% formulation produced a mixture of spheres and short worms whereas the 20 wt% formulation yielded longer worms. Finally, for the 40 wt% formulation, the authors observed another pure worm phase in which the worms appear significantly larger. These results show that it is possible to control the length and diameter of worm-like nanoparticles via the concentration at which the particles are formed.

The size of vesicles can also be controlled by PISA. This has been achieved not only by using a binary mixture of relatively long and short poly(methacrylic acid) macro-CTAs (as shown by Gonzato et al.),^[70] but more recently by the topological engineering of the solvophobic block of the amphiphilic copolymer in PISA.^[71] Specifically, the topology of the solvophobic block could be regulated in a facile manner by RAFT dispersion copolymerization of BzMA and stearyl methacrylate (SMA). These two monomers were selected because they possess distinct molecular geometries. By varying the feed ratio of BzMA/SMA, the size of the resultant vesicles varied from 200 to 1500 nm. Novel nanostructures such as large compound micelles and large compound vesicles of several micrometers were also obtained by systematically varying the DP of the BzMA/SMA core-forming copolymer. To understand this phenomenon, the authors undertook molecular simulations. The results showed that the topological composition of the solvophobic block also changed the packing parameter, which is well-known to dictate final nanoparticle morphology. To further establish that such topological engineering of the solvophobic block could be exploited to control vesicle size, RAFT dispersion copolymerization of BzMA and 2-(perfluorooctyl)ethyl methacrylate was carried out. This polymerization also generated vesicles with tunable sizes, confirming that topological engineering has considerable utility for controlling the size of vesicles.

The membrane thickness of PISA vesicles can also be controlled by core DP. In 2016, Derry et al. reported the synthesis of poly(stearyl methacrylate)-poly(benzyl methacrylate) (PSMA-*b*-PBzMA) diblock copolymer nanoparticles in mineral oil.^[72] Such a formulation enabled a range of morphologies (spherical micelles, worm-like micelles, vesicles) to be synthesized. The different morphologies were characterized via TEM, DLS, and for the first time small angle X-ray scattering (SAXS). When examining the PSMA-PBzMA formulation that produced

Figure 4. TEM images of the PDMAEMA-*b*-PSt block copolymers with different PDMAEMA DP: A,B) PDMAEMA DP = 22; C,D) PDMAEMA DP = 36; PDMAEMA DP; E,F) PDMAEMA DP = 60, PDMAEMA DP; G,H) PDMAEMA DP = 98, PDMAEMA DP; I,J) PDMAEMA DP = 113, PDMAEMA DP; K,L) PDMAEMA DP = 247. Reproduced with permission.^[68] Copyright 2014, The Royal Society of Chemistry.

vesicles via SAXS, it was found that the vesicle membrane thickness increased monotonically as PBzMA DP increased with no significant increase in outer core radius. This effect was further investigated by targeting a range of final PBzMA DP (from 100 to 400). Consequently, increasing the final PBzMA DP from 100 to 400 resulted in an increase in vesicle membrane thickness from 9 to 30 nm. Targeting core PBzMA DPs above 400 resulted in vesicle destruction. The DLS data indicated similar overall vesicle dimensions for PBzMA DPs of 100–400, thus suggesting an “inward growth” mechanism.

The size of fluorinated PISA nanoparticles has also been controlled by varying the DP of the core-forming block. Semi-fluorinated methacrylates possess many desirable properties that make their polymers suitable for applications in self-assembly, ^{19}F NMR imaging, coatings, etc. Furthermore, they are soluble in common organic solvents. This represents an opportunity to enhance the monomer/solvent combinations of PISA. To this end, in a recent report, a series of semi-fluorinated methacrylates was systematically assessed for their applicability to PISA. Alcoholic RAFT dispersion polymerizations of 2-(perfluorobutyl)ethyl methacrylate (FBEMA), 2-(perfluorohexyl)ethyl methacrylate (FHEMA), and 2-(perfluorooctyl)ethyl methacrylate (FOEMA) were investigated.^[73] PISA of FBEMA in ethanol resulted in the production of spheres, worm-like micelles, and vesicles depending on the DP of PFBEMA and the solids content. In contrast, PISA of FHEMA (which has a higher fluorine content than FBEMA) resulted solely in spheres regardless of the DP of FHEMA. The authors opined that the fluoro-containing side chains may hinder the segmental movement and the morphology reorganization for these materials. Perhaps more interestingly, due to the liquid crystalline nature of PFOEMA, only cylindrical micelles could be prepared by RAFT dispersion polymerization of FOEMA. Furthermore, the diameter of the PFOEMA cylinders increased linearly with the DP of PFOEMA, suggesting that the PFOEMA blocks are substantially extended.

3. RAFT Emulsion Polymerization

3.1. Controlling Particle Shape

The first report of nonspherical PISA particles by emulsion polymerization was published in 2009.^[74] Shortly after, in 2010, the first example of nonspherical PISA particles prepared by RAFT emulsion polymerization was reported by Boisse et al.^[53] This work targeted the in situ preparation of nanofibers by using surfactant-free aqueous emulsion polymerization of styrene in the presence of a poly(AA)-*b*-poly(ethylene glycol) methyl ether acrylate (PEGA) macro-CTA. Firstly, when homopolymer macro-CTAs comprising either PAA or PEGA were employed, only spherical micelles were obtained. However, copolymer macro-CTA of PAA-*co*-PEGA resulted in worm-like micelles together with spherical micelles and small vesicles. Furthermore, it was found that the pH and salt concentration of the polymerization affected the final block copolymer morphology. As such, increasing the degree of ionization of AA (higher pH) resulted in a transition from mainly vesicles/fibers to mainly spheres as the electrostatic repulsion between the stabilizer

chains inhibited the reorganization of the spherical micelles to form the nanofiber structures. Ultimately, careful control of the pH and salt concentration of the polymerization medium led to the synthesis of very long nanofibers.

In addition to pH and salt concentration, core-forming polystyrene block length can also dictate final block copolymer morphology.^[75] Zhang et al. studied the effect of polymerization conditions, styrene/macro-CTA ratio, and macro-CTA structure.^[76] A series of RAFT aqueous emulsion polymerizations of styrene in the presence of PMAA-*co*-PEOMA macro-CTA were conducted. With regard to the final copolymer morphology, decreasing the [macro-CTA] (while keeping [styrene] constant) resulted in morphology transition from spheres, to fibers, and finally to vesicles as the proportion of the polystyrene block relative to the entire block copolymer increased. However, fibers morphology was only observed within a narrow window of polystyrene chain lengths when compared to spherical and vesicular morphology. Targeting higher styrene feed ratios (while maintaining [macro-CTA]) also resulted in the morphological evolution of spheres, then fibers, and finally vesicles. Again, only a narrow window of concentrations was found for the fiber phase. These experiments show that the final copolymer morphology was ultimately dependent on the proportion of the hydrophobic polystyrene block in the amphiphilic block copolymer. Similar to other PISA formulations (such as RAFT dispersion polymerization), the block copolymers initially formed spherical micelles with a short hydrophobic block and then change morphology as the hydrophobic block length increases. The authors' reasoning was that at intermediate conversion, the growing core is swelled by unreacted monomer which enhances chain mobility and enables reorganization. After near-complete consumption of the monomer, the aggregates are kinetically frozen (no effect of post-polymerization dilution or pH changes were observed). This behavior is consistent with polystyrene-based amphiphilic block copolymers that are known to form kinetically frozen rather than dynamic micellar aggregates in water.

In follow-up work, the chain length of the PEO monomers and the pH were shown to be important parameters that dictated the final block copolymer morphology.^[77] RAFT emulsion polymerization of styrene at pH 3.5 resulted only in spherical nanoparticles. This observation was attributed to the poor segregation between the hydrophilic and hydrophobic component of the system, which is caused by the low ionization state of the macro-CTA ($\text{pK}_a = 5.8$). Here, the same system was conducted at pH 5.0 to increase ionization of the MAA units in the macro-CTA (20–24% ionization) and subsequently increase the segregation between the hydrophilic and hydrophobic blocks. Under these conditions, an increase in the polystyrene block molar mass resulted in initial formation of spherical micelles, followed by fibers, and finally vesicles. However, at pH 7.0 (62% ionization), only spheres were obtained. This result revealed that the better-stabilized macro-CTA chains were not able to undergo the reorganization process needed for higher order morphologies. Finally, the authors investigated the effect of modulating the molar masses of the PMAA-*co*-PEOMA macro-CTA and the polystyrene block. Interestingly, regardless of the experiment series, the average hydrophobic/hydrophilic weight ratio for the formation of fibers was in the 70/30 to 80/20 range.

Lower ratios led to the formation of spheres and higher ratios led to the formation of vesicles. Overall, these results show that careful control of the polymerization pH is needed in order to access multiple morphologies in the RAFT aqueous emulsion polymerization of styrene with a PMAA-*co*-PEOMA.

Insertion of a PEGA block into a poly(*N*-acryloylmorpholine) (PNAM) macro-CTA has been found to promote sphere-to-vesicle morphology evolution. In this report, the authors synthesized four different hydrophilic macro-CTAs with PEGA units introduced either at the beginning, statistically, or at the end of a PNAM backbone: PNAM, PNAM-*b*-P(NAM-*co*-PEGA), PNAM-*co*-PEGA, and P(NAM-*co*-PEGA)-*b*-PNAM.^[78] A series of RAFT aqueous emulsion polymerizations of styrene in the presence of these four hydrophilic macro-CTAs was conducted. As reported in the previous study, the use of pure PNAM macro-CTA for emulsion polymerization of styrene resulted solely in spherical nanoparticles. In contrast, using PNAM-*b*-P(NAM-*co*-PEGA) macro-CTA for the emulsion polymerization of styrene resulted in large vesicles rather than spherical nanoparticles. This vesicular morphology persisted regardless of the polystyrene block molar mass that was synthesized. To confirm whether this effect was a result of the specific location of the PEGA units in the macro-CTA, the emulsion polymerization of styrene with the PNAM-*co*-PEGA macro-CTA was carried out. Instead of large vesicles, a mixture of small spherical nanoparticles (14 nm) and small vesicles was observed, confirming that the proximity of the PEGA units to the water interface was responsible for the formation of large vesicles when using the P(NAM)-*b*-P(NAM-*co*-PEGA) macro-CTA. When using the P(NAM-*co*-PEGA)-*b*-P(NAM) macro-CTA, a mixture of small spherical nanoparticles and vesicles was observed on the TEM images. Taken as a whole, this series of experiments revealed that positioning the PEGA block further from the polystyrene block resulted in a packing parameter value that is intermediate between that of the pure P(NAM) system and the system with the PEGA block closer to the polystyrene block (P(NAM)-*b*-P(NAM-*co*-PEGA)). As a result, mixed morphologies of spheres and vesicles were favored when using PNAM-*co*-PEGA and P(NAM-*co*-PEGA)-*b*-PNAM macro-CTA. This study demonstrates for the first time that the presence of hydrophilic side chain species in the macro-CTA is a factor in controlling the final block copolymer morphology in RAFT emulsion polymerization systems.

Significantly, the monomer solubility has been found to be a key parameter in accessing nonspherical morphologies via RAFT emulsion polymerization.^[79] 2-Hydroxybutyl methacrylate (HBMA, solubility $\approx 20 \text{ g dm}^{-3}$ at 70 °C), was utilized instead of BzMA (solubility $\approx 40 \text{ g dm}^{-3}$ at 70 °C) to undergo RAFT aqueous emulsion polymerization.^[78] Using HBMA for the core-forming block allowed access to an unusual “monkey nut” copolymer morphology over a limited range of target DP when using a PMAA macro-CTA. Decreasing or increasing the target DP outside of the “monkey nut” range results in the formation of well-defined spheres. These results suggested that aqueous solubility of the monomer can play an important role in determining the copolymer morphology obtained during PISA syntheses.

Recently, end group and initiator concentration have been demonstrated as new parameters to access spheres, worms,

and vesicles via RAFT aqueous emulsion polymerization.^[80] A series of RAFT aqueous emulsion polymerization of styrene with carboxylic acid and methyl ester terminated macro-CTAs were carried out.^[81] Under the same experimental conditions, the carboxylic acid-terminated diblock copolymer formed spherical nanoparticles whereas the methyl ester-terminated nanoparticles formed vesicles (Figure 5). It was hypothesized that the increase in RAFT end group hydrophobicity could have increased the packing parameter, and thus resulted in higher order morphologies such as worms and vesicles. To test this, the authors reduced the packing parameter by targeting lower molecular weights of the polystyrene block. By decreasing the styrene feed ratio of the experiments, the formation of worm-like nanoparticles and vesicles was observed, therefore completing the classic suite of nanoparticle morphologies (spherical micelles, worms, and vesicles). Another hypothesis for this profound morphological transformation was that increasing the end group hydrophobicity increased the number of chains aggregated in one particle. To test this hypothesis, the concentration of the radical initiator for the methyl ester-terminated diblock copolymer was halved. Interestingly, the morphology transitioned from vesicles to spheres just by halving the initiator concentration. This effect was also exploited for the carboxylic acid-terminated diblock copolymers (which previously did not undergo any morphological transformation), where the initiator concentration was doubled and the morphology changed from spheres to vesicles. Additionally, decreasing the molecular weight of the polystyrene block in these vesicles led to the formation of worms. This work demonstrates that RAFT end group hydrophobicity and initiator concentration are key parameters that can be exploited to enable access to sphere, worm, and vesicle morphology via RAFT aqueous emulsion polymerization.

Similarly to using thermoresponsive macro-CTA in RAFT dispersion polymerization, thermoresponsive methacrylate polymers with short OEG side chains can be applied toward the synthesis of nanoparticles with both spherical and nonspherical morphologies. DEGMA was copolymerized with HPMA under RAFT solution polymerization conditions to produce a PDEGMA-*co*-PHPMA macro-CTA, which was then used for the RAFT emulsion polymerization of styrene to produce P(DEGMA-*co*-HPMA)-*b*-PSt.^[82] Three emulsion polymerizations with increasing styrene feed ratios were used to produce P(DEGMA-*co*-HPMA)-*b*-PSt with increasing molecular weight. After polymerization, the hot latex solutions (70 °C) were slowly cooled to room temperature with and without added toluene (as a plasticizer). Varying the amount of toluene added to the hot latex solutions resulted in the formation of different morphologies. For all three (PDEGMA-*co*-PHPMA)-*b*-PSt, the absence of added toluene resulted in spherical nanoaggregates (Figure 6a). With the P(DEGMA-*co*-HPMA)-*b*-PSt of lowest and intermediate molecular weight, increasing the amount of toluene added resulted in morphological transitions from spherical nanoaggregates to long worm-like nanoparticles, to a mixture of worm-like nanoparticles and vesicles, and finally to vesicles (Figure 6b–e). However, for the P(DEGMA-*co*-HPMA)-*b*-PSt with the highest molecular weight, the spherical nanoaggregates transitioned to smaller spheres, and then to smaller spheres with short worm-like nanoparticles and finally long

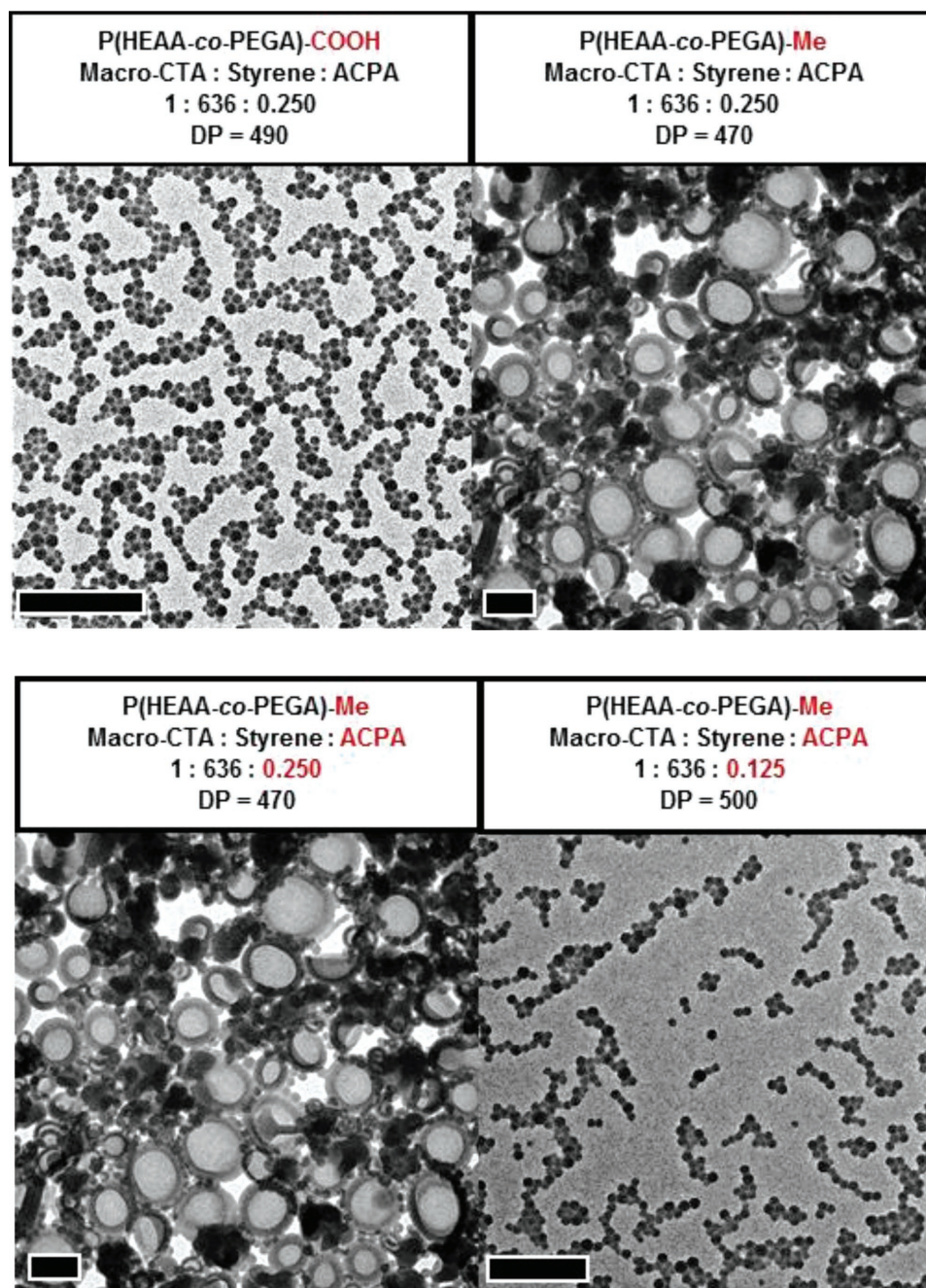


Figure 5. TEM images of particles formed via RAFT aqueous emulsion polymerization of styrene with A) P(HEAA-co-PEGA)-COOH macro-CTA and B) P(HEAA-co-PEGA)-Me macro-CTA. TEM images of particles formed via RAFT aqueous emulsion polymerization of styrene with P(HEAA-co-PEGA)-Me with the following macro-CTA:initiator feed ratios: A) 1:0.250 and B) 1:0.125. Reproduced with permission.^[81] Copyright 2017, American Chemical Society.

worm-like nanoparticles. Further, the filomicelle morphology could be obtained for polystyrene, PBzMA, PMMA, PEMA, and PPMA cores.^[83] Moreover, by randomly incorporating a hydrophilic component with ≈ 21 ethylene glycol units on the side chain of PDEGMA-co-PPMA, sphere, worms, and vesicles were successfully prepared by surfactant-free RAFT emulsion polymerization.^[84] Significantly, noncross-linked nano-objects prepared by RAFT emulsion polymerization using PDEGMA-co-PPMA as a macro-CTA are tolerant to high concentration of

surfactants, thus overcoming the surfactant tolerance challenge mentioned in earlier critical appraisals of PISA.^[85]

3.2. Controlling Particle Size

The diameter of spherical micelles obtained via RAFT emulsion polymerization has been shown to be dictated primarily by the core polymer DP. For example, RAFT emulsion

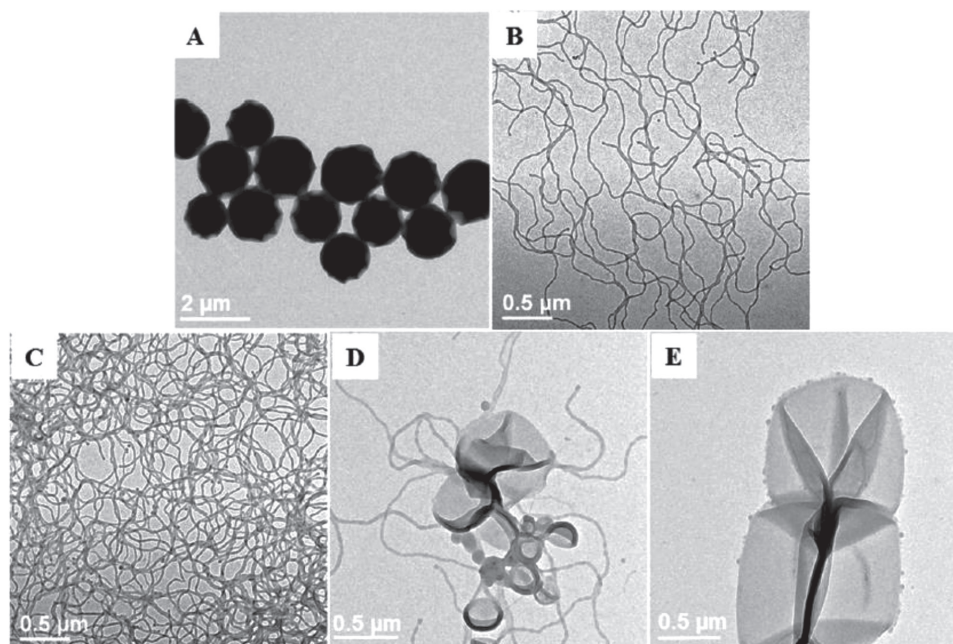


Figure 6. TEM images of a P(DEGMA-*co*-HPMA)-*b*-PSt block copolymer after polymerization and addition of different volumes of toluene: A) 0 $\mu\text{L mL}^{-1}$, B) 20 $\mu\text{L mL}^{-1}$, C) 40 $\mu\text{L mL}^{-1}$, D) 80 $\mu\text{L mL}^{-1}$, and E) 160 $\mu\text{L mL}^{-1}$, and then cooling to ambient temperature for 24 h. Reproduced with permission.^[82] Copyright 2016, The Royal Society of Chemistry.

polymerization of styrene was carried out in a one-pot process using a PMAA-*co*-PEOMA macro-CTA with two different ratios of MAA/PEOMA.^[86] These polymerizations were carried out keeping the [styrene] constant and varying the [macro-CTA] in order to alter the styrene: macro-CTA feed ratio. For all experiments, this polymerization formulation resulted in the formation of spherical particles with narrow particle size distribution (i.e., low polydispersity index). An observation was made that the higher the styrene: macro-CTA molar ratio, the higher the DP and the narrower the particle size distribution. In addition, it was found that the final spherical nanoparticle diameter increased significantly with the core polystyrene DP. For instance, for a polystyrene DP = 150, small particles of approximately 37 nm in diameter were formed. When the polystyrene DP = 970, particles of approximately 170 nm in diameter were obtained. The fact that only spherical particles were observed stands in contrast to other results obtained with the same macro-CTA used in the emulsion polymerization of styrene, where fibers and vesicles were obtained. While most of the experimental conditions were comparable, the key difference was that the pH of the emulsion polymerization was maintained at 3.5 in this work compared to 5.0 for the previous study. This lower pH ensured that the MAA units were largely nonionic, which the authors claim to lead to poor segregation between the hydrophilic and the hydrophobic component of the system, therefore resulting in spheres.

In a recent study, Truong et al. reported the use of a novel macro-CTA composed of *N*-hydroxyethyl acrylamide (HEAA) and PEGA units for the RAFT aqueous emulsion polymerization of styrene.^[87] By judicious selection of the macro-CTA components and the polymerization conditions, well-defined polymers and spherical particles were obtained. After confirming

that the macro-CTA with PHEAA₂₁-PEGA₂₁ was an excellent stabilizer and suitable macro-CTA for RAFT emulsion polymerization of styrene, a series of polystyrene diblock copolymers using this macro-CTA were synthesized. By appropriate variation of the styrene to macro-CTA ratio, well-defined spherical particles with narrow size distributions were obtained. The authors observed that there was a relationship between particle size and molecular weight, resulting in spherical particles ranging from 124 to 183 nm in diameter (corresponding to increasing the styrene to macro-CTA ratio from 2790: 1 to 5253: 1).

4. Biomedical Applications of PISA Nanoparticles

4.1. Delivery of Small Molecule Drugs

PISA has recently attracted increasing attention as a reproducible and scalable method for the facile preparation of nanomaterials for drug delivery. With the advantage of producing concentrated nanoparticles on a larger scale, PISA has great potential to address the challenges inherent in the scaling-up nanomaterial synthesis, one of the major obstacles hindering the market reach of nanoparticle drug delivery systems.^[88] Further, emulsion polymerization, one of the two ways to conduct PISA, is environmentally friendly and widely used in industry.^[39,89] In PISA, the shape of nanoparticles can be easily controlled, therefore enabling fundamental studies into the role of nanoparticle shape in drug delivery. On the other hand, there are challenges associated with loading drugs into PISA nanoparticles without interfering with the PISA process. In addition, controlling the drug release from PISA nanoparticles also requires specific particle design and chemistry.

To covalently attach a model drug and subsequently release it via a change of environmental conditions (i.e., pH), Karagoz et al. employed vinyl benzaldehyde (VBA) in the RAFT dispersion polymerization of styrene with a POEGMA macro-CTA.^[90] After the polymerization, the aldehyde functional groups in the polystyrene core allowed the conjugation of doxorubicin (DOX) via pH-labile bonds (Schiff base or imine). In this study, a family of polymeric nanoparticles with different morphologies (spherical, worm-like micelle, rod-like micelle, and vesicle) was prepared to study the effect of nanoparticle shape on both the cellular uptake in MCF-7 breast cancer cells and the IC₅₀ of DOX. Morphology control was achieved by manipulating the DP of the core P(St-co-VBA) block. As the DP of the core P(St-co-VBA) block increased, the morphology of the resultant POEGMA-*b*-P(St-co-VBA) block copolymer particles progressed from spherical micelles, to worm-like micelles, rod-like micelles, and finally vesicles. The aldehyde groups in the core were reacted with amino compounds to i) cross-link the nanostructure using pH-sensitive imine bonds, or ii) conjugate DOX via pH-sensitive imine bonds. Interestingly, cross-linking the block copolymers via reaction of the aldehyde groups with diamines did not affect the nanoparticle morphology even in the presence of THF. DOX was loaded into the nanoparticles with various shapes via conjugation of DOX amine groups with the aldehyde groups in the nanoparticles. MCF-7 breast cancer cells were then treated with the DOX-loaded nanoparticles for 24 h. After 1 h, differential nanoparticle cell uptake was observed, with rod-like micelles showing the highest MCF-7 cell uptake and micelles showing the lowest MCF-7 cell uptake. At 24 h, further uptake enhancement was observed for rod-like micelles and worm-like micelles. This cell uptake behavior was attributed to the higher aspect ratio of the worm- and rod-like nanoparticles, resulting in higher surface contact with cell membranes and then higher cell uptake (Figure 7). Additionally, IC₅₀ values for worm- and rod-like structures were seven times lower than that for spherical micelles, which is likely related to the higher cell uptake. Taken together, these results indicate that increasing cell uptake by changing nanoparticle morphology could be employed as a strategy for increasing cytotoxicity of DOX nanoparticles.

Using the same POEGMA-*b*-P(St-co-VBA) PISA nanoparticles, Hinde et al. sought to examine, in greater detail, the cellular uptake and route of intracellular transport for spherical micelles, rods, and worms in MCF-7 cells.^[91] A novel fluorescence microscopy method was developed to monitor intracellular routes of diffusion across subcellular compartments. Upon examining the mobility of nanoparticles across the extracellular space, the cytoplasm, and the nucleus, higher aspect ratio nanoparticles such as rod- and worm-shaped nanoparticles were found in the nucleus, whereas spherical nanoparticles (micelles and vesicles) were barely detectable (Figure 8a). This result suggested that the nuclear envelope acted as a barrier for spherical nanopar-

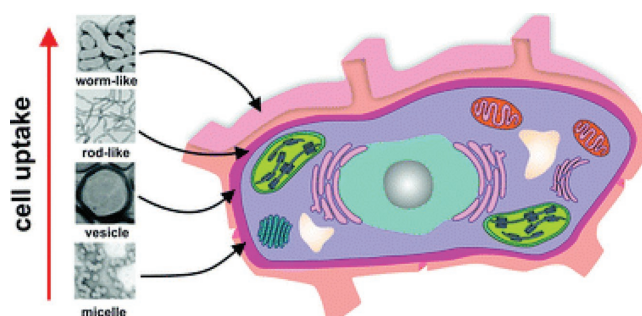


Figure 7. The morphology of POEGMA-*b*-P(St-co-VBA) block copolymers influences cellular uptake by MCF-7 breast cancer cells. Reproduced with permission.^[90] Copyright 2014, The Royal Society of Chemistry.

ticles. As such, rods and worms could potentially deliver more DOX into the nucleus than spherical nanoparticles, which may account for the higher toxicity observed with these drug carriers. Furthermore, by examining how rods and worms overcame the nuclear envelope, the authors gained interesting insights into the gate-keeping function of this barrier. First, they established that these higher aspect ratio nanoparticles entered the nucleus via passive diffusion. Second, they noted that diffusion across the nuclear envelope was bidirectional, which prevented higher nuclear accumulation of rods and worms even after longer incubation times. Third, to further

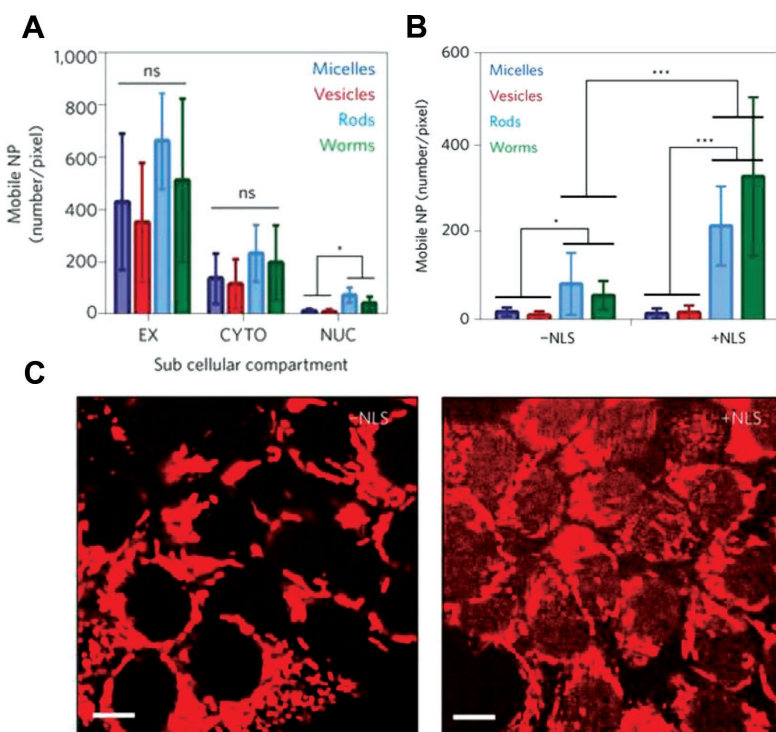


Figure 8. A) The concentration of mobile nanoparticles with various morphologies (micelles, vesicles, rods, worms) across the extracellular space (EX), cytoplasm (CYTO), and nucleus (NUC) of MCF-7 cells. B) The concentration of mobile nanoparticles with various morphologies (micelles, vesicles, rods, worms) with/without NLS modification in the nucleus of MCF-7 cells. C) Fluorescence images of MCF-7 cells incubated with worm-like nanoparticles without/with NLS modification. Reproduced with permission.^[91] Copyright 2016, Springer Nature.

improve nuclear accumulation, the authors tagged worm nanoparticles with a nuclear localization signal (NLS) protein and found that this enhanced diffusion of worm nanoparticles into the nucleus (Figure 8b,c). Curiously, the NLS protein functionalization of spherical nanoparticles did not enable nuclear entry (Figure 8b). This shape-dependent nuclear entry inferred that the physical barrier function of the nuclear envelope overrides the biochemical selection conferred by the NLS tag. Finally, with regard to nanoparticle drug delivery, overcoming the barrier function of the nuclear envelope seemed more critical than bulk accumulation within the nucleus, suggesting that strategies to enhance nucleus import are more promising for drug delivery to the nucleus than blocking nuclear export. Overall, these results show that drug delivery across the nuclear envelope is important for DOX efficacy and can be achieved with appropriately shaped nanoparticles.

In a different study, Qiu et al. also employed the pH-breakable bonds (Schiff base or imine) to conjugate DOX onto PISA nanoparticles for drug delivery application.^[92] RAFT dispersion polymerization of methacryloxyethoxy benzaldehyde (MAEBA) using PDMAEMA as the macro-CTA was carried out and the DP of MAEBA was tuned to obtain four well-defined morphologies. The authors synthesized spherical, nanorod-like, and vesicular nanoparticles with dimensions less than 200 nm based on literature evidence that the upper size limit of endocytosis is 200 nm. The nanorods synthesized had a length of 2000 nm. After that, DOX was conjugated onto the nanoparticles via a condensation reaction of primary amine groups in DOX with aldehyde groups in PMAEBA. The authors reported that DOX conjugation did not affect the overall morphology of the nanoparticles but increased their sizes when compared to pre-DOX loading (size increase of 10% for spheres, 12.7% for nanorods, and 28.5% for vesicles). Drug release studies under neutral pH conditions confirmed that the pH-labile aromatic imine bond formed after DOX conjugation was stable with less than 1% of DOX released from the nanoparticles. As expected, under acidic conditions (pH 5.0 and pH 6.0), the amount of DOX released increased but with no significant differences between the different nanoparticle morphologies. An in vitro cytotoxicity assay with HeLa cells was carried out to characterize the IC₅₀ of the DOX-loaded nanoparticles. The IC₅₀ of DOX-loaded nanorods was nearly 30 times higher than free DOX, indicating that the nanowires were not being internalized by HeLa cells. For the other shapes, IC₅₀ increased in the following order: nanorods, vesicles, and spheres. Curiously, the endocytosis tests showed that the nanorods were internalized at a slower rate compared to the vesicles but faster than spheres (Figure 9). This behavior indicated that the DOX rate of release in the acidic cellular organelles was faster for nanorods compared to vesicles. Hence, DOX-nanorods has lower IC₅₀ (more cytotoxic) when compared to vesicles although the internalization rate of nanorods is slower than vesicles. Overall, this study revealed that the aspect ratio of nanoparticle morphology had a significant impact on the IC₅₀ of DOX.

In addition to Schiff base chemistry, Par's group has also developed reductive-responsive prodrug PISA nanoparticles which enable anticancer drugs to be released in the reductive environment of tumors (which exhibit a higher concentration of glutathione [GSH] than healthy tissues).^[93] Camptothecin

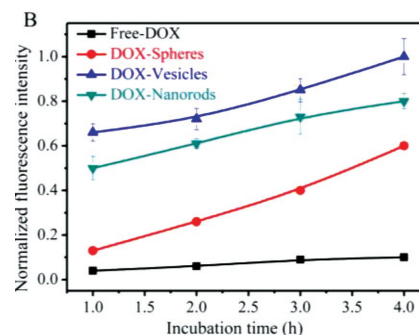


Figure 9. Kinetics of the accumulation of free DOX and DOX-loaded PDMAEMA-*b*-PMAEBA diblock copolymer spherical micelles, rods, and vesicles in HeLa cells via the normalized fluorescence intensity derived from CLSM images. Reproduced with permission.^[92] Copyright 2016, American Chemical Society.

(CPT) was chosen as the model drug due to its anticancer activity and the ability to readily conjugate it to a polymerizable group via appropriate chemistries. A CPT-containing monomer was synthesized and copolymerized with 2-(2-methoxyethoxy) ethyl methacrylate (MEO₂MA) by RAFT solution polymerization, resulting in a CPTM-MEO₂MA macro-CTA. RAFT dispersion polymerization of BzMA and a reductive-sensitive cross-linker in the presence of the CPTM-MEO₂MA macro-CTA was carried out, and yielded cross-linked micelles bearing CPT. The resultant cross-linked structure remained stable in THF, with no morphology change observed. In vitro drug release experiments for prodrug nanoparticles with varying CPT content were carried out at various concentrations of glutathione (GSH). Under high GSH concentration (similar to concentrations encountered in the cytosol), the reductive-sensitive cross-linker in the core was cleaved, and CPT liberation was observed. Cytotoxicity tests against HeLa cells showed that cytotoxicity was correlated with CPT content in the prodrug nanoparticles, with CPT release occurring over 16 h regardless of initial CPT content.

Another route for loading small molecules into PISA nanoparticles is through electrostatic interactions.^[94] Zhang et al. reported the fabrication of stimuli-responsive PISA nanoparticles based on RAFT dispersion polymerization of the photosensitive monomers 2-nitro-benzyl methacrylate (NBMA) and 7-(2-methacryloyloxyethoxy)-4-methyl-coumarin (CMA) in the presence of a PHPMA macro-CTA. Various PHPMA-*b*-P(NBMA-*co*-CMA) block copolymer morphologies (micelles, worm-like micelles, lamellae, and vesicles) were obtained by varying the DP of the photosensitive P(NBMA-*co*-CMA) core. UV irradiation was carried out to cleave the 2-nitrobenzyl group from the NBMA units, thus forming PHPMA-*b*-P(MAA-*co*-CMA) nanoparticles. DOX was efficiently encapsulated (up to 24.9 wt %) by the electrostatic interaction between -COO⁻ and -NH₃⁺ groups in PMAA and DOX, respectively. Intracellular drug release studies showed that the electrostatically loaded DOX nanoparticles were able to release DOX rapidly in the intracellular region of HeLa cells.

Aside from cytotoxic drugs, other small molecules have been conjugated to PISA nanoparticles.^[95] For example, Ladmira et al. synthesized a range of galactose-decorated block

copolymers with various morphologies (micelles, worm-like micelles, and vesicles). To test their glycotargeting ability, these glycosylated polymers with different morphologies were subjected to lectin-binding assays. These experiments revealed that not only did all the galactosylated polymers interact strongly with galactose-specific lectins, but the sensitivity of such binding was dependent on the morphology of the block copolymers. At the same copolymer concentration, the use of galactose-decorated worm-like micelles and vesicles led to greater lectin sensitivity compared to the galactose-decorated spherical micelles. Furthermore, this study showed that galactosylated vesicles were rapidly taken up by primary human dermal fibroblast cells.

4.2. Delivery of Large Therapeutics

In addition to small molecule drugs, controlled release of large payloads (e.g., proteins, antibodies) offers considerable scope for targeted drug delivery applications. To that end, various chemistries have been explored to induce the release of large cargos from PISA particles.^[96,97] For example, Armes' group carried out RAFT aqueous dispersion polymerization of HPMA in the presence of 5–35 wt% silica nanoparticles as a model of large payloads.^[98] After confirming encapsulation of the silica nanoparticles within purified vesicles, the feasibility of controlled release of the encapsulated silica nanoparticles was explored. By cooling the temperature down to between 0 and 10 °C, vesicle dissociation and subsequent silica nanoparticle release could be induced (Figure 10). In fact, time-resolved SAXS indicated that this vesicle dissociation was complete after 12 min at 0 °C. Finally, to demonstrate the utility of this encapsulation technique for other cargoes, bovine serum albumin (BSA) was chosen as a model biological cargo. To avoid protein denaturation, RAFT aqueous dispersion polymerization of HPMA with BSA was carried out at 37 °C with a low-temperature initiator (VA-044). The rate of HPMA polymerization was significantly slower at 37 °C, but nevertheless, near-complete conversion was achieved (99%) and a pure vesicle morphology was observed. Moreover, the vesicle morphology was not affected by this low-temperature PISA formulation, suggesting that it may be possible to encapsulate proteins or other biomolecules (DNA, RNA, antibodies) under mild conditions. BSA encapsulation was confirmed by fluorescence spectroscopy, demonstrating that this in situ vesicle loading via PISA is translatable to biologically relevant cargoes. In this example, the vesicle-to-sphere transition was only observed when cooling such vesicles from 20 to 0 °C. This thermal trigger operating at sub-ambient temperature is likely undesirable for most commercial applications.

To develop PISA nanoparticles having morphological transitions at ambient temperature, Dent et al. incorporated water-soluble 3-aminophenylboronic acid (APBA) into PGMA-*b*-PHPMA diblock copolymer vesicles. First, PISA was used to prepare PGMA-*b*-PHPMA diblock copolymer vesicles in concentrated aqueous solution.^[99] This diblock copolymer was chosen because i) the PGMA block contained pendent cis-diol groups that could bind selectively to water-soluble phenylboronic acid derivatives, and ii) the PHPMA block is weakly

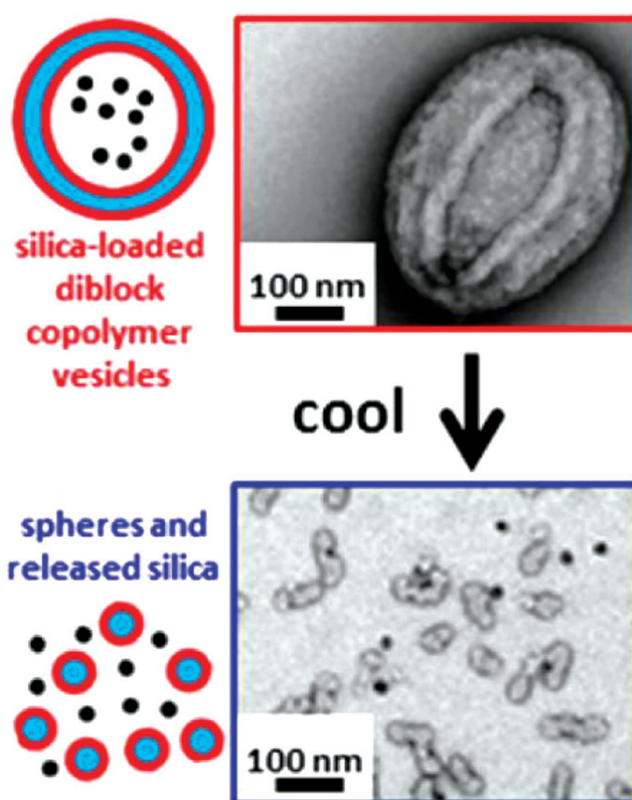


Figure 10. TEM images of A) silica-loaded P(GMA)-*b*-P(HPMA) vesicles, and after cooling, B) P(GMA)-*b*-P(HPMA) spheres and released silica nanoparticles. Reproduced under the terms of the Creative Commons Attribution license.^[98] Copyright 2015, American Chemical Society.

hydrophobic, which facilitates the desired order–order morphological transition. In the presence of 5.8 mM APBA, the original vesicles were transformed into a mixture of worms and spheres after 15 h. This change was attributed to the APBA selectively binding to the PGMA chains via phenylboronate ester bond formation. This effectively increased the volume fraction of the PGMA stabilizer block by increasing its effective mass and introducing anionic charge, which in turn reduced the geometric packing parameter for the copolymer chains. Importantly, increasing the [APBA] resulted in mainly vesicle–sphere transitions and decreasing the [APBA] resulted in mainly vesicle–worm transitions. Furthermore, adding APBA to thicker-walled vesicles (which do not typically exhibit morphological transition behavior) at ambient temperature caused transformation from vesicles to a mixture of worms and spheres. This morphological transition required a much higher [APBA] and longer time. Finally, PGMA-*b*-PHPMA vesicles with various PHPMA DPs were loaded with silica nanoparticles and treated with different levels of [APBA]. From these studies, the authors observed that the rate of release of the silica nanoparticle cargo can be fine-tuned by varying the [APBA] as well. Altogether, the authors demonstrated that phenylboronic acid chemistry can be used to induce morphological transition of vesicles under ambient temperature conditions. Furthermore, this strategy can be applied to thick-walled vesicles that do not normally exhibit stimulus-responsive behavior.

Aside from nonfunctional entities such as BSA and silica nanoparticles, an emerging biomedical application of PISA nanoparticles is the encapsulation of functional proteins. The use of PISA to encapsulate functional proteins is advantageous compared to other synthetic routes because of the purely aqueous conditions and high concentrations possible. In 2017, Blackman et al. reported the synthesis of enzyme-loaded permeable vesicles under mild, aqueous conditions.^[37] It should be noted that while enzyme-loaded vesicles via PISA have been prepared by Tan et al., the activity of the vesicle encapsulated enzyme was not investigated. To enable the successful encapsulation of thermo-sensitive enzymes, Blackman et al. synthesized PEG-*b*-PHPMA block copolymer vesicles using initiator-free visible light-mediated PISA. This one-pot, mild approach proved highly versatile and was applied to encapsulate a range of functional enzymes. In the initial experiments, green fluorescent protein (GFP) was used to i) confirm the successful encapsulation of proteins and ii) confirm the location of GFP in the vesicle lumens. Next, catalytic enzymes such as horseradish peroxidase (HRP) and glucose oxidase (GOx) were loaded into vesicles to investigate the permeability of the vesicle membrane toward small molecule substrates. These experiments revealed that the loading efficiency of the PEG-*b*-PHPMA block copolymer vesicles was up to 54% for HRP and 41% for GOx. After demonstrating that HRP and GOx could permeate through the vesicle membrane, the authors mixed HRP-loaded vesicles and GOx-loaded vesicles in a 1:1 ratio in phosphate buffer to see if they could interact with one another and result in an enzymatic cascade reaction. When compared with free enzymes, the cascade occurred with 46% activity, which the authors attributed to hindrance of substrate passage through the membrane.

After confirming the permeability of the PEG-*b*-PHPMA vesicle membrane and demonstrating successful enzyme encapsulation, Blackman et al. also studied the encapsulation of a commercially available protein therapeutic, L-asparaginase (ASNS).^[36] Proteins such as ASNS are usually covalently PEGylated, which modifies the protein's hydrophobicity and surface charge.^[100] Physical encapsulation of unmodified proteins protects them against proteases, which helps evade the immune system, and essentially allows the protein to function from within the confined domain. In this spirit, aqueous photo-PISA was carried out in the presence of ASNS, yielding ASNS-loaded vesicles with a PEG shell and PHPMA membrane. These ASNS-loaded vesicles displayed excellent proteolytic stability when exposed to a protease, α -chymotrypsin (α -CT), whereby retention of activity was observed after 18 h of α -CT exposure. In contrast, free ASNS and PEGylated ASNA both completely lost their catalytic ability within the same time period. Based on these results, Blackman et al. hypothesized that antibodies with larger molar mass than α -CT would be precluded from entering into the vesicle lumen, effectively inhibiting antibody recognition. To test this hypothesis, the binding affinity of anti-ASNS toward PEGylated ASNS and ASNS-loaded vesicles was tested using a sandwich enzyme-linked immunosorbent assay (ELISA), and compared to the binding affinity of anti-ASNS toward native ASNS. While the binding affinity of anti-ASNS toward PEGylated ASNS and native ASNS was similar, the binding affinity of anti-ASNS toward ASNS-loaded vesicles was two orders of magnitude lower than native ASNS. Therefore,

as an alternative to PEGylated ASNS, treating hypersensitive patients with encapsulated ASNS could lower the risk of an immune response. Finally, the efficacy of the ASNS-loaded vesicles against a cancer cell line and its biological disposition and pharmacokinetics in vivo were tested and found to be comparable to the free ASNS, highlighting ASNS-loaded vesicles as an attractive alternative to PEGylated ASNS.

4.3. Delivery of Imaging Contrast Agents

In addition to the delivery of small and large therapeutics, PISA nanoparticles have also been employed to deliver inorganic contrast agent for magnetic resonance imaging (MRI) applications. The in situ preparation of iron oxide nanoparticle-functionalized polymeric nanoparticles with various morphologies via PISA has been recently developed by Karagoz et al.^[101] The authors carried out RAFT alcoholic dispersion polymerizations of styrene with a diblock copolymer of POEGMA-*b*-PMAA. The incorporation of MAA provided carboxylic acid groups that were used to complex a mixture of ferrous and ferric ions ($\text{Fe}^{2+}/\text{Fe}^{3+}$), and so form iron oxide nanoparticles. Triblock copolymer nanoparticles with various morphologies (spherical micelles, rod-like micelles, and vesicles) were obtained by tuning the DP of the polystyrene block. To complex the iron ion mixture, an excess of Fe^{2+} and Fe^{3+} ions to carboxylic acid groups was employed. In the first set of experiments, the authors found that iron oxide nanoparticles readily formed on the PISA nanoparticles with no disruption to the morphology. Further experiments showed that triblock copolymers containing an increasing number of MAA units with the same [Fe] resulted in increasing size of the iron oxide nanoparticles. Finally, this ion complexing protocol was repeated for micelles and worms and iron oxide nanoparticles were also observed on these morphologies. As superparamagnetic iron oxide nanoparticles have been extensively studied for applications as negative MRI contrast agents, the triblock copolymer/iron oxide nanoparticle hybrids with different morphologies were tested using a high field MRI scanner. Interestingly, the micelle morphology showed the highest transverse relaxivity ($582 \text{ mM}^{-1} \text{ s}^{-1}$), which was several times higher than that observed for the commercially available contrast agent, for example, Feridex ($\approx 100 \text{ mM}^{-1} \text{ s}^{-1}$). Rod-like micelles had a measured relaxivity of $412 \text{ mM}^{-1} \text{ s}^{-1}$ and vesicles $277 \text{ mM}^{-1} \text{ s}^{-1}$. This difference in relaxivity was attributed to the distribution of iron oxide nanoparticles within the polymer aggregates. In the micelles, iron oxide nanoparticles are closer to one another, which results in an enhancement of their relaxivity due to cluster formation.

To deliver positive contrast agents for MRI, Esser et al. sought to prepare gadolinium-loaded nanoparticles via the PISA technique.^[38] Firstly, a novel macro-CTA of poly(glycidyl methacrylate)-*b*-POEGMA (PGlyMA-*b*-POEGMA) was synthesized to mediate the RAFT alcoholic dispersion polymerization of styrene. From the resultant PGlyMA-*b*-POEGMA-*b*-PSt triblock copolymer, a range of sizes and shapes (spherical micelles, filomicelles, and vesicles) were successfully created by tuning the DP of the core-forming polystyrene block (**Figure 11a–c**). Next, the versatility of the epoxide functional groups for post-polymerization functionalization was demonstrated by

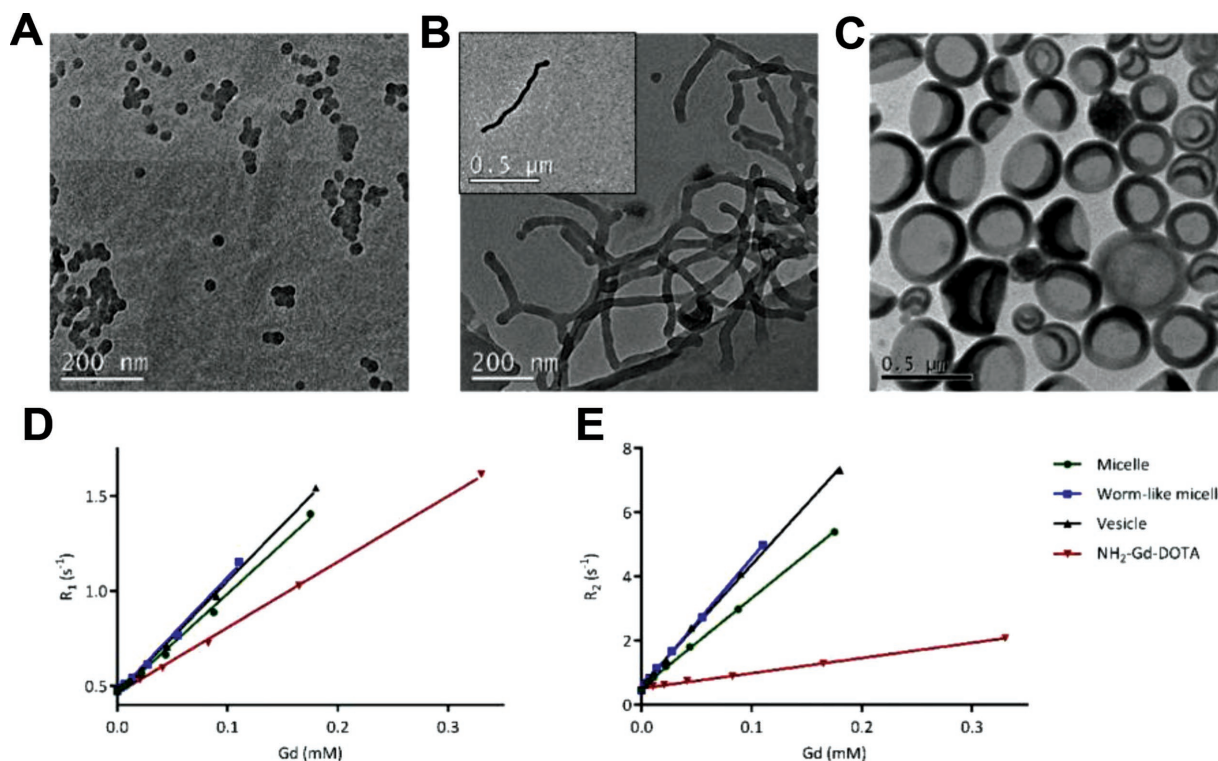


Figure 11. TEM images of gadolinium-functionalized A) spherical micelles, B) filomicelles, and C) vesicles. D) Longitudinal (R_1) and E) transversal (R_2) relaxation rates for nanoparticles with different morphologies and various gadolinium concentrations. Reproduced with permission.^[38] Copyright 2016, The Royal Society of Chemistry.

ring-opening through primary amines, thiols, and sodium azide. Importantly, these post-polymerization modifications did not affect the final nanoparticle morphology. A pre-synthesized cyclic gadolinium chelate was then conjugated to PGlyMA-*b*-POEGMA-*b*-PSt spherical micelles, filomicelles, and vesicles via primary amines, and their application as positive contrast MRI agents was investigated. These tests showed that the filomicelle shape was the most promising candidate as it combined good gadolinium-labeling efficiency with a high T_1 relaxivity (Figure 11d,e). The vesicles have a comparable relaxivity to filomicelles but lower gadolinium loading. In view of earlier results demonstrating that filomicelles exhibited enhanced blood circulation times, gadolinium-functionalized filomicelles synthesized via PISA could have potential applications for magnetic resonance angiography and in cancer diagnostics/theranostics.^[34]

Fluorine-19 (¹⁹F) MRI imaging is a promising strategy to overcome the existing limitations of conventional ¹H MRI imaging. Fluorine presents comparable magnetic resonance sensitivity to protons while exhibiting physiological rarity within the body, which minimizes background signal in imaging. As such, fluorine-containing polymeric nanomaterials are receiving increasing attention as imaging probes for ¹⁹F MRI to enable quantitative in vivo detection of cells.^[102] In this work, Zhao et al. synthesized a range of nanoparticle morphologies, including spheres, worm-like particles, and vesicles via PISA. These nanoparticles were produced via a RAFT dispersion polymerization of styrene and VBA with a POEGMA-*co*-poly(2,2,2-trifluoroethyl acrylate) (POEGMA-*co*-PTFEA) macro-CTA. The different

nanoparticle morphologies were obtained by stopping the polymerization at different reaction times that corresponded to the morphological evolution of spherical micelles, worms, and then vesicles. After obtaining the various morphologies, the aldehyde groups in the nanoparticle cores were exploited to conjugate fluorescent dye molecules for the purpose of the biological studies. This process did not alter the final nanoparticle morphology. When analyzed by ¹⁹F NMR, the ¹⁹F relaxation times T_1 and T_2 remained constant for all nanoparticles, showing no dependence on morphology. Finally, using Chinese hamster ovarian (CHO) cells, the cellular uptake of the nanoparticles was investigated. Consistent with previous cellular uptake studies, higher aspect ratio nanoparticles (worm-like) entered cells more readily than their spherical counterparts (spherical micelle and vesicle). This supports the prevailing hypothesis that surface area is correlated with cellular uptake. It is worth noting that confocal microscopy confirmed the accumulation of all nanoparticles in the cytoplasm regardless of morphology. The authors concluded that these ¹⁹F-containing nanoparticles with different morphologies could be applied toward in vivo cell tracking.

To increase the sensitivity of X-ray computed tomography (CT) imaging in the clinic, Ding et al. used PISA to conduct a one-pot synthesis of iohexol nanoparticles as a potential CT contrast agent. The iohexol nanoparticles were achieved using iohexol acrylate as a cross-linking agent, and in this way, the iohexol content could be tuned. In addition, using PISA meant that the nanoparticle sizes could be tuned by varying the feed ratio of iohexol acrylate, HPMA, and the PEG macro-CTA.

In vivo and in vitro studies revealed that when compared to iohexol, the iohexol nanoparticles displayed longer circulation time, higher accumulation in tumors, and negligible toxicity.

4.4. Worm Gels for Cell Culture and Blood Cryopreservation

Nanoworms prepared via PISA have recently been used as sterilizable hydrogels for biomedical applications.^[103–106] For example, the Armes group reported the synthesis of well-defined PGMA-*b*-PHPMA diblock copolymer worm-like nanoparticles that could form free-standing physical hydrogels due to interworm entanglements.^[107] Upon cooling to 4 °C, an unusual worm-to-sphere order–order transition was observed. Bringing the temperature back up to room temperature caused the spherical micelles to transform back to worm-like micelles. The authors proposed that this order–order transition could be exploited for biomedical applications. As a proof of concept, a cold dispersion of diblock copolymers was deliberately contaminated with FITC-labeled *Staphylococcus aureus* bacteria at 4 °C and then warmed to room temperature, where regelation occurred as expected. The bacteria-loaded copolymer sample was then readily sterilized by cooling back to 4 °C and then filtered through a 0.45 µm membrane filter. This method removes the micrometer-sized bacteria but allows passage of the low-viscosity copolymer nanoparticles through the filter. The bacteria contaminated copolymer showed strong fluorescence whereas negligible fluorescence was observed for the reformed sterile copolymer gel after ultrafiltration. To confirm complete removal of bacteria, the filtered and unfiltered copolymer solutions were cultured for 24 h at 37 °C. As expected, the ultrafiltered copolymer gel showed no bacterial growth, whereas the bacteria-contaminated copolymer gel showed bacterial growth. The authors propose that this copolymer worm gel could be employed as an injectable scaffold for stem cell growth due to its sterilizable properties.

Three years later, the Armes group further demonstrated the application of these PGMA-*b*-PHPMA thermoresponsive diblock copolymers for embedding cells in mesh sheets for 3D cell culture. 3D in vitro cell cultures (such as Matrigel) are generally considered to be superior to 2D in vitro cell cultures in terms of providing a microenvironment that more closely resembles living tissue. However, the use of 3D cell cultures often requires specialized histology and optical techniques in order to observe the cells. Since the PGMA-*b*-PHPMA worm gels can undergo reversible transition from worms to spheres upon cooling, they could provide a thermoresponsive hydrogel from which cells can be embedded and recovered. Furthermore, commercially available protein-based gels need to be stored in the fridge to prevent irreversible chemical degradation whereas the PGMA-*b*-PHPMA synthetic hydrogel can be stored indefinitely at room temperature and gel reversibly on demand. In the preliminary experiments, PGMA-*b*-PHPMA worm gels were supported by paper or polyester meshes. However, these worm gels became partially detached from the sheets after 9 days. Thereafter, a new gel containing disulphide bonds within the PGMA stabilizer chains was prepared, and could be used to evaluate the effects of cell-ECM proteins for at least 12 days without detaching from the mesh substrate. To examine if cells

embedded in these disulfide-based worm gels were capable of proliferation, fluorescent A549-GFP cells were spotted into the worm gels and the changes in fluorescence intensity were measured as a function of cellular proliferation. Over 12 days of cell culture, the fluorescence intensity increased linearly over time and confirmed that the cells were viable and proliferative for a minimum of 12 days while being embedded in the worm gel. To isolate the cells, the worm gels were cooled to cause degelation (i.e., worm-to-sphere transition) and release the cells from the gel matrix. The authors incubated A549-GFP cells in worm gels in cold saline solution and showed that approximately 91% of the cells detached from the mesh sheets after 1 h in the cold saline solution. Furthermore, the A549-GFP cells released from the worm gels remained viable and could be further cultured and analyzed directly for up to 7 days after release. Altogether, the authors have demonstrated that this reversible worm gel has the potential as a viable alternative to Matrigel as a 3D cell culture support.

Human pluripotent stem cells rapidly proliferate to maintain their undifferentiated state. However, for mammals exhibiting delayed gestation, mucin-coated embryos can remain dormant for days or months in the uterus with their component pluripotent stem cells remaining pluripotent under these conditions. Secreted mucins possess unusual viscoelastic properties and can provide a passive protective barrier against pathogens and other environmental toxins. However, growing evidence suggests that secreted mucins can have an undesired influence on cell morphology and junction dynamics during embryonic development. These observations suggest that synthetic mucin mimics may be promising active biomaterials for regenerative medicines. In this spirit, Armes and colleagues proposed the use of a synthetic PGMA-*b*-PHPMA diblock copolymer worm gel that can undergo reversible degelation via a worm-to-sphere order-to-order transition upon cooling from 37 to 5 °C.^[33] The authors recognized that the hydroxyl-rich PGMA block is a biocompatible polymer that can potentially minimize cell adhesion. Moreover, these synthetic worm gels exhibit comparable gel moduli to natural mucins. As such, the authors explored whether immersing pluripotent stem cell colonies within worm gels can induce long-term stasis while maintaining both pluripotency and viability. The initial experiments in this work revealed that human pluripotent stem cell colonies immersed in worm gel remained intact for up to 8 days. In contrast, human pluripotent stem cell colonies immersed in Matrigel began fragmenting at Day 4. Immunolabeling assays confirm that the pluripotent stem cell colonies immersed in worm gels enter stasis within 24 h at 37 °C. Remarkably, this state of suspended animation was reversible upon degelation and enables survival of pluripotent human stem cells up to 2 weeks without any passaging. In addition, the mucin-like nature of such soft hydroxyl-functional worm gels was observed to induce stasis for up to 8 days after worm gel immersion. Such synthetic worm gels offer considerable utility for the short-term storage (i.e., weeks) of either pluripotent stem cells or human embryos without cryopreservation.

Aside from cell culture applications, the PGMA-*b*-PHPMA worm gels have been recently applied in cryopreservation of red blood cells. Current strategies for cryopreservation of red blood cells entail the addition of large quantities of water-miscible

organic solvents such as glycerol or DMSO to promote vitrification (ice-free state) or dehydration. A major source of cell damage in cryopreservation is ice crystal growth during the thawing process. Typically, hydroxyethyl starch (HES) is used as a nontoxic biopolymer for ice inhibition. However, HES has recently been partially withdrawn from clinical use due to a possible increase in mortality for critically ill patients. As such, synthetic mimics of HES are urgently needed. Gibson and coworkers investigated the use of diblock copolymer PGMA-*b*-PHPMA worms as synthetic biomimetic alternatives to HES for cellular cryopreservation.^[108] To assess if the PGMA-*b*-PHPMA worms could inhibit ice crystal formation/growth-associated cell damage that occurs during the thawing process, they were tested against poly(vinyl alcohol) (PVA), which is a potent ice recrystallization inhibitor. The results showed that PVA was highly active for inhibiting ice recrystallization even at a low concentration of 1.0 mg mL⁻¹. However, the PGMA-*b*-PHPMA worms showed no inhibition activity even at 20 mg mL⁻¹. Overall, this data showed that PGMA-*b*-PHPMA

worms caused neither ice growth nor nucleation, making them a good candidate for synthetic nonpenetrative cryoprotectants like HES. When tested against frozen red blood cells and then thawed, the PGMA-*b*-PHPMA worms alone resulted in just 20% cell survival after thawing (Figure 12a). Treatment with HES resulted in 40% cell survival and combination with PVA boosted cell recovery to 70%. Finally, when PGMA-*b*-PHPMA worms were added to PVA, the worms gave 68% recovery which was statistically insignificant to the co-treatment of HES and PVA. As such, these diblock copolymer worm gels show promise as the first synthetic alternative to biopolymers such as HES and show excellent ice-recrystallization inhibitor when combined with PVA.

5. Conclusions and Outlook

In the last decade, the PISA technique has been extensively studied and developed. This review highlights various biomedical applications of PISA nanoparticles from their early use in drug delivery to recent applications in tissue culture, blood preservation, and magnetic resonance imaging. Importantly, the ability to control nanoparticle size and shape via PISA have paved the way for the comprehensive study of nano-bio interactions and may be able to address the significant challenge in the scaling-up synthesis of nanomaterials. We anticipate that new applications for PISA nanomaterials, not limited to biomedical science, will continue to emerge as further advances are made on the parameters that control size and shape of PISA nanoparticles are made. So far, polymer chemists have made significant contributions to the field by establishing various design principals for tuning the size and shape of PISA nanomaterials. Several parameters summarized in this review include changing the DP of the macro-CTA and core-forming polymers, the concentration of macro-CTA and core-forming monomers, the solid content of final products, macro-CTA architecture and topology, solution pH, salt concentration and monomer solubility as well as using cosolvents, thermoresponsive macro-CTA, and additional macro-CTA or CTA (Tables 1 and 2).

It is worth noting that several limitations and challenges highlighted in a critical appraisal of PISA in 2016,^[109] such as surfactant tolerance of PISA nanoparticles and kinetically trapped spherical morphology found in RAFT emulsion polymerization, have been now addressed. Not only RAFT dispersion polymerization, but size and shape of PISA particles prepared by RAFT emulsion polymerization have also been recently well-controlled. Beyond the limitations and challenges mentioned in the critical review by Armes and coworkers, the ability to simultaneously control two physicochemical properties has also been demonstrated.^[110] That said, further efforts are necessary to address remaining limitations and challenges of PISA. For example, it remains challenging to control the length of worm-like particles, simultaneously control all physicochemical properties of PISA nanoparticles, predict the morphology of PISA particles without a comprehensive study of the phase diagram, expand the zone of pure morphology in the phase diagram, and fully understand the mechanism of PISA leading to the ability to control size and shape of all amphiphilic copolymers by both RAFT dispersion and emulsion polymerization. It is also

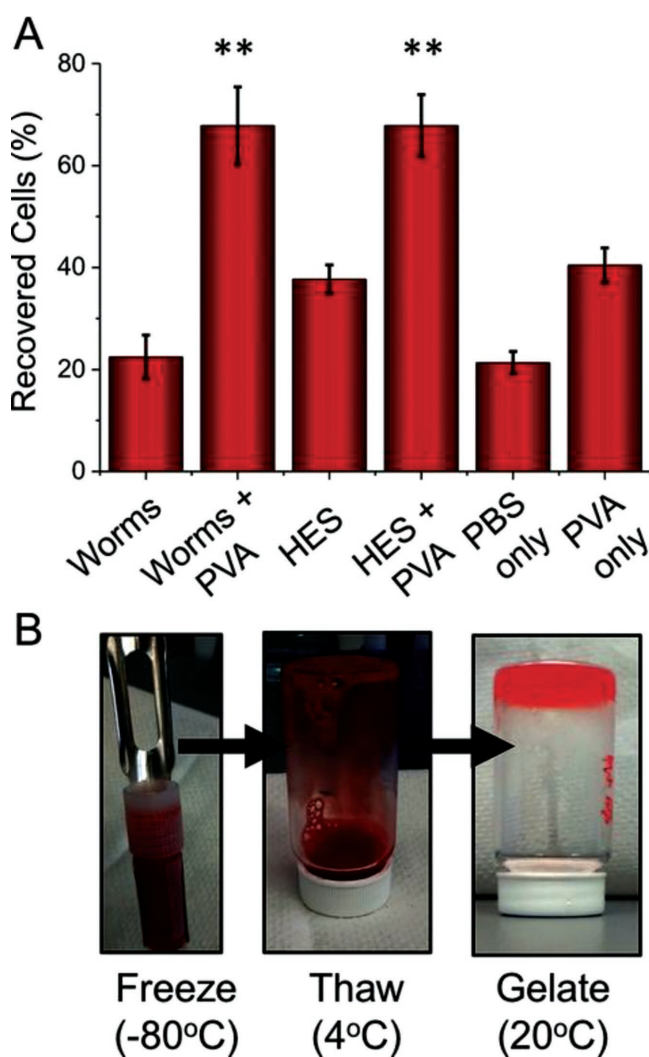


Figure 12. A) Cell recovery after cryopreservation for 3 days. B) Gelation following a freeze/thaw cycle. Reproduced under the terms of the Creative Commons Attribution license.^[108] Copyright 2016, Wiley-VCH.

Table 1. Experimental factors that have been used to control the morphology of particles synthesized via RAFT dispersion polymerization. M = micelles, W = worm-like micelles, V = vesicles, and L = lamellae.

Shape-controlling factor/s	Core monomer/s	Macro-CTA	Morphology	Reference
Core DP	HPMA	PDMAEMA	M, W, V	[49]
		PEG	M, W, V	[60]
	St	P(4-vinylpyridine)	M, W	[41]
		PEG	M, W, L	[8]
Core DP, macro-CTA DP	St, NMI	PMAA	M, W, L	[48]
	BzMA	PLMA	M, W, V	[59]
Core DP, [core monomer]	St	PEO	M, W, V	[43]
		t-BA	mPEG ₄₅	M, W, V
	HPMA	PGMA	M, W, V	[44]
		PSBMA	M, W, V	[45]
	BzMA	PDMAEMA	M, W, V	[42]
		PLMA	M, W, V	[46]
Core DP, pH, temperature	HPMA	PGMA	M, W, V	[61]
Macro-CTA architecture	DAAM	PEG	M, V	[55]
Macro-CTA DP, [macro-CTA]	HPMA	PKPSMA	M, V	[54]
Macro-CTA and CTA mixture, solids content	BzMA	PDMAEMA	M, W, V	[56]
Core DP, solvent composition	BzMA	P(MAA-co-PEO)	M, W	[47]

Table 2. Experimental factors that have been used to control the morphology of particles synthesized via RAFT emulsion polymerization. M = micelles, W = worm-like micelles, V = vesicles, and L = lamellae.

Shape-controlling factor/s	Core monomer/s	Macro-CTA	Morphology	Reference
[Macro-CTA], [core monomer]	St	P(MAA-co-PEOMA)	M, W, V	[75]
Core DP	HBMA	P(MAA)	O	[78]
	MMA, St	P(MAA-co-PEOMA)	M, W, V	[74]
Core DP, macro-CTA DP	St	P(MAA-co-PEOMA)	M, W, V	[85]
Core DP, macro-CTA end group, [initiator]		P(HEAA-co-PEGA)	M, W, V	[80]
Macro-CTA composition, pH, salt		P(AA-co-PEGA)	M, W, V	[76]
Macro-CTA composition	St	P(NAM)	M, V	[77]
		P(NAM-co-PEGA)		
		P(NAM-co-PEGA)-b-P(NAM)		
Post-polymerization monomer addition	St	P(DEGMA-co-HPMA)	M, W	[82]
	EMA			
	BzMA			
	PMA			
Post-polymerization plasticizer addition	St	P(DEGMA-co-HPMA)	M, W, V, L	[83]
	St	P(DEGMA-co-HPMA-co-PEGMA)	M, W, V	[81]
	MMA			
	–			
	St	P(DEGMA-co-HPMA)	W, V, L	[84]
	PMA			



worth highlighting that controlling the morphology of PISA particles via aqueous RAFT emulsion polymerization formulation remains much more limited compared to RAFT dispersion polymerization and hence, significant efforts are still urgently needed. The ability to reproducibly manufacture nanomaterials in concentrated solution via aqueous RAFT emulsion polymerization is expected to increase the impact of PISA nanoparticles in biomedical applications and to be scalable for industrial manufacturing. Simultaneously, in addition to the synthetic challenges aforementioned, more effort is required to investigate the in vivo characteristics (degradability, responsiveness, biocompatibility, etc.) of PISA nanoparticles in order to successfully apply them in a clinical setting.

To further increase the utility of the PISA technique, reversible-deactivation radical polymerization (RDRP) techniques other than RAFT may be considered. Nitroxide-mediated polymerization (NMP) is another RDRP technique that is commonly used for PISA formulations. For example, the first PISA emulsion polymerization conducted in a single batch step was conducted using NMP.^[11] Since then, NMP-mediated PISA formulations have produced advanced architectures with hybrid morphologies. Further developments in NMP-mediated PISA formulations could provide further biomedical applications for PISA nanoparticles.

In summary, PISA is now a powerful and useful technique for the preparation of polymeric nanoparticles for various applications, and as the field continues to expand rapidly, this technique is expected to soon become a more and more popular technique used by not only polymer chemists but also biologists, materials scientists, and industrial manufacturers.

Acknowledgements

S.Y.K. acknowledges the financial support from the Australian Government Research Training Program scholarship. J.F.Q. acknowledges receipt of a Future Fellowship from the ARC (FT170100144). N.P.T. acknowledges the award of a DECRA Fellowship from the ARC (DE180100076). T.P.D. is grateful for the award of an Australian Laureate Fellowship from the ARC (FL140100052).

Conflict of Interest

The authors declare no conflict of interest.

Keywords

biomedical applications, dispersion polymerization, emulsion polymerization, polymerization-induced self-assembly, reversible addition-fragmentation chain transfer

Received: June 6, 2018

Revised: July 13, 2018

Published online:

[1] N. J. Warren, S. P. Armes, *J. Am. Chem. Soc.* **2014**, *136*, 10174.

[2] B. Charleux, G. Delaittre, J. Rieger, F. D'Agosto, *Macromolecules* **2012**, *45*, 6753.

- [3] J. B. Tan, D. D. Liu, Y. H. Bai, C. D. Huang, X. L. Li, J. He, Q. Xu, X. C. Zhang, L. Zhang, *Polym. Chem.* **2017**, *8*, 1315.
- [4] D. W. Zhou, R. P. Kuchel, P. B. Zetterlund, *Polym. Chem.* **2017**, *8*, 4177.
- [5] J. Rieger, *Macromol. Rapid Commun.* **2015**, *36*, 1458.
- [6] M. J. Derry, L. A. Fielding, S. P. Armes, *Prog. Polym. Sci.* **2016**, *52*, 1.
- [7] N. P. Truong, J. F. Quinn, M. V. Dussert, N. B. T. Sousa, M. R. Whittaker, T. P. Davis, *ACS Macro Lett.* **2015**, *4*, 381.
- [8] X. Chen, L. Liu, M. Huo, M. Zeng, L. Peng, A. C. Feng, X. S. Wang, J. Y. Yuan, *Angew. Chem. Int. Ed.* **2017**, *56*, 16541.
- [9] C. J. Ferguson, R. J. Hughes, B. T. T. Pham, B. S. Hawckett, R. G. Gilbert, A. K. Serelis, C. H. Such, *Macromolecules* **2002**, *35*, 9243.
- [10] H. Tanaka, K. Yamauchi, H. Hasegawa, N. Miyamoto, S. Koizumi, T. Hashimoto, *Physica B Condens. Matter* **2006**, *385–386*, 742.
- [11] N. G. Engelis, A. Anastasaki, G. Nurumbetov, N. P. Truong, V. Nikolaou, A. Shegawal, M. R. Whittaker, T. P. Davis, D. M. Haddleton, *Nat. Chem.* **2016**, *9*, 171.
- [12] S. L. Canning, V. J. Cunningham, L. P. D. Ratcliffe, S. P. Armes, *Polym. Chem.* **2017**, *8*, 4811.
- [13] F. L. Hatton, J. R. Lovett, S. P. Armes, *Polym. Chem.* **2017**, *8*, 4856.
- [14] I. Schreur-Piet, J. P. A. Heuts, *Polym. Chem.* **2017**, *8*, 6654.
- [15] H. T. Ta, N. P. Truong, A. K. Whittaker, T. P. Davis, K. Peter, *Expert Opin. Drug Deliv.* **2017**, *15*, 33.
- [16] N. P. Truong, M. R. Whittaker, C. W. Mak, T. P. Davis, *Expert Opin. Drug Deliv.* **2015**, *12*, 129.
- [17] R. Albiges, P. Klein, S. Roi, F. Stoffelbach, C. Creton, L. Bouteiller, J. Rieger, *Polym. Chem.* **2017**, *8*, 4992.
- [18] M. Chenal, C. Vechambre, J. M. Chenal, L. Chazeau, V. Humblot, L. Bouteiller, C. Creton, J. Rieger, *Polymer* **2017**, *109*, 187.
- [19] M. Guerre, M. Semsarilar, F. Godiard, B. Ameduri, V. Ladmiral, *Polym. Chem.* **2017**, *8*, 1477.
- [20] S. Kaga, N. P. Truong, L. Esser, D. Senyschyn, A. Sanyal, R. Sanyal, J. F. Quinn, T. P. Davis, L. M. Kaminskas, M. R. Whittaker, *Biomacromolecules* **2017**, *18*, 3963.
- [21] M. J. Derry, L. A. Fielding, S. P. Armes, *Polym. Chem.* **2015**, *6*, 3054.
- [22] A. F. Cardozo, C. Julcour, L. Barthe, J. F. Blanco, S. Chen, F. Gayet, E. Manoury, X. W. Zhang, M. Lansalot, B. Charleux, F. D'Agosto, R. Poli, H. Delmas, *J. Catal.* **2015**, *324*, 1.
- [23] D. Nguyen, H. S. Zondanos, J. M. Farrugia, A. K. Serelis, C. H. Such, B. S. Hawckett, *Langmuir* **2008**, *24*, 2140.
- [24] K. L. Thompson, C. J. Mable, J. A. Lane, M. J. Derry, L. A. Fielding, S. P. Armes, *Langmuir* **2015**, *31*, 4137.
- [25] B. Karagoz, C. Boyer, T. P. Davis, *Macromol. Rapid Commun.* **2014**, *35*, 417.
- [26] Q. Zhang, C. J. Wang, M. L. Fu, J. L. Wang, S. P. Zhu, *Polym. Chem.* **2017**, *8*, 5474.
- [27] J. Engstrom, F. L. Hatton, L. Wagberg, F. D'Agosto, M. Lansalot, E. Malmstrom, A. Carlmark, *Polym. Chem.* **2017**, *8*, 1061.
- [28] N. P. Truong, W. Y. Gu, I. Prasad, Z. F. Jia, R. Crawford, Y. Xiao, M. J. Monteiro, *Nat. Commun.* **2013**, *4*, 1902.
- [29] N. P. Truong, J. F. Quinn, M. R. Whittaker, T. P. Davis, *Polym. Chem.* **2016**, *7*, 4295.
- [30] X. Wen, L. M. Tang, B. T. Li, *Chem. Asian J.* **2014**, *9*, 2975.
- [31] H. B. Qiu, Z. M. Hudson, M. A. Winnik, I. Manners, *Science* **2015**, *347*, 1329.
- [32] S. Mandal, Z. H. Eksteen-Akeroyd, M. J. Jacobs, R. Hammink, M. Koepf, A. J. A. Lambeck, J. C. M. van Hest, C. J. Wilson, K. Blank, C. G. Figdor, A. E. Rowan, *Chem. Sci.* **2013**, *4*, 4168.
- [33] I. Canton, N. J. Warren, A. Chahal, K. Amps, A. Wood, R. Weightman, E. Wang, H. Moore, S. P. Armes, *ACS Cent. Sci.* **2016**, *2*, 65.

- [34] Y. Geng, P. Dalhaimer, S. Cai, R. Tsai, M. Tewari, T. Minko, D. E. Discher, *Nat. Nanotechnol.* **2007**, *2*, 249.
- [35] J. T. Sun, Z. Q. Yu, C. Y. Hong, C. Y. Pan, *Macromol. Rapid Commun.* **2012**, *33*, 811.
- [36] L. D. Blackman, S. Varlas, M. C. Arno, Z. H. Houston, N. L. Fletcher, K. J. Thurecht, M. Hasan, M. I. Gibson, R. K. O'Reilly, *ACS Cent. Sci.* **2018**, *4*, 718.
- [37] L. D. Blackman, S. Varlas, M. C. Arno, A. Fayter, M. I. Gibson, R. K. O'Reilly, *ACS Macro Lett.* **2017**, *6*, 1263.
- [38] L. Esser, N. P. Truong, B. Karagoz, B. A. Moffat, C. Boyer, J. F. Quinn, M. R. Whittaker, T. P. Davis, *Polym. Chem.* **2016**, *7*, 7325.
- [39] E. Velasquez, J. Rieger, F. Stoffelbach, F. D'Agosto, M. Lansalot, P. E. Dufils, J. Vinas, *Polymer* **2016**, *106*, 275.
- [40] C. Q. Huang, Y. Wang, C. Y. Hong, C. Y. Pan, *Macromol. Rapid Commun.* **2011**, *32*, 1174.
- [41] W. M. Wan, C. Y. Hong, C. Y. Pan, *Chem. Commun.* **2009**, 5883.
- [42] E. R. Jones, M. Semsarilar, A. Blanazs, S. P. Armes, *Macromolecules* **2012**, *45*, 5091.
- [43] C. Q. Huang, C. Y. Pan, *Polymer* **2010**, *51*, 5115.
- [44] A. Blanazs, A. J. Ryan, S. P. Armes, *Macromolecules* **2012**, *45*, 5099.
- [45] K. E. B. Doncom, N. J. Warren, S. P. Armes, *Polym. Chem.* **2015**, *6*, 7264.
- [46] L. A. Fielding, M. J. Derry, V. Ladmiraal, J. Rosselgong, A. M. Rodrigues, L. P. D. Ratcliffe, S. Sugihara, S. P. Armes, *Chem. Sci.* **2013**, *4*, 2081.
- [47] X. W. Zhang, J. Rieger, B. Charleux, *Polym. Chem.* **2012**, *3*, 1502.
- [48] P. C. Yang, L. P. D. Ratcliffe, S. P. Armes, *Macromolecules* **2013**, *46*, 8545.
- [49] M. Semsarilar, V. Ladmiraal, A. Blanazs, S. P. Armes, *Langmuir* **2013**, *29*, 7416.
- [50] D. W. Zhou, S. M. Dong, R. P. Kuchel, S. Perrier, P. B. Zetterlund, *Polym. Chem.* **2017**, *8*, 3082.
- [51] L. P. D. Ratcliffe, K. J. Bentley, R. Wehr, N. J. Warren, B. R. Saunders, S. P. Armes, *Polym. Chem.* **2017**, *8*, 5962.
- [52] S. Boisse, J. Rieger, G. Pembouong, P. Beaunier, B. Charleux, *J. Polym. Sci. Part A Polym. Chem.* **2011**, *49*, 3346.
- [53] S. Boisse, J. Rieger, K. Belal, A. Di-Cicco, P. Beaunier, M. H. Li, B. Charleux, *Chem. Commun.* **2010**, 46, 1950.
- [54] M. Semsarilar, V. Ladmiraal, A. Blanazs, S. P. Armes, *Langmuir* **2012**, *28*, 914.
- [55] X. Wang, C. A. Figg, X. Q. Lv, Y. Q. Yang, B. S. Sumerlin, Z. S. An, *ACS Macro Lett.* **2017**, *6*, 337.
- [56] A. Q. Zhu, X. Q. Lv, L. L. Shen, B. H. Zhang, Z. S. An, *ACS Macro Lett.* **2017**, *6*, 304.
- [57] J. B. Tan, J. He, X. L. Li, Q. Xu, C. D. Huang, D. D. Liu, L. Zhang, *Polym. Chem.* **2017**, *8*, 6853.
- [58] J. B. Tan, X. L. Li, R. M. Zeng, D. D. Liu, Q. Xu, J. He, Y. X. Zhang, X. C. Dai, L. L. Yu, Z. H. Zeng, L. Zhang, *ACS Macro Lett.* **2018**, *7*, 255.
- [59] L. A. Fielding, J. A. Lane, M. J. Derry, O. O. Mykhaylyk, S. P. Armes, *J. Am. Chem. Soc.* **2014**, *136*, 5790.
- [60] N. J. Warren, O. O. Mykhaylyk, D. Mahmood, A. J. Ryan, S. P. Armes, *J. Am. Chem. Soc.* **2014**, *136*, 1023.
- [61] J. R. Lovett, N. J. Warren, S. P. Armes, *Macromolecules* **2016**, *49*, 1016.
- [62] J. R. Lovett, N. J. Warren, L. P. D. Ratcliffe, M. K. Kocik, S. P. Armes, *Angew. Chem. Int. Ed.* **2015**, *54*, 1279.
- [63] P. Chambon, A. Blanazs, G. Battaglia, S. P. Armes, *Macromolecules* **2012**, *45*, 5081.
- [64] E. R. Jones, O. O. Mykhaylyk, M. Semsarilar, M. Boerakker, P. Wyman, S. P. Armes, *Macromolecules* **2016**, *49*, 172.
- [65] Y. Su, X. Xiao, S. T. Li, M. H. Dan, X. H. Wang, W. Q. Zhang, *Polym. Chem.* **2014**, *5*, 578.
- [66] G. Y. Liu, Q. Qiu, W. Q. Shen, Z. S. An, *Macromolecules* **2011**, *44*, 5237.
- [67] Y. T. Li, S. P. Armes, *Angew. Chem. Int. Ed.* **2010**, *49*, 4042.
- [68] W. J. Zhang, C. Y. Hong, C. Y. Pan, *J. Mater. Chem. A* **2014**, *2*, 7819.
- [69] Y. Pei, K. Jarrett, L. G. Garces, M. Saunders, J. P. Croue, P. J. Roth, C. E. Buckley, A. B. Lowe, *RSC Adv.* **2016**, *6*, 28130.
- [70] C. Gonzato, M. Semsarilar, E. R. Jones, F. Li, G. J. Krooshof, P. Wyman, O. O. Mykhaylyk, R. Tuinier, S. P. Armes, *J. Am. Chem. Soc.* **2014**, *136*, 11100.
- [71] M. Huo, Z. Y. Xu, M. Zeng, P. Y. Chen, L. Liu, L. T. Yan, Y. Wei, J. Y. Yuan, *Macromolecules* **2017**, *50*, 9750.
- [72] M. J. Derry, L. A. Fielding, N. J. Warren, C. J. Mable, A. J. Smith, O. O. Mykhaylyk, S. P. Armes, *Chem. Sci.* **2016**, *7*, 5078.
- [73] M. Huo, D. Li, G. J. Song, J. Zhang, D. C. Wu, Y. Wei, J. Y. Yuan, *Macromol. Rapid Commun.* **2018**, *39*, 1700840.
- [74] G. Delaittre, C. Dire, J. Rieger, J. L. Putaux, B. Charleux, *Chem. Commun.* **2009**, 2887.
- [75] W. J. Zhang, F. D'Agosto, P. Y. Dugas, J. Rieger, B. Charleux, *Polymer* **2013**, *54*, 2011.
- [76] X. W. Zhang, S. Boisse, W. J. Zhang, P. Beaunier, F. D'Agosto, J. Rieger, B. Charleux, *Macromolecules* **2011**, *44*, 4149.
- [77] W. J. Zhang, F. D'Agosto, O. Boyron, J. Rieger, B. Charleux, *Macromolecules* **2012**, *45*, 4075.
- [78] J. L. de la, X. W. Haye, I. Zhang, F. Chaduc, M. Brunel, F. Lansalot, D'Agosto, *Angew. Chem. Int. Ed.* **2016**, *55*, 3739.
- [79] A. A. Cockram, T. J. Neal, M. J. Derry, O. O. Mykhaylyk, N. S. J. Williams, M. W. Murray, S. N. Emmett, S. P. Armes, *Macromolecules* **2017**, *50*, 796.
- [80] L. D. Blackman, K. E. B. Doncom, M. I. Gibson, R. K. O'Reilly, *Polym. Chem.* **2017**, *8*, 2860.
- [81] S. Y. Khor, N. P. Truong, J. F. Quinn, M. R. Whittaker, T. P. Davis, *ACS Macro Lett.* **2017**, *6*, 1013.
- [82] N. P. Truong, M. R. Whittaker, A. Anastasaki, D. M. Haddleton, J. F. Quinn, T. P. Davis, *Polym. Chem.* **2016**, *7*, 430.
- [83] N. P. Truong, J. F. Quinn, A. Anastasaki, D. M. Haddleton, M. R. Whittaker, T. P. Davis, *Chem. Commun.* **2016**, 52, 4497.
- [84] N. P. Truong, J. F. Quinn, A. Anastasaki, M. Rolland, M. Vu, D. Haddleton, M. R. Whittaker, T. P. Davis, *Polym. Chem.* **2017**, *8*, 1353.
- [85] N. P. Truong, C. Zhang, T. A. H. Nguyen, A. Anastasaki, M. W. Schulze, J. F. Quinn, A. K. Whittaker, C. J. Hawker, M. R. Whittaker, T. P. Davis, *ACS Macro Lett.* **2018**, *7*, 159.
- [86] W. J. Zhang, F. D'Agosto, O. Boyron, J. Rieger, B. Charleux, *Macromolecules* **2011**, *44*, 7584.
- [87] N. P. Truong, M. V. Dussert, M. R. Whittaker, J. F. Quinn, T. P. Davis, *Polym. Chem.* **2015**, *6*, 3865.
- [88] V. R. Devadasu, V. Bhardwaj, M. N. V. R. Kumar, *Chem. Rev.* **2013**, *113*, 1686.
- [89] I. Chaduc, E. Reynaud, L. Dumas, L. Albertin, F. D'Agosto, M. Lansalot, *Polymer* **2016**, *106*, 218.
- [90] B. Karagoz, L. Esser, H. T. Duong, J. S. Basuki, C. Boyer, T. P. Davis, *Polym. Chem.* **2014**, *5*, 350.
- [91] E. Hinde, K. Thammasaraphop, H. T. Duong, J. Yeow, B. Karagoz, C. Boyer, J. J. Gooding, K. Gaus, *Nat. Nanotechnol.* **2017**, *12*, 81.
- [92] L. Qiu, C. R. Xu, F. Zhong, C. Y. Hong, C. Y. Pan, *ACS Appl. Mater. Interfaces* **2016**, *8*, 18347.
- [93] W. J. Zhang, C. Y. Hong, C. Y. Pan, *Biomacromolecules* **2016**, *17*, 2992.
- [94] W. J. Zhang, C. Y. Hong, C. Y. Pan, *Biomacromolecules* **2017**, *18*, 1210.
- [95] V. Ladmiraal, M. Semsarilar, I. Canton, S. P. Armes, *J. Am. Chem. Soc.* **2013**, *135*, 13574.
- [96] C. J. Mable, M. J. Derry, K. L. Thompson, L. A. Fielding, O. O. Mykhaylyk, S. P. Armes, *Macromolecules* **2017**, *50*, 4465.



- [97] K. Li, P. Y. Dugas, E. Bourgeat-Lami, M. Lansalot, *Polymer* **2016**, *106*, 249.
- [98] C. J. Mable, R. R. Gibson, S. Prevost, B. E. McKenzie, O. O. Mykhaylyk, S. P. Armes, *J. Am. Chem. Soc.* **2015**, *137*, 16098.
- [99] R. H. Deng, M. J. Derry, C. J. Mable, Y. Ning, S. P. Armes, *J. Am. Chem. Soc.* **2017**, *139*, 7616.
- [100] V. Gaberc-Porekar, I. Zore, B. Podobnik, V. Menart, *Curr. Opin. Drug Discov. Devel.* **2008**, *11*, 242.
- [101] B. Karagoz, J. Yeow, L. Esser, S. M. Prakash, R. P. Kuchel, T. P. Davis, C. Boyer, *Langmuir* **2014**, *30*, 10493.
- [102] W. Zhao, H. T. Ta, C. Zhang, A. K. Whittaker, *Biomacromolecules* **2017**, *18*, 1145.
- [103] V. J. Cunningham, L. P. D. Ratcliffe, A. Blanazs, N. J. Warren, A. J. Smith, O. O. Mykhaylyk, S. P. Armes, *Polym. Chem.* **2014**, *5*, 6307.
- [104] K. A. Simon, N. J. Warren, B. Mosadegh, M. R. Mohammady, G. M. Whitesides, S. P. Armes, *Biomacromolecules* **2015**, *16*, 3952.
- [105] R. H. Deng, Y. Ning, E. R. Jones, V. J. Cunningham, N. J. W. Penfold, S. P. Armes, *Polym. Chem.* **2017**, *8*, 5374.
- [106] K. X. Ren, J. Perez-Mercader, *Polym. Chem.* **2017**, *8*, 3548.
- [107] A. Blanazs, R. Verber, O. O. Mykhaylyk, A. J. Ryan, J. Z. Heath, C. W. I. Douglas, S. P. Armes, *J. Am. Chem. Soc.* **2012**, *134*, 9741.
- [108] D. E. Mitchell, J. R. Lovett, S. P. Armes, M. I. Gibson, *Angew. Chem. Int. Ed.* **2016**, *55*, 2801.
- [109] S. L. Canning, G. N. Smith, S. P. Armes, *Macromolecules* **2016**, *49*, 1985.
- [110] S. Y. Khor, M. N. Vu, E. H. Pilkington, A. P. R. Johnston, M. R. Whittaker, J. F. Quinn, N. P. Truong, T. P. Davis, *Small*, <https://doi.org/10.1002/smll.201801702>.
- [111] G. Delaittre, J. Nicolas, C. Lefay, M. Save, B. Charleux, *Chem. Commun.* **2005**, 614.

Thiol-Reactive Star Polymers Display Enhanced Association with Distinct Human Blood Components

Joshua J. Glass,[†] Yang Li,^{‡,§} Robert De Rose,[†] Angus P. R. Johnston,[‡] Ewa I. Czuba,[‡] Song Yang Khor,[‡] John F. Quinn,[‡] Michael R. Whittaker,[‡] Thomas P. Davis,^{*,‡,§} and Stephen J. Kent^{*,†,‡}

[†]ARC Centre of Excellence in Convergent Bio-Nano Science and Technology, and Department of Microbiology and Immunology, Peter Doherty Institute for Infection and Immunity, The University of Melbourne, Melbourne, Victoria 3010, Australia

[‡]ARC Centre of Excellence in Convergent Bio-Nano Science and Technology, and Drug Delivery, Disposition and Dynamics, Monash Institute of Pharmaceutical Sciences, Monash University, Parkville, Victoria 3052, Australia

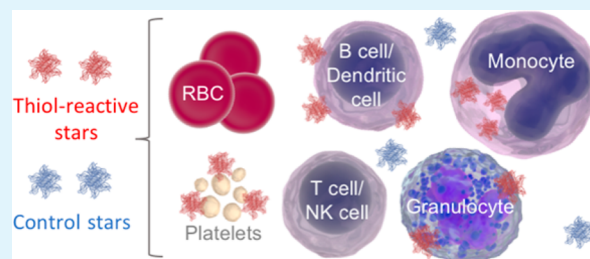
[§]Department of Chemistry, University of Warwick, Gibbet Hill, Coventry CV4 7AL, United Kingdom

[‡]Melbourne Sexual Health Centre and Department of Infectious Diseases, Alfred Health, Central Clinical School, Monash University, Melbourne, Victoria 3800, Australia

Supporting Information

ABSTRACT: Directing nanoparticles to specific cell types using nonantibody-based methods is of increasing interest. Thiol-reactive nanoparticles can enhance the efficiency of cargo delivery into specific cells through interactions with cell-surface proteins. However, studies to date using this technique have been largely limited to immortalized cell lines or rodents, and the utility of this technology on primary human cells is unknown. Herein, we used RAFT polymerization to prepare pyridyl disulfide (PDS)-functionalized star polymers with a methoxy-poly(ethylene glycol) brush corona and a fluorescently labeled cross-linked core using an arm-first method. PDS star polymers were examined for their interaction with primary human blood components: six separate white blood cell subsets, as well as red blood cells and platelets. Compared with control star polymers, thiol-reactive nanoparticles displayed enhanced association with white blood cells at 37 °C, particularly the phagocytic monocyte, granulocyte, and dendritic cell subsets. Platelets associated with more PDS than control nanoparticles at both 37 °C and on ice, but they were not activated in the duration examined. Association with red blood cells was minor but still enhanced with PDS nanoparticles. Thiol-reactive nanoparticles represent a useful strategy to target primary human immune cell subsets for improved nanoparticle delivery.

KEYWORDS: star polymers, blood, thiols, platelets, targeting



1. INTRODUCTION

Efficient cellular delivery is a critical hurdle in the development of effective nanotherapeutics. Most targeting approaches employ antibody-based strategies.¹ However, this poses design challenges as antibody constructs are generally relatively large molecules, which may distort the desired nanoparticle (NP) size or structure. This is particularly problematic for very small NPs, which may otherwise have the benefit of deeper penetration into tumor tissues.^{2,3} Exploiting the differential expression of cell-surface (exofacial) thiol groups (-SH) across different cell subtypes is an alternative method to target small molecules and NPs.^{4–6} It has been postulated that targeting exofacial thiols might represent a natural mechanism of cell uptake.⁷ Cancer cells have been reported to express higher levels of cell-surface thiol groups than nontransformed equivalents. These include greater levels of glutathione, cysteine, and/or thioredoxin,^{8,9} which may be further upregulated in the hypoxic regions of tumors.¹⁰ In vitro studies using immortalized cell lines and rodent studies have shown that NPs can bind cell-surface thiol groups and can efficiently

target some cancer cells.⁷ In a murine model of adoptive T cell therapy for cancer, two cytokines known to promote in vivo T cell expansion and antitumor effector function were encapsulated within thiol-reactive liposomes.¹¹ These liposomes were conjugated to exofacial thiols present on CD8+ T cells in serum-free media ex vivo. After readministering the liposome-conjugated T cells into B16-melanoma-bearing mice, T cell proliferation increased, and established tumors were eradicated. NPs can also be engineered to present pyridyl disulfide (PDS) groups which can potentially exchange with cell-surface thiols, thereby enhancing NP binding. Whether NPs decorated with PDS groups target cells within primary human blood is currently unknown but of considerable interest given the wide range of cell types in blood and the critical role they play in coagulation and immunity.

Received: December 12, 2016

Accepted: March 24, 2017

Published: March 24, 2017

Human blood contains myriad cell types that can be broadly divided into (1) phagocytic and nonphagocytic white blood cells (WBC), (2) red blood cells (RBC), and (3) platelets. Phagocytic WBCs include monocytes and granulocytes that act in the primary defense against infection and are essential components of the innate immune response to pathogens. They are primed to clear pathogens and also avidly phagocytose many NP preparations. Dendritic cells are also phagocytic and play a principal role in initiating the adaptive immune response, referred to as antigen presentation. They process pathogens or vaccines for presentation to important cells of the adaptive immune system—B cells and T cells, which generate antibody- and cell-mediated immune responses.^{12,13} Natural killer (NK) cells are innate immune cells primed to kill those cells infected by viruses or transformed into cancers. RBCs are the most common cell type in blood (1000-fold more abundant than WBCs) and play a critical role in oxygen transport. Platelets (or “thrombocytes”) are small (2–3 μm) anuclear cell fragments involved in the process of hemostasis. They form “platelet plugs” that adhere to damaged endothelium and become activated. Activated platelets release factors including adenosine diphosphate (ADP) that attracts additional platelets to the site and forms the foundation of the blood clot. Platelet activation is also associated with the formation of intravascular clots adjacent to atherosclerotic plaques in subjects with cardiovascular disease.¹⁴

We and others have previously used whole human blood assays to measure NP association with multiple immune cell subsets.^{15–18} Herein we have modified our previous approaches to also allow examination of RBCs and platelets. Using human blood to evaluate bionano interactions offers numerous benefits over traditional in vitro cell line or purified cell models as it contains: (1) primary human cells, (2) multiple immune cell types, (3) components of the coagulation cascade (e.g., platelets and proteins), and (4) autologous human plasma.

Due to their nanoscale dimensions, controlled polymerization and efficient coupling chemistries, star polymers¹⁹ are attracting considerable attention as potential carriers for both therapeutic agents²⁰ and genetic material.²¹ In particular, the preparation of stars by an arm-first methodology using reversible addition–fragmentation chain transfer (RAFT) polymerization represents a convenient route for preparing materials with both reactive sites for subsequent functionalization and an antifouling mPEG brush corona.^{22,23} By incorporating reactive moieties, star polymers have been subsequently modified with drug,²⁰ radiolabel,²⁴ and gadolinium chelates for enhancing MRI contrast.²⁵ We have recently demonstrated that star polymers exhibit enhanced circulation time (depending on the size)²⁴ and that the biodistribution is affected by the route of administration.²⁶ However, to date there have been no investigations of the extent to which star polymers associate with human blood cells. This is an essential step toward better understanding these NPs and is an important precursor to future clinical use.

Molecules such as PDS that react with exofacial thiols can readily be incorporated into star polymers to facilitate enhanced binding to target cells or carrier cells in blood. Herein we characterize how PDS modification affects NP interaction with major cellular subsets of human blood: WBCs, RBCs, and platelets. We demonstrate PDS modification enhanced association with transformed cells and some (but not all) WBC subsets, as well as platelets and to a lesser degree RBCs.

2. EXPERIMENTAL SECTION

2.1. Nanoparticle Synthesis. **2.1.1. Materials.** The functional RAFT agents (3-(benzylsulfanylthiocarbonylsulfanyl)-propionic acid (BSPA) and 2-(pyridine-2-ylidysulfanyl) ethyl 2-(((dodecylthio)carbonothioyl)thio)propanoate (PDSD) were synthesized using published procedures.²⁷ 2-Vinyl-4,4-dimethyl-5-oxazolone (VDM) was synthesized using the method of Li et al.^{28,29} Cyanine5 amine (Lumiprobe), oligo(ethylene glycol) methyl ether acrylate (Aldrich, OEGA, $M_w = 480 \text{ g mol}^{-1}$, 99%), N,N' -methylenebis(acrylamide) (Aldrich, 98%) and azobis(isobutyronitrile) (Aldrich, AIBN) were used as received. All other reagents were AR grade.

2.1.2. Synthesis of Coronal Functional PEGylated Stars Using Arm-First RAFT Polymerization. The synthesis of functional PEGylated stars using an arm-first method is detailed in Figure 1.

2.1.3. Arm Synthesis. The typical arm synthesis for benzyl functional POEGA using BSPA RAFT agent is given as follows (Entry 1, Table S1): BSPA RAFT agent (16.3 mg, 0.06 mmol), OEGA₄₈₀ (1 g, 2.08 mmol), AIBN (1.0 mg, 0.006 mmol), and toluene (3 mL) were all mixed in a 5 mL vial equipped with a magnetic stirrer bar. The vial was then sealed, and the mixture was deoxygenated by sparging with nitrogen for 20 min. The deoxygenated reaction mixture was stirred at 70 °C; after 6 h, the reaction was quenched by placing the vial in ice water. The polymer arms were recovered by precipitating the reaction mixture three times from toluene into a mixture of petroleum ether and diethyl ether (1:1 v/v). For the synthesis of pyridyl disulfide functional arms PDSD RAFT agent (31.2 mg, 0.06 mmol) was substituted for BSPA. The arms were characterized using both gel permeation chromatography (GPC) and ¹H NMR.

2.1.4. Arm-First Star Polymer Synthesis. A typical synthesis procedure is given below for the benzyl functional arm-first star polymer (Entry 3, Table S1): Benzyl functional POEGA arms (Entry 1, Table S1: 600 mg, 0.068 mmol), VDM (13.9 mg, 0.1 mmol), AIBN (2.46 mg, 0.015 mmol), cross-linker [N,N' -methylenebis(acrylamide)] (53.9 mg, 0.35 mmol), and 5 mL of toluene were mixed in a vial equipped with a magnetic stirrer bar. The vial was then sealed, and the mixture was deoxygenated by sparging with nitrogen at 0 °C for 20 min. The deoxygenated reaction mixture was then stirred at 70 °C for 24 h. An aliquot of the reaction mixture was sampled periodically for GPC analysis to facilitate monitoring of the star formation process. The reaction mixture was then quenched in ice water. For pyridyl disulfide functional stars pyridyl disulfide functional POEGA arms (Entry 2, Table S1) were substituted for benzyl functional POEGA arms. The stars were isolated by precipitating the reaction mixture three times from toluene into diethyl ether/chloroform (90:10 v/v).

2.1.5. Cyanine5 (Cy5)-Labeled Star Polymer Synthesis. A typical Cy5 labeling reaction is as follows: BSPA-POEGA Star (Entry 3, Table S1: 200 mg, 0.0017 mmol), Cyanine5 amine (0.7 mg, 0.001 mmol), and triethylamine (0.5 mg, 0.005 mmol) were dissolved into 2 mL of N,N -dimethylformamide and allowed to react at room temperature for 48 h while being carefully protected from light. The Cy5-labeled star polymer was recovered after exhaustive dialysis in the dark against methanol using Snakeskin dialysis tubing (MWCO 3000 Da). Successful labeling with Cy5 was confirmed via GPC using dual RI and UV–vis detection, and fluorescence spectroscopy.

2.2. Nanoparticle Characterization. **2.2.1. Gel Permeation Chromatography (GPC).** GPC analyses of the polymers were carried out on a Shimadzu modular system composed of an SIL-20AD auto-injector, a PL 5.0 mm bead-size guard column (50 \times 7.8 mm) followed by four 300 \times 7.8 mm linear columns (500, 104, 103, and 105 Å pore size) using N,N -dimethylacetamide [DMAC; w/v LiBr, 0.05% 2, 7-dibutyl-4-methylphenol (BHT)] at 50 °C as the eluent (flow rate = 1 mL min⁻¹). An RID-20A differential refractive-index and UV–vis detector was used. Samples were filtered through 0.45 μm PTFE filters before injection. Calibration was performed with narrow-polydispersity polystyrene standards ranging from 500 to 3 \times 10⁶ g mol⁻¹.

2.2.2. Nuclear Magnetic Resonance (NMR). ¹H NMR spectroscopy using a Bruker UltraShield 400 MHz spectrometer (Bruker Daltronics Inc., NSW, Australia) running Topspin, version 1.3. All spectra were recorded in CDCl₃.

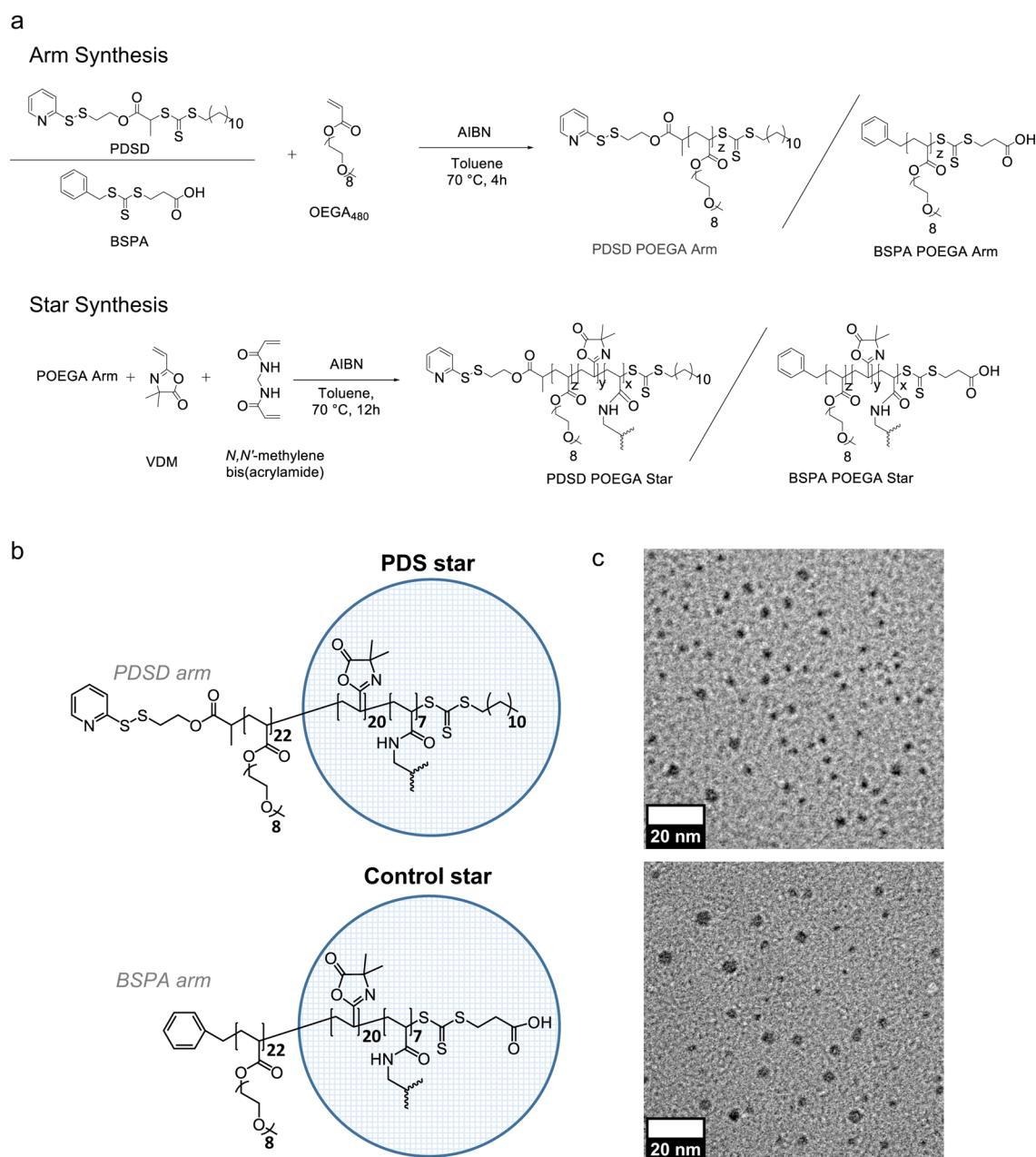


Figure 1. Star polymer synthesis. (a) Synthesis and (b) schematic of peripherally functional star polymers via an arm-first RAFT method. (c) Transmission electron microscopy analysis of PDS–POEGA star-Cy5 (PDS star, top) and BSPA-POEGA Star-Cy5 (control star, bottom).

2.2.3. Dynamic Light Scattering (DLS). Dynamic light scattering measurements were performed on a solution of star polymer (1 mg mL⁻¹ in PBS) using a Malvern Zetasizer Nano Series running DTS software and operating a 4 mW He–Ne laser at 633 nm at an angle of 173°. Data was collected at a constant temperature of 25 °C and analyzed using Malvern supplied DTS software. The number-average hydrodynamic diameter is reported.

2.2.4. Fluorescence Measurements. Fluorescence spectra were obtained using a fluorescence spectrophotometer (Shimadzu RF-5301 PC). Slit widths were set at 2.5 nm for both excitation and emission of Cyanine 5. The photomultiplier voltage was set at 950 V.

2.2.5. Transmission Electron Microscopy (TEM). TEM figures were recorded using a Tecnai F20 transmission electron microscope operating at an accelerating voltage of 200 kV. TEM grids were prepared as follows: 10 μ L of a 0.1 wt % solution was deposited on a Formvar-coated copper grid (GSCu100F-50, Proscitech) and allowed to dry in air at room temperature for at least 12 h.

2.3. Blood Acquisition. Blood was collected from healthy human donors after obtaining informed consent in accordance with the University of Melbourne Human ethics approval 1443420 and the Australian National Health and Medical Research Council Statement on Ethical Conduct in Human Research. For WBC studies, blood was drawn by venipuncture into Vacuette collection tubes (Greiner Bio-One) containing sodium heparin and gently inverted 5 times. For studies involving platelets/RBCs, the tourniquet was applied loosely and the first 2 mL of blood was discarded before collecting into ACD-B Vacutainer collection tubes (BD Biosciences).

2.4. Cell Line Association Studies. C1R cells were cultured in DMEM supplemented with 10% fetal bovine serum (FBS), 100 U mL⁻¹ penicillin, and 100 μ g mL⁻¹ streptomycin. Cells were seeded at 9.0×10^4 cells per well in 96-well plates on the day of the experiment. Five microliters of particles (300 μ g mL⁻¹) was added to cells in 145 μ L of media to give a final concentration of 10 μ g mL⁻¹ of particles in 150 μ L. Cells were incubated with particles for between 10 and 120 min at either 4 or 37 °C and then washed four times in 1% BSA/PBS.

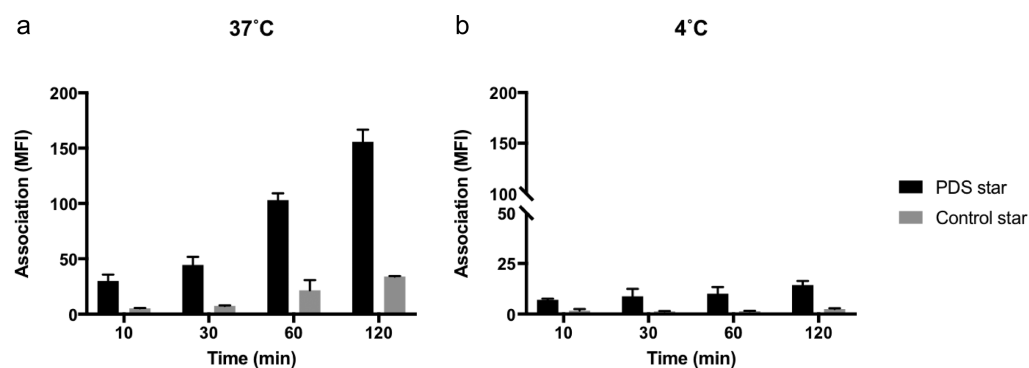


Figure 2. PDS nanoparticles display enhanced uptake by human C1R cell line. C1R cells were seeded at 9.0×10^4 cells per well in 96-well plates and incubated with star polymers at a final concentration of $10 \mu\text{g mL}^{-1}$ in DMEM supplemented with 10% FBS. Cells were incubated with particles for between 10 and 120 min at either (a) 37 °C (left) or (b) 4 °C (right). Cells were washed four times in 1% BSA/PBS and resuspended in PBS containing the viability dye propidium iodide (PI; $0.5 \mu\text{g mL}^{-1}$) for analysis by flow cytometry (Stratedigm S100EXi). All experiments were performed in triplicate. FBS: fetal bovine serum.

Samples were resuspended in PBS containing propidium iodide (PI; $0.5 \mu\text{g mL}^{-1}$) for analysis by flow cytometry (Stratedigm S100EXi). All experiments were performed in triplicate.

2.5. Association with WBC Populations. Freshly drawn blood (100 μL) was added to 5 mL polystyrene round-bottom tubes (“FACS tubes”; Falcon) before incubating on ice or at 37 °C for 10 min. NPs (diluted in PBS) were added directly into whole blood at a final concentration of $10 \mu\text{g mL}^{-1}$ and incubated for 1 h, before placing all tubes on ice. RBCs were lysed with Pharm Lyse buffer (BD Biosciences) at 20 \times blood volume and topped up to 4 mL using 1 \times PBS. WBCs were pelleted (500g, 5 min) and washed twice more with PBS. Cells phenotyped on ice (1 h) using titrated concentrations of antibodies against CD3 (AF700, SP34-2), CD14 (APC-H7, M Φ P9), CD20 (BV421, 2H7), CD45 (V500, HI30), CD56 (PE, B159), Lineage-1 cocktail (FITC), and HLA-DR (PerCP-Cy5.5, G46-6). All antibodies from BD Biosciences, except CD20 (BioLegend). Cells washed twice in cold (4 °C) FACS wash buffer (FWB; WB; 1 \times PBS containing 0.5% w/v bovine serum albumin (Sigma-Aldrich) and 2 mM EDTA pH 8 (Ambion)), fixed (1% formaldehyde) and analyzed by flow cytometry (LSRFortessa, BD Biosciences). Data was analyzed on FlowJo V10 and graphed using GraphPad Prism 6.

For high-dimensional viSNE analysis, NP cell association data from five donors was concatenated using FlowJo V10, before exporting to Cytobank for viSNE analysis.^{30,31} viSNE analysis allows 2D representation of high-dimensional single-cell data based on the t-Distributed Stochastic Neighbor Embedding (t-SNE) algorithm. First, 10 000 events were uniformly subsampled from each condition (PBS only, PDS NP or control nanoparticle). Second, viSNE analysis was performed to cluster cells in two dimensions based on their expression of CD3, CD14, CD20, CD56, Lineage-1 cocktail, and HLA-DR. Color was used to represent the (a) identity of cells based on conventional manual gating strategies or (b) associated Cy5-NP fluorescence.

2.6. Confocal Microscopy. The NP-blood incubation was repeated by the method described in section 2.5 using a single blood donor. However, star polymers were added at $100 \mu\text{g mL}^{-1}$, and a modified antibody panel was used: CD3 (AF488, SP34-2), CD14 (PE-Cy7, M5E2), CD19 (PE, HIB19), and CD66b (BV421, 2H70), all purchased from BD Biosciences. Cells were sorted into FWB on a BD FACS ARIA III (100 μm nozzle). Coverslips (#1.5, Menzel-Glaser) treated with poly-L-lysine (Sigma-Aldrich) for 2 h, room temperature (RT), washed thrice with 1 \times PBS before sorted cells were added to coverslips and allowed to set for 1 h, RT. Cells were fixed with 1% formaldehyde, rinsed twice in PBS, and mounted onto glass slides using ProLong Diamond Antifade with DAPI (Thermo Fisher). Cells were imaged by confocal microscopy using 20 \times and 63 \times oil objectives (Zeiss LSM710 and ZEN 2012 Black software).

2.7. Association with RBC and Platelets. Freshly drawn blood (5 μL) was added to FACS tubes, containing approximately 25×10^6 RBC and 1×10^6 platelets. In the tubes, the volume was made 100 μL

through the addition of 1 \times PBS, before preincubating on ice or 37 °C for 10 min. NPs (1–10 μg in PBS) were added to blood and incubated for a further 1 h, before placing all tubes on ice. Cells phenotyped on ice using titrated concentrations of antibodies (BD Biosciences) against CD42b (PE, HIP1), CD45 (V500, HI30), and CD235a (FITC, GA-R2). Cells were washed four times with 4 mL of PBS (800g, 15 min), fixed (1% formaldehyde), and analyzed by flow cytometry (LSRFortessa).

2.8. Human Platelet Activation. NPs (0.1, 1, 10 μg) or equal volume of PBS were added to FACS tubes, before carefully transferring blood (100 μL) immediately after collection and swirling gently. Adenosine diphosphate (ADP, 1 μM final concn, Sigma-Aldrich) was used as a positive control for platelet activation.^{32,33} Blood was incubated for 10 min at room temp, before adding 400 μL of cold (4 °C) BSA-Tyrode’s buffer as per ref 34 (1 \times PBS containing 130 mM NaCl, 2.6 mM KCl, 0.42 mM NaH_2PO_4 , 5.5 mM D-glucose, 10 mM HEPES and 0.3% w/v bovine serum albumin). Platelets were phenotyped by transferring 100 μL into FACS tubes containing titrated concentrations of antibodies (BD Biosciences) against CD42b (PE, HIP1), CD45 (V500, HI30), CD62P (BV650, AK-4), CD235a (FITC, GA-R2), and using the gating tree in Figure 9A. Samples were diluted 20-fold further using BSA-Tyrode’s buffer, and samples were analyzed immediately by flow cytometry (BD LSRFortessa).

2.9. Statistical Analyses. Results were analyzed using Wilcoxon nonparametric two-tailed matched pairs signed rank test (GraphPad Prism 7).

3. RESULTS

3.1. Synthesis and Characterization. Functionalizing the surface of NPs with nonantibody molecules that can facilitate interactions with cell subsets is a potential avenue toward targeted use of NPs. To this end, we synthesized star polymers having pyridyl disulfide (PDS)-terminated arms as an exemplar NP with a thiol reactive group in the particle corona. The stars were prepared by using RAFT polymerization to first synthesize the arms, followed by star formation via chain extension with a difunctional cross-linker (i.e., an “arm-first” approach) (Figure 1A). In order to provide PDS moieties on the distal end of the star arms, we employed a RAFT agent with a PDS group conjugated to the “R” group of the RAFT agent (2-(pyridine-2-yl)disulfanyl)ethyl 2-(((dodecylthio)carbonothioyl)thio)propanoate, PDS-D), thus ensuring that the PDS group was located away from the cross-linked core of the star. An antifouling corona of mPEG brushes was provided by employing oligo-ethylene glycol methyl ether acrylate (OEGA, $M_n = 480 \text{ g mol}^{-1}$) as the monomer for the arm synthesis. The resulting poly(OEGA) (POEGA) arms were

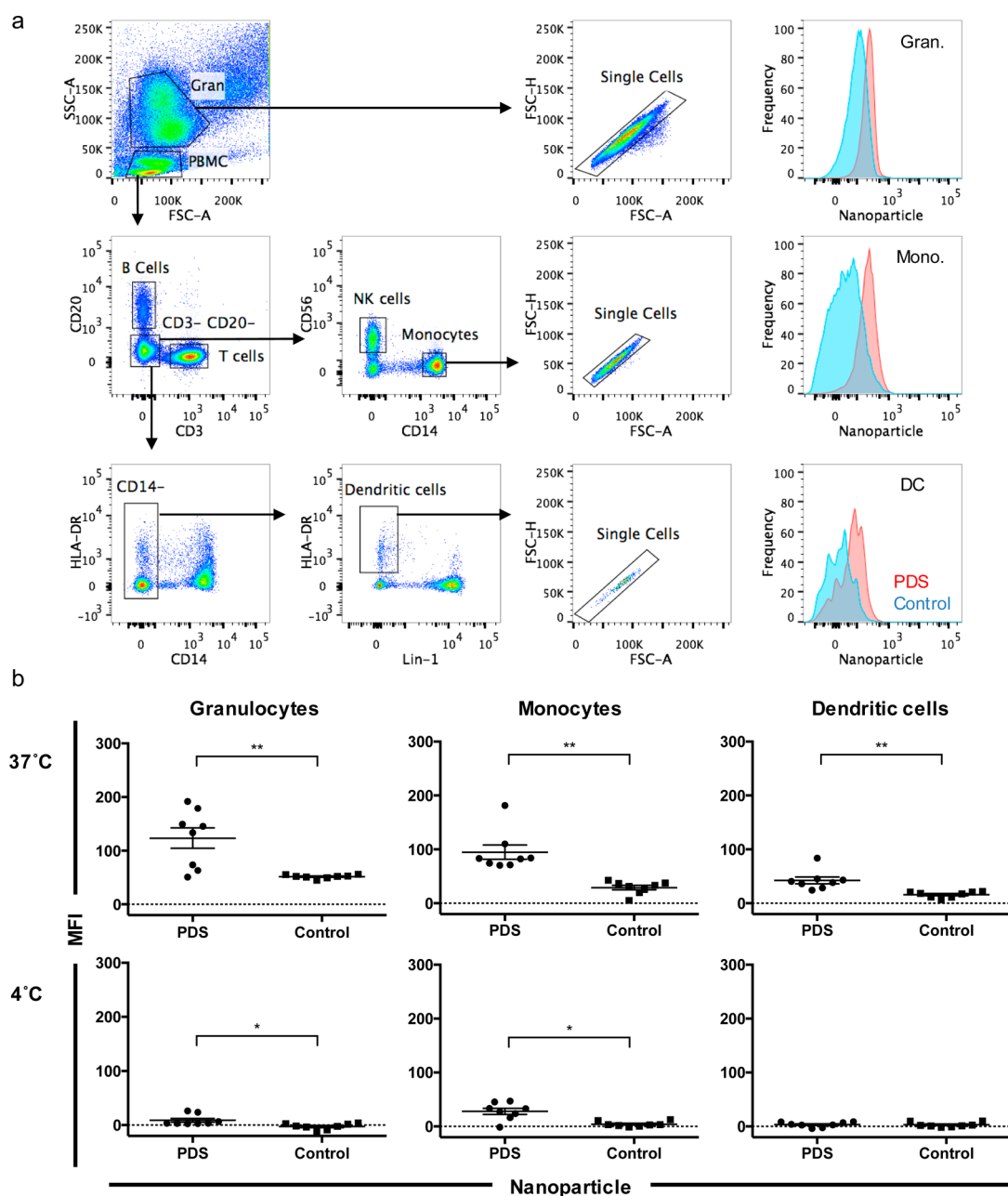


Figure 3. PDS nanoparticles display enhanced association with primary phagocytic cells in whole human blood. PDS and BSPA control nanoparticles were incubated with freshly drawn, heparin-treated human blood at $10 \mu\text{g mL}^{-1}$ for 1 h, 4 or 37 °C. Free nanoparticles were washed and RBCs lysed, before phenotyping cells on ice. Cell association with Cy5-labeled nanoparticles was determined by flow cytometry and represented by a median fluorescence index (MFI). (a) Representative gating tree from a single donor, demonstrating identification of granulocytes (gran), monocytes (mono), and dendritic cells (DC) at 37 °C. Red histograms represent cell association with PDS nanoparticles, blue with control nanoparticles. (b) Summary of cell association profiles from 7 healthy donors across independent experiments. Cell association was analyzed at 37 °C (top) and 4 °C (bottom). * $p < 0.05$, ** $p < 0.01$.

characterized using ^1H NMR, with the number-average molecular weight determined to be approximately 9800 g mol^{-1} . Moreover, further analysis by gel permeation chromatography (GPC) revealed that the POEGA exhibited unimodal molecular weight distribution ($M_n = 12000 \text{ g mol}^{-1}$ vs polystyrene standards, $\text{PDI} = 1.20$) with little evidence of high molecular weight coupled material or low molecular weight tailing (Table S1). Subsequent chain extension using N,N' -methylenebis(acrylamide) in the presence of the functional monomer 2-vinyl-4,4-dimethyl-5-oxazolone provided star

polymers with $M_n = 123000 \text{ g mol}^{-1}$ and $\text{PDI} = 1.18$ (Figure S1; Table S1).

The stars were successfully isolated from the residual arm by precipitating into a mixture of diethyl ether and chloroform (90:10 v/v) and were fluorescently labeled by reacting the 2-vinyl-4,4-dimethyl-5-oxazolone units in the core with Cyanine5 (Cy5) amine. After exhaustive dialysis against methanol ($\text{MWCO} = 3000 \text{ g mol}^{-1}$), successful fluorescent labeling was confirmed using fluorescence spectroscopy and by GPC with dual UV-vis and RI detection (Figure S2). Control particles without thiol-reactive moieties were prepared by replacing the

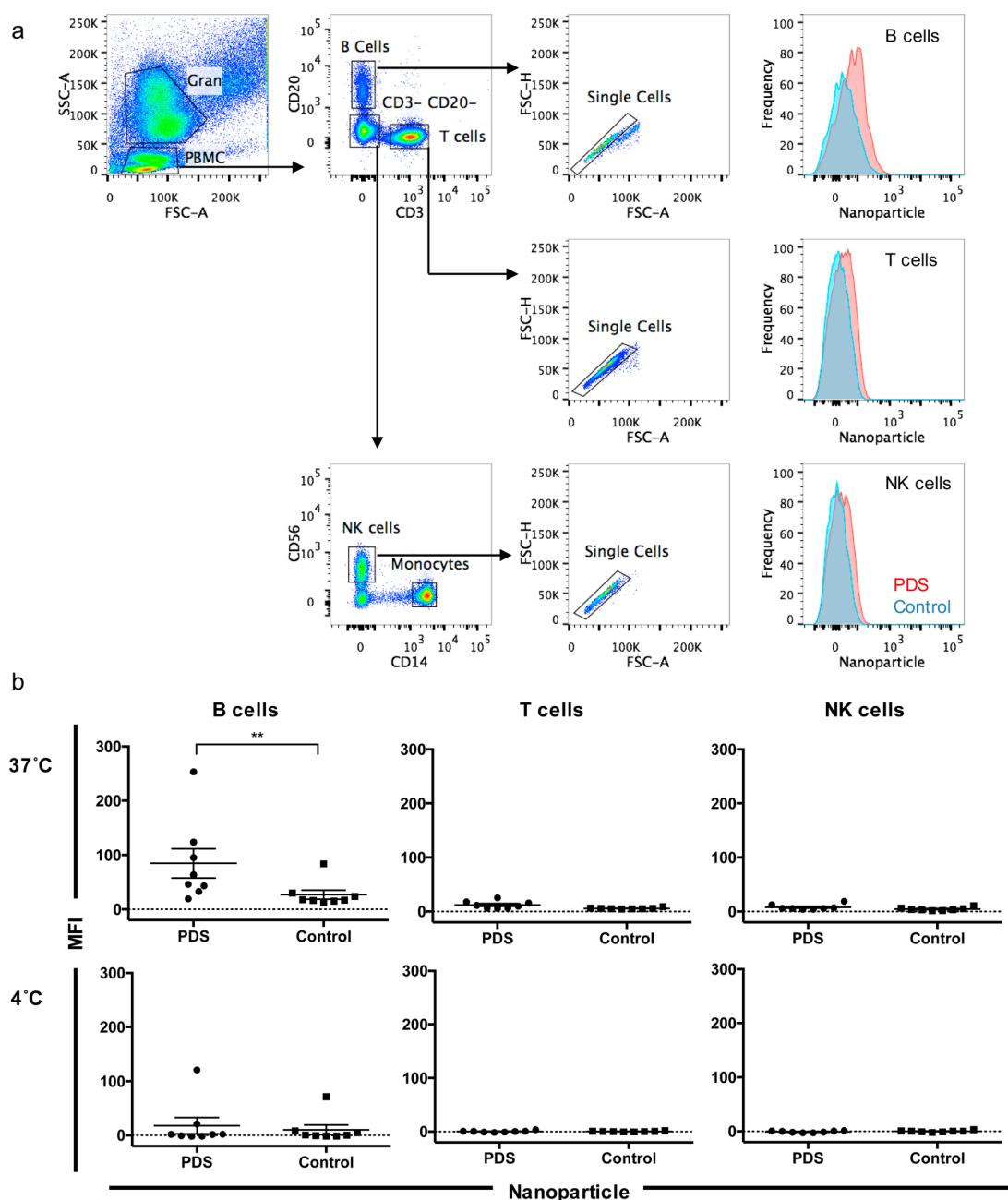


Figure 4. PDS nanoparticles display enhanced association with B cells but not other nonphagocytic cells in whole human blood. PDS and BSPA control nanoparticles were incubated with freshly drawn, heparin-treated human blood at $10 \mu\text{g mL}^{-1}$ for 1 h, at 4 or 37 °C. Free nanoparticles were washed and RBCs lysed, before phenotyping on ice. Cell association with Cy5-labeled nanoparticles was determined by flow cytometry and represented by a median fluorescence index (MFI). (a) Representative gating tree from a single donor, demonstrating cell identification at 37 °C. Red histograms represent cell association experiments with PDS nanoparticles, blue with control nanoparticles. (b) Summary of cell association profiles from 7 healthy donors across independent experiments. Cell association was analyzed at 37 °C (top) and 4 °C (bottom). ** $p < 0.01$.

PDS with the nonfunctional RAFT agent 3-(benzylsulfanylthiocarbonylsulfanyl)propionic acid (BSPA), as shown in Figure 1A,B. We estimate from the molecular weight analysis of the arms and stars that each star has approximately 10 arms attached. By dynamic light scattering (DLS), the hydrodynamic diameter of PDS-POEGA Star Cy5 (PDS stars) was 17 ± 0.9 nm and control BSPA-POEGA Star Cy5 (BSPA stars) were 14 ± 0.6 nm (Table S1). By transmission electron microscopy (Figure 1C), the stars measured <10 nm.

3.2. PDS Functionality Enhances Association with Cell Lines. It has previously been shown that various immortalized cancer cell lines express substantial levels of free thiols. To first

confirm that the PDS NPs interact with cell-surface thiols, we incubated PDS and BSPA NPs with the C1R human B lymphoblast cell line (Figure 2). An enhanced association of PDS NPs was observed as early as 10 min at 37 °C (Figure 2A). At 4 °C, PDS NPs demonstrated enhanced cell association at 120 min (Figure 2B). Very little cell association with control star polymers not presenting thiol-reactive groups was observed at both temperatures.

3.3. Phagocytic WBC Association Is Enhanced by PDS Functionality. Many NP applications will involve intravenous injection of NPs, where they will first encounter a wide range of circulating cells in a process that is not well modeled by

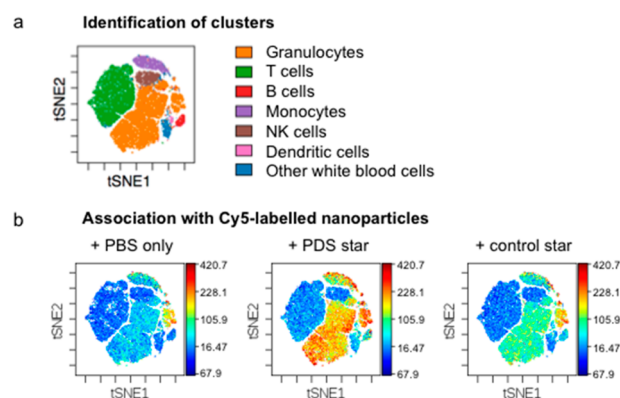


Figure 5. Global analysis of star nanoparticle association with white blood cells. To examine the global change in nanoparticle association with all white blood cell subsets, we performed a viSNE analysis (Cytobank) on the concatenated flow cytometry data of 5 donors at 37 °C. Each dot represents a single cell and spatially distinct clusters represent cell subsets based on the combination of cell-surface markers they express. Clustering is based on the t-Distributed Stochastic Neighbor Embedding (t-SNE) algorithm. (a) Reference plot indicating the cellular identity of viSNE clusters. Colors represent the identity of cell subsets based on conventional manual gating strategies. (b) Global cell association with Cy5-labeled nanoparticles. Individual cells are colored based on their Cy5 fluorescence. PBS only demonstrates different autofluorescence profiles based on cell type, while changes in the intensity of association with Cy5-labeled nanoparticles reveals global association changes between PDS and control stars.

studying immortalized cell lines. Blood cells with specialized phagocytic capacity, such as monocytes, granulocytes, and dendritic cells, will typically actively associate with NPs. We employed a previously described whole blood NP association model,^{15,16,18} where NPs are incubated with fresh human blood from healthy donors, to study the influence of PDS groups on NP association with blood phagocytic cells by flow cytometry (Figure 3). The gating tree to identify the phagocytic populations is shown in Figure 3A, with an example of PDS and control NP association in a representative donor. We first noted that control star polymer NPs without thiol-reactive functionality had remarkably low association with fresh human blood phagocytes at both 4 and 37 °C, suggesting nonspecific clearance of these NPs may be low (Figure 3B). In contrast, PDS NPs displayed a statistically significant enhanced association with all three phagocytic populations compared with control NPs, as indicated by the elevated median fluorescence intensity (MFI) per cell. Whole population shifts (Figure 3A) suggest most cells have associated with particles. At 37 °C, the presence of PDS groups enhanced mean association (measured by MFI) with granulocytes by 2.4×, monocytes by 3.2×, and dendritic cells by 2.6×. PDS NPs associated with more granulocytes and monocytes than dendritic cells. While human monocyte cell lines (e.g., THP-1) are frequently used to investigate NP phagocytosis, it is interesting that in multicellular blood where competition between cells is present, the granulocyte cell type displayed greater mean association with PDS NPs than monocytes. A greater variability in association was observed across the 7 healthy human donors in granulocytes than other phagocytic cells.

3.4. PDS Functionality Enhances Association with Distinct Lymphocyte Populations in Fresh Blood. Lymphocyte populations within whole blood, such as B, T, and NK cells, are specialized cells of the adaptive and innate

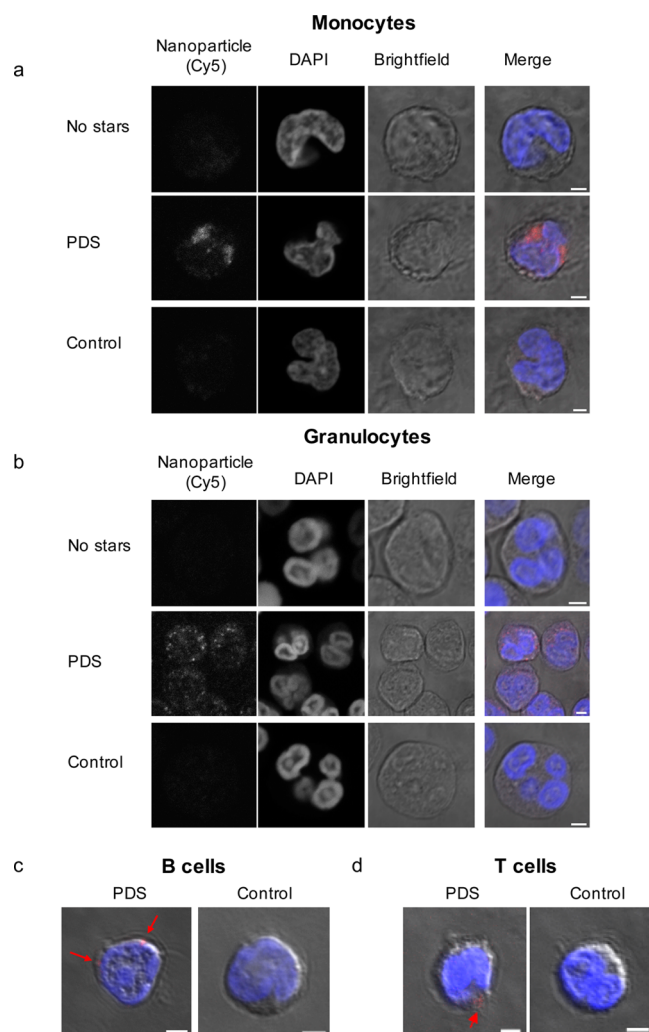


Figure 6. Imaging cell interactions of star nanoparticles with primary blood cells. PDS and BSPA control nanoparticles were incubated with freshly drawn, heparin-treated human blood at 100 $\mu\text{g mL}^{-1}$ for 1 h, at 4 or 37 °C. Free nanoparticles were washed and RBCs lysed, before phenotyping cells on ice and sorting individual populations by fluorescence activated cell sorting. Sorted (a) monocytes, (b) granulocytes, (c) B cells, and (d) T cells were mounted onto polylysine coverslips and imaged by confocal microscopy. Middle slice from representative cell z-stacks is displayed. Merged images false-colored with Cy5 nanoparticles (red), DAPI (blue). Scale bar = 2 μm .

immune systems. Targeting these cells to modulate immunity is of growing interest, with several monoclonal antibody products marketed to suppress aberrant immune responses.^{35–37} We therefore assessed whether thiol-reactive PDS star polymer NPs could interact with lymphocyte populations within fresh human blood (Figure 4). The gating strategy is shown in Figure 4A. Notably, B cells demonstrated a clear association preference for PDS NPs at 37 °C, with a 3.2-fold greater mean association than control NPs (Figure 4B). In contrast, T and NK cells displayed little association with either NP at both temperatures.

Taking this data altogether, we concatenated the flow cytometry data of 5 different donors at 37 °C and performed high-dimensional viSNE analysis³¹ (Figure 5). Each dot represents a single cell that is clustered in 2D space based on its expression of cell-surface markers. This enabled the visualization of global changes in NP association across all studied WBC subsets. We used the manual gating strategies of

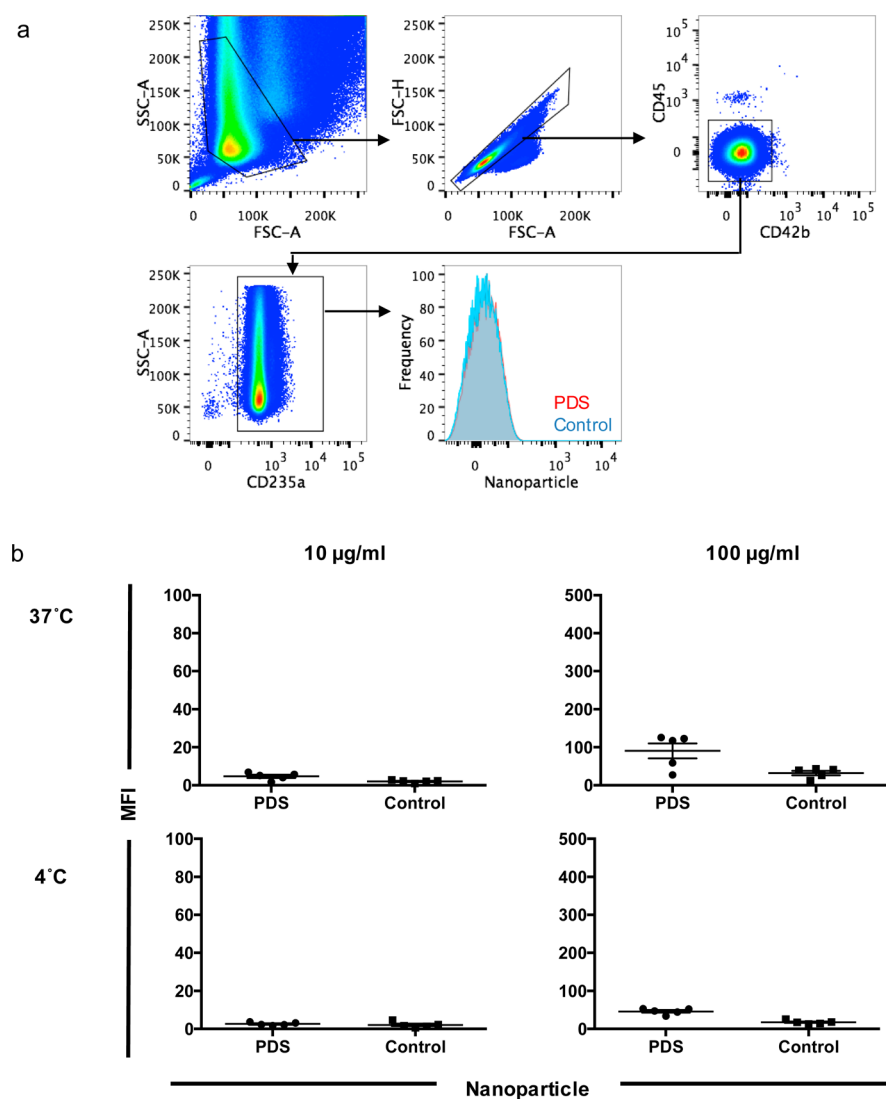


Figure 7. PDS nanoparticles display minimally enhanced binding to red blood cells at the maximum concentration tested. PDS and BSPA control nanoparticles were incubated with freshly drawn, ACD-B treated human blood for 1 h, at 4 or 37 °C. Free nanoparticles were removed by washing before phenotyping on ice. Red blood cell association with Cy5-labeled nanoparticles was determined by flow cytometry and represented by a median fluorescence index (MFI). (a) Representative gating tree from a single donor, demonstrating association at 10 $\mu\text{g mL}^{-1}$, 37 °C. Red histograms represent association with PDS nanoparticles, blue with control nanoparticles. (b) Summary of association profiles at 37 °C (top) and 4 °C (bottom) from 5 healthy donors across independent experiments.

Figure 3A and Figure 4A to identify the clustered cell populations (Figure 5A). As the clusters consist largely of one color, viSNE clustering confirmed the accuracy of our manual gating strategies. These plots also demonstrate the relative abundance of each cell subset that NPs are exposed to in blood. For example, granulocytes comprise a large proportion of WBCs while dendritic cells are very rare. When cell clusters are colored based on their association with Cy5-labeled NPs, we observed clear global changes in NP association due to the presence of PDS groups (Figure 5B).

3.5. Nanoparticle Cellular Localization Using Confocal Microscopy. The above analyses demonstrated enhanced association of PDS NPs to various blood WBCs compared with BSPA control NPs. Binding of PDS NPs to exofacial thiols may subsequently lead to enhanced NP uptake, particularly among phagocytic cells. The flow cytometry studies above however do not provide spatial information on whether NPs have been internalized or remain surface bound. To study NP uptake, we

performed the fresh blood association assays as above, before obtaining purified individual cell populations using fluorescence-activated cell sorting and then imaged the cells by confocal microscopy (Figure 6). We found that PDS NPs were internalized by monocytes, with Cy5-NPs localized within the cytoplasm and frequently observed in cytoplasmic and surface clusters (Figure 6A). In most cells, PDS NPs filled the cytoplasm but did not enter the nucleus, as determined by DAPI staining. BSPA control NPs did not associate with monocytes. Similarly, granulocytes internalized PDS NPs into clusters, while also displaying very strong, diffuse intracellular signals suggesting possible endosomal escape (Figure 6B). Even though the star polymers were small (<10 nm by TEM), the PDS NPs were largely restricted from the nucleus. BSPA control NPs were rarely observed associating with granulocytes. In contrast, B-cell-localized NPs were restricted to the cell surface (Figure 6C), consistent with their nonphagocytic nature. T cells very rarely associated with any NPs, although

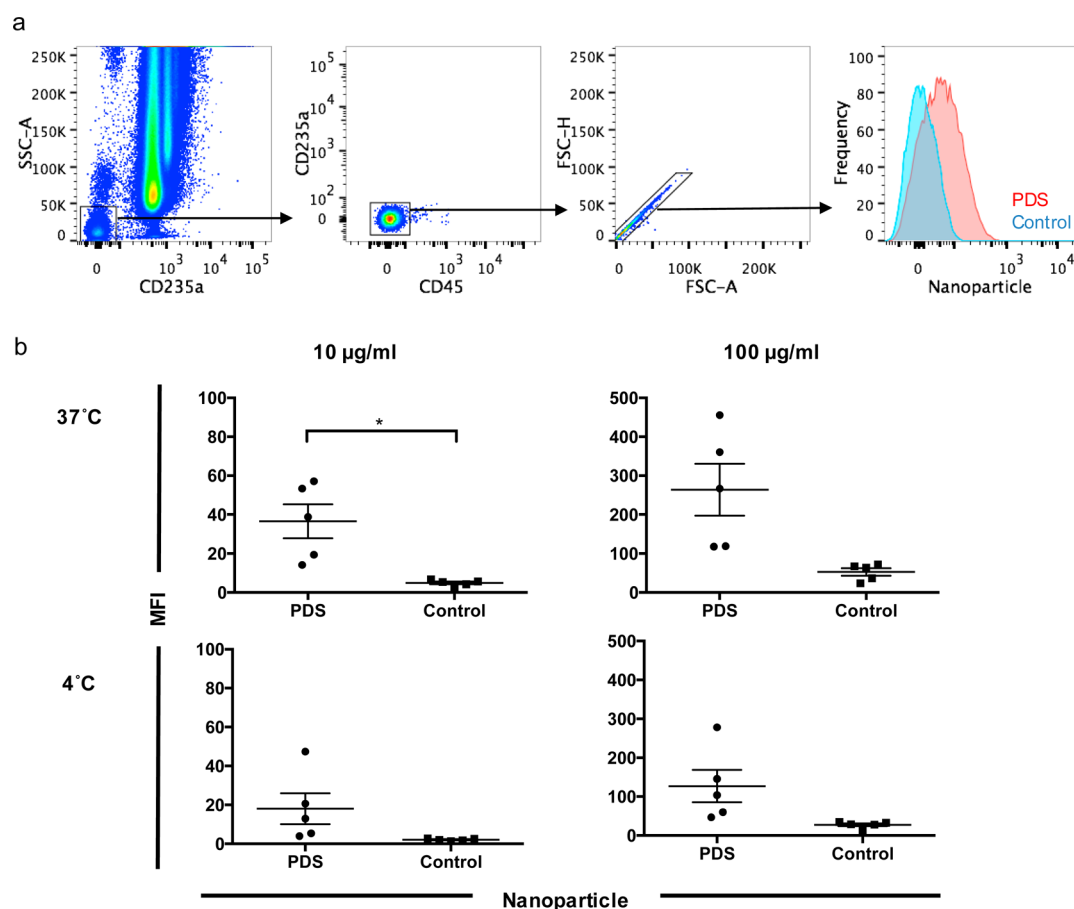


Figure 8. PDS nanoparticles display enhanced binding to platelets. PDS and BSPA control nanoparticles were incubated with freshly drawn, ACD-B treated human blood for 1 h, at 4 or 37 °C. Free nanoparticles were removed by washing before phenotyping on ice. Platelet association with Cy5-labeled nanoparticles was determined by flow cytometry and represented by a median fluorescence index (MFI). (a) Representative gating tree from a single donor, demonstrating association at 10 µg mL⁻¹, 37 °C. Red histograms represent platelet association with PDS nanoparticles, blue with control nanoparticles. (b) Summary of association profiles at 37 °C (top) and 4 °C (bottom) from 5 healthy donors across independent experiments. * $p < 0.05$.

when NPs did associate with T cells (Figure 6D), they remained on the cell surface.

3.6. RBC Association Is Marginally Altered by PDS Functionality. RBCs are the most common cell type in blood, outnumbering WBCs by ~1000-fold. These cells are impaired in a number of genetic diseases such as sickle-cell disease and targeted by certain infections, such as malaria parasites. Although RBCs do not leave the circulation, many studies have examined the utility of RBCs for cellular hitchhiking of NPs to intravascular targets³⁸ due to their long circulating lifetimes of approximately 120 days.^{39,40} We therefore assessed the association of star polymer NPs with this important cell subset (Figure 7). Gating on RBC (Figure 7A) demonstrated no association preference at 10 µg mL⁻¹ at either 4 or 37 °C (Figure 7B). There was a large variability in RBC association with PDS star polymers across the donors tested at 100 µg mL⁻¹, and there was a nonsignificant trend ($p = 0.0625$) toward an increased RBC association preference for PDS over control NPs at this concentration.

3.7. PDS Functionality Enhances Association with Platelets. Platelets adhere to damaged endothelium, where they become activated and recruit additional platelets and clotting factors to form a platelet plug. Platelets are an interesting component of blood, which could be used to direct therapeutics to sites of vascular damage and were therefore

assessed for NP association (Figure 8). After gating on platelets (Figure 8A), we assessed NP-platelet association in 5 healthy donors (Figure 8B). At 37 °C, we observed a large association preference for PDS NPs at 10 µg mL⁻¹ and 100 µg mL⁻¹ (5.0- and 7.5-fold, respectively). At 4 °C, there was still a trend for increased platelet association with PDS NPs, suggesting a biological process (e.g., uptake) is not solely responsible for the enhanced association.

3.8. Platelets Are Not Activated by Star Polymers. Aberrant platelet activation is associated with cardiovascular disease and NPs that lead to platelet activation could potentially have long-term undesirable side effects. Since the PDS NPs had enhanced platelet association, we examined how these NPs might affect platelet activation status. We studied the expression of the surface activation marker CD62P (P-selectin)^{32,33} immediately after incubating particles in fresh ACD-anti-coagulated blood and identified single platelets by flow cytometry (Figure 9A). This assay is traditionally performed at room temperature, where higher platelet activation responses are observed.³³ Incubation of the blood with 10 µM ADP, a known positive control of platelet activation, increased the number of CD62P-expressing platelets ~2-fold compared to PBS incubations across 6 separate blood donors (Figure 9B). Incubating with either NP at 1–100 µg mL⁻¹ did not increase CD62P expression above baseline levels.

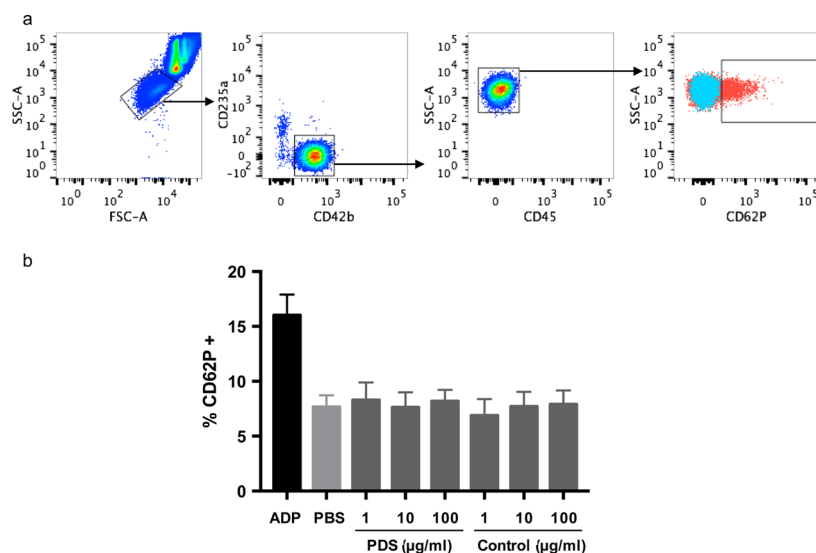


Figure 9. Platelet activation (CD62P) is not altered by PDS or BSPA control nanoparticles. Stars were added to 100 μL of freshly drawn, ACD-B treated blood and incubated for 10 min before examining CD62P expression by flow cytometry. (a) Platelets were gated by low forward (FSC) and side scatter (SSC), before removing contaminating red blood cells and cell debris (CD42b+, CD235a-). CD45- events were selected to remove any contaminating white blood cells/debris. ADP (10 μM) was used as a positive control for CD62P activation (red), and activation gates were based on CD62P FMO (fluorescence minus one) samples (blue). (b) The percentage of platelets expressing CD62P is summarized from 6 healthy human donors across independent experiments.

4. DISCUSSION

The rational design of NPs can be used to target cell subtypes (using antibodies/aptamers/peptides) and/or functionalize NPs with low-fouling polymers such as PEG to reduce clearance. The small size of the multiarmed star polymers described herein (<10 nm by TEM) introduces design challenges when targeting with conventional moieties, such as antibodies, which can outsize the NP and therefore dramatically alter its properties. In this study, we used primary human blood to demonstrate how tuning the functional group of small star polymer NPs can direct their association profiles with key cellular components of the circulation.

Thiol-reactive groups have previously been used for the conjugation of antigen or other biomolecules onto NPs, while others have investigated thiol-reactive chemistries to enhance cell uptake or association with cell lines or purified cell subsets *in vitro*.^{7,11,41–43} One example is the PDS functional group, which is commonly used for peptide and protein modification due to its high rate of exchange with native or engineered free thiols.^{44–48} Harnessing both the high reactivity of the PDS group to thiols and the differential distribution of exofacial thiols on primary blood cells, we demonstrate that PDS functional groups can direct star polymer NPs with a mPEG brush corona to distinct cellular components in whole human blood—in effect, modeling systemic administration of these NPs.

The level of exofacial thiols expressed by hematopoietic cells is graded, with granulocytes > monocytes > lymphocytes (B cells > T cells) > RBC,^{4,5,11} although less is known about the relative exofacial thiol levels on dendritic cells and platelets. However, platelets express protein disulfide isomerase on their surface,⁴⁹ which catalyzes thiol–disulfide interchange⁵⁰ and may facilitate enhanced association with PDS star polymers. The multicellular nature of our human blood model captures competition between cell types, and the association of the PDS star polymers studied mirrors the ranking of exofacial thiols in blood cells. In contrast, BSPA control NPs displayed stealth

properties, and we observed relatively low association with phagocytic WBC, along with nonphagocytic WBC, RBC, and platelets. Altering the arm number and size of the PDS star polymers reported herein would likely alter their interactions with blood cell components and is currently under investigation. We note that blood proteins can also contain free thiol groups (such as albumin)⁴⁷ and may influence the availability of PDS star polymers to interact with blood cell components.

Many tumors express surface thiol groups and targeting tumors with NPs displaying PDS groups may allow for the efficient delivery of cytotoxic drugs or imaging agents.⁵¹ We speculate that incorporating a PDS group may also be beneficial for nanovaccinology applications. PDS star polymers displayed enhanced association with dendritic cells—professional antigen presenting cells essential in the immune response to vaccination. Moreover, B cell association was enhanced upon PDS incorporation. This may be beneficial in the treatment of B cell diseases, such as lymphomas, or manipulating humoral immunity for improved antibody responses to vaccination.

The utility of blood cells as natural NP carriers has been extensively explored. This concept, termed “cellular hitchhiking”, has been studied in cell lines and rodent models also with some success in avoiding immune clearance and improving tissue targeting.^{52,53} RBCs have been investigated for their ability to improve the pharmacokinetics (circulation) and biodistribution (enhanced lung targeting) of NPs.^{38,54} RBCs have low levels of free exofacial thiols,¹¹ which may explain the relatively low association we observed with PDS NPs. In contrast, monocytes display levels of exofacial thiols that far exceed RBCs and lymphocytes,¹¹ which is consistent with the high association of monocytes with PDS star polymers that we observed. Monocytes have a half-life of 20 h,⁵⁵ after which they extravasate from the circulation and become tissue macrophages. Following extravasation, these can migrate to inflamed tissues⁵⁶ or deep into hypoxic regions of tumors.⁵⁷ Monocytes have therefore served as Trojan horses to increase the delivery of therapeutics to sites of inflammation,⁵² tumors,^{58,59} and even

deliver these across the blood brain barrier.^{60,61} The PDS NPs described herein also demonstrated enhanced association with platelets, which have a circulating lifespan of 7–9 days.⁶² The engineering of NPs to mimic platelets has been investigated for the treatment of vascular injuries,⁶³ and hitchhiking NPs onto platelets represents another strategy to harness their innate ability to target vascular damage and/or alter hemostasis. We adapted our previously published whole blood assay^{15,16,18} to facilitate the study of platelet association and their activation state through examining the cell-surface molecule CD62P (P-selectin). The PDS NPs were nonactivating under the conditions studied; however, further safety studies are warranted.

5. CONCLUSIONS

Engineering PDS groups onto small star polymer NPs resulted in significant changes in NP association with a variety of human blood cell components and will likely alter intravenous biodistribution profiles. There are several potential applications in both tumor targeting and immune cell targeting for this technology that warrant further investigation.

■ ASSOCIATED CONTENT

■ Supporting Information

The Supporting Information is available free of charge on the ACS Publications website at DOI: 10.1021/acsami.6b15942.

Physical characterization summary of POEGA arms and POEGA star polymers, GPC analysis of arms and stars, fluorescence spectra and GPC chromatograms of Cy5-labeled stars (PDF)

■ AUTHOR INFORMATION

Corresponding Authors

*E-mail: thomas.p.davis@monash.edu.

*E-mail: skent@unimelb.edu.au.

ORCID

Joshua J. Glass: 0000-0001-9727-8356

Angus P. R. Johnston: 0000-0001-5611-4515

Thomas P. Davis: 0000-0003-2581-4986

Stephen J. Kent: 0000-0002-8539-4891

Present Address

#Beijing Laboratory of Biomedical Materials, Beijing University of Chemical Technology, Beijing 100029, China

Author Contributions

The manuscript was written through contributions of all authors. All authors have given approval to the final version of the manuscript.

Notes

The authors declare no competing financial interest.

■ ACKNOWLEDGMENTS

We thank Ms Sheilajen Alcantara, Ms Thakshila Amarasena and Ms Julia Prier for their technical assistance and advice. The authors acknowledge the facilities, and the scientific and technical assistance, of the Biological Optical Microscopy Platform, The University of Melbourne. Research was supported by the Australian Research Council Centre of Excellence in Convergent Bio-Nano Science and Technology (project number CE140100036). J.J.G acknowledges the support of an Australian Government Research Training

Program Scholarship. T.P.D wishes to acknowledge the award of an Australian Laureate Fellowship.

■ REFERENCES

- (1) Brannon-Peppas, L.; Blanchette, J. O. Nanoparticle and Targeted Systems for Cancer Therapy. *Adv. Drug Delivery Rev.* **2004**, *56* (11), 1649–1659.
- (2) Wong, C.; Stylianopoulos, T.; Cui, J.; Martin, J.; Chauhan, V. P.; Jiang, W.; Popović, Z.; Jain, R. K.; Bawendi, M. G.; Fukumura, D. Multistage Nanoparticle Delivery System for Deep Penetration into Tumor Tissue. *Proc. Natl. Acad. Sci. U. S. A.* **2011**, *108* (6), 2426–2431.
- (3) Pluen, A.; Boucher, Y.; Ramanujan, S.; McKee, T. D.; Gohongi, T.; di Tomaso, E.; Brown, E. B.; Izumi, Y.; Campbell, R. B.; Berk, D. A.; Jain, R. K. Role of Tumor–Host Interactions in Interstitial Diffusion of Macromolecules: Cranial Vs. Subcutaneous Tumors. *Proc. Natl. Acad. Sci. U. S. A.* **2001**, *98* (8), 4628–4633.
- (4) Lawrence, D. A.; Song, R.; Weber, P. Surface Thiols of Human Lymphocytes and Their Changes after in Vitro and in Vivo Activation. *J. Leukocyte Biol.* **1996**, *60* (5), 611–618.
- (5) Sahaf, B.; Heydari, K.; Herzenberg, L. A.; Herzenberg, L. A. Lymphocyte Surface Thiol Levels. *Proc. Natl. Acad. Sci. U. S. A.* **2003**, *100* (7), 4001–4005.
- (6) Yan, Y.; Wang, Y.; Heath, J. K.; Nice, E. C.; Caruso, F. Cellular Association and Cargo Release of Redox-Responsive Polymer Capsules Mediated by Exofacial Thiols. *Adv. Mater.* **2011**, *23* (34), 3916–3921.
- (7) Torres, A. G.; Gait, M. J. Exploiting Cell Surface Thiols to Enhance Cellular Uptake. *Trends Biotechnol.* **2012**, *30* (4), 185–190.
- (8) Ceccarelli, J.; Delfino, L.; Zappia, E.; Castellani, P.; Borghi, M.; Ferrini, S.; Tosetti, F.; Rubartelli, A. The Redox State of the Lung Cancer Microenvironment Depends on the Levels of Thioredoxin Expressed by Tumor Cells and Affects Tumor Progression and Response to Prooxidants. *Int. J. Cancer* **2008**, *123* (8), 1770–1778.
- (9) Pendyala, L.; Velagapudi, S.; Toth, K.; Zdanowicz, J.; Glaves, D.; Slocum, H.; Perez, R.; Huben, R.; Creaven, P. J.; Raghavan, D. Translational Studies of Glutathione in Bladder Cancer Cell Lines and Human Specimens. *Clin. Cancer Res.* **1997**, *3* (5), 793–798.
- (10) Moreno-Merlo, F.; Nicklee, T.; Hedley, D. Association between Tissue Hypoxia and Elevated Non-Protein Sulphydryl Concentrations in Human Cervical Carcinoma Xenografts. *Br. J. Cancer* **1999**, *81* (6), 989–988.
- (11) Stephan, M. T.; Moon, J. J.; Um, S. H.; Bershteyn, A.; Irvine, D. J. Therapeutic Cell Engineering with Surface-Conjugated Synthetic Nanoparticles. *Nat. Med.* **2010**, *16* (9), 1035–1041.
- (12) Reuter, A.; Panozza, S. E.; Macri, C.; Dumont, C.; Li, J.; Liu, H.; Segura, E.; Vega-Ramos, J.; Gupta, N.; Caminschi, I.; Villadangos, J. A.; Johnston, A. P. R.; Mintern, J. D. Criteria for Dendritic Cell Receptor Selection for Efficient Antibody-Targeted Vaccination. *J. Immunol.* **2015**, *194* (6), 2696–2705.
- (13) Kastenmüller, W.; Kastenmüller, K.; Kurts, C.; Seder, R. A. Dendritic Cell-Targeted Vaccines – Hope or Hype? *Nat. Rev. Immunol.* **2014**, *14* (10), 705–711.
- (14) Lippi, G.; Franchini, M.; Targher, G. Arterial Thrombus Formation in Cardiovascular Disease. *Nat. Rev. Cardiol.* **2011**, *8* (9), 502–512.
- (15) Cui, J.; De Rose, R.; Alt, K.; Alcantara, S.; Paterson, B. M.; Liang, K.; Hu, M.; Richardson, J. J.; Yan, Y.; Jeffery, C. M.; Price, R. I.; Peter, K.; Hagemeyer, C. E.; Donnelly, P. S.; Kent, S. J.; Caruso, F. Engineering Poly(Ethylene Glycol) Particles for Improved Biodistribution. *ACS Nano* **2015**, *9* (2), 1571–1580.
- (16) De Rose, R.; Zelikin, A. N.; Johnston, A. P.; Sexton, A.; Chong, S.-F.; Cortez, C.; Mulholland, W.; Caruso, F.; Kent, S. J. Binding, Internalization, and Antigen Presentation of Vaccine-Loaded Nano-engineered Capsules in Blood. *Adv. Mater.* **2008**, *20* (1–6), 4698–4703.
- (17) Baumann, D.; Hofmann, D.; Nullmeier, S.; Panther, P.; Dietze, C.; Musyanovych, A.; Ritz, S.; Landfester, K.; Mailänder, V. Complex Encounters: Nanoparticles in Whole Blood and Their Uptake into

Different Types of White Blood Cells. *Nanomedicine (London, U. K.)* **2013**, *8* (5), 699–713.

(18) Mann, S. K.; Dufour, A.; Glass, J. J.; De Rose, R.; Kent, S. J.; Such, G. K.; Johnston, A. P. R. Tuning the Properties of Ph Responsive Nanoparticles to Control Cellular Interactions in Vitro and Ex Vivo. *Polym. Chem.* **2016**, *7* (38), 6015–6024.

(19) Ren, J. M.; McKenzie, T. G.; Fu, Q.; Wong, E. H.; Xu, J.; An, Z.; Shanmugam, S.; Davis, T. P.; Boyer, C.; Qiao, G. G. Star Polymers. *Chem. Rev.* **2016**, *116* (12), 6743–6836.

(20) Liu, J.; Duong, H.; Whittaker, M. R.; Davis, T. P.; Boyer, C. Synthesis of Functional Core, Star Polymers Via Raft Polymerization for Drug Delivery Applications. *Macromol. Rapid Commun.* **2012**, *33* (9), 760–766.

(21) Boyer, C.; Teo, J.; Phillips, P.; Erlich, R. B.; Sagnella, S.; Sharbeen, G.; Dwarthe, T.; Duong, H. T.; Goldstein, D.; Davis, T. P.; Kavallaris, M.; McCarroll, J. Effective Delivery of Sirna into Cancer Cells and Tumors Using Well-Defined Biodegradable Cationic Star Polymers. *Mol. Pharmaceutics* **2013**, *10* (6), 2435–2444.

(22) Syrett, J. A.; Haddleton, D. M.; Whittaker, M. R.; Davis, T. P.; Boyer, C. Functional, Star Polymeric Molecular Carriers, Built from Biodegradable Microgel/Nanogel Cores. *Chem. Commun.* **2011**, *47* (5), 1449–1451.

(23) Ferreira, J.; Syrett, J.; Whittaker, M.; Haddleton, D.; Davis, T. P.; Boyer, C. Optimizing the Generation of Narrow Polydispersity ‘Arm-First’ star Polymers Made Using Raft Polymerization. *Polym. Chem.* **2011**, *2* (8), 1671–1677.

(24) Khor, S. Y.; Hu, J.; McLeod, V. M.; Quinn, J. F.; Williamson, M.; Porter, C. J.; Whittaker, M. R.; Kaminskas, L. M.; Davis, T. P. Molecular Weight (Hydrodynamic Volume) Dictates the Systemic Pharmacokinetics and Tumour Disposition of Polypeg Star Polymers. *Nanomedicine* **2015**, *11* (8), 2099–2108.

(25) Li, Y.; Duong, H. T.; Laurent, S.; MacMillan, A.; Whan, R. M.; Elst, L. V.; Muller, R. N.; Hu, J.; Lowe, A.; Boyer, C.; Davis, T. P. Nanoparticles Based on Star Polymers as Theranostic Vectors: Endosomal-Triggered Drug Release Combined with Mri Sensitivity. *Adv. Healthcare Mater.* **2015**, *4* (1), 148–156.

(26) Khor, S. Y.; Hu, J.; McLeod, V. M.; Quinn, J. F.; Porter, C. J.; Whittaker, M. R.; Kaminskas, L. M.; Davis, T. P. The Pharmacokinetics and Biodistribution of a 64 Kda Polypeg Star Polymer after Subcutaneous and Pulmonary Administration to Rats. *J. Pharm. Sci.* **2016**, *105* (1), 293–300.

(27) Liu, J.; Bulmus, V.; Barner-Kowollik, C.; Stenzel, M. H.; Davis, T. P. Direct Synthesis of Pyridyl Disulfide-Terminated Polymers by Raft Polymerization. *Macromol. Rapid Commun.* **2007**, *28* (3), 305–314.

(28) Li, Y.; Duong, H. T.; Jones, M. W.; Basuki, J. S.; Hu, J.; Boyer, C.; Davis, T. P. Selective Postmodification of Copolymer Backbones Bearing Different Activated Esters with Disparate Reactivities. *ACS Macro Lett.* **2013**, *2* (10), 912–917.

(29) Ho, T. H.; Levere, M.; Soutif, J.-C.; Montembault, V.; Pascual, S.; Fontaine, L. Synthesis of Thermoresponsive Oxazolone End-Functional Polymers for Reactions with Amines Using Thiol-Michael Addition “Click” Chemistry. *Polym. Chem.* **2011**, *2* (6), 1258–1260.

(30) Kotecha, N.; Krutzik, P. O.; Irish, J. M. Web-Based Analysis and Publication of Flow Cytometry Experiments. *Curr. Protoc. Cytom.* **2010**, *10.17.1–10.17.24*.

(31) Amir, E. D.; Davis, K. L.; Tadmor, M. D.; Simonds, E. F.; Levine, J. H.; Bendall, S. C.; Shenfeld, D. K.; Krishnaswamy, S.; Nolan, G. P.; Pe’er, D. Visne Enables Visualization of High Dimensional Single-Cell Data and Reveals Phenotypic Heterogeneity of Leukemia. *Nat. Biotechnol.* **2013**, *31* (6), 545–552.

(32) Bihari, P.; Holzer, M.; Praetner, M.; Fent, J.; Lerchenberger, M.; Reichel, C. A.; Rehberg, M.; Lakatos, S.; Krombach, F. Single-Walled Carbon Nanotubes Activate Platelets and Accelerate Thrombus Formation in the Microcirculation. *Toxicology* **2010**, *269* (2), 148–154.

(33) Ramström, S.; Södergren, A. L.; Tynngård, N.; Lindahl, T. L. Platelet Function Determined by Flow Cytometry: New Perspectives? *Semin. Thromb. Hemostasis* **2016**, *42* (03), 268–281.

(34) Dobrovolskaia, M. A.; Patri, A. K.; Simak, J.; Hall, J. B.; Semberova, J.; De Paoli Lacerda, S. H.; McNeil, S. E. Nanoparticle Size and Surface Charge Determine Effects of Pamam Dendrimers on Human Platelets in Vitro. *Mol. Pharmaceutics* **2012**, *9* (3), 382–393.

(35) Sliwkowski, M. X.; Mellman, I. Antibody Therapeutics in Cancer. *Science* **2013**, *341* (6151), 1192–1198.

(36) Weiner, G. J. Building Better Monoclonal Antibody-Based Therapeutics. *Nat. Rev. Cancer* **2015**, *15* (6), 361–370.

(37) Santana-Davila, R.; Bhatia, S.; Chow, L. Q. Harnessing the Immune System as a Therapeutic Tool in Virus-Associated Cancers. *JAMA Oncol.* **2017**, *3*, 106–112.

(38) Villa, C. H.; Anselmo, A. C.; Mitragotri, S.; Muzykantov, V. Red Blood Cells: Supercarriers for Drugs, Biologicals, and Nanoparticles and Inspiration for Advanced Delivery Systems. *Adv. Drug Delivery Rev.* **2016**, *106*, 88–103.

(39) Shemin, D.; Rittenberg, D. The Life Span of the Human Red Blood Cell. *J. Biol. Chem.* **1946**, *166* (2), 627–636.

(40) Hattangadi, S. M.; Wong, P.; Zhang, L.; Flygare, J.; Lodish, H. F. From Stem Cell to Red Cell: Regulation of Erythropoiesis at Multiple Levels by Multiple Proteins, Rnas, and Chromatin Modifications. *Blood* **2011**, *118* (24), 6258–6268.

(41) Digilio, G.; Menchise, V.; Gianolio, E.; Catanzaro, V.; Carrera, C.; Napolitano, R.; Fedeli, F.; Aime, S. Exofacial Protein Thiols as a Route for the Internalization of Gd (Iii)-Based Complexes for Magnetic Resonance Imaging Cell Labeling. *J. Med. Chem.* **2010**, *53* (13), 4877–4890.

(42) Kommareddy, S.; Amiji, M. Preparation and Evaluation of Thiol-Modified Gelatin Nanoparticles for Intracellular DNA Delivery in Response to Glutathione. *Bioconjugate Chem.* **2005**, *16* (6), 1423–1432.

(43) Saito, G.; Swanson, J. A.; Lee, K.-D. Drug Delivery Strategy Utilizing Conjugation Via Reversible Disulfide Linkages: Role and Site of Cellular Reducing Activities. *Adv. Drug Delivery Rev.* **2003**, *55* (2), 199–215.

(44) Lybaert, L.; Vanparijs, N.; Fierens, K.; Schuijs, M.; Nuhn, L.; Lambrecht, B. N.; De Geest, B. G. A Generic Polymer–Protein Ligation Strategy for Vaccine Delivery. *Biomacromolecules* **2016**, *17* (3), 874–881.

(45) van der Vlies, A. J.; O’Neil, C. P.; Hasegawa, U.; Hammond, N.; Hubbell, J. A. Synthesis of Pyridyl Disulfide-Functionalized Nanoparticles for Conjugating Thiol-Containing Small Molecules, Peptides, and Proteins. *Bioconjugate Chem.* **2010**, *21* (4), 653–662.

(46) Boyer, C.; Liu, J.; Bulmus, V.; Davis, T. P. Raft Polymer End-Group Modification and Chain Coupling/Conjugation Via Disulfide Bonds. *Aust. J. Chem.* **2009**, *62* (8), 830–847.

(47) Liu, J.; Liu, H.; Bulmus, V.; Tao, L.; Boyer, C.; Davis, T. P. A Simple Methodology for the Synthesis of Heterotelechelic Protein–Polymer–Biomolecule Conjugates. *J. Polym. Sci., Part A: Polym. Chem.* **2010**, *48* (6), 1399–1405.

(48) Roth, P. J.; Boyer, C.; Lowe, A. B.; Davis, T. P. Raft Polymerization and Thiol Chemistry: A Complementary Pairing for Implementing Modern Macromolecular Design. *Macromol. Rapid Commun.* **2011**, *32* (15), 1123–1143.

(49) Essex, D. W.; Chen, K.; Swiatkowska, M. Localization of Protein Disulfide Isomerase to the External Surface of the Platelet Plasma Membrane. *Blood* **1995**, *86* (6), 2168–2173.

(50) Jiang, X.-M.; Fitzgerald, M.; Grant, C. M.; Hogg, P. J. Redox Control of Exofacial Protein Thiols/Disulfides by Protein Disulfide Isomerase. *J. Biol. Chem.* **1999**, *274* (4), 2416–2423.

(51) Shahnaz, G.; Kremser, C.; Reinisch, A.; Vetter, A.; Laffleur, F.; Rahmat, D.; Iqbal, J.; Dünnhaupt, S.; Salvenmoser, W.; Tessadri, R.; Griesser, U.; Bernkop-Schnurch, A. Efficient Mri Labeling of Endothelial Progenitor Cells: Design of Thiolated Surface Stabilized Superparamagnetic Iron Oxide Nanoparticles. *Eur. J. Pharm. Biopharm.* **2013**, *85* (3), 346–355.

(52) Anselmo, A. C.; Gilbert, J. B.; Kumar, S.; Gupta, V.; Cohen, R. E.; Rubner, M. F.; Mitragotri, S. Monocyte-Mediated Delivery of Polymeric Backpacks to Inflamed Tissues: A Generalized Strategy to

Deliver Drugs to Treat Inflammation. *J. Controlled Release* **2015**, *199*, 29–36.

(53) Anselmo, A. C.; Mitragotri, S. Cell-Mediated Delivery of Nanoparticles: Taking Advantage of Circulatory Cells to Target Nanoparticles. *J. Controlled Release* **2014**, *190*, 531–541.

(54) Anselmo, A. C.; Gupta, V.; Zern, B. J.; Pan, D.; Zakrewsky, M.; Muzykantov, V.; Mitragotri, S. Delivering Nanoparticles to Lungs While Avoiding Liver and Spleen through Adsorption on Red Blood Cells. *ACS Nano* **2013**, *7* (12), 11129–11137.

(55) Yona, S.; Kim, K.-W.; Wolf, Y.; Mildner, A.; Varol, D.; Breker, M.; Strauss-Ayali, D.; Viukov, S.; Guillems, M.; Misharin, A.; Hume, D. A.; Perlman, H.; Malissen, B.; Zelzer, E.; Jung, S. Fate Mapping Reveals Origins and Dynamics of Monocytes and Tissue Macrophages under Homeostasis. *Immunity* **2013**, *38* (1), 79–91.

(56) Shi, C.; Pamer, E. G. Monocyte Recruitment During Infection and Inflammation. *Nat. Rev. Immunol.* **2011**, *11* (11), 762–774.

(57) Murdoch, C.; Giannoudis, A.; Lewis, C. E. Mechanisms Regulating the Recruitment of Macrophages into Hypoxic Areas of Tumors and Other Ischemic Tissues. *Blood* **2004**, *104* (8), 2224–2234.

(58) Smith, B. R.; Ghosn, E. E. B.; Rallapalli, H.; Prescher, J. A.; Larson, T.; Herzenberg, L. A.; Gambhir, S. S. Selective Uptake of Single-Walled Carbon Nanotubes by Circulating Monocytes for Enhanced Tumour Delivery. *Nat. Nanotechnol.* **2014**, *9* (6), 481–487.

(59) Choi, J.; Kim, H.-Y.; Ju, E. J.; Jung, J.; Park, J.; Chung, H.-K.; Lee, J. S.; Lee, J. S.; Park, H. J.; Song, S. Y.; Jeong, S.-Y.; Choi, E. K. Use of Macrophages to Deliver Therapeutic and Imaging Contrast Agents to Tumors. *Biomaterials* **2012**, *33* (16), 4195–4203.

(60) Dou, H.; Grotepas, C. B.; McMillan, J. M.; Destache, C. J.; Chaubal, M.; Werling, J.; Kipp, J.; Rabinow, B.; Gendelman, H. E. Macrophage Delivery of Nanoformulated Antiretroviral Drug to the Brain in a Murine Model of Neuroaids. *J. Immunol.* **2009**, *183* (1), 661–669.

(61) Choi, M.-R.; Bardhan, R.; Stanton-Maxey, K. J.; Badve, S.; Nakshatri, H.; Stantz, K. M.; Cao, N.; Halas, N. J.; Clare, S. E. Delivery of Nanoparticles to Brain Metastases of Breast Cancer Using a Cellular Trojan Horse. *Cancer Nanotechnol.* **2012**, *3* (1–6), 47–54.

(62) Harker, L. A.; Roskos, L. K.; Marzec, U. M.; Carter, R. A.; Cherry, J. K.; Sundell, B.; Cheung, E. N.; Terry, D.; Sheridan, W. Effects of Megakaryocyte Growth and Development Factor on Platelet Production, Platelet Life Span, and Platelet Function in Healthy Human Volunteers. *Blood* **2000**, *95* (8), 2514–2522.

(63) Anselmo, A. C.; Modery-Pawłowski, C. L.; Menegatti, S.; Kumar, S.; Vogus, D. R.; Tian, L. L.; Chen, M.; Squires, T. M.; Sen Gupta, A.; Mitragotri, S. Platelet-Like Nanoparticles: Mimicking Shape, Flexibility, and Surface Biology of Platelets to Target Vascular Injuries. *ACS Nano* **2014**, *8* (11), 11243–11253.